EVAPORATION IN THE ATACAMA DESERT

FELIPE LOBOS ROCO

Propositions

1. Evaporation in the Atacama desert, the driest place on earth, is unlimited by available water

   (this thesis)

2. In the Altiplano of the Atacama Desert, salt-lake evaporation suffocates itself in the absence of wind

   (this thesis)

3. As in science, society benefits more from collaboration than competition

4. Applying science-based actions in non-English-speaking local communities is hampered by the fact that scientific publications are written in English

5. The effort put into writing a scientific paper negatively correlates with the size of the audience it reaches

6. Sandwich and full-contracted PhD students are expected to produce a thesis with equal requirements under unequal working conditions

Propositions belonging to the thesis, entitled
Evaporation in the Atacama Desert

Felipe Lobos Roco
Wageningen, 29 March 2022

Evaporation in the Atacama Desert

Felipe Lobos Roco

Thesis committee

Promotor:
Prof. Dr J. Vilà Guerau de Arellano
Professor of Meteorology
Wageningen University & Research

Co-promotors:
Dr O.K. Hartogensis
Researcher, Meteorology and Air Quality group
Wageningen University & Research

Dr F. Suárez Poch
Associate Professor, Hydraulic and Environmental Engineering Department
Pontificia Universidad Católica de Chile

Other members:
Dr A.J. Teuling, Wageningen University & Research
Prof. Dr D.G. Miralles, Ghent University, Belgium
Dr A.M.J. Coenders, Delft University of Technology
Dr A. Graf, Forschungszentrum Jülich, Germany

This research was conducted under the auspices of the Graduate School
for Socio-Economic and Natural Sciences of the Environment (SENSE)

Evaporation in the Atacama Desert

Felipe Lobos Roco

Thesis
submitted in fulfilment of the requirements for the degree of doctor
at Wageningen University
by the authority of the Rector Magnificus,
Prof. Dr A.P.J. Mol,
in the presence of the
Thesis Committee appointed by the Academic Board
to be defended in public
on 29 March, 2022
at 4 p.m. in the Aula.

Felipe Lobos Roco
Evaporation in the Atacama Desert
210 pages.

PhD thesis, Wageningen University, Wageningen, NL (2022)
With references, with summary in English

DOI: https://doi.org/10.18174/564760
ISBN 978-94-6447-116-8

Summary

Understanding evaporation in arid regions is essential for climate change assessment and optimizing water resources management under a changing climate. This thesis analyses the physical processes that govern local evaporation in a representative salt flat setting at the Altiplano region of the Atacama Desert. Such physical processes are analyzed from climatic to sub-diurnal scales. Moreover, regional (>100 km) to local (<1 km) scales are integrated, through the analysis of the ocean-desert circulation and its influences on the atmospheric boundary layer and surface fluxes. Firstly, findings show that wind-driven turbulence is the primary evaporation controller at the sub-diurnal scale, whereas radiation plays a major role at the seasonal scale. Secondly, at the local scale, surface fluxes are mainly controlled by mechanical turbulence, which is only present in the afternoon due to a regional-scale flow resulting from the thermal contrast between the cool Pacific Ocean and the warm Atacama Desert. Thirdly, the regional flow that triggers evaporation in the Altiplano origins from the marine boundary layer, whose stability regime dominates the formation of fog and the inland moisture transport. Finally, the role of surface heterogeneity on turbulent fluxes measurements is quantified at the sub-kilometer scale, where footprint and MOST functions play an important role. This thesis contributes to untangling and linking processes driving evaporation from local to regional-scale and from sub-diurnal to inter-annual scale, across confined saline lakes in arid regions.

Resumen

Investigar los pocesos que controlan la evaporación en regiones áridas es esencial para mejorar nuestra comprensión del cambio climático, su impacto, y optimizar el manejo de los recursos hídricos bajo un clima cambiante. Esta tesis investiga los procesos físicos que gobiernan la evaporación local en un típico salar del Altiplano del desierto de Atacama. Estos procesos físicos son analizados desde escalas climáticas a sub diurnas. En nuestro estudio ponemos especial énfasis en integrar desde escalas regionales (>100 km) a locales (<1 km) a través del análisis de la circulación océano-desierto y su influencia en la capa límite y los flujos superficiales. Primero, nuestros hallazgos muestran que la turbulencia impulsada por el viento es el principal controlador de la evaporación a escala sub diurna, mientras que la radiación juega un papel más preponderante a escala estacional. Segundo, a escala local, los flujos superficiales son controlados principalmente por turbulencia mecánica (cizalladura) impulsada por el viento, la cual está presente exclusivamente durante la tarde. Este viento a escala regional se produce debido al contraste térmico entre un frío océano Pacífico y un desierto de Atacama caliente. Tercero, el flujo a escala regional que controla la evaporación en el Altiplano se origina en la capa límite marina, cuyo régimen de estabilidad domina la formación de niebla y el transporte de humedad hacia el interior del continente. Finalmente, el rol que tiene la heterogeneidad de la superficie en la medición de los flujos turbulentos se cuantifica a escala sub kilométrica, donde la huella de las mediciones y las funciones de la Teoría de Similitud de Monin-Obukhov juegan un papel importante. El resultado final de este trabajo doctoral es una mejora en la comprensión de los procesos físicos y sus interconexiones en escalas espaciales y temporales que gobiernan la evaporación en lagos salinos presentes en regiones áridas.

Contents

Chapter 1

Introduction

1.1 Motivation

Evapotranspiration is a turbulent exchange process that has enormous implications for Earth's water, energy, and carbon balances (McColl et al., 2019). It plays a key role in the interchange between the water and surface energy budgets of the land and atmosphere. Evapotranspiration, understood as the mass- (water vapor) or energy (latent heat) exchange of plants (transpiration), and soil and water surfaces (evaporation), connects the water and energy balance (Moene & Van Dam, 2014). In arid regions, such as the Atacama Desert, evaporation from open water is an important component in the water cycle, as lakes represent highly localized pathways for evaporation in a landscape devoid of moisture (Suárez et al., 2020). Figure 1.1 shows the dramatic seasonal changes in the surface area of a shallow saline lake in the Altiplano region (highlands) of the Atacama Desert. These significant spatial and temporal changes show the importance of evaporation for water resource management and the need to understand the physical processes that govern it. Although understanding the evaporation in this area has significant social relevance in terms of water availability, accurately quantifying this phenomenon poses a scientific challenge (Houston, 2006a).

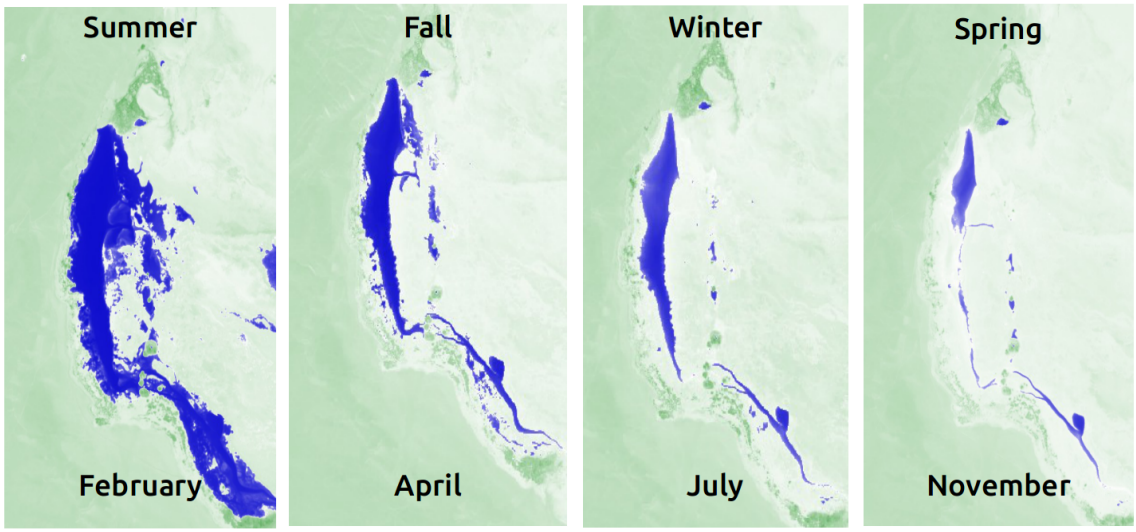

Figure 1.1: Seasonal variability of the shallow saline lake in the Salar del Huasco in 2018, as viewed by the normalized difference water index (NDWI) from Copernicus Sentinel data from 2019 processed by Sentinel Hub.

The social relevance of understanding evaporation relies on the complexity of water management in arid regions where water resources are in high demand, but scarcely available. Two factors describe this complexity, triggering environmental-social conflicts between different stakeholders, such as the mining industry, indigenous inhabitants and fragile ecosystems (Budds, 2004). First, surface waters in the desert are geographically

confined to a few specific places such as rivers, wetlands resulting from groundwater upwelling, and shallow lakes in closed basins (Houston 2006). This confined localization makes it difficult to access water resources, mostly underground, increasing the pressure to exploit them. Second, the tradable water rights promoted by the Water Code in Chile concentrate water accessibility into the industry to the detriment of other social actors. An industry is currently putting additional pressure on the water demand, for example, is lithium mining. In this industry, groundwater is extracted and subsequently evaporated in enormous plains. With 9.2 million tons (USGS, 2021), Chile possesses large lithium reservoirs, and the demand for lithium is increasing globally due to its role in new energy technologies. Unfortunately, lithium and related-minerals production also represent an environmental threat since groundwater is taken from natural reservoirs that sustain fragile ecosystems. This combination of low water accessibility and tradable water rights concentration define the complex water management in the Atacama Desert. In this context, evaporation plays a fundamental role in accurately quantifying water resources. Therefore, understanding evaporation will, for example, improve the water use efficiency in such industries, contributing to finding an equilibrium between economic growth and environmental preservation.

The interplay of the scientific challenge that evaporation presents in the Atacama Desert and its social relevance is sketched in Figure 1.2 as an interaction between the will to understand the processes that drive evaporation, which acts at a range of spatiotemporal scales (top) and the need to quantify evaporation for water management (bottom) through measurement (left) and modelling methodologies (right). The quantification of evaporation is addressed directly through in-situ observations. Based on observations, we can infer relationships to improve the representation of the key physical processes governing evaporation. These physical relationships, or parameterizations, can then be tested and implemented in hydrometeorological models to improve larger-scale evaporation estimates. Where observations typically represent the local conditions and, as such, overlook processes occurring at larger scales, with numerical models we quantify and understand the physical processes that act at larger spatial scales. In addition, numerical models allow to quantify evaporation where observations are limited.

Regarding observations, large global networks such as Fluxnet (Pastorello et al., 2020) or Ameriflux (Ameriflux, 2021) do not have surface flux stations in the Atacama Desert, which is evidence of the low evaporation data density in arid regions. This lack of observations is mainly due to the inhospitable geography of the desert characterized by strong topographic gradients and limited accessibility. Hydrometeorological models often fail at accurately representing evaporation in arid regions, as evaporation is limited to localized wet surfaces, which are poorly represented in models. Examples are lakes, wetlands, and salt flats, which are usually smaller in size than the spatial resolution in hydrometeorological models. Moreover, the complexity of the multiscale processes involved in evaporation, such as mesoscale atmospheric circulation between the ocean

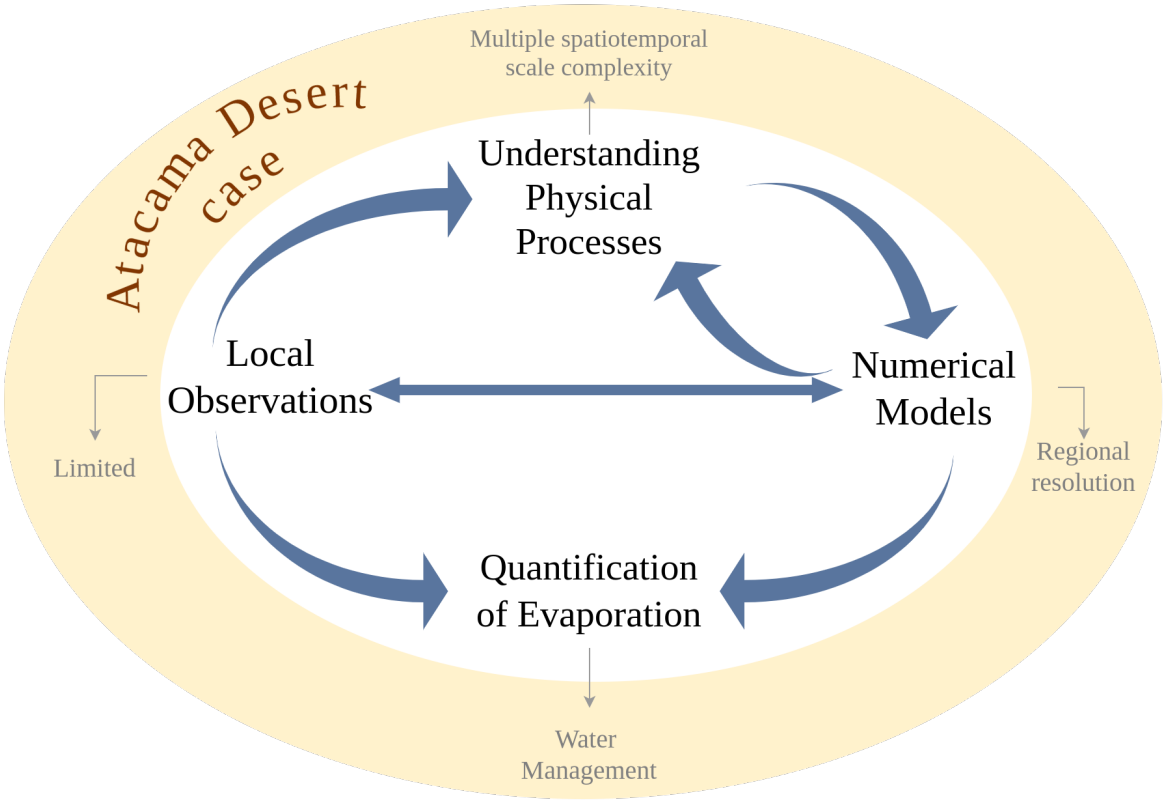

Figure 1.2: The scientific challenge of understanding evaporation in the Atacama Desert addressed in this thesis. Arrows indicate the methodological flow followed; yellow ring depicts the Atacama Desert case.

and the desert, the diurnal evolution of the atmospheric boundary layer (ABL), surface heterogeneity and long-term temporal variability, is challenging to disentangle. In this thesis, we combine a measuring and modelling strategy that contributes to solve this scientific problem.

Evaporation in the Atacama Desert has been studied using different approaches involving the hydrogeology, hydrology, and meteorology of the region. Johnson et al. (2010) assessed daily bare soil evaporation to understand relationships that could be used to relate evaporation with the water table depth all around the Chilean Altiplano. Uribe et al. (2015) developed a hydrological model in the Salar del Huasco basin where evaporation was estimated using information from evaporation pans, and regional changes in evaporation were calculated as a function of elevation. In the same way, Houston (2006a) studied the spatiotemporal variations of potential evaporation in the Atacama Desert, using empirical data from evaporation pans. This study also introduced the first investigations of a long-term evaporation (1977-1991) analysis and its relationship with the ENSO phenomenon. At a more local scale, Kampf et al. (2005) measured turbulent

fluxes from heterogeneous surfaces in the Salar de Atacama, analysing their diurnal cycles in a seasonal campaign. de la Fuente & Meruane (2017) developed a thermodynamic model to predict potential evaporation in Salar del Huasco using meteorological reanalysis data. Nonetheless, the hydrological perspective upon which these evaporation studies were made, missed the link with the atmospheric processes that govern it.

Concerning the link of the evaporation and the meteorology of the study area, previous studies have demonstrated how large-scale atmospheric phenomena are influenced by the Pacific Ocean, steep Andean topography, and the Amazon basin at different scales. For example, Garreaud et al. (2003) analysed the climatic conditions of the Altiplano region from interseasonal to glacial-interglacial timescales. Rutllant & Ulriksen (1979) and Rutllant et al. (2003) described the dry regional atmospheric flow on the occidental face of the Andes in the Atacama Desert. Falvey & Garreaud (2005) studied the summer westward airflow from the Amazon basin, which transports a significant amount of moisture over the Altiplano, defining the onset of the rainy season. Although the main large-scale atmospheric circulations have been described for this region, the connection between these atmospheric circulations and evaporation has received little attention.

Supported by these pioneering studies, we laid the plans for this Ph.D. thesis investigation. We aimed to understand the physical mechanisms that connect surface conditions to the ABL dynamics and its subsequent interplay with the larger-scale atmospheric phenomena that drive local evaporation. This thesis addresses the following overarching research question:

Which are the physical mechanisms that drive the evaporation in the Atacama Desert at different spatio-temporal scales?

To answer this general question, we designed a specific methodology that combines surface and airborne measurements gathered in a dedicated field experiment called E-DATA (**E**vaporation caused by **D**ry **A**ir **T**ransport in the **A**tacama Desert) supported with regional atmospheric modelling. The E-DATA experiment and regional modelling is addressed in detail in Chapter 2. This research is focused on a specific place in the Altiplano of the Atacama Desert, the Salar del Huasco (20.2 °S, 68.8 °W, 3,790 m above sea level (asl), Fig. 1.1). The ecosystem of the Salar del Huasco is representative of the natural hydrological systems in the region, characterized by a closed basin surrounded by complex topography (altitude ranging from 3,790 to 5,300 m asl). It is an ideal site for this study since rainfall along the catchment infiltrates and recharge the aquifer, which upwells in a terminal shallow lake at the basin bottom (Fig. 1.1). Here, all water loss occurs by evaporation. We carried out the E-DATA experiment between the 13^{th} and 24^{th} of November 2018, since it is the driest month (with the lowest rainfall probability). In addition, several studies related to water, climate, and ecosystems have already been carried out in this basin since it has remained untouched by human activities (Uribe et al., 2015), being declared a Ramsar site (a wetland site of international importance) in 1996

(LePage, 2011) and a national park in 2020. Therefore, investigating this place is helpful as a baseline of natural ecosystems and their bio-geo-physical relations in the context of climate change.

1.2 Multiscale processes driving evaporation in the Atacama Desert

This thesis investigates the physical processes that govern local evaporation in a representative salt flat located in the Altiplano (highlands) region of the Atacama Desert. Our approach aims to study the physical processes ranging from climatic to sub-diurnal scales and the interaction between spatial scales ranging from the regional (>100 km) to local scales (∼10 km). Therefore, we analysed how the ocean-desert circulation influences the ABL dynamics and the surface flux evolution over areas within the Salar del Huasco with different surface characteristics.

Figure 1.3 is the road map of this Ph.D. investigation. It shows how we have broken down the spatio-temporal complexity of the physical processes involved in the evaporation in the Atacama Desert. The specific scientific motivation, research questions, and methods of each chapter are introduced in the following sub-sections.

1.2.1 Evaporation climatology (Chapter 3)

Understanding evaporation in arid regions like the Atacama Desert from a short-, medium- and long-term temporal perspective is essential for climate change assessment and water management. This can be seen when connecting the seasonal spatial changes, as shown in Figure 1.1, to the multi-annual variability of the saline lake surface area, as shown in Figure 1.4. The Figure shows the significant spatial differences in the water extend of the saline lake between the summers of 2019 and 2021.

We will more closely examine the long-term processes that are driven by climate variability and affect evaporation (see Fig. 1.3a Box III). At the seasonal time scales, synoptic atmospheric circulation is responsible for the moisture transport over the Altiplano region (Falvey & Garreaud, 2005). This circulation is predominant during autumn, winter, and spring (April to November). Its main characteristic is a periodic eastward airflow (orange arrow, Fig. 1.3a-Box III and Fig. 1.5) that transports dry air masses from above the marine boundary layer and is part of the subtropical Pacific high-pressure system (Chang, 1995). An opposite flow with a westward direction is dominant during the summer (December to March) and transports air masses with large amounts of moisture, leading to the onset of the rainy season (green arrow, Fig. 1.3a-Box III and Fig. 1.5). The governing phenomena behind the rainy season is the Bolivian low-pressure synoptic system that pumps humid air from the Amazon basin to the Altiplano of the Atacama Desert (Falvey & Garreaud, 2005).

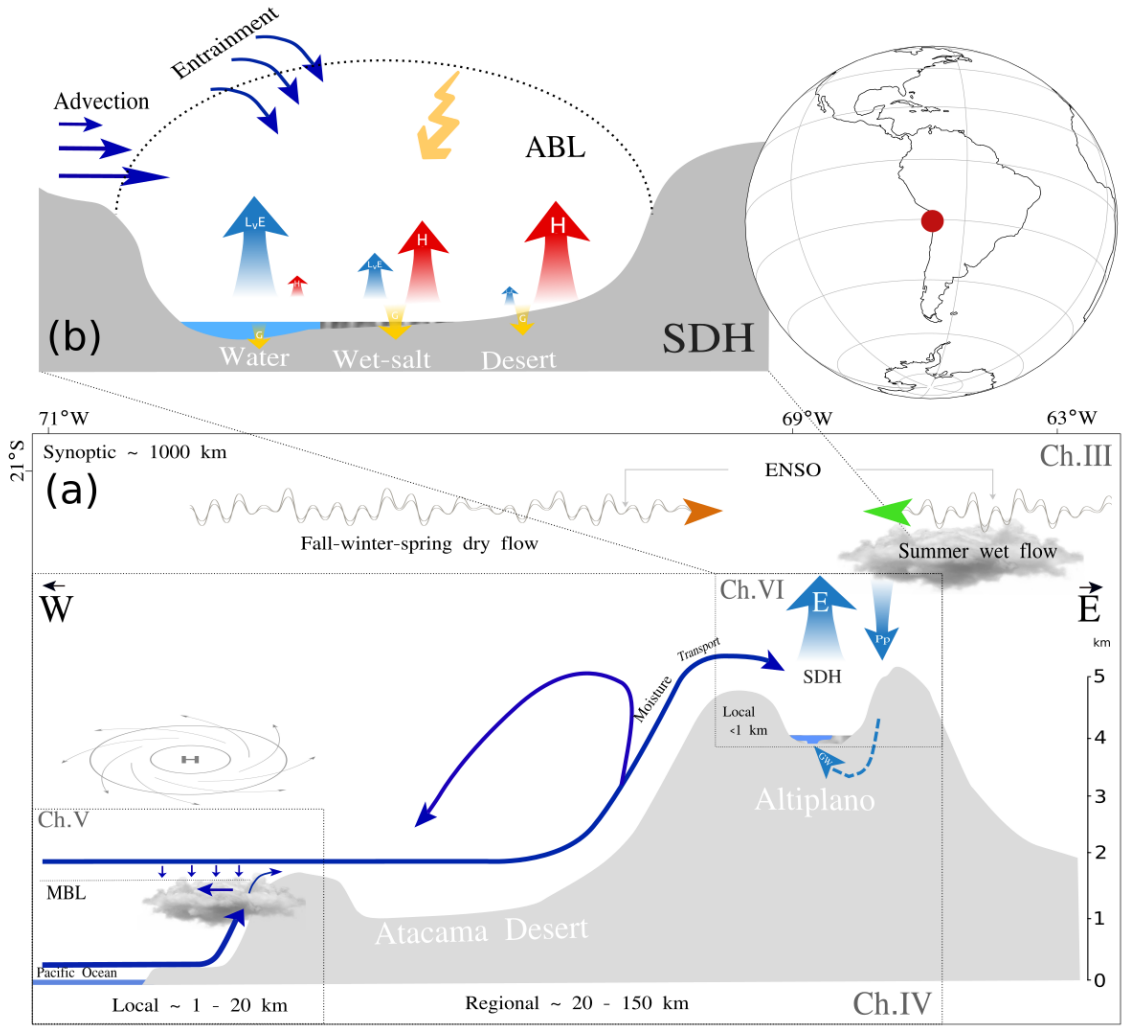

Figure 1.3: Overview of the temporal and spatial physical processes involved in evaporation at Salar del Huasco (SDH) in the Atacama Desert. (a) Corresponds to a vertical cross-section of the western slope of the Andes, where dark blue arrows represent the atmospheric circulation, light blue arrows represent the fluxes of water balance, and orange and green arrows represent the temporal variability of the larger-scale ENSO phenomenon. (b) Corresponds to a W-E vertical cross-section of the Salar del Huasco basin, where dark blue arrows represent the multispatial scale processes that affect the ABL, light blue (latent heat flux, (L_vE)), red (sensible heat flux, H), and yellow (ground heat flux, G) represent the surface energy balance, and jagged yellow the radiation. Roman numerals inside the boxes frame the physical processes further explored in the thesis chapters and the spatial scales.

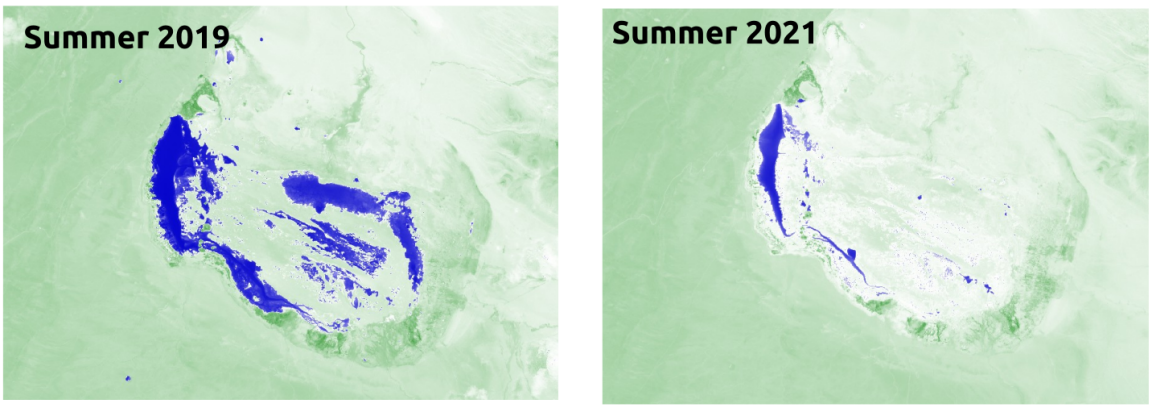

Figure 1.4: Interannual summer variability of the saline lake in Salar del Huasco as viewed by the normalized difference water index (NDWI) from Copernicus Sentinel data from 2021 processed by Sentinel Hub.

The seasonal moisture transport resulting from the synoptic circulation is highly variable from year to year, since it is influenced by global interannual climate phenomena such as the El Niño Southern Oscillation (ENSO) (Garreaud & Aceituno, 2001). The ENSO phenomenon corresponds to changes in the sea surface temperature (± 1-3 °C degrees) at the eastern tropical Pacific Ocean that impact global climate, especially in the southern hemisphere (Philander, 1983). This oscillating cycle presents three phases, warm, cool and neutral, which strongly affect the precipitation pattern along the Pacific Ocean and the South-American continent. The warm phase, known as El Niño, corresponds to the above-average warming of the eastern tropical Pacific Ocean and the weakness of easterly winds that, depending on the phenomenon's intensity, can even blow from west to east (Timmermann et al., 2018). The cool phase, known as La Niña, is characterized by the cooling of the ocean surface and by the strengthening of easterly winds. The neutral phase refers to surface temperature and winds close to the historical average (Philander, 1985). In the case of the Altiplano region of the Atacama Desert, the ENSO phenomenon affects moisture transport impacting the summer rainfall patterns (Böhm et al., 2020). Warm ENSO phases are associated with dryer rainy seasons, whereas cool ENSO phases are associated with wetter rainy seasons (Aceituno, 1988). Even though several studies have analysed the effects of ENSO on precipitation in the Altiplano region (Aceituno, 1988; Vuille et al., 2000; Garreaud & Aceituno, 2001), the effects on evaporation are still poorly understood (Houston, 2006a), mainly because of the lack of extended long-term records for evaporation.

Motivated by these former studies that show the climate variability in the atmospheric circulation, we formulated the following research question to investigate how evaporation is controlled by multiple temporal scales and how this relates to evaporation climatology:

What processes are involved in sub-diurnal, seasonal, and interannual open water evaporation variability?

This question is answered in Chapter 3. Two hypotheses regarding long-term evaporation variability were tested to answer this question. The first hypothesis is that at the sub-diurnal scale wind speed is the principal evaporation driver, whereas at a seasonal scale the main driver is radiation. The second hypothesis we investigated is that the clear sky and warm conditions from El Niño favour higher evaporation rates, whereas cloudy and cool conditions from La Niña, lead to decreased evaporation rates. The strategy followed to test these hypotheses was to analyse the open water evaporation climatology at the saline lake of Salar del Huasco. First, historical (1950-2020) standard meteorological variables at hourly intervals taken from the ERA5 re-analysis dataset (Hersbach et al., 2020) were downscaled to local conditions observed during the E-DATA experiment. Second, we used the ERA5 downscaled data to estimate long-term open water evaporation estimates applying the Penman equation for open water evaporation (Penman, 1948) adapted to the Salar del Huasco.

1.2.2 Ocean-land circulation influence on local evaporation (Chapter 4)

Connecting with the previous studies, but now focusing on the spatial scales of the atmospheric circulation in the Atacama Desert, we studied the influence of the ocean-land circulation during November. This period is especially critical for the water resources of the Altiplano, as demonstrated in Figure 1.1, but it also represents the warmest month without rainfall. The main large-scale atmospheric circulation affecting the Altiplano region evaporation is characterized by two main regimes, shown in Figure 1.5. First, the flows from the west (orange and blue arrows) represent the dry air masses that are regularly transported from above the marine boundary layer (MBL) to the Altiplano. Second, the flow from the east (green arrow) transports a significant amount of moisture during summer, influencing the rainy season in the Altiplano region.

Our research strategy to study how the large-scale processes connect to local evaporation is shown in Figure 1.3a (Box IV). Moving from large to small scales, the thermal contrast between the cold Pacific Ocean and the warm surface of the Atacama Desert (Rutllant et al., 2003) drives a mesoscale circulation. It is characterized by a spatial scale of ∼150 km, transporting air masses from above the MBL to the Altiplano region of the Atacama Desert (dark blue arrows in Fig. 1.3a-Box IV and Fig. 1.5). In the morning, this regional-scale phenomenon is defined by a small land-ocean thermal contrast resulting in a low wind speed. During the morning, the thermal contrast builds up and a sudden change occurs around noon with the arrival of an afternoon flow driven by a strong ocean-land breeze (Muñoz et al., 2018). This circulation pattern decreases towards the evening, forming a return cell that enhances the subsidence at the coast (Rutllant & Ulriksen, 1979). Going to more local scales, the arrival of this sea-breeze flow influences the ABL

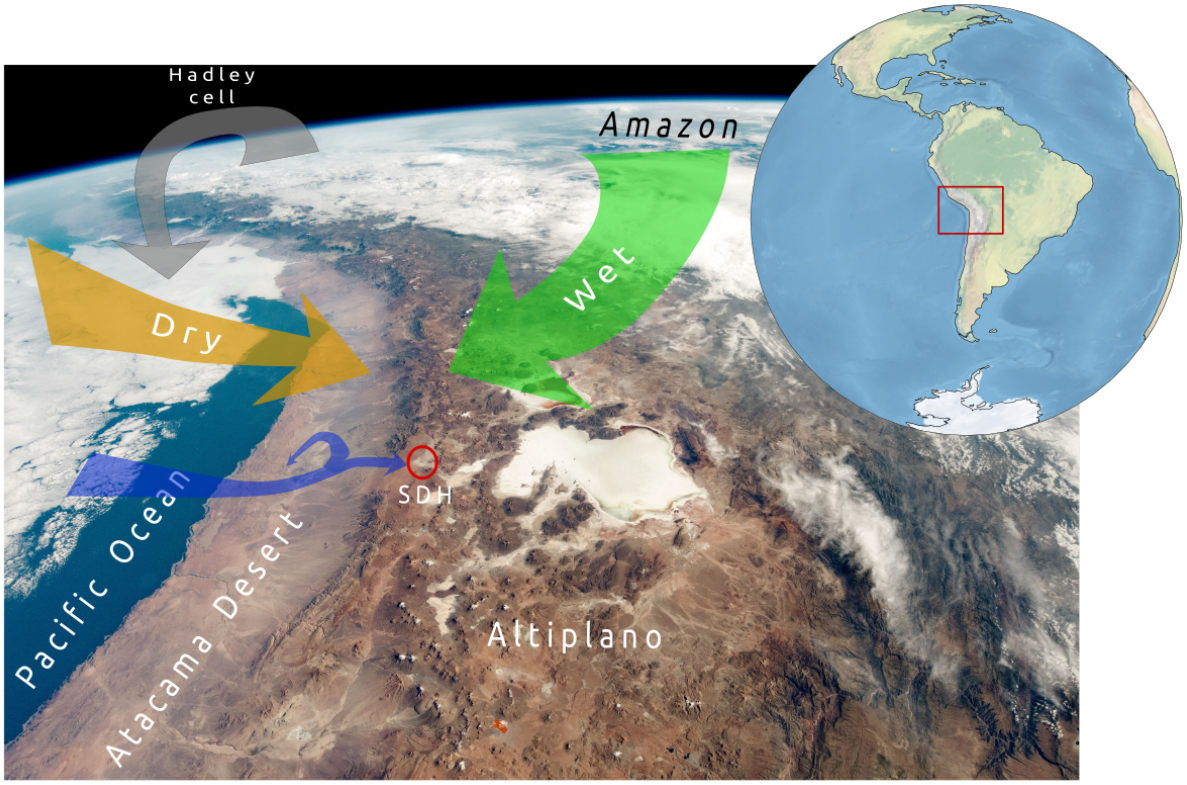

Figure 1.5: Large-scale atmospheric circulation over the Altiplano region. Blue arrows correspond to diurnal regional circulation, orange arrow autumn-winter-summer seasonal synoptic flow, green arrow summer synoptic flow, and grey arrow the Hadley cell. A red circle surrounds the Salar del Huasco (SDH). The image is from the U.S. Geological Survey (1974), Geology of Salars in Northern Chile.

development and the evaporation of the saline lake in the Salar del Huasco. A few studies have been performed regarding the ABL development in the Altiplano region (Falvey & Garreaud, 2005; Rutllant et al., 2003). These studies mainly focused on the link between the ABL and the larger-scale processes that affect its development. However, the link between ABL and wet surface evaporation in the Atacama Desert has never been studied. Finally, at a very localized scale two processes related to surface heterogeneity are involved in evaporation (see Fig. 1.3a-Box VI and Fig. 1.3b): the surface energy balance and groundwater upwelling. The surface energy balance describes the energy partitioning (radiation), where evaporation is one of the main components. Here, variables such as albedo, soil moisture, and surface roughness characteristics play key roles in evaporation (Kampf et al., 2005). Groundwater upwelling (light blue dashed line in Fig. 1.3a-Box VI) determines the water availability on each surface type (Uribe et al., 2015).

The themes introduced before lead us to formulate the following research question:

In the interplay between regional and local scales, what is the role of the wind-induced turbulence in controlling the diurnal cycle of evaporation as compared to radiation and vapor pressure deficit?

Our hypothesis is that wind, rather than radiation or the water vapor deficit, is the limiting factor in controlling evaporation. We investigated the regionally driven wind regime with fine-resolution (1 x 1 km) numerical experiments based on the Weather Research and Forecasting (WRF) model. The local interaction with the surface was studied with surface energy balance data gathered over water, wet-salt, and desert surfaces, which were continually measured during the 10-day E-DATA experiment. Moreover, the interaction with the ABL was measured with radiosondes launched every 3 hours along with unmanned aerial vehicles every 30-min.

1.2.3 The influence of the marine boundary Layer on the Atacama Desert (Chapter 5)

One branch of the regional circulation presented in Figure 1.3a requires special attention, as it brings clouds and fog to the coastal region in the lower part of the Atacama Desert (see Fig. 1.3a-Box V). This marine boundary layer (MBL) circulation interacts with the free troposphere circulation, which controls evaporation in the Altiplano. Rutllant et al. (2003) described two regional-scale diurnal circulations on the western slope of the Andes in the Atacama Desert. The first one, introduced in Section 1.2.2, corresponds to the afternoon regional-scale (∼150 km) wind resulting from the thermal contrast between the Pacific Ocean and the Atacama Desert. The second circulation is the topic of Chapter 5 and corresponds to a local (∼10 km) sea breeze formed within the MBL interacting with the coastal mountains. Here, the most relevant process is the formation of inland fog, which results from the interaction between the Pacific Ocean stratocumulus cloud (Sc) deck and the topography of the coastal Atacama Desert (Cereceda et al., 2008a; Rutllant et al., 2003). This circulation within the MBL is defined by three main factors, depicted in Figure 1.6. The first one corresponds to the sea surface that provides the moisture flux. The second one is the subsidence motions at ∼1,000 m height promoted by the Pacific anticyclone (H in Fig. 1.3). Finally, steep coastal mountains with an altitude of ∼1,200 m encumber moisture transport from the MBL inland to the Atacama Desert (Cereceda et al., 2002). Our main aim was to elaborate on these studies by placing special emphasis on the interaction between the MBL, including the land-fog system, and the circulation above it, and how this interaction is connected with the development of the afternoon advection influencing the Altiplano circulation.

To better understanding the interaction between the MBL and the Atacama Desert that play an important role in the regional circulation controlling evaporation in the highlands, in Chapter 5, we address the following research question:

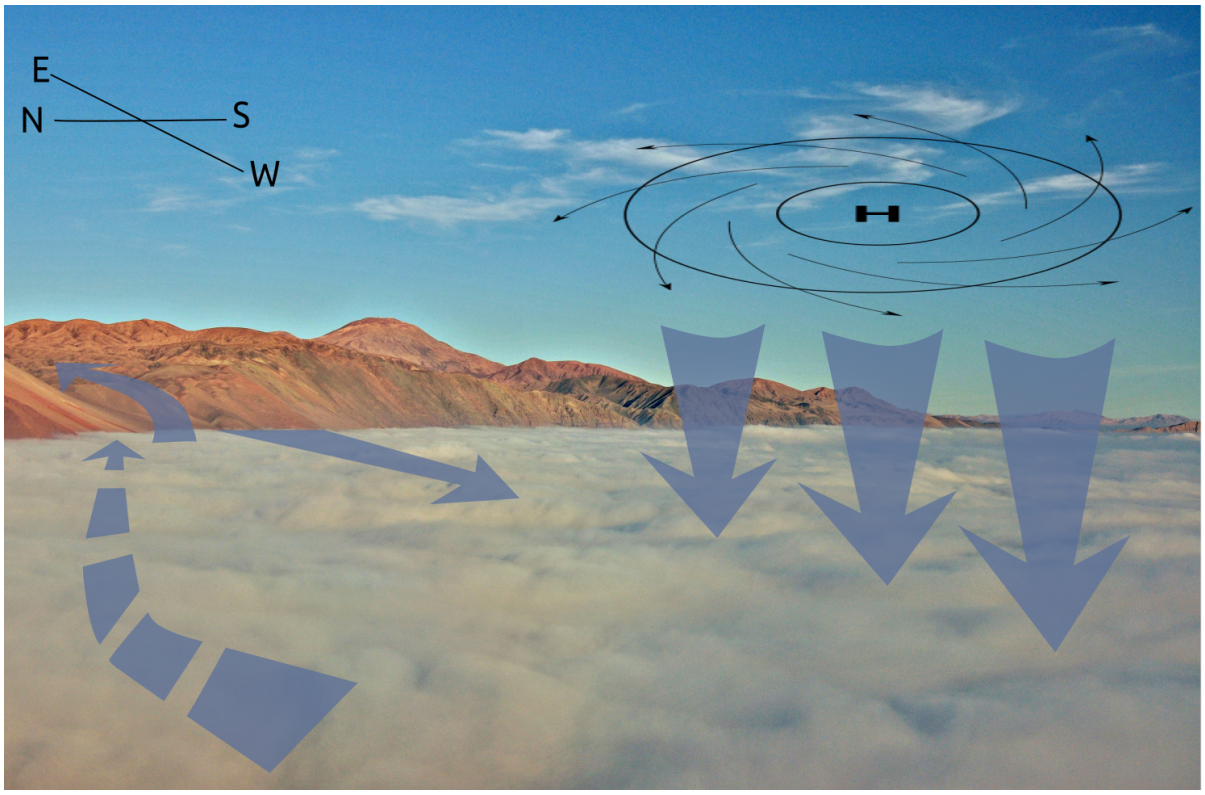

Figure 1.6: Local sea breeze circulation within the MBL of the Atacama Desert. Arrows indicate the atmospheric circulation and H the Pacific Anticyclone (high pressure system), both shown in box V of Figure 1.3a.

What is the influence of the marine stratocumulus cloud in the formation, maintenance, and dissipation of the land-fog system in the Atacama Desert?

The central hypothesis we followed is that the thermal stratification of the MBL is the main driver of fog formation or dissipation. We designed a methodology which entailed analysing different sources of surface observations, which were complemented with required high-resolution numerical modelling. Surface observations of standard meteorological variables and fog collection over vertical transect (40 to 1,200 m) were analysed to characterize the evolution of the MBL structure.

1.2.4 The role of surface heterogeneity on local evaporation (Chapter 6)

A deep understanding of processes involved in evaporation in arid regions requires accurate measurements at a local scale (Houston, 2006a). However, in arid regions, measuring evaporation in and around saline lakes is particularly challenging due to the extreme surface heterogeneity (see Fig. 1.3a). Figure 1.7 shows an illustrative example of the sub-kilometre contrast between a water and wet-salt surface, which differ by one order of magnitude in terms of their surface fluxes, resulting in Bowen ratio values of 0.2 and 4, respectively. Measuring fluxes over open water bodies is a challenge since

footprints require installing instruments above the water. This issue is an unavoidable complication for Eddy Covariance (EC) instrumentation since they must be installed on floating platforms, biasing the measurements (Nordbo et al., 2011). An alternative technique, the Optical-Microwave Scintillometer (OMS), can overcome this problem since it can be installed on opposite shores, concentrating the footprint in the centre of the water body. It has the additional advantage that its landscape-scale footprint (1-10 km) is more appropriate to integrate different surfaces, being a useful ground-truth for remote sensing estimations or hydrometeorological models (Meijninger et al., 2002a). Despite these advantages, the OMS technique also requires specific assumptions in inferring the surface turbulent fluxes from the direct measurement of wavelength refractivity. The algorithms that are used for this, assuming surfaces are homogeneous, are part of the so-called Monin-Obukhov Similarity Theory (MOST) (Moene & Van Dam, 2014). These assumptions are questionable when non-local contributions to the exchange process intervene (Kooijmans & Hartogensis, 2016). The Salar del Huasco has ideal conditions to evaluate the advantages and disadvantages of the OMS method to estimate open water evaporation. These conditions are the presence of heterogeneous and contrasting surfaces (Fig. 1.7), including a shallow saline lake where standard measurements like EC can be easily installed as references.

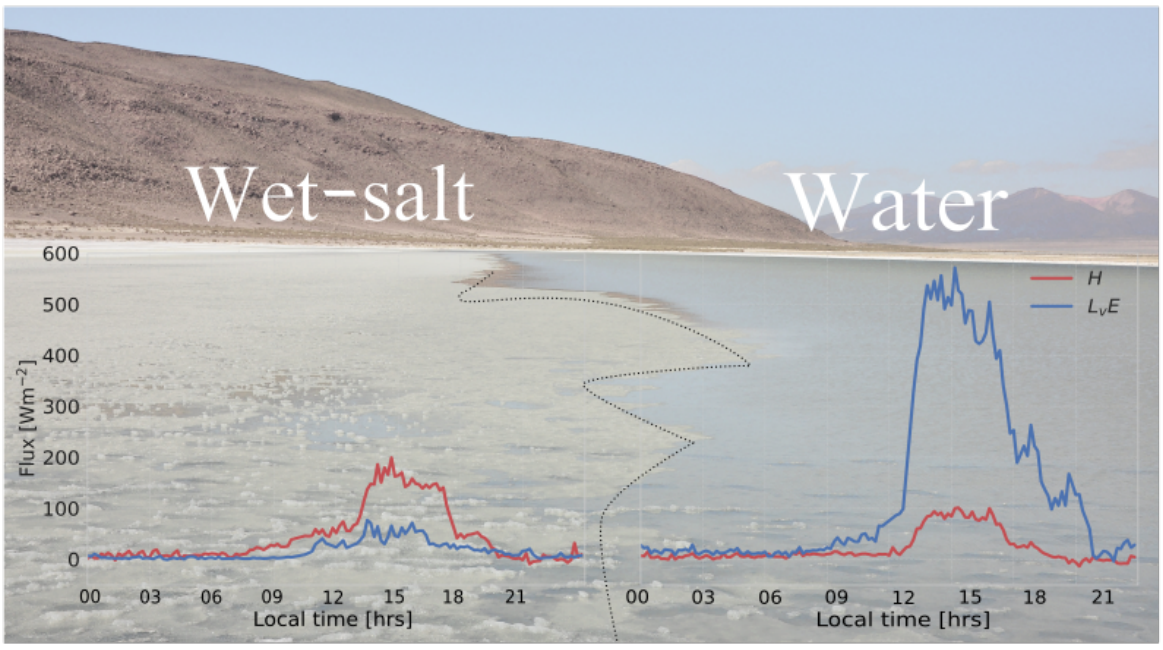

Figure 1.7: Sensible (H) and latent heat (L_vE) fluxes from heterogeneous surfaces in Salar del Huasco.

In Chapter 6, we aim to answer the following research question:

How accurate are the evaporation measurements performed by an OMS over an open water body under arid and windy atmospheric conditions?

The central hypothesis is that the contrast between wet-salt and water within the OMS footprint affects the OMS measurements and violates MOST. The contrasting surfaces, typical of evaporative environments in the Atacama Desert, are influenced by the surrounding arid conditions and the non-local processes. As a reference for the OMS flux estimates, we used EC flux measurements over water and wet-salt surfaces. Our analysis integrates the dynamic of the surface and ABL conditions, the impacts of the footprint on evaporation measurements, the representativity of standard MOST functions, and the implication of measuring below the so-called blending height.

1.3 Thesis outline

The main physical processes involved in local evaporation in the Atacama Desert described in Section 1.2 range from the large to the short timescale and from the synoptic to the local spatial scale. The analysis of such processes is organized along with the thesis chapters as follows:

Chapter 2 describes the general methodology followed in this thesis. This chapter integrates local evaporation measurements, fine-resolution regional modelling, and climatological reanalysis data. We accurately describe the design of the E-DATA experiment in terms of energy balance surface observations, radiosondes, and unmanned aerial vehicles (UAV) vertical profiles, as well as horizontal transects of meteorological stations. Moreover, an overview of the WRF model setup is provided, and the results are validated against E-DATA surface and airborne observations. Finally, to complete the local-scale measurements obtained during the E-DATA experiment and the regional-scale WRF simulations, long-term meteorological variables downscaled from ERA5 are validated against observations from Salar del Huasco.

Chapter 3 describes the temporal variability of evaporation from the climatological to the sub-diurnal scales. This chapter focuses on the physical processes involved in the temporal variability of local evaporation in the Atacama Desert, including sub-diurnal scale processes like radiation and turbulence to interannual ones like the ENSO phenomena. Moreover, it gives an overview of the role of evaporation in the water balance of the saline lake of Salar del Huasco.

In chapters 4 to 6, we describe the physical processes involved in evaporation from a spatial perspective. In chapter 4, we analyse the influence of the mesoscale atmospheric circulation produced between the Pacific Ocean and the Atacama Desert on local evaporation. Moreover, we analyse the ABL dynamics and its interaction with the surface fluxes

of the Salar del Huasco. In Chapter 5, we describe the local circulation that produces the regional circulation described in Chapter 4. Here, we focus on the influence of the marine boundary layer on the inland moisture transport and the land-fog system, which affects the regional circulation from the ocean to the Altiplano. Finally, in Chapter 6, we describe turbulent fluxes variability in the Salar de Huasco as a function of several surface conditions as heterogeneity and roughness length, among others. This information is used as part of the validation of OMS measurements over the saline lake in the Salar del Huasco, which includes a footprint analysis of the OMS and EC systems. Special attention is paid to the evaluation of MOST functions used by the OMS for the flux estimation.

Finally, in Chapter 7, we connect and discuss the main results of each chapter. Here, we show the main conclusions of this study by providing answers to the proposed research questions and giving an outlook for further research.

Chapter 2

Integrating local evaporation measurements to regional and climatological modeling

This chapter is based on:

Suárez, F., Lobos-Roco, F., De La Fuente, A., Vilà-Guerau de Arellano, J., Prieto, A., Meruane, C., & Hartogensis, O. (2020). E-DATA: A comprehensive field campaign to investigate evaporation enhanced by advection in the hyper-arid altiplano. *Water*, 12(3), 745.

Abstract

In the endorheic basins of the Altiplano, water is crucial for sustaining unique ecological habitats. Here, the wetlands act as highly localized evaporative environments, and little is known about the processes that control evaporation. Understanding evaporation in the Altiplano is challenging because these environments are immersed in a complex topography surrounded by desert and are affected by atmospheric circulations at various spatial scales. Also, these environments may be subject to evaporation enhancement events resulting from dry air advection. To better characterize evaporation processes in the Altiplano, the novel **E**vaporation caused by **D**ry **A**ir **T**ransport over the **A**tacama Desert (E-DATA) field experiment was designed and tested at the Salar del Huasco, Chile. The E-DATA combines surface and airborne measurements to understand the evaporation dynamics over heterogeneous surfaces, with the main emphasis on open water evaporation. The weather and research forecasting model was used for planning the instruments installation strategy to understand how large-scale airflow affects evaporation. Moreover, ERA5 reanalysis data were used to analyse long-term meteorological conditions. Instrumentation deployed included: meteorological stations, eddy covariance systems, scintillometers, radiosondes and an unmanned aerial vehicle, and fiber-optic distributed temperature sensing. Additional water quality and CO_2 fluxes measurements were carried out to identify the link between meteorological conditions and the biochemical dynamics of Salar del Huasco.

2.1 Introduction

The hydrological functioning of the high Andean basins in the Altiplano region is characterized by semi-arid to hyper-arid climate and endorheic conditions (Hernández-López et al., 2016). In this area, water is crucial for natural habitats, industry, and agriculture. The area is rain-fed by occasional convective showers that are spatially very localized and temporally rapidly changing in intensity (<1 hour). These rainstorms are the source of aquifer recharge and thus they sustain wetlands that are formed in the basins due to surface discharge and groundwater upwelling. The high Andean wetlands sustain unique ecological habitats, being home to the most threatened bird species (Kampf et al., 2005; Johnson et al., 2010). The wetlands act as highly evaporative environments and thus, it is where nearly all the water of the basin is lost to the atmosphere (Johnson et al., 2010). In this region, a reliable understanding of the evaporation processes is extremely essential for several reasons. First, the correct quantification of water fluxes enhances the performance of water balance models, e.g., by assimilating the evaporation data or improving the fluxes parametrizations. As a result, the estimation of the basin's water recharge can be improved (Johnson et al., 2010). Second, water availability is fundamental for terrestrial and aquatic ecosystems that sustain the native flora and fauna (de la Fuente & Niño, 2010; Johnson et al., 2010; Dorador et al., 2010, 2013). Lastly, for sustainable water use with minimum impact into the environment (Evans et al., 2012; Gunson et al., 2012).

The climatic conditions of the Altiplano region, on the other hand, are closely related to the zonal winds, in which easterly zonal flows favor wet conditions in summer (mid-December to mid-March) because of the entry of humid air from the Amazon region, and westerly zonal flows have associated drier conditions mainly during winter and spring (Garreaud et al., 2003). In this way, the combination of synoptic and mesoscale phenomena has an important role in the evaporation rates of this region. Furthermore, these environments may also be subject to evaporation enhancement episodes as the result of dry air advection, changes in wind speed, and air and soil temperature, which complicate even more the determination of the evaporation fluxes (Philip, 1987; Higgins et al., 2013). These episodes occur at sub-hourly temporal scales. The relevant spatial scales for studying evaporation in these environments are typically in between the scales that can be resolved using traditional evaporation methods (Shuttleworth, 2008): much larger than those of traditional in-situ methods (e.g., evaporation pans, lysimeters), but typically smaller than those based on remote sensing through satellites. Similarly, the heterogeneity of the surface conditions, i.e., water, wet salt, and desert, is characterized by 100-m scales, which requires parameterizations in weather forecast and climate models, as well as hydrological models, i.e., sub-grid scale phenomena.

Evaporation is strongly influenced by the connection between the land surface and the atmosphere (Haghighi et al., 2018), but there is a few of this information in the Alti-

plano region (Kampf et al., 2005). In the open waters of the high Andean wetlands, de la Fuente & Niño (2010) used a thermodynamic model to estimate mean daily evaporation rates of ∼8 mm day^{-1}, with peaks reaching values of ∼40 mm day^{-1}. Also, mean daily pan evaporation rates as large as ∼11 mm day^{-1} have also been reported (DIHA-PUC, 2009). The evaporation rates measured in these lagoons and their wetlands exceeded the evaporation values that can be expected from net-radiation estimates, but the processes associated to these large fluxes have not been studied. Consequently, we hypothesize that advection of dry air combined with high wind enhancing mechanical turbulence coming from the surroundings of shallow lagoons in endorheic basins of the Altiplano region is the responsible for large actual evaporation rates. To truly understand the contribution of advection to evaporation in these environments, the transport processes that occur in the atmospheric boundary layer (ABL) must be explored. The ABL is a variable-thickness layer that connects the land surface with the free troposphere, and where transport of momentum, thermal energy, and specific humidity occurs (Stull, 1988; Vilà G. A. et al., 2015).

The coupling between evaporation and the ABL processes that occurs in the highly evaporative environments of the Altiplano has not been fully explored yet. To improve the understanding of the relevant processes that drive evaporation in these environments, we designed and carried out an extensive field experiment called **E**vaporation caused by **D**ry **A**ir **T**ransport over the **A**tacama Desert (E-DATA). This experiment focuses on the effect that advection has on evaporation rates, and to obtain diurnal budgets of heat and water under the most characteristic surfaces in these Altiplano environments. The 10-day field campaign was designed to understand the evaporation dynamics over heterogeneous surfaces with emphasis on open water evaporation at different spatial scales, and under the extreme conditions in Salar del Huasco, Chile (high radiation levels, large daily thermal oscillation, and strong winds during the afternoon). The novelty of this field experiment is that it combines surface and airborne measurements to quantify the moisture and heat transport, accounting for the interaction between the ABL and the regional circulation. In addition, the collected data is combined with numerical simulations using the weather and research forecasting (WRF) model (Skamarock et al., 2008) and long-term reanalysis data (ERA5) to understand the main processes that control evaporation in these environments at multiple spatial and temporal scales.

This chapter presents the methods used in this research, related to the E-DATA field experiment, but also atmospheric simulations and long-term reanalysis data. First, this chapter presents the experimental design, the implementation of the E-DATA field experiment and preliminary results. Second, the chapter shows the WRF modeling setup and validation used for analyzing the regional atmospheric circulation over the Salar del Huasco. Finally, we briefly introduce the downscaling process and its validation used to count with long-term meteorological data using ERA5 reanalysis.

2.2 Study site

The Salar del Huasco basin is located between 19°54' and 20°27' S and between 68°40' and 69°00' W in the Atacama Desert (Figure 2.1) and sits on the so-called Depresión de los Salares (salt flats depression), surrounded by high peaks ranging between 4,000 and 5,200 m asl (Houston, 2006b). This closed basin has high environmental relevance as it hosts a variety of camelids and birds in high-altitude wetlands. In the case of Salar del Huasco, it is located at an altitude of ∼3,800 m asl and is home to protected bird species such as flamingos (de la Fuente, 2014). Because of that, Salar del Huasco is protected under the international Ramsar convention, which recognizes the ecological, economic, cultural, and scientific value of different wetlands around the world (LePage, 2011).

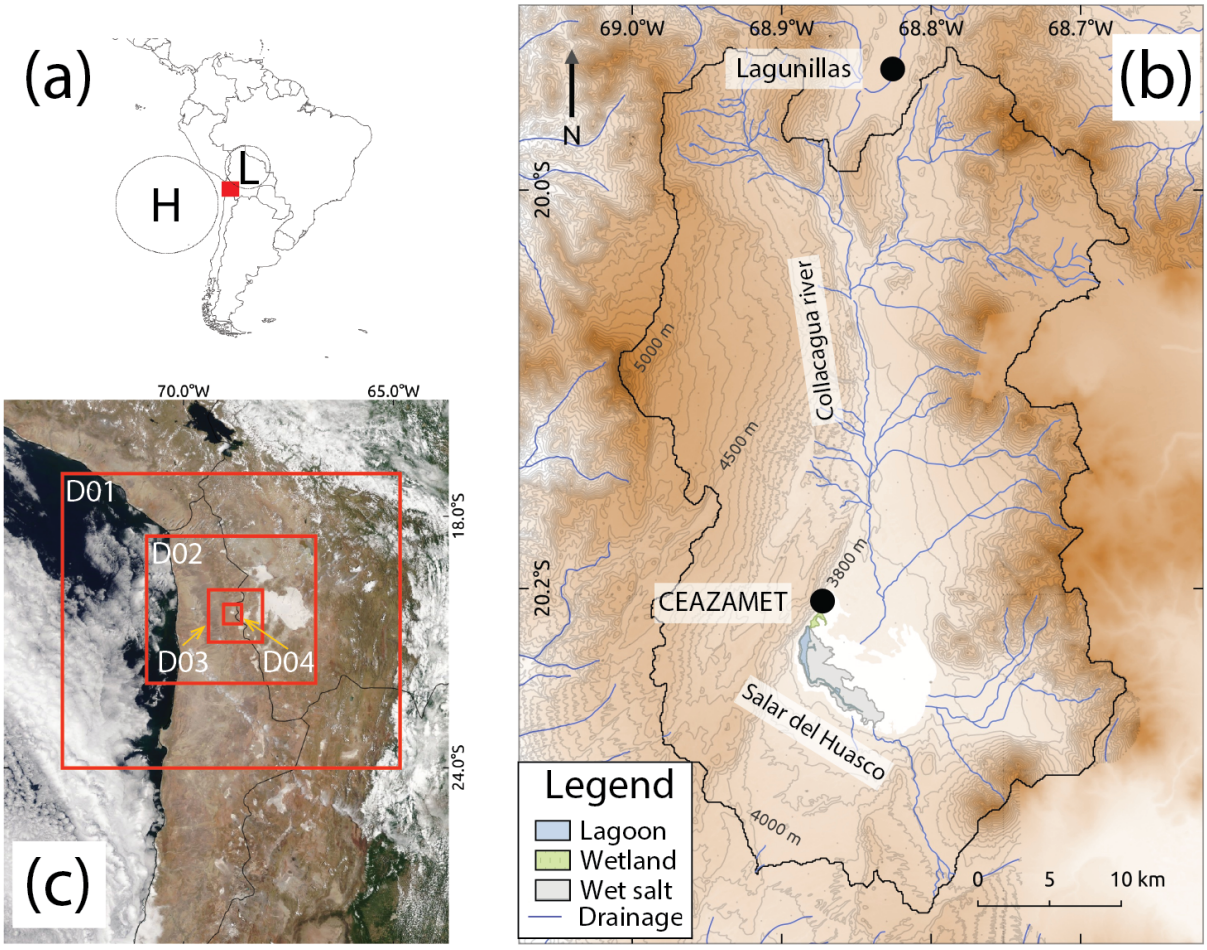

Figure 2.1: (a) General location of the study site. H and L depicts high- and low-pressure systems, respectively, which controls the meteorological behavior in the basin. (b) Salar del Huasco basin and meteorological stations used in the climatological analysis. (c) Domains (D01, D02, D03 and D04) used in the Weather and Forecasting (WRF) model simulations for the design of the field experiment.

Rainfall in the basin and across the Altiplano region is convective with more than 80%

occurring between December and March (Uribe et al., 2015; Houston, 2006b). The annual mean precipitation in the basin is 135 mm for the 1962–2014 time period. Interannual precipitation variability is high, partially due to the El Niño southern oscillation (ENSO) phenomenon, but mostly due to the wind patterns in the area (Garreaud & Aceituno, 2001). Mean annual potential evaporation is approximately 1,200 mm and it has been relatively stable between 1950 to present with variations of up to 20% in the last two decades (de la Fuente & Meruane, 2017). Rainfall and evaporation from the wetlands seem to be the only water inputs and outputs in the basin (Uribe et al., 2015).

The Salar del Huasco was selected as the study site because it is one of the few places in the Altiplano region in which evaporation data have been previously collected and thus there is evidence that dry air advection may be occurring (Johnson et al., 2010; de la Fuente & Meruane, 2017; Houston, 2006a). In this closed basin, local atmospheric circulation may be relevant for the surface energy balance (Whiteman et al., 2004).

2.3 Design and implementation of E-DATA field experiment

2.3.1 Design of the study

To improve the understanding of the relevant processes that drive evaporation it is important to couple the land-surface processes to those occurring in the ABL. For this reason, the first stage of the study was to define the month in which the field campaign was going to take place. Then, a thorough analysis of the wind patterns at both the local and regional scales was performed, with a focus on the open waters of the Salar del Huasco basin. This analysis was used to define the location of the different instruments in the field experiment.

A climatological analysis was carried out using historical meteorological information obtained from the Lagunillas and Salar del Huasco meteorological stations (Figure 2.1). Using these data, we analyzed the wet and dry seasons. On the one hand, the wet season, which occurs between mid-December and mid-March, is characterized by small daily thermal oscillations, high specific humidity (>5.0 g kg^{-1}) and precipitation that is spatially very localized and rapidly changing in time. On the other hand, the dry season that occurs between mid-March and mid-December, is characterized by large daily thermal oscillations, low specific humidity (<2.5 g kg^{-1}) and no precipitation. Hence, we selected November as the best month in the dry season to test our working hypothesis, because of the temperature contrast between ambient and water temperature, large availability of solar radiation, and absence of precipitation, which are the more optimal conditions to study dry advection episodes.

The spatial configuration of the different instruments used in the E-DATA field

campaign was designed by analyzing the wind patterns for the months of November 2015–2017. This analysis was carried out using in-situ surface observations from the Salar del Huasco meteorological station and simulation results of a WRF (version 3) model (Skamarock et al., 2008) in the study site. The WRF model setup and its validation is fully explained in section 2.4 of this Chapter.

The criteria to select the locations of the instruments was to deploy them in different surfaces and align them in the principal wind directions. On the one hand, the in-situ data showed a predominant wind direction coming from the southwest and provided a point-in-space temporal overview of the wind behavior. On the other hand, the WRF simulations, which gave a perspective of the spatiotemporal patterns of the atmospheric circulation in the study area, showed that the main wind directions are southwest and west, where topographic effects result in air being channeled from the southwest direction at the location of the Salar del Huasco meteorological station. Figure 2.2 shows the location of each instrument used during the E-DATA field experiment. The instrumentation, which is described in more detail in the next subsection, was deployed to monitor evaporation and other relevant meteorological variables that help to understand the ABL processes, as well as to investigate biogeochemical processes in open waters and their surroundings that could also be driven by evaporation.

2.3.2 Implementation of E-DATA field experiment

The E-DATA field experiment was carried out between November 12^{th} and 26^{th}, 2018, and data were collected for ∼10 days, making it the longest field experiment that has been performed in the Altiplano region with the aim of studying evaporation. Instrumentation deployed included: eight meteorological stations, three eddy covariance (EC) systems, one optical-microwave scintillometer (OMS), 16 radiosondes and an unmanned aerial vehicle (UAV), and fiber-optic distributed temperature sensing (DTS) measurements along a 620-m path. The link between meteorological conditions and the biochemical dynamics of open waters in the saline lake was also investigated, and the following biogeochemical parameters were measured: CO_2 fluxes, water temperature, turbidity, and dissolved oxygen (DO), and several water quality parameters. Table 2.1 presents the sensor types and manufacturer information of each measuring system. Figure 2.3 presents photographs of the saline lake and of the different instruments used in the field campaign. These instruments were used to monitor evaporation and other relevant variables in the ABL. In the next subsections, each instrumentation group is described.

Within the following subsections, we describe every instrument installed and variable measured during the E-DATA experiment. In addition, we present examples of preliminary results. To be concise, and given that the results are relatively similar among the different days of the field campaign, results are presented and discussed for specific days that are considered representative of the whole experiment. For this reason, and to avoid

Table 2.1: Description of the instrumentation used in the E-DATA field experiment. Numbers refer to the footnotes of the Table, where sensor type and manufacturer information is provided.

Variable	EC_{water}	EC_{desert}	$EC_{wet-salt}$	OMS	DTS	Met. St. 1-8	SDH Met. St.
Incoming shortwave rad.	1	-	-	-	-	-	22
Incoming longwave rad.	1	-	-	-	-	-	-
Outgoing shortwave rad.	1	-	-	-	-	-	-
Outgoing longwave rad.	1	-	-	-	-	-	-
Net shortwave radiation	1	8	-	-	-	-	-
Net longwave radiation	1	8	-	-	-	-	-
Total net radiation	1	8	12	-	-	-	-
Photosynthetic active rad.	-	-	13	-	-	-	-
Latent heat flux	2	2	2	14, 15	-	-	-
Sensible heat flux	2	2	2	14, 15	-	-	-
Soil heat flux	3	9, 10	9, 10	-	-	-	-
Soil temperature	-	4, 11	4, 10	-	-	-	-
Water temperature	4	-	-	-	17	-	-
Wind speed	2, 5	2	2	16	-	18, 19	5
Air temperature	2, 6	2, 4	2	16	17	20, 21	23
Relative humidity	2, 6	2	2	16	-	20, 21	23
Atmospheric pressure	2, 7	2, 7	2	16	-	21	7
Precipitation	-	-	-	16	-	-	24

[1] CNR4 Net radiometer, Kipp & Zonen, Delft, The Netherlands; [2] IRGASON, Campbell Sci., Logan, UT, USA; [3] 31/32 Heat flux meter, TNO Institute of Applied Physics, The Netherlands; [4] 107 Temperature probe, Campbell Sci., Logan, UT, USA; [5] 05108-45-L Wind Monitor-HD, R. M. Young Company, Traverse City, Michigan, US; [6] HPM155 Humidity and temperature probe, Vaisala, Helsinki, Finland; [7] PTB110 Barometer, Vaisala, Helsinki, Finland; [8] CNR2 Net radiometer, Kipp & Zonen, Delft, The Netherlands; [9] HFP01SC Self-calibrating heat flux sensor, Hukseflux, Delft, The Netherlands; [10] HFP01 Heat flux sensor, Hukseflux, Delft, The Netherlands; [11] TCAV-L Averaging soil thermocouple probe, Campbell Sci., Logan, UT, USA; [12] NR2 Lite, Kipp & Zonen, Delft, The Netherlands; [13] PAR Lite, Kipp & Zonen, Delft, The Netherlands; [14] LAS MkII Scintillometer, Kipp & Zonen, Delft, The Netherlands; [15] RPG-MWSC-160, RPG Radiometer Physics GmbH, Meckenheim, Germany; [16] WXT520 Vaisala weather transmitter, Vaisala, Helsinki, Finlandia; [17] XT-DTS, Silixa, Elstree, UK; [18] Atmos-22, METER Group, Inc., Pullman, WA, USA; [19] DS-2, Decagon Devices, Pullman, WA, USA; [20] VP-3 Vapor pressure, humidity and temperature sensor, Decagon Devices, Pullman, WA, USA; [21] VP-4 Vapor pressure, humidity, temperature and atmospheric pressure sensor, Decagon Devices, Pullman, WA, USA; [22] LI-200R Pyranometer, LI-COR, Inc., Lincoln, NE, USA; [23] CS215 Temperature and relative humidity, Campbell Sci., Logan, UT, USA; [24] TE525MM Metric Rain Gage, Campbell Sci., Logan, UT, USA.

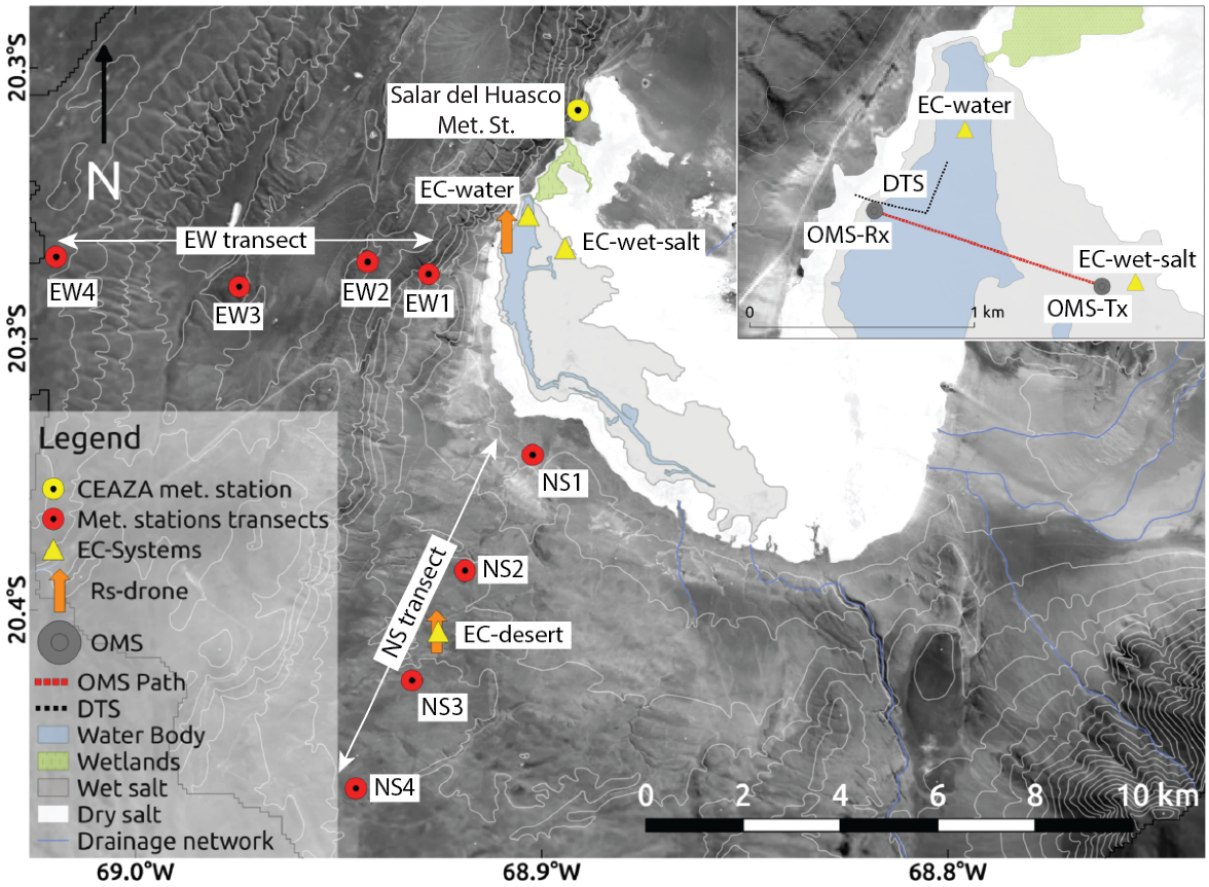

Figure 2.2: Location of the instruments in the E-DATA field campaign.

showing days with too many data gaps, we selected November 15^{th} and 17^{th}, 2018, as examples of the collected data.

Meteorological stations

Two meteorological station transects -each comprised by four stations- were deployed (Table 2.2). The NS and EW transects shown in Figure 2.2 were selected to coincide with the predominant day- and night-time wind directions and considering the closed basin conceptual model suggested by Whiteman et al. (2004). As described before, these directions were obtained from both the in-situ observations of the CEAZA meteorological station and the WRF simulation results. The spacing between the meteorological stations was defined to have only one station per cell in the fine domain (D04 in Fig. 2.1c) of the WRF simulations. Figures 2.3b, c present photographs of some of these stations. The meteorological data from these transects were collected at 2-m height, 5-min intervals, and were complemented with the data from the CEAZA meteorological station, which collects data at 60-min intervals.

The data collected in both transects of meteorological stations show a similar behav-

Figure 2.3: Photographs of the instrumentation used in the E-DATA field campaign: (a) Salar del Huasco lagoon during the morning; (b) meteorological station 1 of the EW transect (EW1); (c) meteorological station 1 of the NS transect (NS1); (d) EC-water; (e) EC-desert; (f) EC-wet-salt; (g) OMS Receptor; (h) DTS system in which the cool and ambient reservoirs are shown; (i) radiosonde preparation at the lagoon; (j) radiosonde launched at the desert location; and (k) UAV with the atmospheric sensor.

Table 2.2: Geographical information of the meteorological stations, eddy covariance (EC) systems, and optical-microwave scintillometer (OMS). OMS-T_x and OMS-R_x refer to the OMS transmitter and receiver, respectively.

Name of Station	Type	Latitude	Longitude	Elevation (m asl)
Salar del Huasco	Met. station	20°15.5' S	68°52.4' W	3,803
NS1	Met. station	20°19.3' S	68°52.9' W	3,807
NS2	Met. station	20°20.6' S	68°53.7' W	3,921
NS3	Met. station	20°21.8' S	68°54.3' W	3,973
NS4	Met. station	20°23.0' S	68°55.0' W	3,996
EW1	Met. station	20°17.3' S	68°54.1' W	3,938
EW2	Met. station	20°17.2' S	68°54.9' W	4,134
EW3	Met. station	20°17.4 'S	68°56.4' W	4,139
EW4	Met. station	20°17.1' S	68°58.5' W	4,284
EC-water	EC/Met. Station	20°16.2' S	68°52.8' W	3,790
EC-desert	EC/Met. Station	20°21.0' S	68°54.0' W	3,953
EC-wet-salt	EC/Met. Station	20°16.8' S	68°52.2' W	3,90
OMS-T_x	Scintillometer	20°17.1' S	68°52.6' W	3,791
OMS-R_x	Scintillometer/Met. Station	20°16.8' S	68°53.3' W	3,790

ior. For conciseness, we only present the data collected in the EW transect for November 15^{th}, 2018 (Fig. 2.4). Two wind regimes are observed from the meteorological data. The first regime occurs during the morning where both wind speed and specific humidity are small. The second regime occurs between 12:00 and 21:00 LT, when air circulation coming from the west increases wind speed up to $\sim$12 m s^{-1} and brings air with a specific humidity of $\sim$3.5 g kg^{-1} into the basin. The afternoon wind regime also results in a sudden decrease of potential temperature, thus controlling the daily cycle of the meteorological conditions.

Evaporation measurement systems and surface energy balance

To understand the evaporation dynamics and the surface energy balance over heterogeneous surfaces and at different spatial scales, we used three EC systems (IRGASON, Campbell Sci., Logan, UT, USA) and one OMS (see Fig. 2.2 and Table 2.2).

The first EC system, named EC-water, was deployed in the north part of the saline lake (1.5-m height), as shown in Figure 3d, taking advantage of its shallow water level (0.07–0.15 m). The second EC system (EC-desert) was installed $\sim$5 km south from the salt flat (2.5-m height), in a location where there is sparse vegetation and mostly rocky soil (Fig. 2.3e). The third EC system, called EC-wet-salt, was located to the east of the lagoon in a wet-salt crust (2.0-m height, Fig. 2.3f). All these EC systems had their footprint within the surfaces described before for the afternoon's wind regime, which is responsible for the large actual evaporation rates. Note also that the EC systems allowed

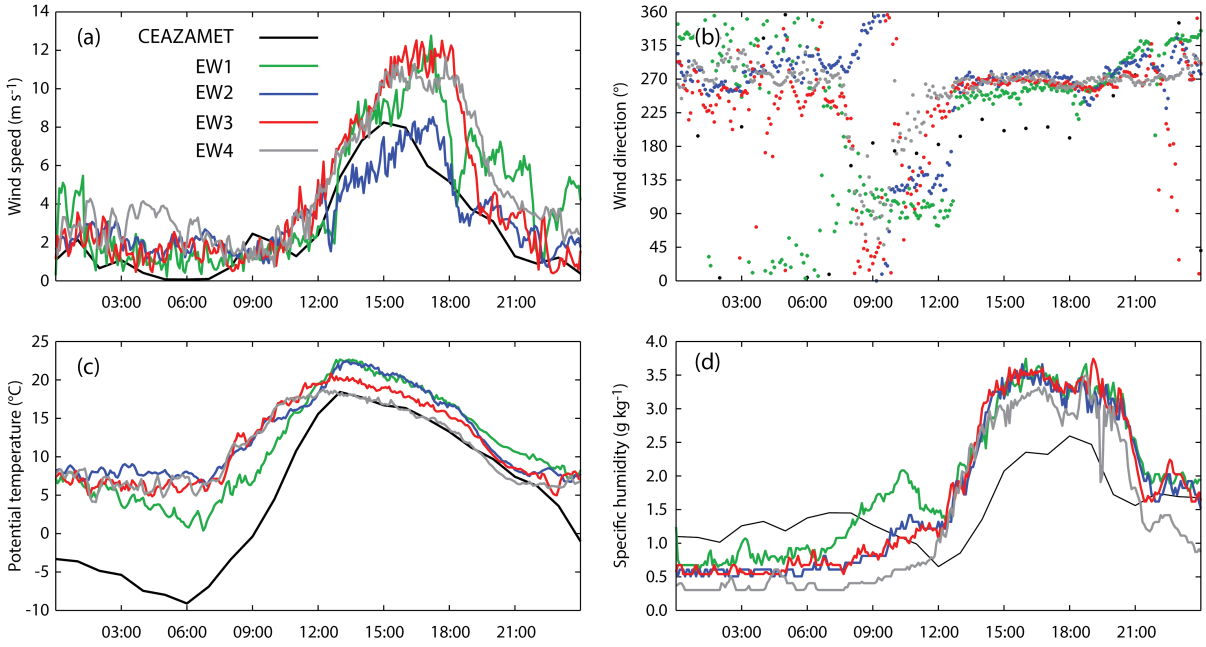

Figure 2.4: Meteorological data obtained in the EW transect for November 15^{th}, 2018: (a) wind speed; (b) wind direction; (c) potential temperature; and (d) specific humidity. The location of the meteorological stations is shown in Figure 2.2.

to measure CO_2 fluxes in the lagoon and its surroundings. The EC data were analyzed using the EddyPro 6.2.2 software and activating the default recommended correction procedures (Fratini & Mauder, 2014). The EC data were obtained at 20 Hz and averaged using 10-min intervals.

The OMS, shown in Figure 2.3g, is composed of a large aperture scintillometer (LAS MkII, Kipp & Zonen) and a microwave scintillometer (MWS, RPG-MWSC-160, Radiometer Physics GmbH), and measures simultaneously sensible (H) and latent (L_vE) heat fluxes over heterogeneous terrains (Beyrich et al., 2012; Meijninger et al., 2002a). The OMS was deployed in a ∼1.1 km path, with an effective height of 2.8 m and in the east-west direction. The OMS was installed in the northern end of the saline lake (Fig 2.2), with its path perpendicular to the main wind direction, and its estimated footprint covered the water from the saline lake and the wet salt. A novel aspect of the E-DATA field campaign is that it is the first time that an OMS is used in an open water body. The OMS data were averaged using 10-min intervals, and analyzed using the structure parameter coefficients defined by Ward et al. (2013), the temperature-humidity correlation coefficient estimated through the Hill (1997) method, and the Monin-Obukhov similarity theory (MOST) stability functions described by Kooijmans & Hartogensis (2016).

To investigate the surface energy balance, each EC system had different radiometers to estimate net radiation (R_n), as well as heat flux plates to measure the ground heat flux (G) at a specific depth (31/32 Heat flux meter, TNO Institute of Applied Physics,

The Netherlands; HFP01 and HFP01SC heat flux sensors, Hukseflux, Delft, The Netherlands). At the water surface, the four components of radiation were measured (CNR4 Net radiometer, Kipp & Zonen, Delft, The Netherlands). At the desert surface, only the net shortwave and net longwave radiation were available (CNR2 Net radiometer, Kipp & Zonen, Delft, The Netherlands), whereas at the wet-salt surface only an integrated measurement of net radiation was collected (NR2 Lite, Kipp & Zonen, Delft, The Netherlands). Additionally, the thermal conductivity and the volumetric heat capacity of the water, wet salt and desert were measured using a thermal properties analyzer (KD2 Pro, Decagon Devices, Pullman, WA, USA). These properties were used to estimate G at the surface of each measuring location using the calorimetric method to account for heat storage (Heusinkveld et al., 2004).

No efforts were made to measure evaporation in the wetlands of the northern end of the saline lake (see Fig. 2.2), located downwind, as our main interest was to investigate the impact of advection on the evaporation rates at the lake.

The characterization of the surface energy fluxes at the water, desert and wet-salt surfaces measured with the EC systems is shown in Figure 2.5 for November 17^{th}, 2018. Also, the energy balance closure is presented for the entire field campaign. Over the water surface, L_vE and G were the dominant surface heat fluxes with maximum values reaching ∼400 and ∼550 W m^{-2}, respectively, whereas the maximum H values were of ∼100 W m^{-2} (Fig. 2.5a). The total daily evaporation in this day was of 4.3 mm. The orthogonal regression for the energy balance at the water surface –calculated using 10-min integration time– had a slope of 0.58 with an $R^2 = 0.89$ (Fig. 2.5b). At the desert surface, the H was dominant with maximum values of 450 W m^{-2} and G reached maximum values of 200 W m^{-2}, with almost zero L_vE (Fig. 2.5c). A total evaporation of 0.1 mm was measured for this day. As shown in Figure 2.5d, the slope of the energy balance orthogonal regression was of 0.77 ($R^2 = 0.92$). G was the dominant surface heat flux at the wet-salt surface with maximum values of ∼350 W m^{-2}, and the maximum values of H reached ∼250 W m^{-2}. The maximum L_vE values are small and of the order of ∼60 W m^{-2} (Fig. 2.5e). The total daily evaporation in this day was of 0.5 mm. The slope of the energy balance was of 0.79, with $R^2 = 0.84$ (Fig. 2.5f).

A comparison of the surface energy fluxes at the water, measured by the EC-water system and the OMS on November 15^{th}, 2018, reveals that the EC system measures a larger L_vE than that measured by the OMS (Fig. 2.6). Accordingly, the H measured by the EC system is lower than that of the OMS. The maximum values of L_vE and H measured with the OMS are of ∼300 and ∼120 W m^{-2}, respectively. The differences between the surface energy fluxes measured by the EC-water and OMS are expected as their footprints are different. The EC-water system had its footprint on the saline lake, whereas the OMS footprint falls mainly over the water, but also cover a small part of the wet salt (Fig. 2.2). As shown in Figure 2.5, L_vE in the wet salt is almost zero, whereas

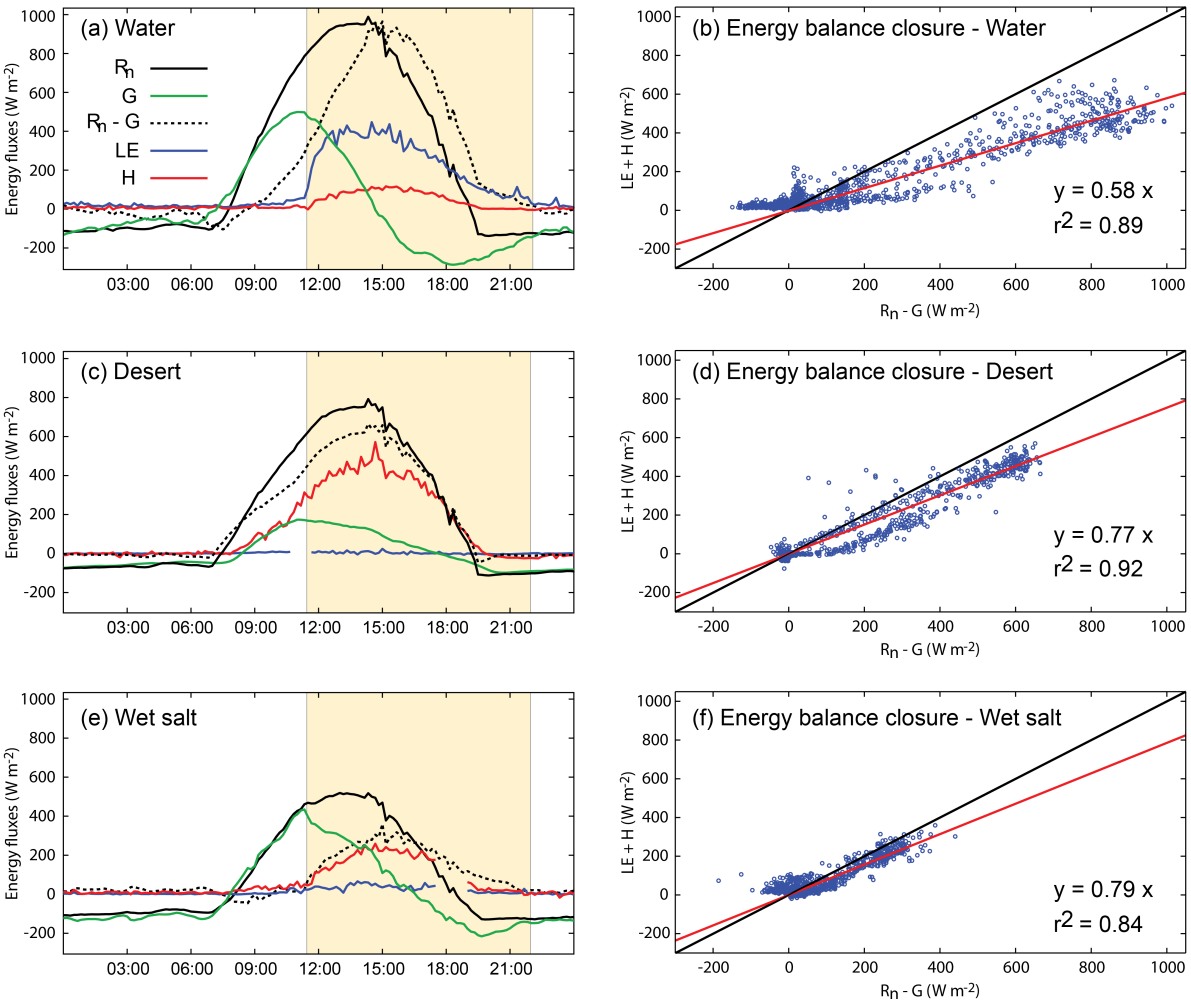

Figure 2.5: Characterization of the surface energy fluxes at the water, wet salt and desert surfaces, measured with the EC systems using an integration time of 10 min (November 17^{th}, 2018). Left: temporal daily evolution of the surface energy fluxes (R_n, G, L_vE and H) and the available energy (R_n-G) for the water (a), desert (c) and wet-salt (e) surfaces. The yellow background corresponds to the time period of the afternoon wind regime in which the wind speed is significant (> 4 m s^{-1}). Right: energy balance closure at the water (b), desert (d) and wet-salt (f) surfaces. The black line corresponds to the 1:1 line, the red line is the fitted line from orthogonal regression and the dots correspond to the 10-min values of (R_n-G) and (L_vE-H).

the H is larger than that measured by the EC-water system. Therefore, one would expect to have smaller values of L_vE and larger values of H in the OMS measurements compared to those of the EC-water system (Fig. 2.6). However, we are aware that these results are preliminary since no proper data quality treatment, footprint analysis, or theoretical adjustments have been performed. A detailed comparison between EC and OMS is addressed in Chapter VI, including a proper data analysis.

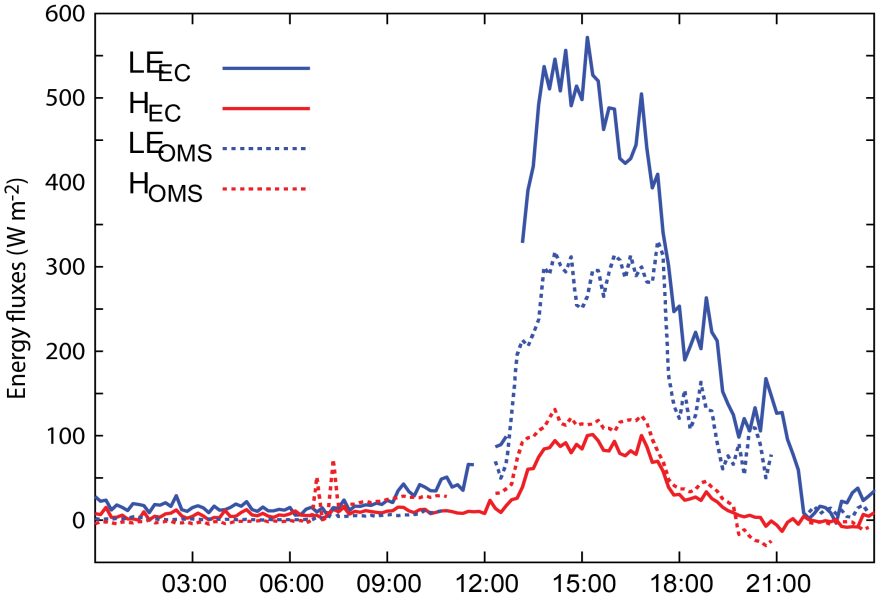

Figure 2.6: Latent (L_vE) and sensible (H) heat fluxes measured by the EC-water system and the OMS (November 15^{th}, 2018).

ABL investigation using radiosondes and an UAV

To have detailed information of the ABL, a radiosonde campaign was performed between November 18^{th} and 22^{nd}, 2018 (Table 2.3). We combined a relatively small balloon for boundary layer radiosounding with the iMet-4 Radiosonde (InterMet Systems, Grand Rapids, MI, USA) to obtain temperature, humidity, wind speed and direction, and height. Radiosondes were launched from the saline lake (near the receptor of the OMS) and from the desert (where EC-desert was deployed) (Fig. 2.2), for a total of 16 radiosondes launched during the E-DATA field experiment. Figures 2.3i, j show photographs of the radiosonde launching at the salt flat and at the desert location, respectively.

To complement the radiosonde campaign, detailed observation of pressure, temperature, and relative humidity at elevations between 0 and 500 m above the saline lake and above the desert were performed with an atmospheric sensor (iMet-XQ2, InterMet, Grand Rapids, MI, USA) installed in an UAV (Phantom 4 Professional, DJI, Shenzhen, Guangdong, China), as shown in Figures 2.2 and 2.3k. In this case, the ABL information was obtained with a resolution of ∼1 m. The UAV flights were performed every 30 min

Table 2.3: Schedule of the radiosonde campaign.

Date and Local Time	Location	Date and Local Time	Location	Date and Local Time	Location
18-11-2018 09:00	Lake	21-11-2018 09:00	Lake	22-11-2018 09:00	Desert
18-11-2018 12:00	Lake	21-11-2018 12:00	Lake	22-11-2018 12:00	Desert
18-11-2018 18:00	Lake	21-11-2018 15:00	Lake	22-11-2018 15:00	Desert
19-11-2018 09:00	Desert	21-11-2018 18:00	Lake	22-11-2018 17:00	Desert
19-11-2018 12:00	Desert	21-11-2018 21:00	Lake	22-11-2018 21:00	Desert
19-11-2018 18:00	Desert				

between 9:00 and 12:00 LT. On November 21^{st} the flights were carried out above the saline lake, and on November 22^{nd} the flights were performed above the desert (Fig. 2.2). Due to the strong winds during the afternoon, no flights were performed after 12:00 LT.

The results of the radiosonde campaign and UAV flights obtained over the lake (November 21^{st}, 2018) and the desert (November 22^{nd}, 2018) are presented in Figure 2.7. The vertical profile measurements show a complex thermal diurnal evolution of the ABL vertical structure (Figs. 2.7a, 2.7b). As shown in Figure 2.7a, above the water, a thermal stratification exists during the morning (09:00–12:00 LT), whereas in the afternoon, a strong capping (15:00 LT) followed by an unstable boundary layer are observed. In the evening (20:00 LT), a relatively shallow well-mixed boundary layer (∼400 m) is observed. In terms of specific humidity, the boundary layer goes from a very dry and windless condition to a less dry windy condition. At the desert location, there is a convective evolution from thermally stratified structure to a well-mixed boundary layer that reaches a height of ∼1,500 m at noon (Fig. 2.7b). In the afternoon, an internal cooler and moister 600-m thick boundary layer is observed (15:00 to 18:00 LT), and a strong wind from the southwest persists in the first 1800 m above the ground until the evening (20:00 LT).

The results obtained from the UAV flights reveal the details of the thermal vertical structure of the first ∼450 m within the ABL that develops during the morning. The measurements above the water and the desert surfaces obtained from the UAV flights agree with those collected with radiosoundings, although the UAV data has better spatial and temporal resolution. Recall that UAV data were only collected in the morning due to strong winds during the afternoon. Above the water, there is a cool air that is well-mixed in the first 200 m. Then, the air presents a strong stratification even until midday (Fig. 2.7c). At the desert location, a normal convective boundary layer growth is observed, where at 09:30 a stratified layer is formed that rapidly mixes towards midday (Fig. 2.7d).

DTS measurements

A DTS system (XT-DTS, Silixa, Elstree, UK) was deployed near the location of the OMS with the aim of capturing the horizontal temperature variation along bare ground, air above the ground and lagoon, and at the water-sediment interface (see DTS transect

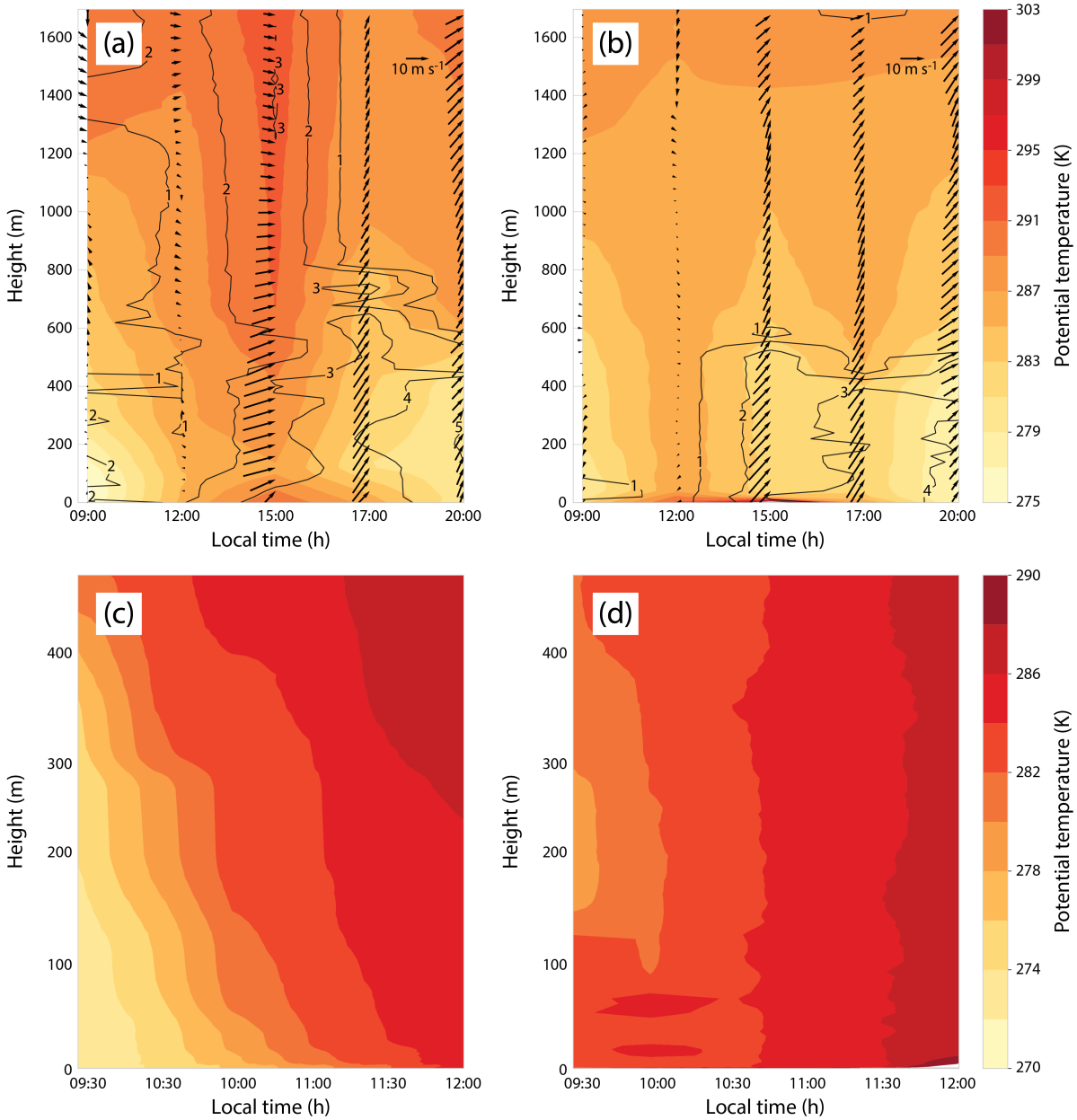

Figure 2.7: Diurnal evolution of the vertical profiles of potential temperature (K, colors), specific humidity (g kg^{-1}, solid lines) and horizontal wind speed and wind direction (m s^{-1}, arrows) measured with the radiosoundings. Measurements performed on November 21st, 2018 above the saline lake (a) and on November 22nd, 2018 above the desert (b). Conventional directions and arrow lengths are shown at the top of panels (a) and (b). Morning evolution of the potential temperature measured with the UAV on November 21st, 2018 above the saline lake (c) and on November 22nd, 2018 above the desert (d). Note the different height and temperature scales between the radiosondes and UAV data.

in the inset of Figure 2.2 and Figure 2.3h for a photograph of the DTS base station). Approximately 620 m of a 900 μm tight-buffered fiber-optic cable (AFL Telecommunications, Duncan, SC, USA) were used in this deployment. Approximately 50 m were used for calibration purposes, ∼100 m were on the ground surface, ∼450 m were deployed at ∼30–40 cm above the water surface (with ∼325 m deployed in the east-west direction and ∼125 m installed in the southwest-northeast direction), and ∼20 m submerged at the water-sediments interface (10–15 cm depth). The fiber-optic cable was connected to the DTS instrument that collected temperature data with a spatial resolution of ∼0.5 m (sampling resolution of 0.25 m) and an integration time of 15 s. The DTS system was calibrated using the manufacturer calibration software and using a single-ended configuration (Hausner et al., 2011; Suárez et al., 2011).

Representative thermal profiles obtained with the DTS system during midday (12:30 LT) and during nighttime (00:30 LT) are shown in Figure 2.8a. A large variability of surface temperatures is observed during the day in the bare ground with differences of up to ∼20 °C. Above the water surface, the air temperatures near the shore of the lagoon were warmer than those observed towards the lagoon center. During night, the opposite behavior occurs: cool and more stable ground temperatures were observed, and the air temperature above the lagoon center was warmer than that near the shore. During day- and night-time, the water-sediments interface temperature was relatively uniform, and variations of up to ∼15 °C were observed along the daily cycle.

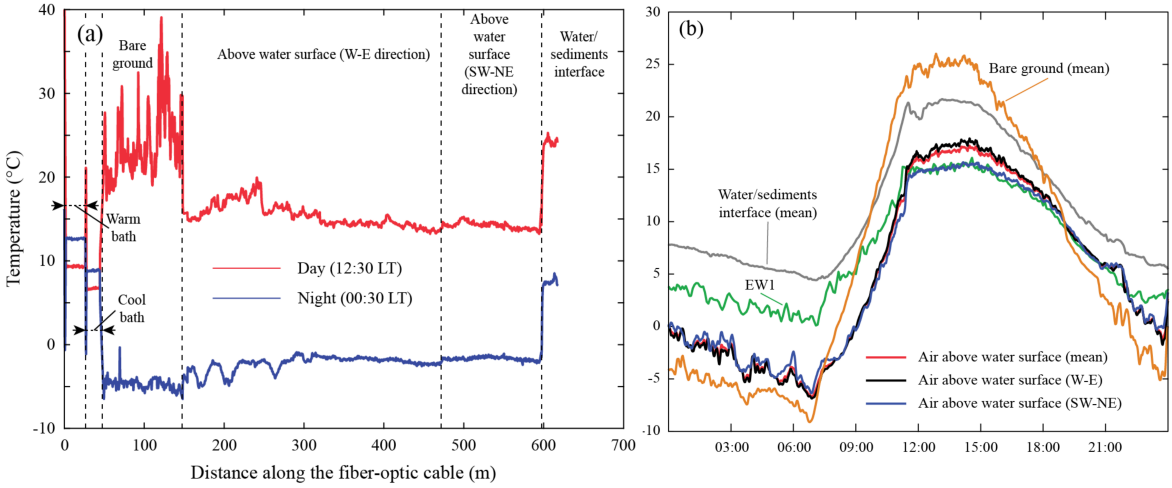

Figure 2.8: (a) DTS data that shows representative thermal profiles along the optical fiber for day- and night-time. The warm and cool bath are sections along the cable used for calibration purposes. (b) Temperatures measured with the EW1 meteorological station and the DTS system (November 17^{th}, 2018). The DTS temperatures shown correspond to the mean values of the different sections depicted in Figure 8a, and are integrated over 5-min to have the same time interval than the records of the EW1 meteorological station.

The temperature time series obtained with the DTS system reveal that there are significant differences between the temperatures measured at the different sections of the fiber-optic cable (Fig. 2.8b). The temperature of the bare ground exhibits a greater amplitude than that of the air and of the water-sediments interface. Further, the DTS air temperatures differ by more than 3 °C with those measured by EW1 during the morning windless regime, and there are also differences of ∼2 °C during the afternoon wind regimen between the air temperature measured in sections along the cable that were deployed in different directions (W-E and SW-NE directions). These results highlight the richness of the collected data and highlight that multiple observations are needed both spatially and temporally to understand the different physical processes that occur at the study site.

CO_2 Flux and meteorological conditions

To study the link between meteorological conditions and the biochemical dynamics of open waters in the saline lake was also an objective of the E-DATA field campaign. Particularly, to investigate the relationship between the wind magnitude and the CO_2 flux exchanged between the atmosphere and the saline lake. To study this link is motivated by the fact that the ecological description of these ecosystems indicates that the trophic chain is supported by benthic primary production (BPP) that occurs in the sediments of the saline lake (Zúñiga et al., 1991; Williams et al., 1995). BPP occurs in a thin active layer at the top of the sediments (de la Fuente, 2014; Revsbech et al., 1986), and it is due to the photosynthesis of benthonic species such as benthic diatoms and cyanobacteria (Dorador et al., 2010; Demergasso et al., 2003).

To relate meteorological factors and the CO_2 fluxes exchanged between the atmosphere and the saline lake, several biogeochemical parameters were measured. CO_2 fluxes were collected in the three EC systems. In the saline lake, the water temperature and DO were continuously measured using the HOBO U26 Dissolved Oxygen Data Logger (Onset Computer Corporation, Bourne, MA). Turbidity was measured with the Cyclops-7 turbidity sensor and loggers (PME, Inc., Vista, CA, USA). All of these measurements were collected at approximately 3 cm above the water-sediment interface. Because of the shallowness of the lake (∼10 cm depth (de la Fuente, 2014)), the water column is well-mixed. Hence, these measurements are representative of the entire water column.

A typical time series of the diverse on-line variables measured during the field experiment are presented in Figure 9. The summary of these observations shows the CO_2 fluxes were directed downwards, implying the saline lake is acting as a CO_2 sink. Furthermore, the magnitude of the CO_2 flux (blue area in Fig. 2.9b) is determined by the afternoon wind (u_*, wind shear velocity, measure for mechanical turbulent mixing), and the incident solar radiation (R_{sw}). On the one hand, wind cycles in the Altiplano region are characterized by calm conditions during the morning and windy conditions in the

afternoon (de la Fuente & Meruane, 2017; de la Fuente, 2014). As shown in Figure 2.9b, this diurnal meteorological cycle has direct influence on other observed variables, thus increasing the magnitude of the CO_2 flux, similar to evaporation (Fig. 2.5) and the lake's turbidity due to sediment resuspension during the afternoon (de la Fuente, 2014). This dynamic behavior of the CO_2 flux in the shallow lake is associated to exchanges with the atmosphere at the air-water interface, to benthic primary production during the day and respiration during the night, and other photochemical processes uniquely attributed to this extreme environment (Dorador et al., 2010, 2013, 2008; de la Fuente, 2014).

With respect to the rest of the variables measured in the water column, water temperature (black line in Fig. 2.9a) follows the characteristic diurnal cycle previously described by de la Fuente (2014) and de la Fuente & Meruane (2017). Briefly, it is larger than the air temperature, reaching maximum values a couple of hours after the peak of the incident solar radiation, and minimum values right before the sunrise. The *DO* concentrations are maximum in the afternoon under windy conditions and start to decrease after sunset, reaching minimum values at sunrise. Specific details are also observed in the DO time series and needs further analysis. For example, a drastic reduction of the *DO* concentration was observed at noon of November 16^{th} and 19^{th} (Fig. 2.9a). DO dynamics are driven by mass exchanges between the saline lake and the atmosphere when the wind blows, and *DO* production by photosynthesis and biochemical consumption (de la Fuente, 2014). Since these drastic *DO* reductions occurred in cloudy days, as seen in the incoming shortwave radiation (Fig. 2.9b), it is argued that these drastic changes in *DO* concentration may be due to rapid changes in the production/consumption ratio driven by cloud passing above the salt flat. However, the sudden drops in *DO* could also be an artifact as a result of sensor vibrations due to the onset of the strong afternoon winds.

2.4 WRF modeling setup and validation

The following subsections include detailed information of WRF numerical settings in Table 2.4. Moreover, this section includes the validation of WRF variables with surface and vertical observations (Fig. 2.10).

2.4.1 Modeling setup

Table 2.4 describes the numerical settings of the model for input files, time control, domains, physics schemes and dynamics. The initial and boundary conditions are obtained from ECMWF ERA-Interim reanalysis data for 20 °S, 68 °W with a spatial resolution of 0.5 °, which includes a 6 h update of the tendencies, due to the large-scale forcing. No additional data sources were analyzed due to the high agreement of the WRF results based on ERA-Interim data sources and surface observations. We modeled the entire period of E-DATA, from 13^{th} to 24^{th} November 2018. As for the spatial domains (Fig. 2.1c), the horizontal distribution includes four two-way nested domains, in which

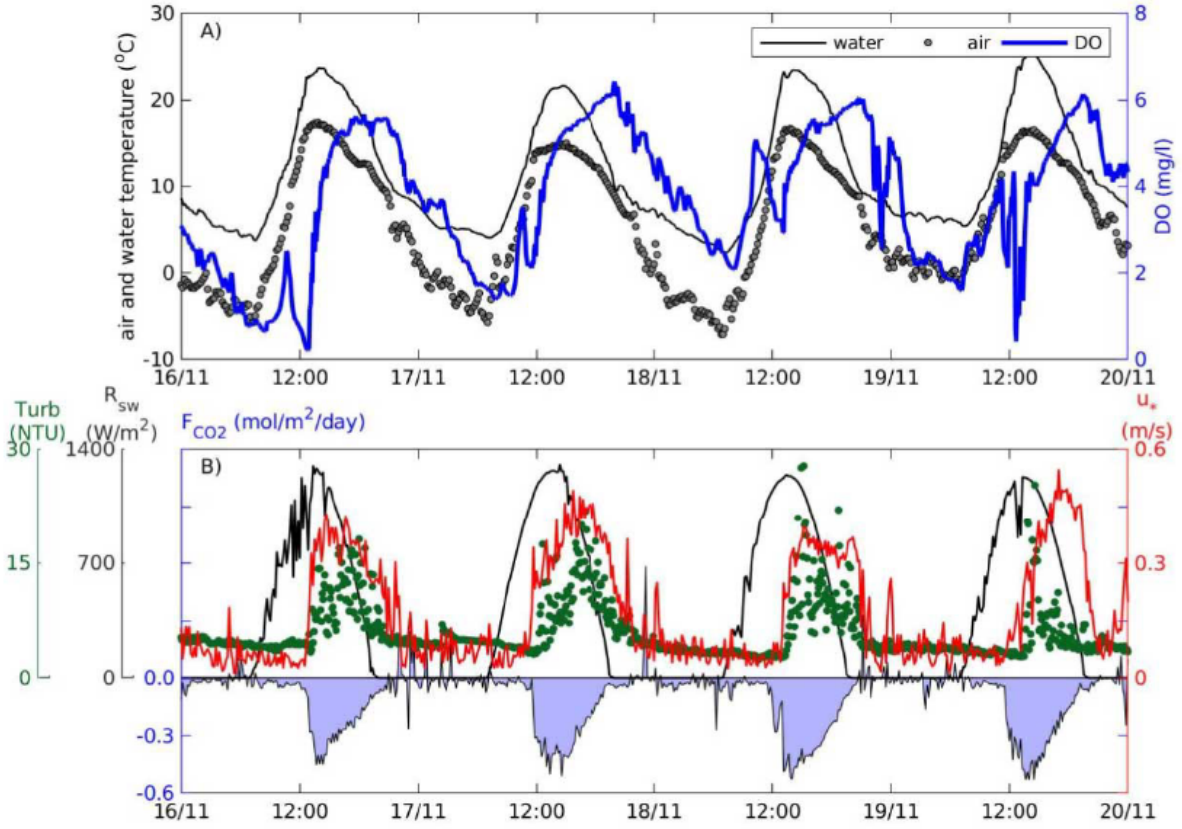

Figure 2.9: Field observation between November 16^{th} and 20^{th}, 2018, in EC-water: (a) Time series of air and water temperature, and dissolved oxygen (DO); (b) time series of incident short wave radiation (R_{sw}), wind shear velocity (u_*), turbidity, and CO_2 flux (F_{CO_2}) exchanged between the air and the water (positive upward).

the grid sizes are respectively 27 km for domain D01, 9 km for domain D02, 3 km for domain D03 and 1 km for the D04 inner domain. The D04 domain closely surrounds the study area. In its vertical direction, we defined 61 levels in an exponential fashion from the surface (including topography) to a height of 15.79 km, grouping 40 levels in the first 2 km. The physical processes represented are the RRTMG model for radiation physics (Iacono et al., 2008), the Monin–Obukhov scheme for the surface layer (Janjić, 1996), the YSU scheme for boundary layer physics (Hong et al., 2006), the unified Noah land-surface model (LSM) for land-surface physics (Ek et al., 2003), the WSM 3-Class simple ice scheme for microphysics, and the Kain–Fritsch scheme (Kain & Fritsch, 1993) for convective scheme. Additionally, we adjusted the land-use map to set the saline lake in domains D03 and D04. Moreover, we also increased the sea surface temperature (SST) 2 K in the WRF inputs of domains D01 and D03 according to the public information of the National Ocean and Atmospheric Administration (NOAA) from US Department of Commerce. We used additional special dynamic parameters within the model to filter

Table 2.4: Numerical settings used in WRF simulations organized by nested domains.

Time control				
Starting date	13^{th}, November 2018			
Ending date	24^{th}, November 2018			
Domains	D01	D02	D03	D04
Time step	50 s			
dx	27 km	9 km	3 km	1 km
dy	27 km	9 km	3 km	1 km
Vertical levels	61			
Top of the model	15,790 m (10,000 p_a)			
Physical parameterizations				
Surface layer	Monin-Obukhov scheme			
Radiation	RRTMG			
Boundary layer	YSU			
Land Surface	Unified Noah LSM			
Microphysics	WSM-3 class simple ice scheme			
Convection	Kain-Fritsch (new eta)			
Dynamics				
Wave damping	yes			
Damping option	w Rayleigh			
z damp	7,000 m			
Damp coefficient	0.2			
Two-way nested	no	yes	yes	yes
Non-hydrostatic	yes			

the effect of the unrealistic gravity waves caused by the strong topography of the Andes. The parameter we used has been the Rayleigh damping layer at 7,000 m with a damp coefficient of 0.2 (Klemp et al., 2008).

2.4.2 Model validation

The results obtained for domain D04 of the WRF model are validated by surface observation of CEAZA MET station (20.2 °S, 68.8 °W), which has been permanently in operation since 2015. The first row of Figure 10 shows the validation of WRF variables U, T and q, for an average period of E-DATA (13^{th}–24^{th} November 2018). The best agreement is during the daytime when evaporation occurs. We also validate our simulation using a station at the Pacific Ocean shore, Diego Aracena airport station at Iquique (20.5 °S, 70.1 °W), shown in the second row of Figure 2.10. This, aiming to validate our results obtained in domain D02, is used for characterizing the regional atmospheric circulation. We observe a good agreement in temperature and a slight overestimation in specific hu-

midity. However, the model follows satisfactorily the diurnal cycle of observations. The radiosoundings launched over the desert site are compared with vertical profiles of WRF shown in the third row of Figure 2.10. We observe a good agreement in U, θ, and q at noon and a good representation of the boundary layer height. Finally, based on our comparison of the wind speed during November 2015, 2016 and 2017, we conclude that our results for November 2018 are representative of the season climatology of the Salar del Huasco, since the wind pattern is very similar during the 4 years.

2.5 ERA5 reanalysis data

To complete the local-scale measurements obtained during the E-DATA experiment and the regional-scale WRF simulations, we used the standard meteorological reanalysis data from the ERA5 dataset at hourly resolution. ERA5 combines many historical surface and satellite observations into global estimates through advanced atmospheric modeling and data assimilation systems (Hersbach et al., 2020). Our aim using this dataset is to count with long-term meteorological data to estimate evaporation's climatology. We used the data corresponding to the grid point of Salar del Huasco at the first level (2-10 m from the surface) and from 1950 to 2020. To represent the local conditions of Salar del Huasco using ERA5 data, we downscaled the 10 km resolution reanalysis grid size to the 0.1 km observed by the meteorological station of Salar del Huasco.

Figure 2.11 shows the results of the downscaling process at the monthly scale of ERA5 raw to Salar del Huasco meteorological station in the period 2016 to 2019. In general terms, we observe that 2 m air temperatures, specific humidity, and wind speed from ERA5 downscaled are satisfactorily in agreement with the ones measured at SDH meteorological station. Here, the downscaling allows better representing the lowest temperatures, the highest specific humidity, and the seasonal evolution of wind speed.

The detailed process of downscaling and evaporation estimates using standard meteorological ERA5 data is described in Chapter 3.

2.6 Conclusions

In the endorheic basins of the Altiplano, water is crucial for sustaining unique ecological habitats, industry, and agriculture. Here, the wetlands act as highly localized evaporative environments, and little is known about the processes that control evaporation on space and on time. In this chapter, we presented the design and methods used in the 10-day E-DATA field experiment, the configuration of WRF modeling for characterizing the atmospheric regional flow, and downscaling of ERA5 reanalysis meteorological data for estimating evaporation's climatology.

The E-DATA field campaign was a specially designed experiment that combined

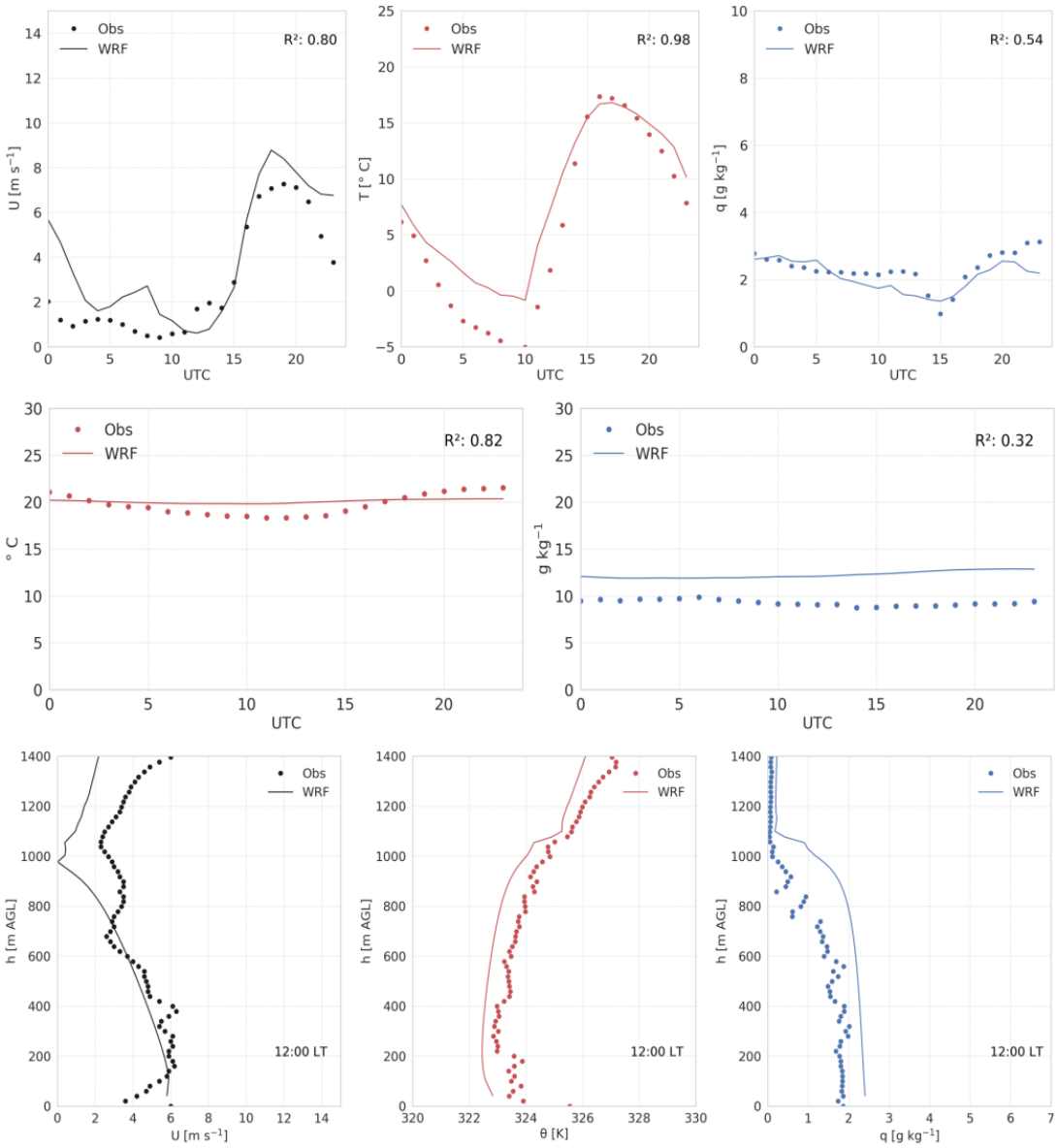

Figure 2.10: First row: diurnal average (13^{th}–24^{th} November 2018) of 2 m U , T and q of WRF domain D04 and CEAZA MET station. Second row: diurnal average (13^{th}–24^{th} November 2018) of 2 m T and q of WRF domain D02 and Diego Aracena airport MET station. Vertical profiles of U , θ and q of WRF domain D04 and radiosounding launched during the E-DATA on 22^{nd} November 2018 at 12:00 LT over the desert.

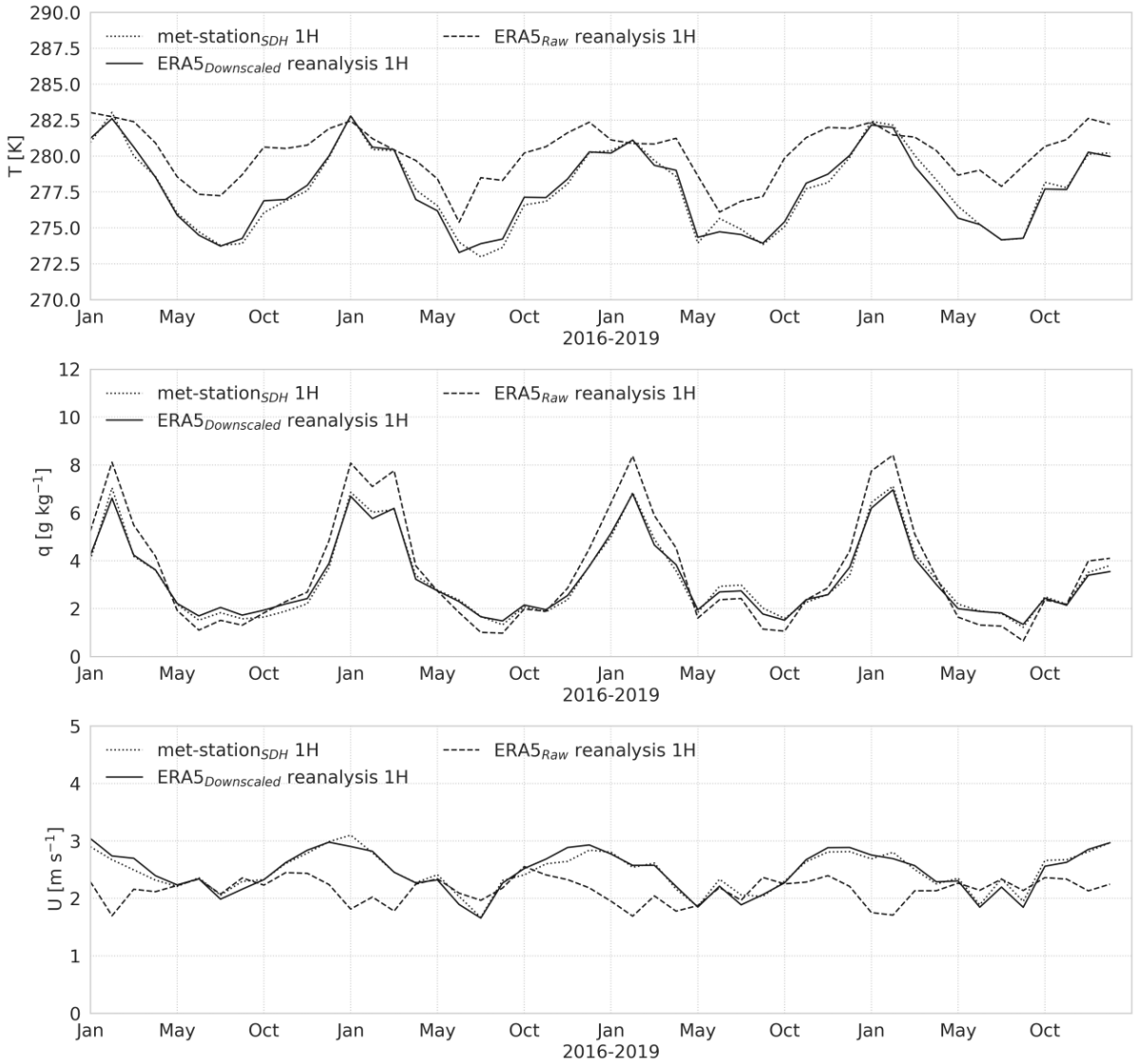

Figure 2.11: Seasonal variability of temperature (upper pannel), specific humidity (middle pannel), and wind speed (bottom pannel) between the available data sources: observations gathered from a meteorological station overland (met-station$_{SDH}$); ERA5 reanalysis raw data (ERA5$_{raw}$); and ERA5 reanalysis downscaled data (ERA5$_{down}$) from 2016 to 2019.

ground and airborne measurements to understand the evaporation dynamics over heterogeneous surfaces, at different spatial scales in the Salar del Huasco, Chile, with main emphasis on open water evaporation, and accounting for the interaction between the ABL and the atmospheric regional circulation. The installation strategy of the instruments used in the field experiment was accomplished using the WRF model, which enabled to identify the best locations for meteorological stations, eddy covariance systems, scintillometers, and a DTS system. These measurements were complemented with an intensive radiosonde campaign and UAV flights for detailed profiling of the ABL. Additional water

quality and CO_2 fluxes measurements were performed to identify the relationship between meteorological conditions and the biochemical dynamics of the Salar del Huasco.

WRF model is configured to simulate the atmospheric circulation at a larger scale for understanding the regional wind patterns that contribute to sub-diurnal evaporation evolution. Finally, ERA5 downscaled data provides reliable long-term meteorological observations for estimating actual evaporation climatology.

Chapter 3

Multi-scale temporal analysis of evaporation on a saline lake in the Atacama Desert

This chapter is based on:

Lobos-Roco, F., Hartogensis, O., Suárez, F., Huerta-Viso, A., Benedict, I., de la Fuente, A. & Vilà-Guerau de Arellano, J. (2022). Multi Temporal Analysis of Evaporation on a Saline Lake in the Atacama Desert. (Manuscript under discussion). *Journal of Hydrology and Earth System Sciences*.

Abstract

Evaporation is a key component of the water cycle in the endorheic basins of the Chilean Altiplano. In this study, sub-diurnal to climatological temporal changes of evaporation in a high-altitude saline lake ecosystem in the Atacama Desert are analysed. We analyse the evaporation trends over 70 years (1950-2020) at a high-spatial-resolution. The method is based on the downscaling of 30-km hourly resolution ERA5 reanalysis data to 0.1-km spatial resolution data using artificial neural networks. This downscaled data is used in the Penman open water evaporation equation, modified to compensate for the energy balance non-closure and the ice cover formation on the lake during the night. Our evaporation estimates show a consistent agreement with eddy-covariance measurements and reveal that evaporation is controlled by different drivers depending on the time scale. At the sub-diurnal scale, mechanical turbulence is the primary driver. At the seasonal scale, more than 70% of the evaporation variability is explained by the radiative contribution term. The seasonal variability of local evaporation follows the larger-spatial scale of moisture transport, which is simulated using the WAM-2layer model. Moreover, seasonal evaporation fluctuations significantly explain the saline lake discharge. At interannual scales, evaporation increased by 2.1 mm per year during the entire study period according to global temperature increases. Last, we find that yearly evaporation depends on the El Niño Southern Oscillation (ENSO), where warm and cool ENSO phases are associated with higher evaporation rates and higher precipitation rates, respectively. Our results show that warm ENSO phases increase evaporation rates by 15%, whereas cold phases decrease them by 2%.

3.1 Introduction

In arid regions, evaporation is one of the most important components in the water cycle since potential evaporation is typically one order of magnitude larger than precipitation (Lictevout et al., 2013; Houston, 2006a). Investigating evaporation in these regions is challenging due to the lack of observations, the landscape complexity, and the poor representation in hydrometeorological models. The climate/large-scale atmospheric circulation and spatially localized zones affect water availability (Lobos-Roco et al., 2021b). At a local level in the Atacama Desert, evaporation occurs (Houston, 2006): i) in rivers and the adjacent riparian zones; ii) in marshlands, where localized groundwater springs support vegetation growth and sometimes contribute to the formation of shallow terminal lakes (de la Fuente & Meruane, 2017), which generally occurs in the Andes Mountains; iii) in salt flats or playas, which are the result of more extensive groundwater discharge in endorheic basins (de la Fuente, 2014; de la Fuente & Meruane, 2017; Suárez et al., 2020); and iv) in bare soils where the water table is shallow (Rosen, 1994; Johnson et al., 2010; Uribe et al., 2015; Blin et al., 2021). The Chilean Altiplano is an arid zone where water evaporates from spatially localized environments, removing water from the basin. The Altiplano region has a unique environmental, economic, and social value due to its location within the Atacama Desert where rainfall provides a source of water for northern Chile. A reliable understanding of the processes that govern evaporation in this region is essential for three main reasons (Suárez et al., 2020). First, water resource management because a correct quantification of these fluxes enhances the performance of water balance models and improves the estimation of the basin's water recharge. Second, terrestrial and aquatic ecosystems that sustain the native flora and fauna of this region. Third, sustainable agricultural and mining production in terms of minimizing environmental impacts and maximizing water use. Within the Altiplano, the Salar del Huasco basin is chosen for studying evaporation due to the perennial terminal saline lake where non-local atmospheric processes occur (Suárez et al., 2020; Lobos-Roco et al., 2021b). This lake, untouched by human activities (Uribe et al., 2015), has been well-studied in recent years. These studies have focused on quantifying and understanding evaporation (de la Fuente & Meruane, 2017; Suárez et al., 2020; Lobos-Roco et al., 2021b,a) for use in water resource management models (Uribe et al., 2015; Blin et al., 2021). Thus, there are many comprehensive datasets of surface and upper-atmospheric observations for the Salar del Huasco basin that can be used to relate large-scale atmospheric phenomena with small-scale processes and, in turn, to advance our understanding of evaporation and its use for water resource conservation.

Synoptic and regional circulation over the Altiplano region, responsible for moisture transport and precipitation, has been studied by Rutllant et al. (2003), Falvey & Garreaud (2005), and Böhm et al. (2020). These studies investigated how large-scale atmospheric phenomena influenced by the Pacific Ocean, steep Andean topography, and the Amazon

basin organize circulations at different scales. These atmospheric circulations are the main contributors of moisture in the region. Two marked phases characterize the principal synoptic atmospheric circulation over the Altiplano region. The first phase occurs during the summer season (December to March). It is characterized by westward winds from the Amazon basin, which transport a significant amount of moisture over the Altiplano (Falvey & Garreaud, 2005). This moisture transport is highly variable from year to year, and it is responsible for convective rains that occur in the region. In the second phase dry air from the free troposphere above the Pacific Ocean is transported to the Altiplano region in the Andes (Rutllant et al., 2003) and occurs from April to November. This dry air transport results from the thermal differences between the western slope of the Atacama Desert and the Pacific Ocean (Lobos-Roco et al., 2021b). Other studies have reported the effects of the El Niño Southern Oscillation (ENSO) and the Pacific Decadal Oscillation (PDO) on precipitation patterns. Böhm et al. (2020) studied the integrated water vapor (IWV) variability and its relationship with the ENSO phenomenon in the Atacama Desert during the 20^{th} century. Their results revealed that cool ENSO phases (associated with the La Niña ENSO phenomenon) yield greater IWV variability which favors more extreme wetter conditions during the austral summer in the Altiplano region. Garreaud et al. (2003) analyzed the climatic conditions from interseasonal to glacial-interglacial timescales. Researchers found that mean zonal airflow over the region modulates interannual changes in the climatic condition over the Altiplano. This airflow respond to sea-surface temperature variability in the tropical section of the Pacific Ocean. Likewise, several studies have pointed out the remarkable control that cool ENSO phases exert over the precipitation in the Altiplano (Aceituno, 1988; Vuille et al., 2000; Garreaud & Aceituno, 2001). This control shows that cool ENSO phases yield wetter rainy seasons, whereas warm ENSO phases (El Niño) results in drier rainy seasons (Garreaud & Aceituno, 2001). This dependence on climatic factors means that temperature-dependent evaporation occurring at local scales is related to such phenomenon.

The spatiotemporal evolution of evaporation has also been investigated in the Altiplano region of the Atacama Desert. These studies aimed to understand the complex diurnal land-atmosphere turbulent transport over different surfaces (Kampf et al., 2005; de la Fuente & Meruane, 2017; Lobos-Roco et al., 2021b), characterizing the larger scale influence on the local evaporation (Suárez et al., 2020; Lobos-Roco et al., 2021b) or simply to assess daily evaporation from bare soils in order to develop relationships that can be used to relate evaporation with the water table depth (Johnson et al., 2010). These investigations mainly focused on short-term field experiments based on either daily measurements (Kampf et al., 2005; Suárez et al., 2020) or applied models used to predict potential evaporation (de la Fuente & Meruane, 2017). Even with these studies, long-term evaporation observations at a local scale are still lacking, especially when trying to construct conceptual models that can be used for water resource management. For instance, Uribe et al. (2015) developed a hydrological model in the Salar del Huasco region

where evaporation was estimated using information from evaporation pans, and regional vertical gradients in evaporation were seen as a function of elevation. Blin et al. (2021) developed a groundwater model for the Salar del Huasco. This groundwater model, which was used to assess climate change impacts on the Salar del Huasco basin, utilized the hydrological model constructed by Uribe et al. (2015) to determine aquifer recharge and to estimate the evaporation discharge to the atmosphere. Unfortunately, these models overlook the influence of the non-local atmospheric processes, such as the entrainment and advection of heat, moisture and momentum, on evaporation rates (Suárez et al., 2020; Lobos-Roco et al., 2021b,a). Attempting to rectify this oversight, recent experimental field campaigns have been carried out in the Altiplano area of the Atacama Desert (Suárez et al., 2020). However, the lack of reliable long-term actual evaporation estimates still limits our complete understanding of the climate change impacts on water availability in these arid areas. Moreover, there are no studies that aim to investigate the myriad of links between these temporal short and large-scale studies. Thus, our objective is to understand seasonal and interannual evaporation variability by examining how surface energy partitioning, turbulence, and moisture supply affect seasonal changes in evaporation. In this way, we aim to bridge this cross-scale knowledge gap which will help to address water availability in the Atacama Desert.

In this study, we applied climatologically robust downscaled reanalysis data to the saline lake of the Salar del Huasco. Although we focused on one particular saline lake, this kind of surface represents the main evaporation pathway of the Altiplano region (Houston, 2006a). We hypothesized that radiative and aerodynamic factors could represent the evaporation of the specific conditions of the saline lake. This representation is performed using an adapted version of the Penman (1948) equation. The confirmation of this hypothesis enables to extend our evaporation calculations to the entire climatological period (1950-2020) and to investigate evaporation fluctuations in different ENSO phases. To complete this analysis, we show how monthly and yearly evaporation and precipitation lead to changes around the saline lake in the Salar del Huasco. Since precipitation in this area is closely related to large-scale atmospheric sources, we tracked the origins of these sources for the Salar del Huasco. In our analysis, we applied the following methodological steps. First, we downscaled the reanalysis meteorological data ($\sim$30 km) to local conditions ($\sim$100 m) observed above the saline lake by applying artificial neuronal networks and validating the downscaled data with eddy-covariance (EC) observations. Second, we developed a site-adapted version of the Penman (1948) equation. Third, we analyzed climatological trends and seasonal changes in evaporation and its drivers. Then, we determined interannual evaporation and precipitation anomalies related to ENSO phases and PDO over the last 70 years. Finally, we quantified local impacts of evaporation in the Salar del Huasco saline lake.

3.2 Methods

3.2.1 Study area

Our study area is located in the Salar del Huasco basin (1,462 km^2), whose highest point sits 5,200 m above sea level (asl), and its lowest point at 3,790 m asl (Uribe et al., 2015). This endorheic basin is located to the west of the Andes, 135 km inland from the Pacific Ocean. Since the basin is so close to the ocean, an intense and recurrent afternoon atmospheric flow from the ocean transports relatively cold and humid air into the Altiplano (Lobos-Roco et al., 2021b). The basin is also affected by the moist atmospheric flow coming from the east which is responsible for a marked rainy season during austral summer, where short convective storms are the main source of aquifer recharge (Blin et al., 2021). Since evaporation occurs where there is available water, our research focused on the basin's sink, which is a wetland in the Salar del Huasco (de la Fuente et al., 2021). Specifically, our attention is placed on the saline lake of the Salar del Huasco (20.2 °S, 68.8 °W, 3790 m asl), which is a perennial water body surrounded by salt crusts, zones with native vegetation patches and zones with bare soils (Fig. 3.1). This terminal lake shows significant seasonal changes in its surface ranging between ∼0.5 to 5 km^2, and has a measured depth of ∼15 cm (Lobos-Roco et al., 2021b). These types of groundwater-fed wetlands are commonly found in the Altiplano region (Kampf et al., 2005), and result in unique ecological habitats for endemic flora and fauna (Dorador et al., 2013).

3.2.2 Data acquisition

This study combines data from different sources including observations, modelling reanalysis data, and remote sensing datasets. Table 3.1 summarizes the datasets, variables, frequency, spatial resolution and sources employed in this research.

Two in-situ observation datasets are used. The first dataset corresponds to measurements integrated at 10-min intervals during the E-DATA field experiment (Suárez et al., 2020). Latent heat (L_vE) data were collected from an EC system (ECwater in Fig. 3.1) installed ∼1 m above the saline lake of the Salar del Huasco (20.27 °S, 68.88 °W; 3790 m asl) between November 13^{th} and 24^{th}, 2018. Meteorological variables, such as net radiation (R_n), air temperature (T), atmospheric pressure (P), relative humidity (RH), and wind speed (U) and direction (WD) were measured using an accompanying weather station to the EC system (Suárez et al., 2020). The second dataset corresponds to 1-hour measurements collected at the Salar del Huasco meteorological station (met-station$_{SDH}$, Fig. 3.1; Table 3.1), which belongs to the Center for Advanced Studies of Arid Zones (CEAZA). This station has been in continuous operation since October 2015 and is located 2 km north (20.25 °S, 68.87 °W 3,800 m asl) of the EC system, over bare soil at a height of 2 m (Fig. 3.1b). This dataset ensures an adequate characterization of the diurnal variability for a relatively long period of 4 years.

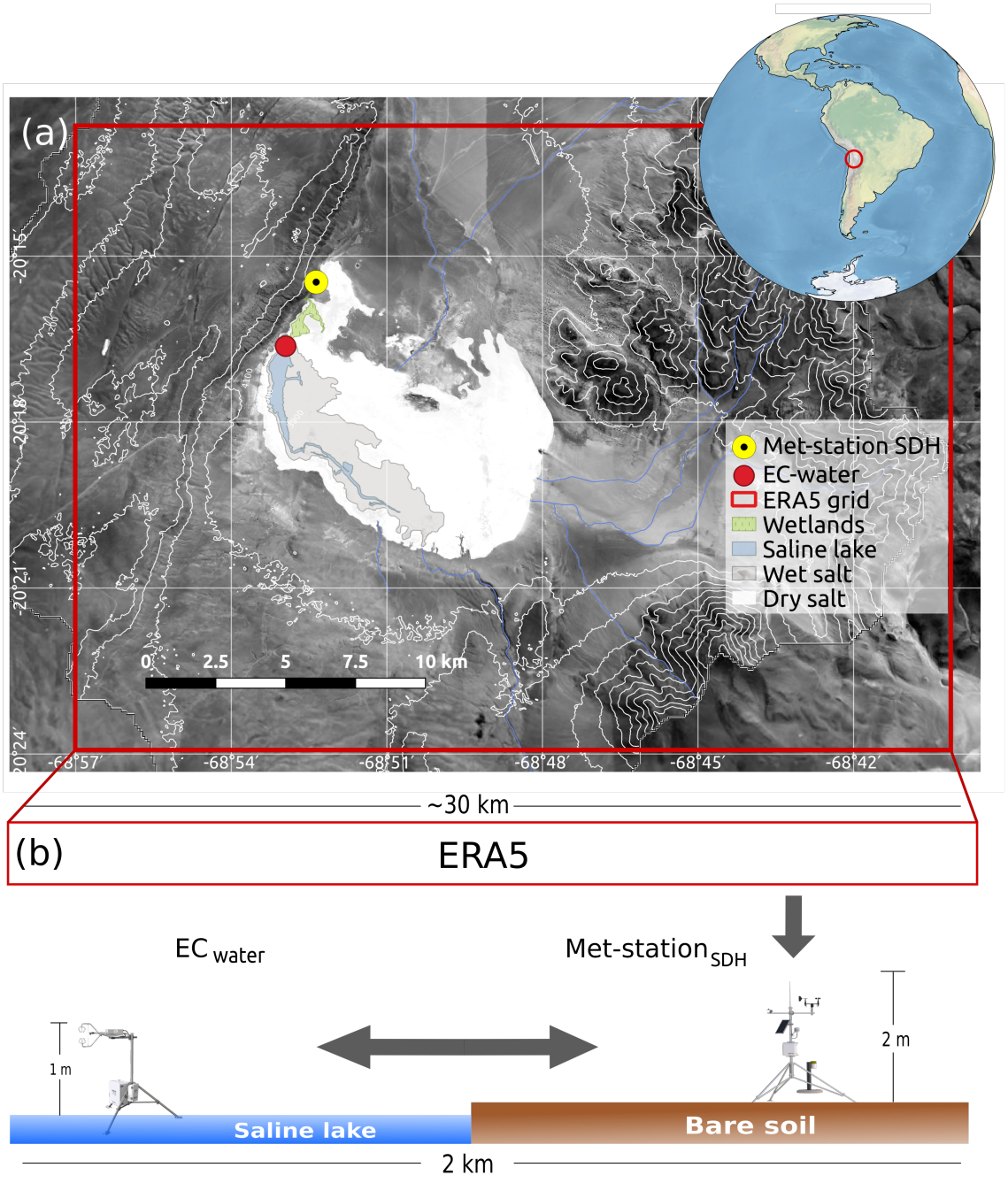

Figure 3.1: (a) Salar del Huasco saline lake and location of the meteorological station and the eddy covariance (EC) system used in this investigation. The red square shows an approximated grid size of the ERA5 reanalysis data. (b) Schematic cross-section of the meteorological downscaling from larger to smaller spatial scales.

Table 3.1: Description of the data used in this research. Variables analyzed are incoming shortwave radiation (Sw_{in}), net radiation (R_n), latent heat flux (L_vE), air temperature (T), air pressure (P), relative humidity (RH), specific humidity (q), wind speed (U), wind direction (WD), zonal wind (u), meridional wind (v), Pacific Decadal Oscillation (PDO), and Oceanic El Niño Index (ONI).

Type	Period	Variables	Height	Time frequency	Spatial resolution	Source
Observations	13/11/2018 24/11/2021	R_n, L_vE, T, P, RH, U, WD	1 m	10-min	∼100m	E-DATA field experiment (Suárez et al. (2020); Lobos-Roco et al. (2020)
	1/1/2016 31/12/2019	Sw_{in}, T, P, RH, U, WD	2 m	1 hour	∼100m	Salar del Huasco Meteorological st. from CEAZA (met-station$_{SDH}$)
Reanalysis	1/1/1950 31/12/2020	Sw_{in}, T, P, q, U, WD, Pp	2/10 m	1 hour	∼30 km	Hersbach et al. (2020)
Modeling (WAM-2layers)	1/1/1997 31/12/2018	E, Pp, q, u, v	1000-100 hPa	6-3 hours	1.5 degrees	Dee et al. (2011)
Remote sensing	1/1/1985 31/12/2020	SDH lake's area	-	1 month	30 m	de la Fuente et al. (2021)
Other	1/1/1950 31/12/2020	PDO, ONI	-	1 month	50°N-50°S 120°-170° W	NCEP-NOAA

The long-term climatological ERA5 reanalysis dataset (Table 3.1; Hersbach et al. (2020)), available at 1-hour resolution and 30 km spatial resolution, is downscaled to the conditions observed at met-station$_{SDH}$ (section 3.2.3). We use the data corresponding to the grid point of Salar del Huasco at the first level (2-10 m above the surface) from 1950 to 2020. The ERA5 dataset combines a vast amount of historical surface and satellite observations into global estimates with the help of advanced atmospheric modeling and data assimilation systems (Hersbach et al., 2020). Additionally, we use ERA-interim data (Dee et al., 2011) from 1997 to 2018, at 1.5 degrees of spatial resolution to track the moisture sources (Section 3.2.3). resulting in precipitation over the region. This data is obtained at 6-hourly timestep for the atmospheric variables (wind and specific humidity) and 3-hourly timestep for the surface variables (evaporation and precipitation).

To obtain the temporal evolution of the water surface of the Salar del Huasco lake, we use the data provided by de la Fuente et al. (2021). In brief, the saline lake water surface is calculated using Landsat 5 (January 1985 - June 2013) and Landsat 8 (March 2015 - December 2019) satellite images through normalized differenced water index (NDWI) at a pixel resolution of 30 × 30 m. The NWDI threshold is adjusted manually and contrasted to the size of the wetland computation based on the NDWI.

Two climatological oceanic indices at a monthly resolution are used to analyze macro-climatic phenomena, such as ENSO and PDO. These indices are obtained from the National Climate Prediction Center (NCEP). The first one is the Oceanic El Niño Index (ONI), which corresponds to sea surface temperature anomalies in the El Niño 3.4 region

(50 °N-50 °S, 120°-170° W) from 1950 to 2020. The second one corresponds to the HC300-based PDO index, a temperature anomaly index based on the heat content anomalies in the first 300 m layer depth of the North Pacific region, 20°N poleward (Kumar & Wen, 2016).

3.2.3 Data processing

Downscaling of meteorological data

The long-term ERA5 data are downscaled from ∼30 km to the local conditions (∼10-100 m) observed at the CEAZA's meteorological station (met-station$_{SDH}$ in Fig. 3.1a). Downscaling is performed using artificial neuronal network (ANN) algorithms (Dibike & Coulibaly, 2006; Kumar et al., 2012). The ANNs are solved using 10-hidden layers and using the Levenberg-Marquardt training algorithm. This process is performed with MATLAB's Neural Fitting tool. Air temperature (T), specific humidity (q), and wind speed (U) from the ERA5 dataset are used as input data for training and validation of the ANNs, whereas T, RH, U, WD, and Sw_{in} collected at met-station$_{SDH}$ are used as target data. Note that conditions observed at the met-station$_{SDH}$ (2 m) shows the same variabilities and magnitudes as the meteorological observations obtained by the EC$_{water}$ above the saline lake (1 m, see Fig. 3.1b) during the E-DATA field experiment.

As validation, Figures 3.2 and 3.3 show the time evolution and orthogonal regression of the ERA5 downscaled and raw variables of T, q, and U compared to surface observations of the met-station$_{SDH}$ and EC$_{water}$. In terms of temperature, Figure 3.2a shows that there are significant differences in the diurnal cycle of T between the ERA5$_{raw}$ data and the observations of met-station$_{SDH}$ and EC$_{water}$, especially at lower temperatures. Nonetheless, the temperatures observed above the water are in agreement with the values from EC$_{water}$ (1 m) and met-station$_{SDH}$ (2 m). Therefore, we can assume that air temperatures above the water and above the land are similar. This similarity allows us to validate ERA5$_{down}$ results on the saline lake using the data observed by the met-station$_{SDH}$. Figure 3.3a shows a satisfactory correlation between the ERA$_{raw}$ and the met-station$_{SDH}$ observations ($R^2 = 0.95$) but a low slope (m = 0.5). This mismatch is overcome when we apply the downscaling, where T increases the correlation coefficient ($R^2 = 0.97$) and the slope (m = 0.92) (Fig. 3.3a).

For specific humidity, there is more scatter in the met-station$_{SDH}$ observations, which results in low $R^2 = 0.38$ (Fig. 3.3b). However, similar to temperature, we observe an improvement after the downscaling, where ERA5 data increases the slope in the orthogonal regression from 0.43 to 0.77. Although the agreement between q-ERA5 and observations is lower than T-ERA5, q-ERA5 has a reasonable agreement with observations in the diurnal cycle (Fig. 3.2b).

In terms of wind speed (U), we observe more differences between EC$_{water}$ and met-

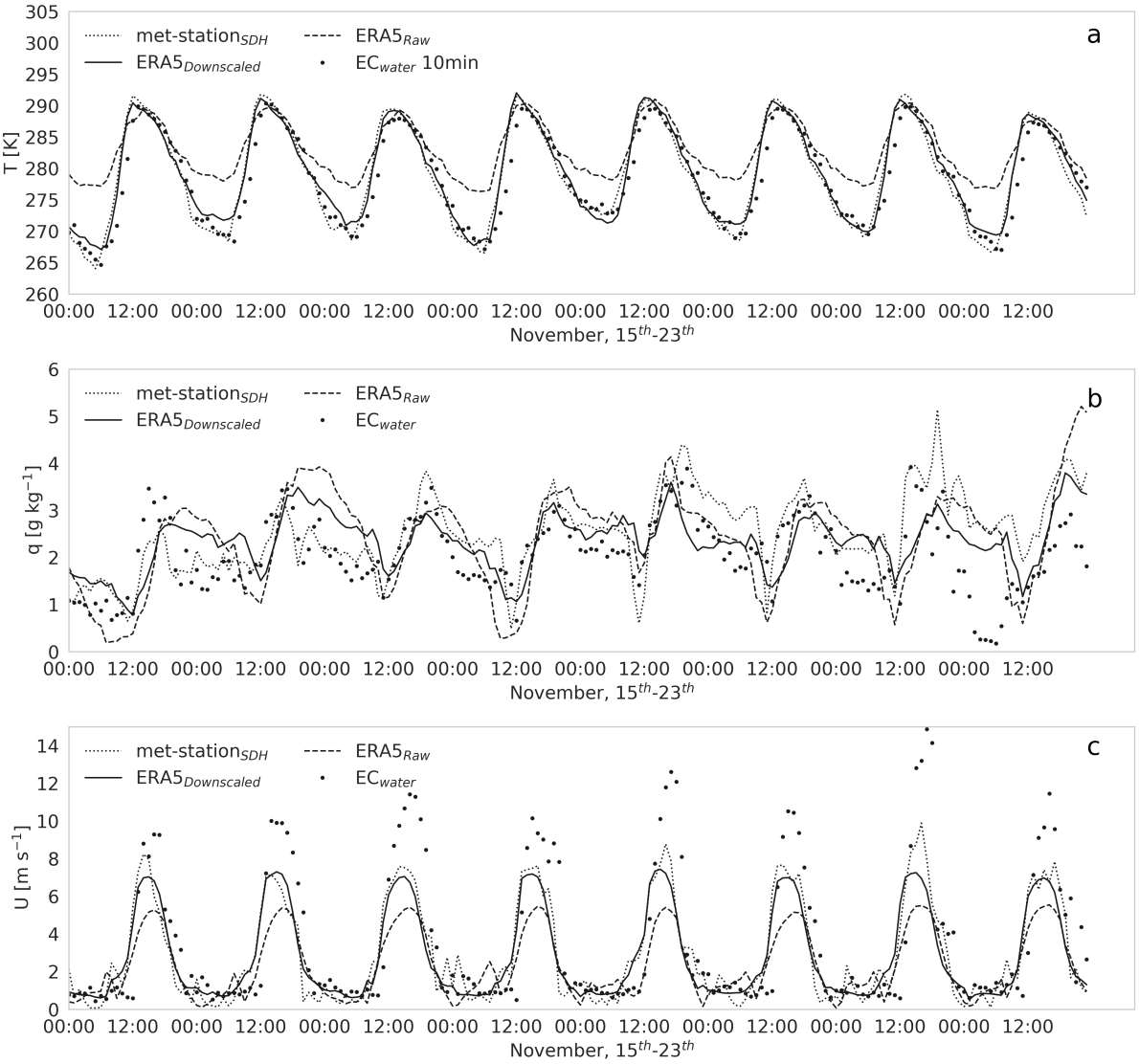

Figure 3.2: (a) Data comparison of temperature, (b) specific humidity, and (c) wind speed between the available data sources: observations gathered from an Eddy Covariance (EC) over water surface (EC_{water}); observations collected from a meteorological station overland (met-station$_{SDH}$); ERA5 reanalysis raw data ($ERA5_{raw}$); and ERA-5 reanalysis downscaled data ($ERA5_{down}$).

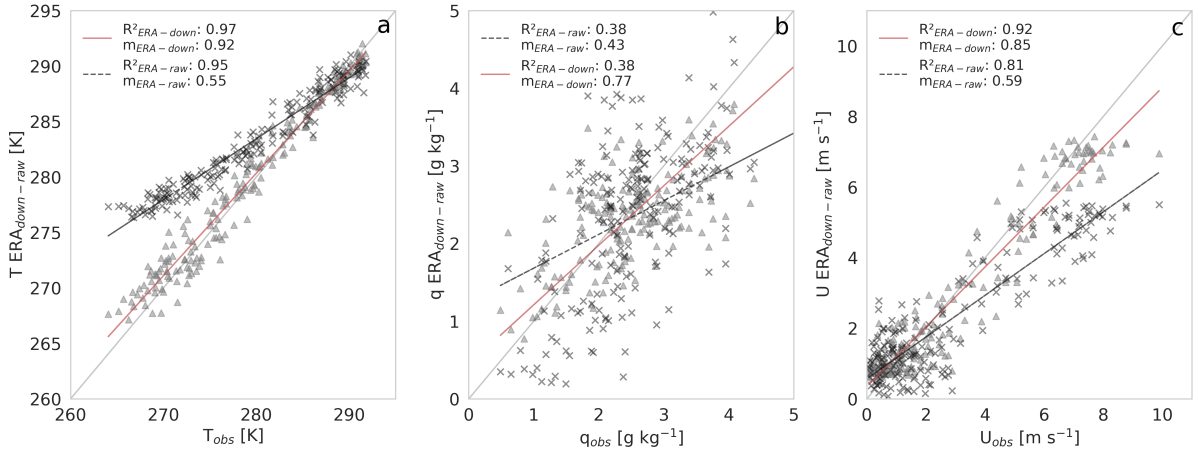

Figure 3.3: Comparison between ERA-5 data before and after the downscaling against the met-station$_{SDH}$ observations for (a) temperature (T), (b) specific humidity (q), (c) and wind speed (U). Crosses represent the ERA5$_{down}$ data and triangles the ERA5$_{raw}$ data.

station$_{SDH}$ during the maximum values. These differences are related to the nature of the surface where both instruments take measurements, EC$_{water}$, and met-station$_{SDH}$ above bare soil (Fig. 3.1). However, our statistical calculations corroborate the benefits of using the downscaling methods: R^2 increases from 0.81 to 0.92 and slopes from 0.59 to 0.85 as compared to ERA$_{raw}$. Finally, although wind direction is not used to estimate the evaporation and not shown in the plots, the ERA5 data have good agreement with observations.

Actual evaporation estimation

To estimate the actual evaporation, we employ an adapted version of the Penman (1948) equation for open water evaporation (Huerta-Viso, 2021), expressed in energy terms L_vE. Our approach is to use standard meteorological data of T, q, U, and Sw_{in} from the downscaled ERA5 dataset, and apply it to the specific conditions of the Salar del Huasco shallow lake. The adapted version of the Penman equation reads as:

$$L_vE = \overbrace{c_{ice}\frac{s}{s+\gamma}c_{EBNC}(R_n - G)}^{\text{Radiative}} + \overbrace{\frac{\rho_a c_p}{s+\gamma}\frac{1}{r_a}(e_s - e)}^{\text{Aerodynamic}}, \tag{3.1}$$

where s [Pa K^{-1}] is the slope of saturated vapor pressure curve, γ [Pa K^{-1}] is the psychrometric constant, R_n [W m^{-2}] is the net radiation, G [W m^{-2}] is the ground heat flux, ρ [kg m^{-3}] is the dry air density, c_p [J K^{-1} kg^{-1}] is the air's specific heat at constant pressure, r_a [s m^{-1}] is the aerodynamic resistance, e_{sat} [Pa] is the saturated vapor pressure, and e_a [Pa] is the vapor pressure at measured level. c_{ice} [-] is the ice coefficient, which is a correction coefficient that represents the evaporation reduction that occurs when

an ice cover is formed above the saline lake (Vergara-Alvarado, 2017), and c_{EBNC} [-] is the energy balance non-closure coefficient, which corrects the available energy (R_n–G) to improve the energy balance closure. Note that Equation 3.1 becomes the Penman (1948) equation when $c_{ice} = c_{EBNC} = 1$. Appendix A describes the details of the calculation for each term in the Equation 3.1.

Climatological analysis

To evaluate the diurnal variability of evaporation, the evaporation estimates are compared with observations using orthogonal regression, where we estimate the error employing the root means squared error (RMSE), the mean absolute error (MAE), and the correlation (R) and determination (R^2) coefficients. The climatology of evaporation estimates (section 3.2.3) and precipitation data obtained from ERA5 is analyzed at seasonal and interannual scales. For seasonal time scales, we use descriptive statistics of mean, maximum, minimums, and quantile 25, 50, and 75 for each averaged month over the entire period (1950-2020). For the interannual time scales, we calculate monthly anomalies as the difference between the 12-month moving average and the mean of the entire period under study. Our reason for using the moving average is to decrease the high scatter that monthly means produce and better evaluate the ENSO and PDO influence on the evaporation and precipitation.

Large-scale moisture transport tracking model

To get an overview of the moisture transport that result in precipitation over the Altiplano region and surrounding areas, we determine the moisture sources of a selected region. This selected region encompasses the Salar del Huasco and an extensive region around it, spanning from 83° W to 57° E, and from 11° N to 27° S (Fig. 3.7). Precipitation over this region is tracked backwards in time to determine where the water originally evaporated, the moisture sources. To determine these moisture sources, we use ERA-Interim data (Dee et al., 2011) from 1997-2018 to force the Water Accounting Model-2layers (WAM-2layers; van der Ent et al. (2010); van der Ent (2014)). WAM-2layers is an Eulerian offline moisture tracking model which solves the atmospheric water balance for every grid cell. Tracking is performed on two layers in the atmosphere, hence the atmospheric input variables from ERA-Interim are integrated over two layers. Well-mixed conditions are assumed for both layers. More information on the model is given by van der Ent et al. (2010); van der Ent (2014). Seasonal averages of moisture sources are shown (1997-2018; summer (JFM), autumn (AMJ), winter (JAS), and spring (OND)) together with the direction and intensity of the moisture fluxes.

Estimation of the long-term mass balance of the lake

The long-term water balance in the saline lake is assessed by combining the mass conservation principle with actual evaporation and precipitation estimates obtained from the downscaled ERA5 dataset. The mass balance is evaluated as follows. First, the volume of the lake in a specific month is estimated using the lake's area and assuming a constant lake depth that varied between 0.05 and 0.20 m. Second, we estimate the monthly lake outflow using the actual evaporation values and the lake's area, assuming no groundwater outflow. Third, we determine the volume reduction of the lake due to evaporation by subtracting the volume of water evaporated in a month from the volume of the lake. Then, the lake area of the next month is computed dividing the lake's volume by its depth. This area is compared to that obtained using remote sensing data to determine the additional monthly water volume required to achieve the observed lake surface. By associating this additional water input with precipitation, we determine the areal extension of precipitation that contributes to represent the observed areas of the lake. Because most of the time there are no surface water inputs, this additional water source must represent groundwater inputs into the lake. The approach followed here is a first order approximation that can be used to understand the key components of the lake's water balance.

3.3 Results and discussion

This section describes the diurnal, seasonal and interannual variability of evaporation at the saline lake of Salar del Huasco. First, we analyse the site-adapted Penman equation evaporation estimates using the L_vE observations taken above the saline lake with an EC as reference. Secondly, we analyze the seasonal variations of evaporation and its main drivers. In addition, we quantify the role of evaporation in the water balance of the saline lake, including precipitation as an essential component of the water cycle. Finally, we close the article by studying the climatological trends of evaporation-precipitation and the influence of macroclimatic effects such as the ENSO and PDO phenomena on their anomalies.

3.3.1 Diurnal cycle perspectives

Within this subsection, we quantify the diurnal cycle of actual evaporation from its energy and aerodynamic contribution using the standard Penman (1948) equation. In addition, we validate the ice coefficient (c_{ice}) and the energy balance non-closure coefficient (c_{EBNC}) compared to the evaporation measurements from E-DATA experiment.

Figure 3.4 shows the averaged L_vE diurnal cycle over the E-DATA period observed by the EC_{water} calculated using the site-adapted Penman equation (P_{SDH}, Eq. 3.1), and the standard Penman (1948) equation (P_{stdr}). Figures 3.4a and 3.4b indicate that there

is a satisfactory agreement between L_vE observed and estimated. The main difference is the two-hour lag during the morning transition (between 11:00 and 13:00 LT) that results from the height at which ERA5 wind is calculated: 10 m. These data have a root mean square error (RMSE) of 73 W m^{-2}, and a mean absolute error (MAE) of 17 W m^{-2}. Likewise, the orthogonal regression of L_vE between the P_{SDH} and EC_{water} observations have acceptable correlation and determination coefficients (R = 0.88 and R^2 = 0.78, respectively) and orthogonal regression slopes (m = 0.98).

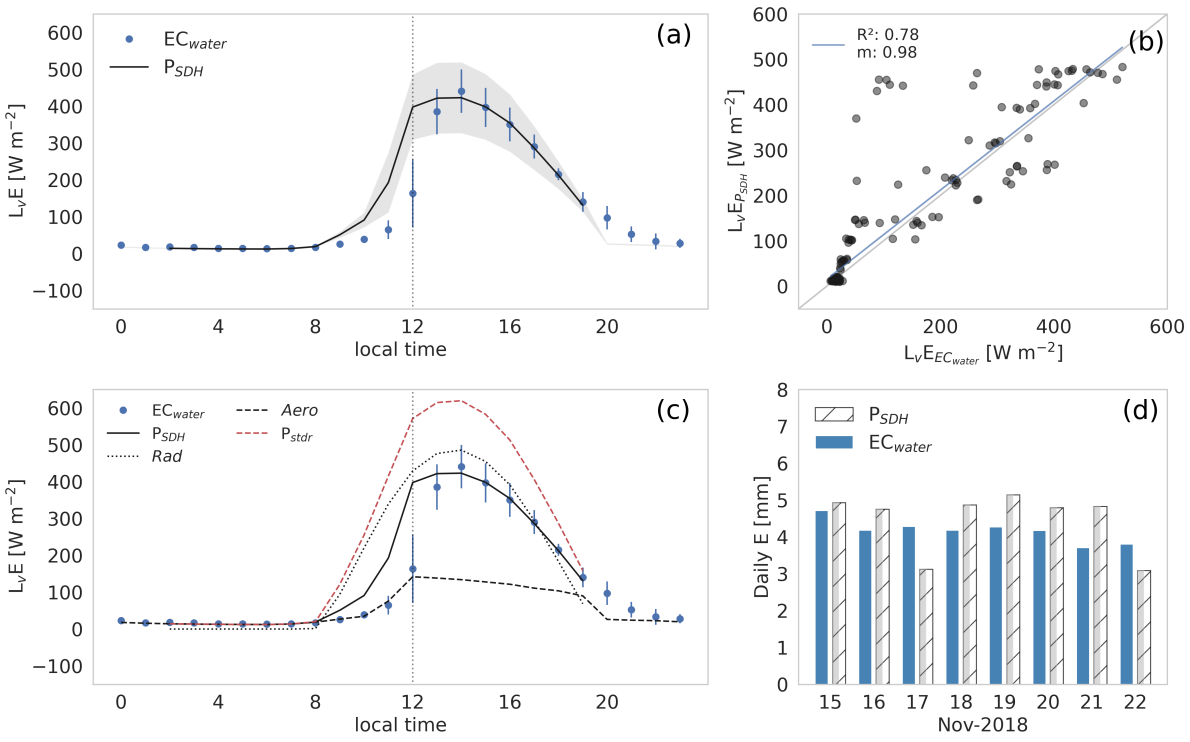

Figure 3.4: (a) E-DATA period averaged and standard deviation of the diurnal cycle of L_vE observed by the EC_{water}, calculated by P_{SDH} equation. (b) Orthogonal regression between L_vE measured by the EC_{water} and those estimated through P_{SDH}. (c) Diurnal cycle of L_vE observed by the EC_{water}, calculated by the P_{SDH}, standard Penman (P_{stdr}), and the aerodynamic (*Aero*) and radiative (*Rad*) contribution. (d) Daily evaporation (mm) measured by the EC system and estimated through P_{SDH}. The vertical dotted line in (a) and (c) indicates the wind regime change.

To better understand the L_vE results obtained by P_{SDH}, we analyze the radiative energy and aerodynamic contributions to the standard Penman L_vE separately, along with the performance of the introduced and coefficients. Figure 3.4c shows the averaged diurnal cycle of the energy and aerodynamic term of the standard Penman equation, compared to the results of P_{SDH} (Eq. 3.1) and the EC observations of L_vE. The L_vE-diurnal pattern shows two distinct regimes: in the morning (before 12:00 LT), the aerodynamic term follows the observations closely whereas in the afternoon (after 12:00 LT), the energy term is

the one with a closer match. Our explanation is based on the limiting regimes, which have been studied by Lobos-Roco et al. (2021b), Lobos-Roco et al. (2021a), and Suárez et al. (2020). During the morning, L_vE is limited by the absence of mechanical turbulence. As a result, the transport from the saturated air above the surface into the dry atmosphere is hampered which results in relatively low values for L_vE. In turn, and during the afternoon, due to the regional wind flow arrival, the enhancement of mechanical turbulence leads to high values of evaporation, and L_vE depends on the amount of the available energy. This radiative energy control is more clearly observed from 14:00-15:00 LT when the radiation decreases yields of L_vE. The addition of energy and aerodynamic contribution to the standard Penman equation shown in Figure 3.4c (dashed red line) demonstrates an overestimation of 88 W m^{-2} concerning the observations, where the diurnal cycle is only followed during the afternoon (windy regime). When comparing the P_{SDH} (Eq. 3.1) and the standard Penman L_vE equation, we observe that and coefficients significantly improve the evaporation estimates. This improvement is given first by the coefficient that reduces the available radiative energy under calm wind conditions, decreasing it by 70% and 30% under windy conditions. Secondly, the coefficient improves L_vE estimations by mitigating the fluxes when the water in the lake is frozen in a factor of 0.3 (Appendix A4). Table 3.2 summarizes comparative statistical metrics between the results obtained using a standard and a site-adapted Penman equation with observations.

Finally, in Figure 3.4d, we integrate sub-diurnal evaporation estimates for validating our results during the entire E-DATA period. The Figure shows the daily evaporation between the EC observations and the P_{SDH}. Daily values show differences of ∼0.65 mm between observations and estimations (RMSE: 0.7 mm; MAE: 0.6 mm). Integrating the whole E-DATA period, the differences are ∼5 mm: 38 mm for P_{SDH} and 33 mm for EC_{water}. To place these differences into perspective, it is worth noting that our focus in this research is to study the climatology of the evaporation in this region. As such, we consider that mean daily errors below 1 mm per day are low enough to use Equation 3.1 using the ERA5 downscaled data for long-term actual evaporation estimations.

Nevertheless, to extend our validation into a longer period analyzed in sections 3.3.2 and 3.3.3, Figure 3.5 shows the L_vE calculated using two methods: (1) the site-adapted Penman monthly evaporation estimates using ERA5 downscaled data and (2) observations from the met-station$_{SDH}$ between 2016-2020. We find a good agreement between both estimates. The results show that ERA5 follows the seasonal cycle (R^2: 0.81) satisfactorily. However, ERA5 evaporation overestimates the observations by 7.6%, which is consistent with the overestimation that ERA5 reported evaporation results with respect to the EC observations during the E-DATA period (6.1%).

The previous evaluation provides enough support to use the site-adapted Penman evaporation results to count with high-quality long-term (1950-2020) actual evaporation estimates at local (saline lake) scales and high time resolution (1-hour).

Table 3.2: Statistical metrics for comparing standard Penman, site-adapted Penman, radiation and aerodynamic contribution for L_vE, compared to L_vE EC_{water} observations. Monthly evaporation integration compares site-adapted evaporation estimates performed using ERA5 and met-station$_{SDH}$ during the period 2016-2020.* Evaporation monthly integration comparison metrics are between P_{SDH} estimates using ERA5 and observation from met-station$_{SDH}$ (Table 3.1).

	RMSE	MAE	R	R^2	m
Site-addapted Penman (P_{SDH})	73 W m^{-2}	17 W m^{-2}	0.88	0.78	0.98
Standard Penman (P_{stdr})	149 W m^{-2}	88 W m^{-2}	0.87	0.76	1.35
Radiative contribution to L_vE	94 W m^{-2}	28 W m^{-2}	0.85	0.73	1.02
Aerodynamic contribution to L_vE	121 W m^{-2}	64 W m^{-2}	0.87	0.76	0.30
P_{SDH} E daily integration	0.7 mm	0.6 mm	-	-	-
P_{SDH} E monthly integration*	14.2 mm	7.2 mm	0.90	0.81	1.34

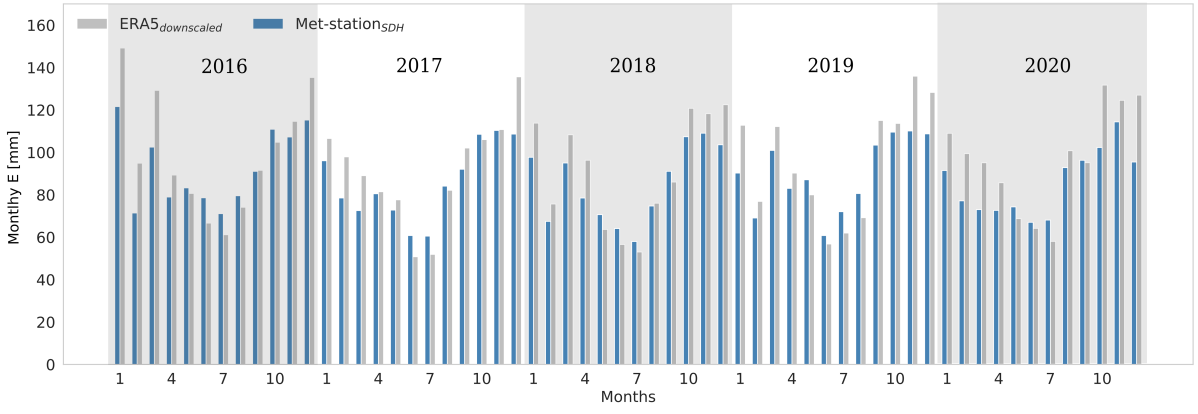

Figure 3.5: Monthly integrated evaporation obtained through the site-adapted Penman equation using ERA5 and met-station$_{SDH}$ standard meteorological data in the period 2016-2020.

3.3.2 Seasonal perspectives of evaporation and precipitation

Evaporation estimated sub diurnally through the Penman equation also presents significant seasonal changes that can have high impacts on water resources. This section first analyzes the seasonal cycles of actual evaporation by describing the changes in its radiative and aerodynamic contributions. In addition, we include the precipitation in the analysis for being an essential component in the water balance. Secondly, we analyze the seasonal evaporation and precipitation impacts on the water balance of the saline lake of the Salar del Huasco.

Evaporation and precipitation seasonal cycles

Figure 3.6a shows the actual evaporation seasonal average from 1950 to 2020 over the saline lake of Salar del Huasco. In general, seasonal changes of evaporation show their highest monthly values (>90 mm) during austral summer (JFM) and spring (OND). Within these seasons, October, November, and December present the highest monthly evaporation (107-120 mm). Even though the summer also presents high monthly evaporation (90-107 mm), these months also show the highest variability (standard deviation of 13.5-16.5 mm). The variability observed during summer months is because of the rainy season that usually extends over the summer (Vuille et al., 2000; Garreaud et al., 2003). Evaporation has its lowest rates during autumn and winter (<78 mm per month). Moreover, within these seasons, the months of June, July, and August show the lowest monthly evaporation (∼50 mm) and the lowest variability of the year (standard deviation of 7 mm per month). On the other hand, the seasonal variability of precipitation is shown in Figure 3.6b. Precipitation in the Salar Huasco basin shows a very clear seasonal cycle, with the onset of the rainy season in late spring (ND) and the offset end of summer (MA). However, this rainy season presents high variability over the years. The rest of the seasons show precipitation values below 25 mm per month, where June and July present a slightly higher variability.

To give a synoptic-scale perspective of the seasonal changes in local evaporation and precipitation present in the saline lake of Salar del Huasco, Figure 3.7 shows the seasonally averaged moisture sources of the Altiplano region. Here, we quantify the regions where evaporation occurs which results in precipitation over the Altiplano region (grey box in Fig. 3.7). As most precipitation occurs in austral summer (Fig. 3.6) the moisture sources are also largest in these seasons. We observe three principal moisture sources that contribute to precipitation in the Altiplano region during the year. The first one comes from the northeast (Amazon basin) and results from the veering of trade winds southwestwardly into the Andes mountains, associated with the continental low formed by the summery south-equator position of the Intertropical Convergence Zone, ITCZ (Aceituno, 1992). This southwestward flux is the most pronounced during the summer, transporting moisture (∼50 mm) into the Altiplano region. This marked moisture flux

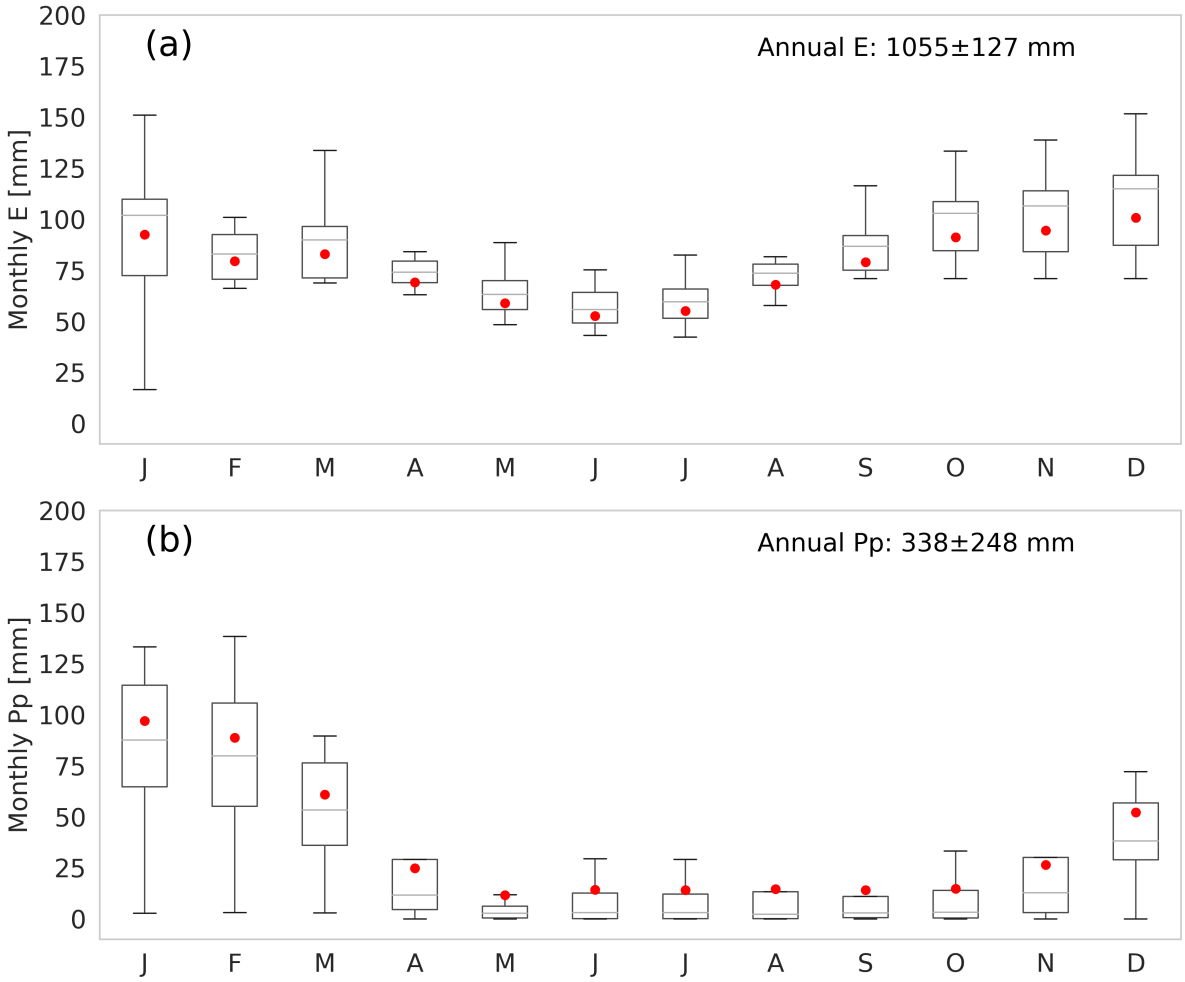

Figure 3.6: Seasonal variability of monthly evaporation (a) and precipitation (b) rates in the period 1950-2020. The boxes represent the 25%-75% interquartile, the grey horizontal line is the median, the red dots are the mean, and the bars represent maximum and minimum values. Outliers have been removed and annual evaporation and precipitation have been calculated over the entire period.

suddenly decreases towards the autumn and winter (∼10 mm). During these seasons, the trade winds return to their normal westwardly direction (Figs. 3.7b and 3.7c), resulting in low moisture transport (∼20 mm) into the region. Besides moisture transport into the region from the northeast, there is also recycling of moisture within the region, which can be considered to be a second moisture flux. Especially during summer, evaporation contributes to precipitation within the region, as can be seen by the high moisture source values around lake Salar del Huasco in JFM and OND (Figs. 3.7a and 3.7d). In addition to the contributions from evaporation over land, there is also a positive moisture source from the Pacific Ocean (south-southwest). In the absence of precipitation over the ocean, we can assume that the evaporation over the ocean contributes to the precipitation over land in the Altiplano region. Finally, this third moisture flux is associated with the subtropical anticyclone and stratocumulus cloud deck (Lobos-Roco et al., 2018; Rutllant et al., 2003). This flux transports a very low but persistent amount of moisture into the Altiplano region (<5 mm) due to the steep topography presented on the western slope of the Andes mountains, which in combination with the anticyclone, limits the eastward flow up to the mountains. Despite the coarse model resolution, this low moisture transport has been reported using high-resolution modeling and airborne observations by Suárez et al. (2020) and Lobos-Roco et al. (2021b).

To unravel the processes involved in the seasonal evaporation, we analyze the seasonal variability of the drivers that control it. Figure 3.8 shows the seasonal cycle of the radiative and aerodynamic contribution of the Penman equation and subsequent correlations with monthly evaporation rates.

Figure 3.8a shows the seasonality of the radiative contribution to evaporation, whose highest values correspond to the spring and summer and slowly decrease towards the winter only to increase again in early spring. The seasonality of the radiative contribution is similar to that of evaporation shown in Figure 3.6b, but it presents two distinctive characteristics. Firstly, from November to March, there is a larger scatter (standard deviation > 12 W m^{-2}), where the radiative contribution to evaporation can be high at 170 W m^{-2} or low at 20 W m^{-2}. This large variability is directly related to the summer rainy season (Vuille et al., 2000), where the presence of clouds largely modulates the available net radiation (Houston, 2006a). This double feedback that precipitation has over the radiation might explain the large scatter in the radiative contribution to evaporation during spring-summer. Secondly, the small variability (standard deviation of ∼3 W m^{-2}) of the radiative contribution during the winter months is related to the atmosphere's stability, characterized by the dry weather and cloudless conditions during most of this period. Therefore, there is enough evidence to support the idea that radiative contribution controls evaporation at a seasonal scale ($R^2 = 0.91$, as shown in Fig. 3.8b).

Figure 3.8c shows the seasonality of the aerodynamic contribution to evaporation, where the highest and lowest values are observed in early spring (SON) and during summer

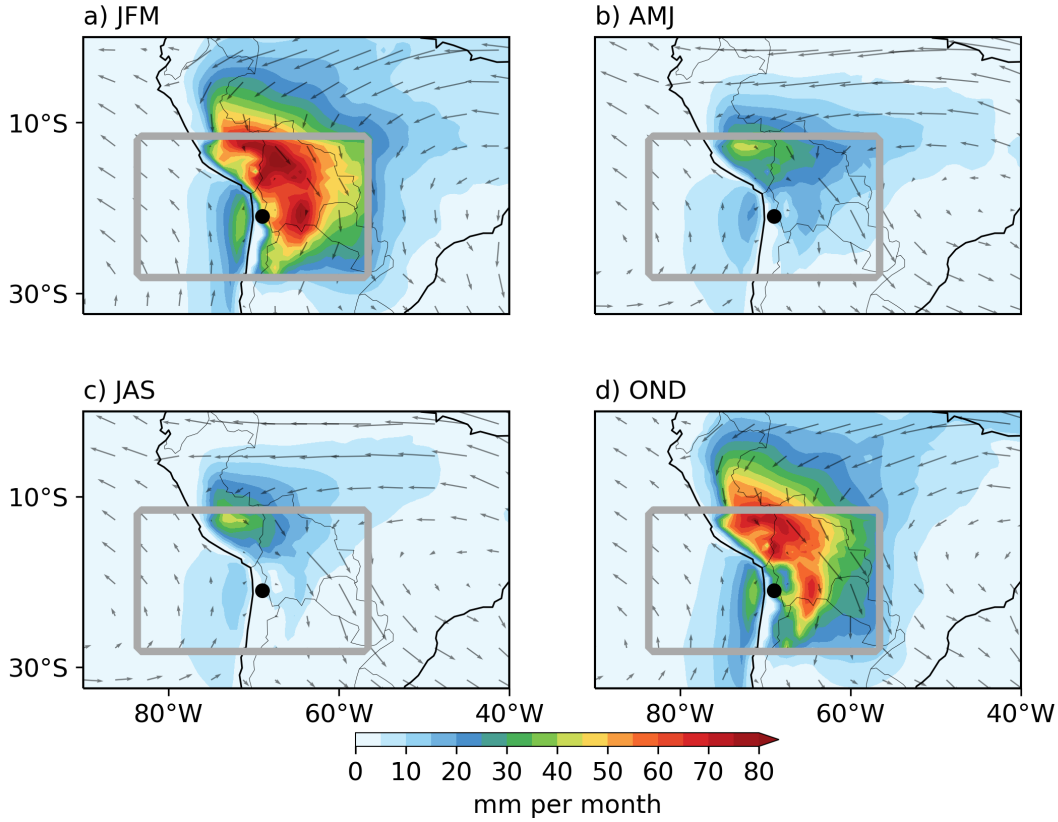

Figure 3.7: Seasonal variability of moisture sources (shaded) in mm per month and vertical integrated moisture transport (arrows) over the Altiplano region for (a) summer, (b) autumn, (c) winter, and (d) spring. The grey square frames the Altiplano regions and surroundings for which the sources are determined. The black dot indicates the Salar del Huasco location.

(JFM), respectively. The variability of the aerodynamic contribution is fairly constant during the whole year (standard deviation of ∼4 W m^{-2}), which is related to the seasonality of the wind circulation patterns (Falvey & Garreaud, 2005). The wind seasonality also explains the highest and lowest aerodynamic contribution to seasonal evaporation. For example, the thermal contrast between the Pacific Ocean and the Atacama Desert reaches its maximum in November, resulting in the strong regional atmospheric eastward flow, responsible for the onset of diurnal evaporation in the Salar del Huasco (Lobos-Roco et al., 2021b). To the contrary, during summer, predominant westward regional circulation from the amazon basin counteracts the eastward regional flow (Garreaud et al., 2003), decreasing the wind speed (as described below). Finally, during winter, the lower thermal contrast between the Pacific Ocean and the Andes Altiplano, along with the absence of the summer westward regional flow, results in lower wind speed. Consequently, there is less aerodynamic contribution to evaporation. The scattered seasonality of the aerodynamic contribution to evaporation also results in a low correlation (R^2 = 0.34, as shown

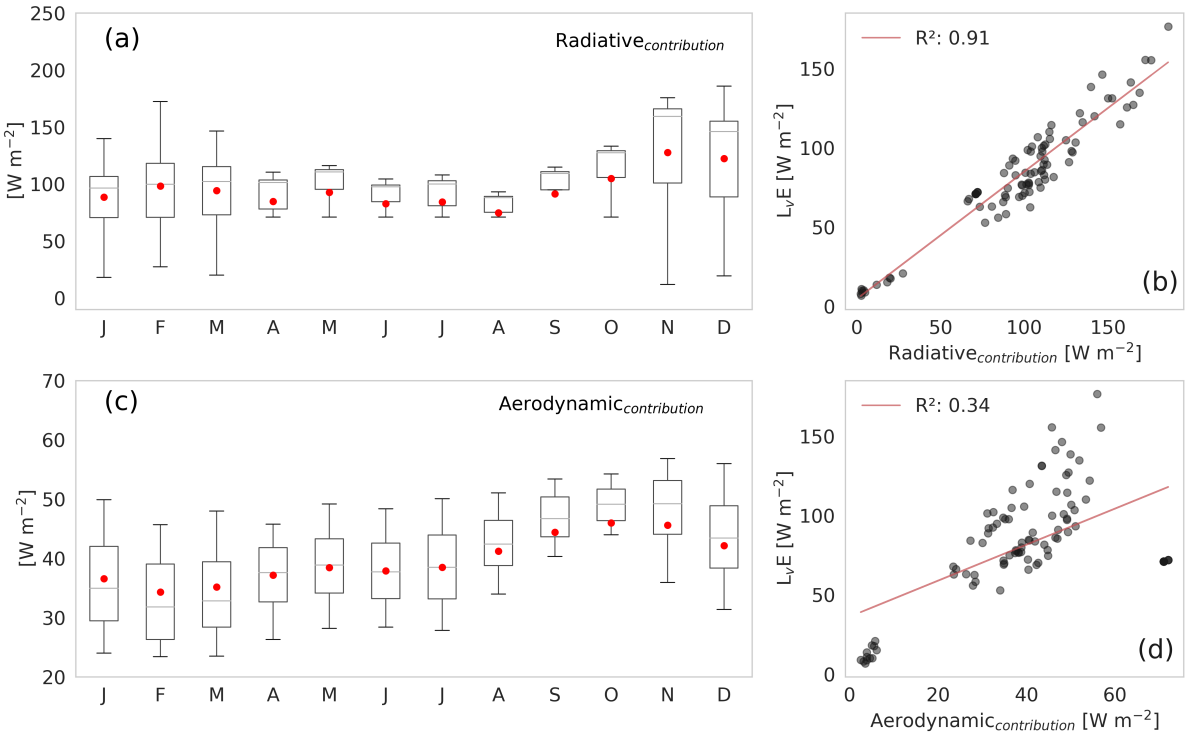

Figure 3.8: (a, c) Seasonal variability of radiative and aerodynamic contribution to evaporation during the period 1950-2020. The boxes represent 25%-75% interquantile, the grey horizontal line is the median, the red dots are the mean, and bars represent maximum and minimum values. Outliers have been removed. (b, d) Orthogonal regression of evaporation rates and its energy and aerodynamic contribution at averaged monthly scale.

in Fig. 3.8d).

In summary, at the seasonal timescale, the radiative contribution term contributes significantly more to evaporation than the aerodynamic term, representing 73% of the energy needed to evaporate the water from the saline lake in the Salar del Huasco. It is important to stress that mechanical turbulence (wind speed) is more relevant at the diurnal scales than available net radiation controlling evaporation (Lobos-Roco et al., 2021b).

Seasonal changes in the saline lake water balance

To complete the seasonal analysis of evaporation in recent decades, we describe the spatial impacts of the evaporation-precipitation variability on the saline lake of Salar del Huasco. Figure 3.9 shows the relationship between the spatial changes of the saline lake and monthly evaporation and precipitation that occurred between 1985 and 2019. The seasonal variability of the lake's area shown in Figure 3.9a reveals that the maximum extension (5 km^2) occurs during winter (JJA). During spring, the lake's area decreases

rapidly to its minimum extension (∼1.3 km^2). The summer season shows high variability in the lake's area (mean: 2 ± 1.8 km^2; mean value ± standard deviation). This variability is relatively constant towards winter and decreases during spring, revealing that there is a significant interannual variation over the years, especially between March and July, where precipitation is typically small (Fig. 3.6d). Thus, the increase in the lake's area is likely due to groundwater inputs (Blin et al., 2021).

Regarding the relationship between the lake's area changes and evaporation, Figure 3.9b shows an orthogonal regression between evaporation and lake extension changes. Here, we find a strong negative correlation (R^2 = 0.92), which reveals the control that evaporation has over the lake discharge. The lowest evaporation rates (winter) coincide with the highest lake extensions, and the highest evaporation rates (spring) coincide with the lowest lake surface. Regarding the relationship between precipitation and lake's surface associated with the water recharge by precipitation, the relationship is indistinctive (Fig. 3.9a). We find a high variability in the onset and offset of precipitation at the seasonal scale, from November to March. This high variability in summer precipitation coincides with the larger variations in the lake area. As such, it is difficult to find a direct relationship between precipitation and the lake's area. However, analyzing the means (solid lines Fig. 3.9a), we observe that high precipitation rates do not directly impact the areal changes of the lake, which is reached 4 to 5 months after the rainy season. For these reasons, the observations suggest that there is another process that modulates the lake recharge. Among the alternatives that might explain the lake recharge, precipitation and groundwater input might play a role.

To unravel the role of ground water input into the Salar del Huasco lake, we perform a simple mass balance assuming a lake depth between 0.05 and 0.20 m. Our lake mass balance results show that the monthly water required to represent the spatial changes in the lake's surface are on the order of ∼345,000 m^3 per month (∼0.1 m^3 s^{-1}). This estimation is reasonable as the only stream that is near the lake has an average flow of 0.13 m^3 s^{-1} (Blin et al., 2021), which is measured about 1-2 km before the river water completely infiltrates into the ground. If one assumes that ERA5 precipitation is responsible of this water flow, then a lake area of ∼13 km^2 is needed to explain it. When varying the water depth between 0.05 and 0.20 m, our results changed less than 1%. As the mean observed lake's area is ∼2 km^2, groundwater is the water source that sustains this habitat. This result agrees with the estimations performed by Blin et al. (2021). They quantified a flow of 0.92 m^3 s^{-1} in the springs that discharge water into the lake, which is similar to the flow estimated in our work. It is important to recall that our approach has important limitations. For instance, as the topography in the basin's sink is very flat, there is no hypsometric curve that can relate the lake's volume as a function of depth. Also, the precipitation considered here corresponds to that estimated in the lower part of the basin, whereas higher precipitation values occur at higher elevations in the basin (Uribe et al., 2015; Blin et al., 2021). Hence, most of the groundwater recharge is

expected to occur at higher elevations and/or in locations where preferential flow exists, e.g., near the rivers of the basin. Then, this water will flow underground until it upwells into the lake. So, even though this approach has limitations, it allows for a first order approximation that can be used to understand the key components of the lake's water balance.

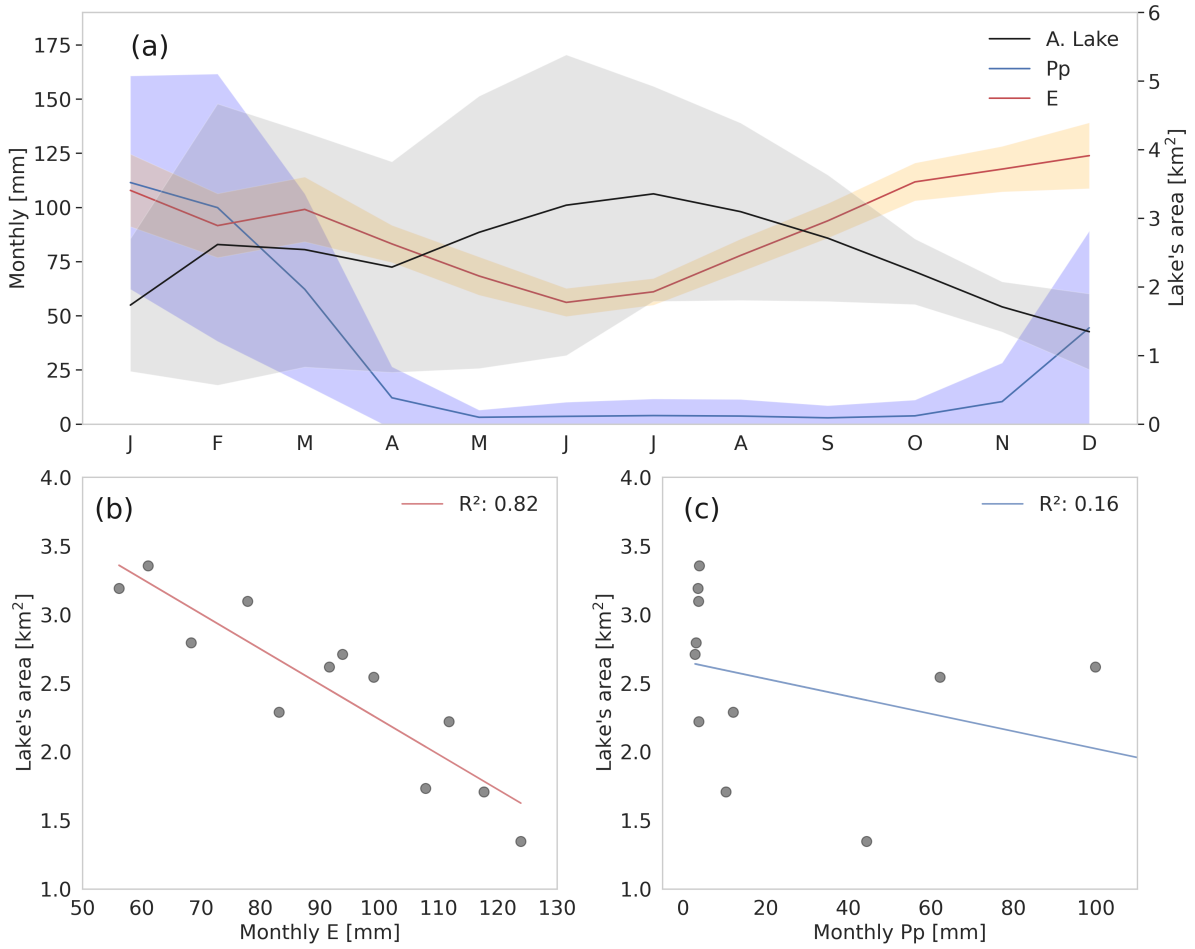

Figure 3.9: (a) Monthly mean variability of lake area, total evaporation, and total precipitation. Shades indicate the standard deviation of each variable. (b) Orthogonal regression between monthly lake area and monthly evaporation. (c) Orthogonal regression between monthly lake area and monthly precipitation.

3.3.3 Interannual perspectives of evaporation and precipitation

This section describes the interannual variabilities of evaporation and precipitation over the saline lake of the Salar del Huasco. First, we describe the climatological trends from 1950 to 2020. Secondly, we analyse the influence of ENSO and PDO global-scale phenomena on local evaporation and precipitation.

Climatological trends of evaporation-precipitation

Evaporation trends in the saline lake of Salar del Huasco show an indubitable increase from 1950 to 2020. The rate of increase is about 2.1 mm per year (0.2 mm per month), with scattered interannual variability showing a significant increase. Figure 3.10a shows a 12-month moving average of monthly total evaporation. For 1950, monthly mean values are approximately 80 mm (950 mm per year), whereas in 2020, these values increased to ∼100 mm (1,150 mm per year). The annual integrated evaporation rates averaged 1,075 mm (± 74 mm) with a minimum of 862 mm (1993) and a maximum of 1,210 mm (2010). This increase in evaporation has a correlation of 0.55 with air temperature (2 m), whose monthly averages increased 3 °C (0.04 °C per year), from 1950 to 2020 (Fig. 3.10a). Likewise, Figure 3.10b shows the precipitation trends in the area of the saline lake from 1950 to 2020. Total precipitation per year is set at 338 mm with a high variability of 248 mm per year. Precipitation shows an increasing trend in the last 70 years of 0.6 mm per year. Although this positive trend in precipitation is less significant than evaporation and presents more scatter, it is also in agreement with temperature increase.

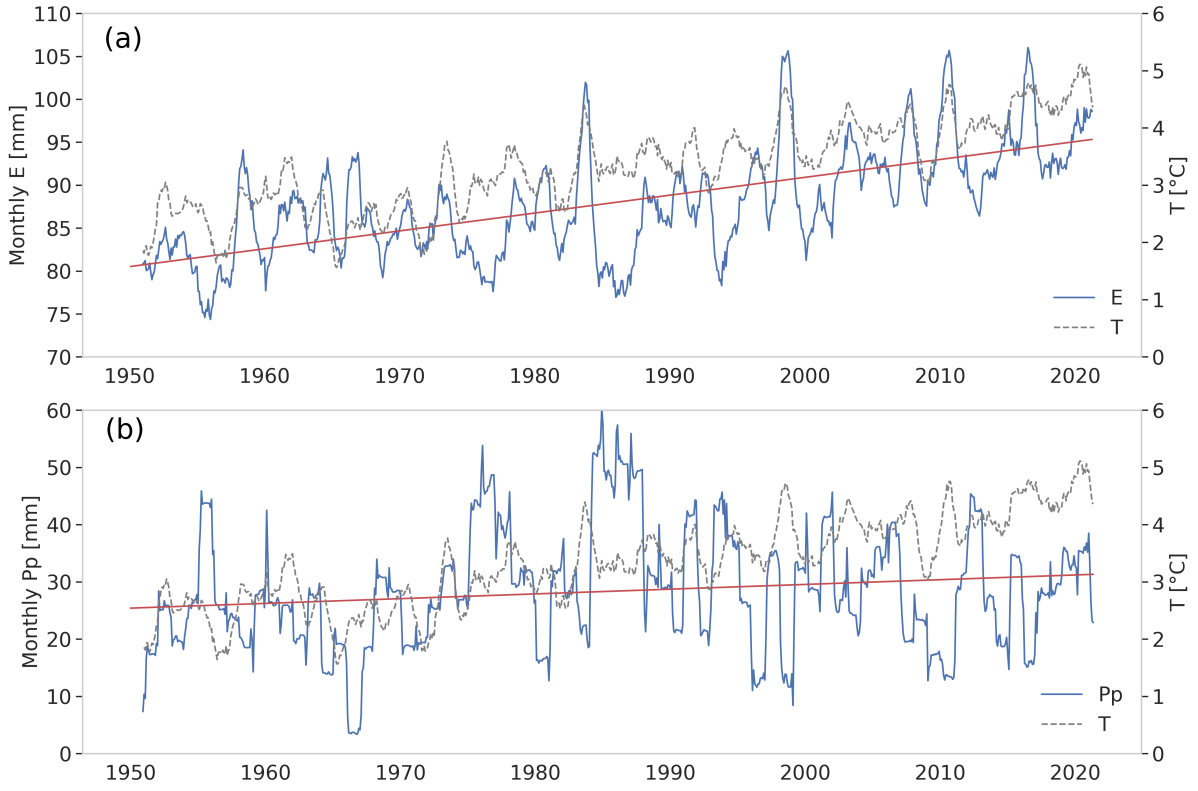

Figure 3.10: 12-month moving average monthly total evaporation (a) and precipitation (b), and 2-m mean air temperature over the saline lake of Salar del Huasco from 1950 to 2020. The evaporation trend line is depicted in red.

Influence of ENSO and PDO phenomena on evaporation-precipitation

Within this subsection, we analyze the influence of the ENSO and the Pacific Decadal Oscillation (PDO) on evaporation and precipitation variability.

Figure 3.11 shows the seasonal variability of monthly evaporation in the period 1950-2020 during cool (ONI < -0.5 °C), neutral (-0.5 °C < ONI < 0.5 °C) and warm (ONI > 0.5 °C) ENSO phases. In general, during cool ENSO phases, evaporation rates are 2% lower than those observed in the neutral ENSO phases, whereas during warm ENSO phases, evaporation is 15% higher than that observed in neutral ENSO phases. This variability becomes more significant from October to May, summer (JFM) being the season with the largest variability. During summer, evaporation under cool ENSO phases decreases by 4% with respect to neutral phases and increases 14% under warm conditions. Moreover, summer variability is the highest during warm ENSO phases, showing standard deviations of ∼15 mm per month. The lowest evaporation variability occurs during the neutral phases, with standard deviations of 11 mm per month. In turn, during late autumn and winter seasons, the ENSO phenomenon influences the evaporation less in the saline lake of the Salar del Huasco since evaporation rate differences between cool, neutral and warm phases are lower than 2%. This analysis suggests that ENSO significantly influences evaporation during summer months, which is in line with other typical meteorological phenomena of the Atacama Desert, such as summer precipitation (Aceituno, 1988), and coastal fog formation (del Río et al., 2021).

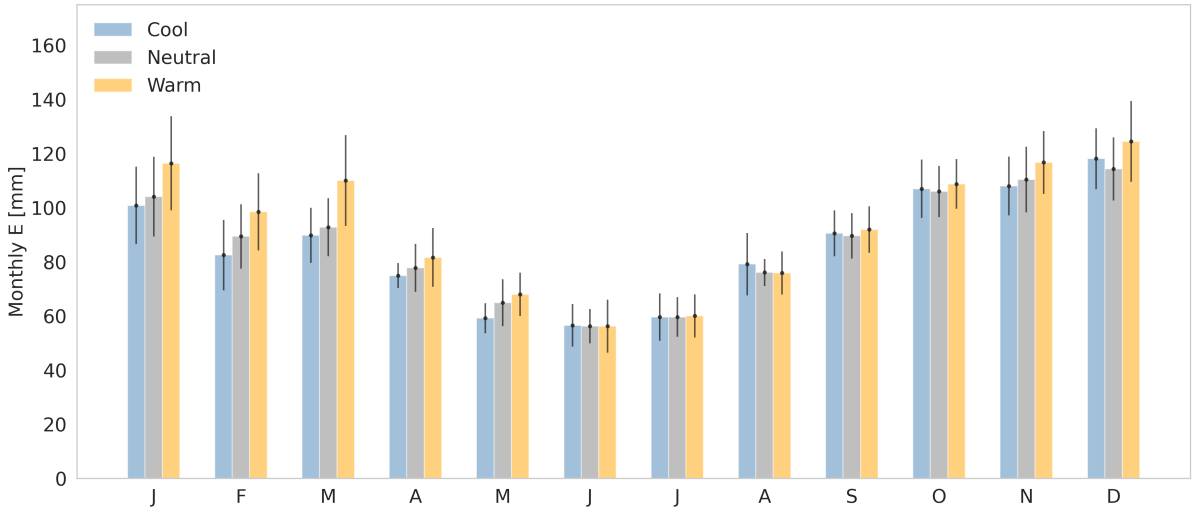

Figure 3.11: Interannual-seasonal variability of monthly evaporation in the period 1950-2020 separated by cool, neutral and warm ENSO phases. Error bars represent the standard deviation of every averaged month.

The ENSO phases influence on evaporation observed at the seasonal scale is also present interannually. Figure 3.12 shows the relationship between ENSO phases and PDO phenomenon, with evaporation anomalies obtained using the site-adapted Penman

equation (eq. 1) and downscaled ERA 5 data, and precipitation anomalies observed from ERA5 in the last seven decades in the shallow lake of the Salar del Huasco. Recall that ENSO is a recurrent phenomenon with an ill-defined periodicity, where in the last 70 years, 24% of the months have been influenced by warm ENSO phases and 26% by cool ones. However, the frequency of this phenomenon is not constant, neither in intensity nor in time. The ONI varied between 0.5 and 2.6 °C during warm phases, and between -2 and -0.5 °C during cool phases, with a frequency between 2 and 10 years (Timmermann et al., 2018).

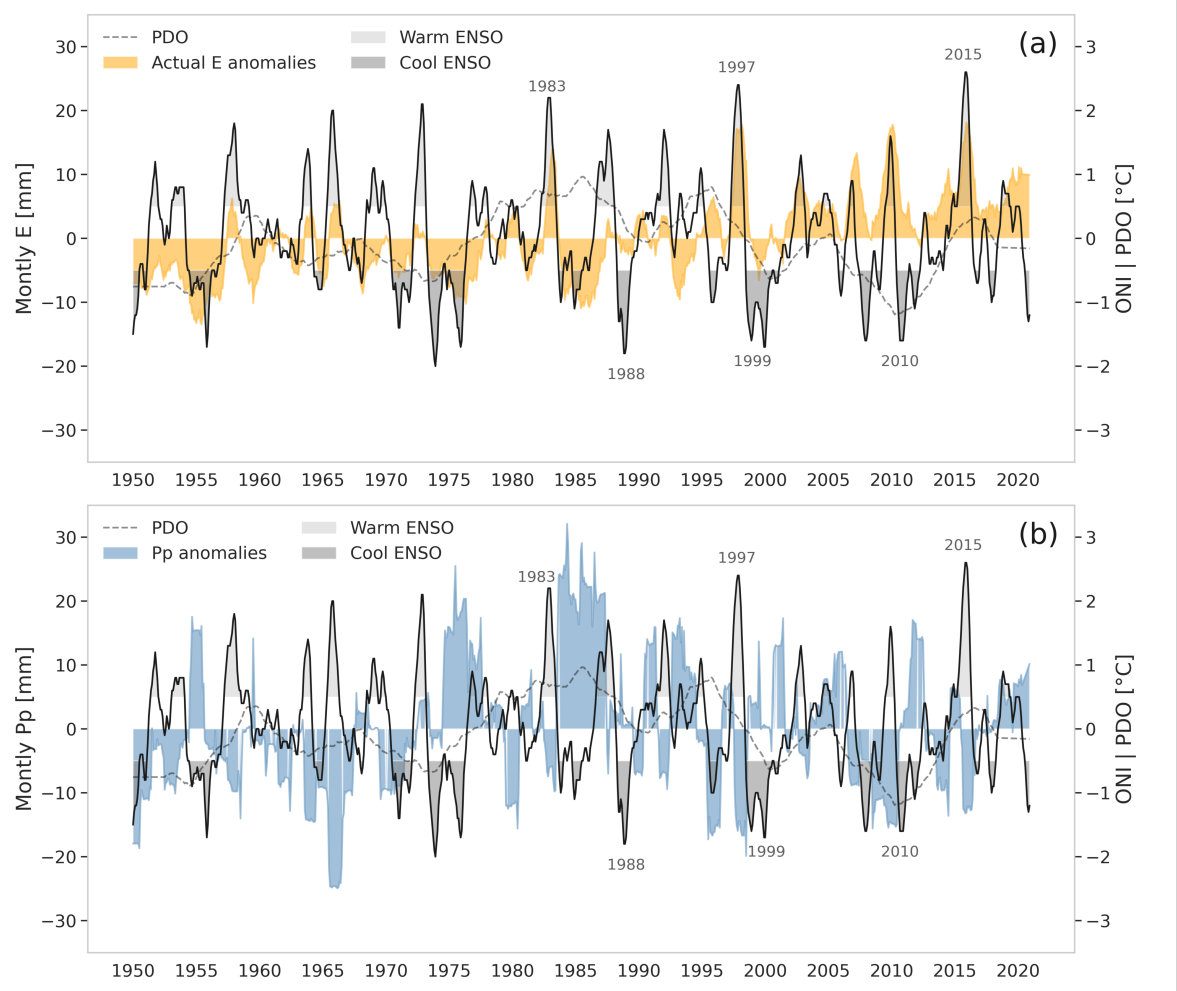

Figure 3.12: (a) Monthly evaporation anomalies compared to ONI and PDO indices. (b) Monthly precipitation anomalies compared to ONI and PDO indices. Anomalies are calculated using the difference between the entire period mean, and 12-month moving averaged anomalies. Evaporation and precipitation anomalies are shown in colors, the ONI with a solid black line, highlighting the warm and cool phases, and PDO with a dashed line.

Figure 3.12a shows the 12-month moving average evaporation anomalies and the ENSO and PDO phenomena from 1950 to 2020. Positive monthly evaporation anomalies ($>$ 5 mm) correlate with warm ENSO phases, whereas negative or non-evaporation

anomalies (< 0 mm) correlate with cool ENSO phases. The correlation between positive evaporation anomalies and warm ENSO phases is evident during the extreme ENSO events, i.e., events which occurred in 1983, 1997, and 2015. Likewise, the correlation between negative evaporation anomalies and cool ENSO phases is evident in 1988, 1998, and 2010. However, this trend is indistinct when monthly evaporation anomalies are close to 0 mm (e.g., in 1970, 1995, and 2001). Evaporation anomalies also have an interdecadal variability. For instance, between 1950 and 1975, negative evaporation anomalies dominate. On the contrary, between 2000 and 2020, positive evaporation anomalies dominate, but only after a transition period that occurred between 1975 and 2000, where both positive and negative evaporation anomalies are present. Regarding larger macroclimatic phenomena, no significant correlation is found between PDO and evaporation anomalies.

The influence of the ENSO phenomenon also affects precipitation at Salar del Huasco. Figure 3.12b shows the 12-month moving average precipitation anomalies and the ENSO and PDO phenomena from 1950 to 2020. The influence of ENSO on precipitation is opposite of that observed for evaporation. Here, positive monthly precipitation anomalies (> 5 mm) coincide with cool ENSO phases, whereas negative monthly precipitation anomalies (< 5 mm) correlate with warm ENSO phases. Contrary to evaporation anomalies, the relationship between precipitation and extreme ENSO events is indistinctive. For example, strong precipitation anomalies observed in 1985 disagree with an extremely cool ENSO phase. The same occurs for the extremely cool ENSO phase that occurred in 1999, where the precipitation anomaly is not correlated with high positive precipitation anomalies. However, the negative correlation trend between ENSO phases and precipitation anomalies is still evident. Precipitation anomalies also have an interdecadal variability that seems to be related to PDO anomalies. For example, between 1950 and 1970, there is a predominance of negative precipitation anomalies, which correlate with negative PDO indices. However, between 1970 and 2000, positive precipitation anomalies predominate along with positive PDO indices. Finally, between 2000 and 2020, negative precipitation anomalies predominate together with negative PDO indices. The negative relationship between precipitation and ENSO phases in the Altiplano region has also been reported by Aceituno (1988), Vuille et al. (2000), and Garreaud & Aceituno (2001).

To further quantify the opposing trend between evaporation and precipitation, Figure 3.13 shows the relationship between evaporation and precipitation anomalies categorized by ENSO phases. The trend between cool ENSO phases and negative evaporation anomalies is significant (∼-10 mm), although it is weaker during extremely cool phases. Likewise, the trend between warm ENSO and positive evaporation anomalies is very clear, even during the most intense warm ENSO phases (> 15 mm). Regarding precipitation anomalies, the trend shows a similar pattern, where negative precipitation anomalies (∼-15 mm) are related to extremely warm ENSO phases, and highest positive precipitation anomalies are related to both cool and neutral ENSO phases.

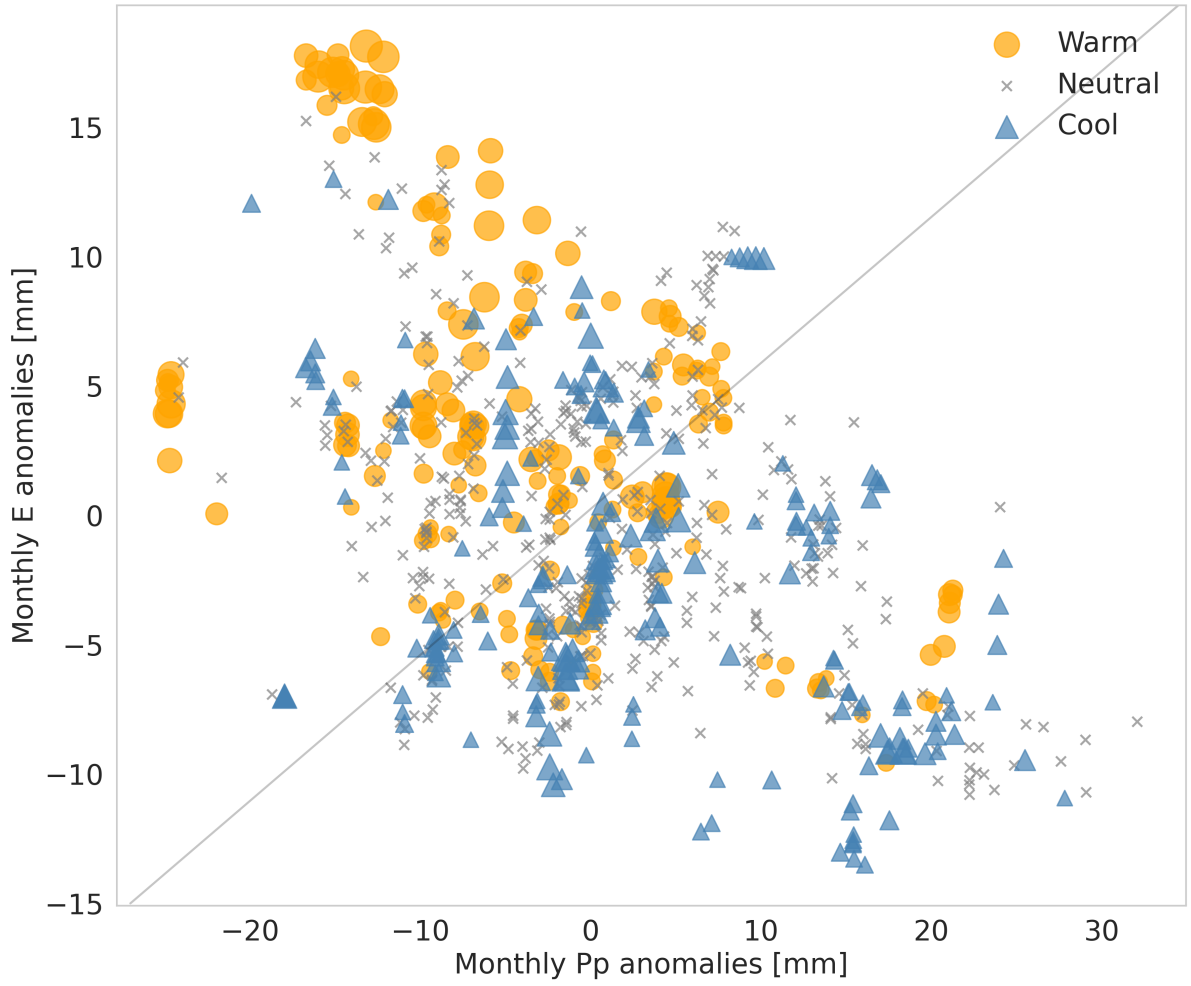

Figure 3.13: Relationship between monthly evaporation and monthly precipitation anomalies between 1950 and 2020. The anomalies are classified into warm, neutral and cool ENSO phases. The symbol size reflects the ONI intensity, where ONI≥1 corresponds to an intense warm phase (circle) and ONI≤-1 to an intense cool phase (triangle).

Opposing behavior of ENSO influences on interannual evaporation and precipitation variability demonstrate the control that global climate phenomena can exert at a local scale in the long term. As shown in Figure 3.10a, air temperature is strongly related to evaporation; thus, atmospherically warmer conditions in the Altiplano region during warm ENSO phases enhance evaporation. This warming intensifies the Pacific Anticyclone through the tropospheric thermal stratification (Falvey & Garreaud, 2009), resulting in cloudless conditions during summer of warm ENSO phases, i.e., an increase in the radiative contribution term of 17% as compared to the cool phases. Increased radiation also leads to an enhancement of the ocean-land thermal contrast, enhancing the aerodynamic contribution to evaporation by 21% during warm ENSO phases in summer with respect to cool ENSO phases. This enhanced ocean-land thermal contrast also

increases the atmospheric capacity to hold water vapor. Conversely, cool ENSO phases promote higher precipitation rates through the weakening of the Pacific Anticyclone, and the strengthening of the Bolivian low (Aceituno, 1988), which negatively affects the evaporation in two ways. First, the cloudy conditions that result from wet seasons inhibit the available energy required for evaporation (from 120 to 100 W m^{-2}), mainly affecting the evaporation rates during the summer season (Fig. 3.11) but also interannual rates (Fig. 3.10a) (Houston, 2006a). Second, during cool ENSO phases, a strong rainy season attenuates the characteristic regional atmospheric flow from the Pacific Ocean into the Andes (Lobos-Roco et al., 2021b), significantly affecting the aerodynamic contribution to evaporation (Fig. 3.8b), decreasing it from 38 to 30 W m^{-2}.

3.4 Conclusions

We investigate the temporal changes of actual evaporation from sub-diurnal to climatological scales in a high-altitude saline lake ecosystem in the Atacama Desert. We complement our study by analyzing the seasonal and interannual variability of precipitation, moisture transport along the entire region, and their impacts on the saline lake water extension.

Our first results reveal that simple meteorological variables from ERA5 downscaled using artificial neural networks and combined with a site-adapted Penman equation successfully estimate the actual evaporation of open water bodies from sub-diurnal to interannual scales. Compared to direct evaporation measurements taken with the eddy-covariance method in a dedicated campaign, our evaporation estimates show diurnal and seasonal errors lower than 7%. At the sub-diurnal scale, the wind regime (aerodynamic contribution in Penman equation driven by wind shear) is the main driver of evaporation, whereas, at the seasonal scale, the principal driver is the available energy (radiative contribution).

Our findings show significant seasonal variations. Maximum rates are reached during the spring (OND), minimum ones during winter (JAS), and a high variability is observed during summer (JFM). The seasonal changes in evaporation are explained 73% by the radiative contribution of the Penman equation, where the seasonality of radiation plays a principal role. Nevertheless, at the sub-diurnal scale, available energy in the site-adapted Penman equation is affected by the wind regime since the energy balance non-closure coefficient depends on the wind regime. The seasonal and local estimates of evaporation and precipitation over the saline lake correlate with synoptic and seasonal variabilities of moisture transport. To this end, we identify three main large-scale fluxes that contribute to the available moisture in the Altiplano region. The principal one transports a significant amount of moisture from the northeast (Amazon basin) and the humidity recycled from the evaporation-precipitation process during the spring and summer. The third moisture flux identified transports a very low but persistent amount of moisture from the Pacific

Ocean into the Atacama Desert consistently over the year. This moisture flux is strongly limited by the subtropical anticyclone and the steep topography. In addition the seasonal variation in evaporation and precipitation along the analyzed period shows impacts the saline lake. Our analysis suggests that evaporation is the principal driver of the lake discharge, explaining 92% of it. However, the recharge of the lake still remains unknown since the role of precipitation remains elusive and hasn't yet been quantified. Analyzing the saline lake mass balance, we conclude that the water input required to explain the lake's spatial changes significantly exceeds the precipitation. Therefore, we conclude that groundwater inputs play an essential role in the lake's recharge.

Evaporation also present a interannual variability, where the ENSO phenomenon plays an important role. Our results reveal that ENSO phases affect the evaporation rates during the summer: warm phases increase evaporation by 15% , whereas cool ones decrease it by 4%. Concerning the driving components of evaporation, radiation controls these interannual changes in summer. This control is maintained by the cloudy or cloudless conditions that characterize ENSO cool and warm phases, respectively. However, this is also explained by the aerodynamic contribution during the cold phases. The weakening of the Pacific Ocean anticyclone promotes the entrance of wet eastern flow that decreases the usual westerly flow, affecting the contribution of wind to evaporation. Analyzing the evaporation and precipitation anomalies compared to the Oscillation El Nino Index (ONI), we find that ENSO phases correlate positively to evaporation anomalies but negatively to precipitation ones. These correlations mean warm ENSO phases are mainly characterized by higher evaporation rates and cool phases with higher precipitation rates. In addition, climatological trends show that evaporation has increased by 2.1 mm per year during the entire study period according to global temperature increases.

Finally, our study gives a first multi-spatiotemporal approach to actual evaporation and its role in the water balance of the Atacama Desert. We demonstrate that long-term actual evaporation can be estimated reliably through a simple approach based on observations and reanalysis data. However, we acknowledge that longer-term actual evaporation measurements are needed to reduce the 7% uncertainty that the site-adapted Penman equation brings. Likewise, further research can be done on the site-adapted Penman equation coefficients to apply the same approach to different but more common surfaces of the desert (wet salt, wetlands, and sparse vegetation lands). Additionally, the interannual variability of evaporation-precipitation and moisture transport must be analyzed by higher-resolution models to better understand the local impacts related to the sharp topography and land-use changes and the ENSO phenomenon.

Chapter 4

Local evaporation controlled by regional atmospheric circulation in the Altiplano of the Atacama Desert

This chapter is based on:

Lobos-Roco, F., Hartogensis, O., Vilà-Guerau de Arellano, J., de la Fuente, A., Muñoz, R., Rutllant, J., & Suárez, F. (2021a). Local evaporation controlled by regional atmospheric circulation in the Altiplano of the Atacama desert. *Atmospheric Chemistry and Physics*, 21-11 (pp. 1–38).

Abstract

We investigate the influence of regional atmospheric circulation on the evaporation of a saline lake in the Altiplano region of the Atacama Desert. For that, we conducted a field experiment in the Salar del Huasco (SDH) basin (135 km east of the Pacific Ocean), in November 2018. The measurements were based on surface energy balance (SEB) stations and airborne observations. Additionally, we simulate the meteorological conditions on a regional scale using the Weather Research and Forecasting model. Our findings show two evaporation regimes: (1) a morning regime controlled by local conditions, in which SEB is dominated by the ground heat flux ($\sim$0.5 of net radiation), very low evaporation ($L_vE < 30$ W m^{-2}) and wind speed <1 m s^{-1}; and (2) an afternoon regime controlled by regional-scale forcing that leads to a sudden increase in wind speed (>15 m s^{-1}) and a jump in evaporation to >500 W m^{-2}. While in the morning evaporation is limited by very low turbulence ($u* \sim$0.1 m s^{-1}), in the afternoon strong winds ($u* \sim$0.65 m s^{-1}) enhance mechanical turbulence, increasing evaporation. We find that the strong winds in addition to the locally available radiative energy are the principal drivers of evaporation. These winds are the result of a diurnal cyclic circulation between the Pacific Ocean and the Atacama Desert. Finally, we quantify the advection and entrainment of free-tropospheric air masses driven by boundary-layer development. Our research contributes to untangling and linking local and regional scale processes driving evaporation across confined saline lakes in arid regions.

4.1 Introduction

The Atacama Desert is known as the driest place on Earth, with precipitation ranging from 0.1 mm per decade (∼0.01 mm yr^{-1}) in the lowlands (Weischet, 1975) to 150-180 mm yr^{-1} (Minvielle & Garreaud, 2011) in the highlands. The Altiplano (highlands) is rain-fed by occasional convective showers, whose source of humidity arrives from the East (Falvey & Garreaud, 2005). These storms are spatially very localized and rapidly changing in intensity (<1 hour), being the sole source of aquifer recharge they sustain the shallow lagoons and wetlands that host unique native floral and faunal environments (de la Fuente & Niño, 2010; Johnson et al., 2010). It is in these confined water-holding environments that nearly all the water of the catchment is lost to the atmosphere, meaning that they act as a preferential pathway for evaporation (E) (Rosen, 1994). Consequently, locally at these lagoons the annual E greatly exceeds annual precipitation (Lictevout et al., 2013). In this study we focus on a particular ∼15-cm deep saline lake, the Salar del Huasco (SDH) located in the Altiplano of the Atacama Desert in the NE region of Chile. The dynamics of the E-process of SDH can be regarded as exemplifying all the saline lakes in the region (Kampf et al., 2005). Figure 4.1 shows the dramatic change in the size of the SDH lake from the rainy season in the summer to the dry season in late spring. Between winter (June-September) and spring (September-December) the size of the lagoon is reduced by 75% in only two months. Our study focuses on this part of the year that represents the peak of the annual E water-loss.

The main mechanisms that drives this high E rate are not yet well understood, yet they are crucial to improve its representation in atmospheric and hydrological models and thus to improve water management efficiency. Atmospheric model calculations of E in arid and semi-arid regions are still uncertain for several reasons. First, the physical processes governing E occur on spatial scales smaller than the usual model grid size (∼1 km), over heterogeneous surfaces and on sub-hourly temporal scales (Eder et al., 2014). Second, modelled E rates are mainly controlled by net radiation (R_n) and water vapour-pressure deficit (VPD) (Ma et al., 2018). However, in reality more complex processes take place over arid regions (McNaughton, 1976; de Bruin et al., 2005). More specifically, induced atmospheric flows driven by local surface heterogeneity play an important role in governing the surface energy balance (SEB) (Moene & Van Dam, 2014) while on a regional scale, advection can enhance E to the point at which it exceeds R_n (de Bruin et al., 2005). This multi-scale interaction between surface and atmosphere impacts the vertical atmospheric boundary layer (ABL) structure, which feeds back into E-related processes at the surface (van Heerwaarden et al., 2010). On larger scales, the meteorological influence at the regional level is particularly relevant in the Atacama Desert due to the complex topography and thermal gradient between the atmosphere above the Pacific Ocean and the western slope of the Andes mountains that results in an energetic atmospheric flow every afternoon (Rutllant et al., 2003). Under these premises the role of the regional atmospheric

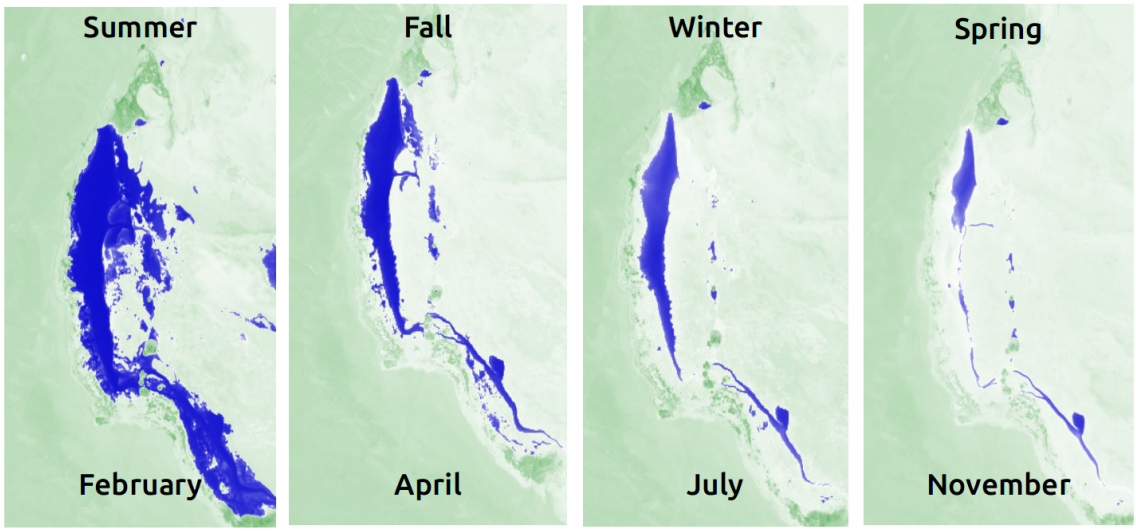

Figure 4.1: Shallow saline lake at Salar del Huasco as viewed by the normalized difference water index (NDWI) from Copernicus Sentinel data 2019 processed by Sentinel Hub. This index combines infrared and visible bands, where dark blue represents water and light green the absence of water. The right-hand image shows the extent of the lake on November 18^{th} 2018, during the field measurements shown in this work.

circulation and its interaction with surface processes is crucial to an understanding of the E diurnal cycle.

The aim of this study is to describe and quantify the physical processes that control the diurnal cycle of E in arid regions characterized by confined water environments and the surfaces of their heterogeneous surroundings over the complex topography of the SDH. More specifically, our main research question is: in the interplay between regional and local scales, what is the role of the wind-induced turbulence in controlling the diurnal cycle of E compared to R_n and VPD as the main drivers? An understanding of this would help to improve representations of E in numerical models and potentially improve the efficiency of water resources management in arid regions.

To unravel what processes and scales control E, we combine observations gathered during a field experiment called E-DATA (**E**vaporation caused by **D**ry **A**ir **T**ransport over the **A**tacama Desert) that took place in the SDH in November 2018. The analysis of the observations is supported by fine-resolution numerical experiments using the Weather Research and Forecasting (WRF) model. The originality of the designed field experiment is that it integrates ground and airborne observations over heterogeneous surfaces to quantify the moisture and energy budgets as well as the interaction between ABL and the regional circulation. The modeling perspective includes multi-day numerical model runs to quantify the regional flow patterns.

This chapter is structured as follows. Section 4.2 presents the basic theoretical concepts utilized in this study. Section 4.3 describes the methods employed and data gathered in the field experiment and modeling. Section 4.4 presents the main results, describing surface fluxes and their relationships and interactions with the environmental conditions in local and regional perspectives. Section 4.5 summarizes the processes involved and discusses the results in the context of other studies. Finally, the main conclusions and future perspectives are presented.

4.2 Basic conceptual framework of evaporation

Environmental conditions in the Atacama Desert are characterized by abundant radiation (incoming shortwave radiation, S_i max > 1,000 W m^{-2}), dry air (specific humidity, $q < 1$ g kg^{-1}), limited soil moisture ($\sim$0 m^3 m^{-3}) and in some parts very low plant transpiration. The main sources of E are the saline lakes in the endorheic (closed) basins, which is controlled by the interplay of energy (radiation), wind (turbulent mixing) and VPD between the confined open surface water and the atmosphere (McNaughton, 1976).

To analyze the relevance of the main processes related to evaporation in our measurements, we employ the concept of the Penman equation for open-water evaporation (Penman, 1948; Monteith, 1965) expressed in terms of energy, i.e., the latent heat flux (L_vE). This analysis aims to demonstrate the qualitative behavior of the Penman-Monteith steering variables to show which mechanisms and conditions are limiting E. The equation reads.

$$L_vE = \overbrace{\frac{s}{s+\gamma}(R_n - G)}^{\text{I}} + \overbrace{\frac{\rho_a c_p}{s+\gamma} \underbrace{\frac{1}{r_a}}_{\text{turbulence}} \underbrace{(e_s - e)}_{\text{VPD}}}^{\text{II}}, \tag{4.1}$$

where s is the slope of saturated vapour pressure curve, γ the psychrometric constant, ρ_a is the dry air density and c_p is the specific heat at constant pressure. We indicate terms in Equation (4.1) that represent the two main processes that contribute to L_vE. The term I is the *energy* contribution (Garratt, 1992), which describes the energy available (R_n - G) to evaporate water where R_n is the net radiation and G the ground heat flux. The term II is the *aerodynamic* contribution, which combines the turbulence and water vapour pressure deficit (VPD) contribution. Here, the first sub-term describes the efficiency of turbulent mixing, where r_a is the aerodynamic resistance defined as:

$$r_a = \frac{1}{ku^*}\Big[\ln\big(\frac{z}{z_{0,h}}\big) + \Psi\big(\frac{z_{0,h}}{L}\big) - \Psi\big(\frac{z}{L}\big)\Big], \tag{4.2}$$

where k is the von Kárman constant (0.4), $u*$ is the friction velocity, z is the height

of measurements and $z_{0,h}$ is the roughness length for heat, Ψ is the integrated stability function for heat in the entire atmospheric surface layer (Paulson, 1970) and L the Monin-Obukhov length. Note that the usual Penman-Monteith equation term referring to the stomatal resistance is omitted, due to the absence of vegetation in the study area. Last, the second sub-term on the right-hand side of Equation 4.1, the VPD contribution, describes the pressure-deficit of the water vapour ($e_s - e$) at the level measured (see Table 4.1).

The two terms in Equation 4.1 represent the main drivers for E. The *energy* contribution (term I) is related to local-scale conditions prescribed by surface processes (section 4.4.1) while the *aerodynamic* contribution (term II) is related to both local and regional scale interactions (sections 4.2 and 4.3). An important aspect of our research is to quantify the relevance of non-local effects. Examples of non-local processes are the advection of heat and moisture and the entrainment of air from above the ABL. Both transports modify the local VPD values and thus influence the diurnal variability of E (de Bruin et al., 1995). These non-local processes impact ABL development in the entrainment zone, which also influences E rates (van Heerwaarden et al., 2009).

Finally, in order to distinguish local from non-local and regional contributions to the changes in the potential temperature, θ and specific humidity, q across a boundary layer with height, h, we make use of the mixed-layer approximation. Here, our aim is to determine under which conditions the θ and q-budget follow the mixed-layer approximation (Stull, 1988). In case the approximations are valid, we can use these equations to quantify the contributions by using the observations. The mixed-layer equations read:

$$\frac{\partial q}{\partial t} = \frac{\overline{w'q'_s} - \overline{w'q'_e}}{h} - U\frac{\partial q}{\partial x} \tag{4.3}$$

and

$$\frac{\partial \theta}{\partial t} = \frac{\overline{w'\theta'_s} - \overline{w'\theta'_e}}{h} - U\frac{\partial \theta}{\partial x}, \tag{4.4}$$

where t is the time, $\overline{w'q'}$ and $\overline{w'\theta'}$ are the kinematic moisture and heat fluxes, subindices s and e are for surface and entrainment at the top of the boundary layer respectively, U is the total wind speed and x the spatial direction aligned with the main horizontal wind.

The first term of the right-hand side of equations 4.3 and 4.4 represents the local and non-local contributions of the vertical fluxes that are distributed over the boundary layer. In our modeling framework, the surface fluxes $\overline{w'q'_s}$ and $\overline{w'\theta'_s}$ are parameterized as a function of resistance and the gradients between the value at the surface and the mixed-layer value (Vilà G. A. et al., 2015). The second term, represents the transport of air with different properties coming from elsewhere, which we refer to as regional

contributions. Typically, the regional contribution is estimated as a residual term from locally measured fluxes and vertical profiles of θ and q (details in Section 2.4).

4.3 E-DATA experiment: observations and modeling

The E-DATA (**E**vaporation caused by **D**ry **A**ir **T**ransport over the **A**tacama Desert) field experiment consisted of horizontally distributed SEB and meteorological (MET) stations over the SDH saline lake and the heterogeneous surfaces that surround it, and vertical atmospheric measurements (Suárez et al., 2020). The E-DATA experiment was designed to analyse both local (∼1 km) and regional scales (∼100 km). The measurements were complemented with a comprehensive 3D-regional modeling study with the WRF atmospheric meso-scale model. In this section we will provide a site description (Section 4.3.1), descriptions of the surface observations (Section, 4.3.2), the profiling measurements (Section 4.3.3) and the WRF modeling set-up (Section 4.3.4).

4.3.1 Site description and instrumentation setup

The E-DATA experiment was performed between 14^{th} and 23^{rd} November 2018 at the SDH (20.1° S - 68.5° W, 3,790 m above sea level (asl)). This date is optimal to study evaporation due to the total absence of precipitation and high mean temperatures. The SDH is a closed basin of 1,417 km^2 (55 km N-S and 35 km W-E) located ∼3.8 km up and over ∼135 km from the Pacific Ocean. Note that at such altitude, the pressure level is very low compared to sea level, ∼650 hPa. Figure 4.2a shows the location of the SDH saline lake and E-DATA experiment in a vertical cross-section over the western slope of the Andes mountains. Figure 4.2b shows an overview of the surface observation installation in the vicinity of the SDH saline lake. Three SEB-stations were installed over representative and homogeneous surfaces of the site: water, wet-salt, and desert. The first SEB-station was installed above a shallow 15-cm deep lagoon (20.27° S - 68.88° W; 3,790 m asl), whose surface covers 4 km N-S by 800 m W-E. The second SEB-station was located over a wet-salt crust (20.28° S, 68.87° W; 3790 m asl), which is a wet soil composed of salt whose surface is covered by a mostly dry crust of slime. The third SEB-station was installed in an area representative of bare rocky-soil-like desert conditions (20.35° S, 68.90° W; 3,953 m asl). Figure 4.2b also shows the profiling measurement points from where radiosonde and an unmanned aerial vehicle (UAV) were launched: water and desert. The first launch site was located on the western -shore of the lagoon (20.28° S - 68.88° W; 3,790 m asl) covering water and wet-salt surfaces. The second point was located next to the desert SEB-station (20.35° S - 68.90° W; 3,953 m asl), covering the desert surface that surrounds the SDH-basin. A transect of four automatic MET-station deployed from 20.28° S - 68.90° W to

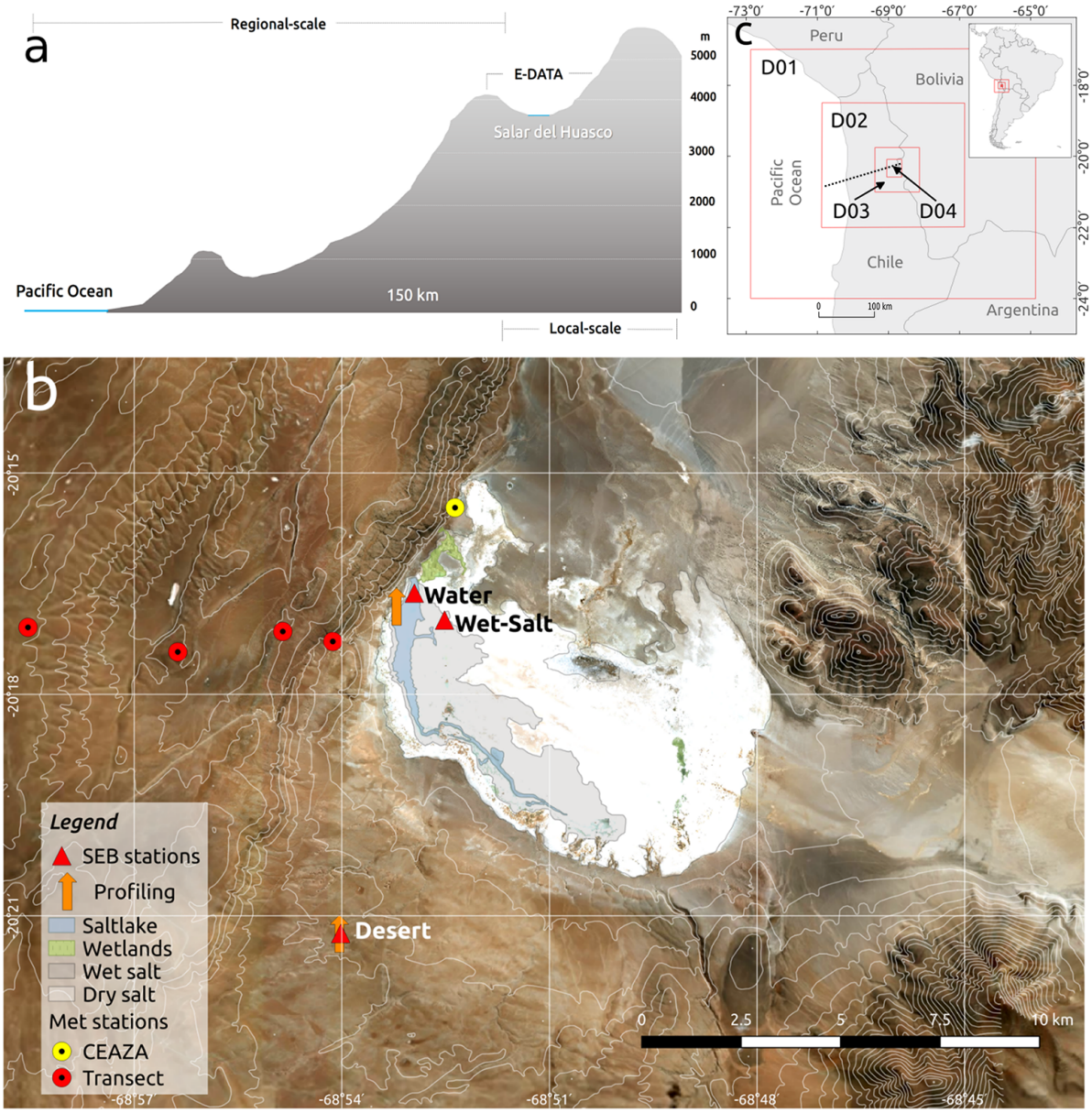

Figure 4.2: Study site. (a) Vertical cross-section of western slope of the Andes, showing the spatial scales involved in the field experiment and modeling. (b) Spatial distribution of surface and vertical observations at SDH site during the E-DATA field experiment used in this study (Contains modified Copernicus Sentinel data processed by Sentinel Hub). (c) WRF outer domains D01 (27 km), D02 (9 km) and inner domains D03 (3 km), D04 (1 km). The SDH saline lake is located at the center of the D04 and dotted line indicates the vertical cross-section shown in Section 4.4.3.

20.28° S - 68.97° W westward of the lagoon was utilized to characterize the advection. Finally, we also made use of a standard meteorological station placed 2 km N from the saline lake (Fig. 4.2b), that has been in continuous operation since 2015 by the Centro de Estudios Avanzados en Zonas Aridas (CEAZA).

4.3.2 Surface observations

We deployed SEB-stations, complemented by additional meteorological measurements, at each of the three main surface types (water, wet-salt, desert) together with a transect of four MET-stations on the western slopes of the study site. Special attention is paid to the measurement of variables that are related to the drivers of E: radiation, turbulence and VPD. Table 4.1a shows the main variables and sensors utilized over each surface type organized by sensor groups. Radiation measurements and sensors differed between surfaces. The four-component radiation measurements were gathered for the water surface, whereas at the desert and wet-salt surfaces only integrated R_n measurements were available. The albedo was measured only at the water site, for the wet-salt it was estimated using the net short-wave radiation and the incoming short-wave radiation measured in the lake. For the desert site we assumed the value 0.21, reported as a typical value for dry sandy soils in Moene & Van Dam (2014). Additionally, the R_n of the desert SEB station was too large so it was corrected by using incoming short-wave measurements from the water SEB-station, and assuming an albedo of 0.21 (Moene & Van Dam, 2014). We used the flux-software package EddyPro v 6.2.2 (Fratini & Mauder, 2014) from LI-COR Biosciences Inc. (Lincoln, Nebraska, USA) to calculate the turbulent fluxes of latent heat (L_vE), sensible heat (H) and the friction velocity ($u*$) at 10-min averaging intervals. All standard data treatment and flux correction procedures were included, most notably axis rotation with the planar-fit procedure (Wilczak et al., 2001), raw data screening including spike removal (Vickers & Mahrt, 1997), interval linear detrending and low-pass filtering correction (Massman, 2000). In addition, quality flags were determined based on Mauder & Foken (2004). The measured ground heat flux (G) was corrected for heat storage above the heat-flux plates by using the calorimetric method (Kimball & Jackson, 1975), and the observations obtained from soil temperature probes buried at different depths (see Table 4.1) in each surface type. Note that over a shallow water layer G is stored in both the water and soil/sediment layers above the heat flux plates (de la Fuente & Meruane, 2017). We corrected for both components of the soil heat storage. Standard meteorological variables such as air temperature (T), relative humidity (RH), atmospheric pressure (P), wind speed (U) and wind direction (WD) were measured in the SEB-stations and at a transect of standard meteorological stations. The details are shown in Table 4.1. The uncertainty related to the energy balance closure at the SEB stations can be found in Appendix B.

Table 4.1: Main variables and sensors utilized during the E-DATA experiment, by sensor-group and surfaces: water (W), wet-salt (WS) and desert (D). (a) Surface main variables: incoming shortwave radiation (Sw_{in}), outgoing shortwave radiation (Sw_{out}), incoming longwave radiation (Lw_{in}) and outgoing longwave radiation (Lw_{out}), shortwave net radiation (Sw_{net}), longwave net radiation (Lw_{net}), net radiation (R_n), latent heat flux (L_vE), sensible heat flux (H), friction velocity ($u*$), ground heat flux (G), soil temperature (T_{soil}), air temperature (T), relative humidity (RH), wind speed (U), wind direction (WD) and pressure (P). (b) Vertical main variables.

Sensor-group	Surface	Main-variable	height [m]	Sensors
a				
	W	$Sw_{in}, Sw_{out}, Lw_{in}, Lw_{out}$	1	CNR4 Net radiometer [a]
Radiation	WS	R_n	1.5	NR Lite Net radiometer [a]
	D	R_n: Sw_{net},Lw_{net}	1	CNR2 Net radiometer [a]
	W	L_vE, H, $u*$, z_0	1	
Eddy covariance fluxes	WS	L_vE, H, $u*$, z_0	1.5	IRGASON [b]
	D	L_vE, H, $u*$, z_0	2	
	W	G, T_{soil}	-0.15;-0.10 to 0.2	
Soil	WS	G, T_{soil}	-0.05;-0.04 to 0.1	T107 [b], HFP01SC [c], HFP01 [c]
	D	G, T_{soil}	-0.05;-0.04 to 0.1	
	W	T, RH, U, WD, P	2.5	107 T-prb [b];05108-45-L Wind[d];HPM155 T-RH prb[e]
Standard meteorology	WS	T, RH, U, WD, P	1.5	107 Temp. probe [a], IRGASON [a]
	W	T, RH, U, WD, P	2.5	107 Temp. probe [a], IRGASON [a]
b				
Radiosonde profile	W	T,RH,U,WD,P	0-↑2,000	iMet-4 Radiosonde [f]
	D	T,RH,U,WD,P	0-↑2,000	
UAV profile	W	T,RH,P	0-500	iMet-XQ2 UAV [f]
	D	T,RH,P	0-500	

[a]Kipp & Zonen, Delft, The Netherlands; [b]Campbell Sci., Logan, Utah, USA
[c]Hukseflux, Delft, The Netherlands; [d]Young Company, Traverse City, Michigan, US
[e]Vaisala, Helsinki, Finland;[f]InterMet Systems inc. Grand Rapids, Michigan

4.3.3 Airborne observations

We used two airborne instrument carriers: a radiosonde balloon and a UAV. These were equipped with similar sensor packages that provided measurements of T, RH, U, WD and P for the radiosonde and T, RH and P for the UAV (details in Table 4.1b and in Suárez et al. (2020). The radiosonde balloons were launched from two locations described in Section 3.1. At both locations, we performed intensive campaigns on November 21^{st} over the water surface and November 22^{nd} over the desert surface (Fig. 4.2b), where we launched balloons at 09:00, 12:00, 15:00, 18:00, and 21:00 local time (LT). Balloons typically reached an altitude of 10 km and drifted away horizontally up to a distance of 50 km northeastward of their launching sites. Vertical profiles of θ, q, U and WD were obtained from the radiosonde to characterise and estimate the ABL height (h), using the surface pressure level of the SDH ($\sim$650 hPa). This height was estimated through the maximum vertical gradient of θ (Sullivan et al., 1998). The UAV was flown simultaneously from the same two locations as the balloon launches (described in 4.3.1) from the ground to up to 500 m above the ground level (agl) from the surface on November 21^{st} and 22^{nd} every 30 min from 09:00 to 12:00 LT. From these flights we obtain the vertical profiles of θ to characterize the first 500 m agl of the ABL. UAV flights were, unfortunately, not possible after 12:00 LT due to high winds.

4.3.4 WRF regional modeling

To complete the analysis of the E-DATA experiment, we reproduce the same period using the Weather Research and Forecasting (WRF) model version 3.7 (Skamarock et al., 2008). We aim to study the atmospheric circulation that is formed daily from the Pacific Ocean to the Andes western slope. We follow the methodology suggested by Jiménez et al. (2016), which consists of performing consecutive, short WRF runs initialized at 0 UTC and running for 48 h. The first 24 h of each run is used as a spin-up for the physical parameterizations and the 24-48 h to represent the weather conditions of the simulated day. Therefore, we only analyzed and evaluated the period 24-28 hours. This methodology ensures that each simulated day starts with its real respective initial and boundary conditions. Initial and boundary conditions are taken from ECMWF ERA-INTERIM reanalysis data for 20°S /68°W with a 0.5° spatial resolution. By using this dataset input, every six-hours there is an update of the tendencies due to the large-scale forcing. Figure 4.2c shows the horizontal distribution of the four two-way nested model domains, detail information can be found in Table 2.4, Section 2.4. The inner domain (D04) includes all the measurements gathered in the E-DATA experiment. In the vertical direction, we imposed 61 non-equidistant grid following an exponential shape that maximizes the number of vertical levels in the boundary layer, i.e. 40 within the first 2000 m. Several physical processes such as radiation, surface and boundary layer, convection, microphysics, and land surface model are parameterized in WRF, they are also detailed in Table 2.4. A comprehensive model validation from both surface and vertical variables

is presented in detail in Section 2.4.

4.4 Results and discussions

The comprehensive data-set of E-DATA enables us to study the main processes governing open water evaporation in arid conditions. The main factors under analysis are radiation, turbulent mixing and water vapour pressure deficit. In this section we systematically study how the local and regional scales contribute to the diurnal variability of E.

The results section is organized as follows. First, it shows the differences in E depending on where the measurements were taken: over water, wet-salt and desert surfaces (Section 4.4.1). Then, the main focus is on the results obtained at the water surface. Additional local surface measurements and boundary layer profiles that help to define the distinct E regimes are presented in Section 4.4.2. Finally, section 4.4.3 shows the WRF modeling results that help us to understand the local measurements of E in the saline lake by adding a regional perspective to the air flow.

4.4.1 Local measurements: surface energy balance

Figure 4.3 displays the average diurnal cycles of the SEB terms, i.e. net radiation (R_n), ground (G), latent (L_vE), and sensible (H) heat fluxes observed above water, desert and wet-salt surfaces. All the sites are located within in a radius of 10 km. Typical daytime values of the SEB terms are summarized in Table 4.2.

Our measurements show exceptionally high R_n levels over the water surface ($\sim$950 W m^{-2}), less for the desert surface ($\sim$700 W m^{-2}) and considerably less for the wet-salt ($\sim$500 W m^{-2}). The R_n daily cycles follow a typical sinusoidal diurnal cycle with the intermittent presence of high clouds (Fig. 4.3). In the absence of four-component radiation measurements at the three sites we cannot provide a detailed breakdown of the short and long-wave radiation components to R_n. Assuming that the incoming short- and long-wave radiation terms are equal for all sites, and taking the near surface soil temperature (<1 cm depth) as a proxy for the long-wave outgoing radiation we can see the following (see also Table 4.2). Maximum incoming shortwave radiation is $\sim$1,250 W m^{-2}, which is close to the solar constant at the top of the atmosphere ($\sim$1,360 W m^{-2}) probably due to the high altitude and dry conditions of the study site. At $\sim$250 W m^{-2} maximum long-wave incoming radiation is rather small, due to the thin atmosphere and mostly cloud-free conditions. The albedo of the desert surface is closer to the albedo of the water than the wet-salt (0.21 vs 0.12), but it is mainly the difference in surface temperature (27 vs 22°C) that leads to a larger long-wave outgoing radiation loss and thus lower R_n. Compared to water, the wet-salt surface has a comparable surface temperature (20 vs 22 °C), but it is the considerable difference in albedo (0.58 vs 0.12) that leads to

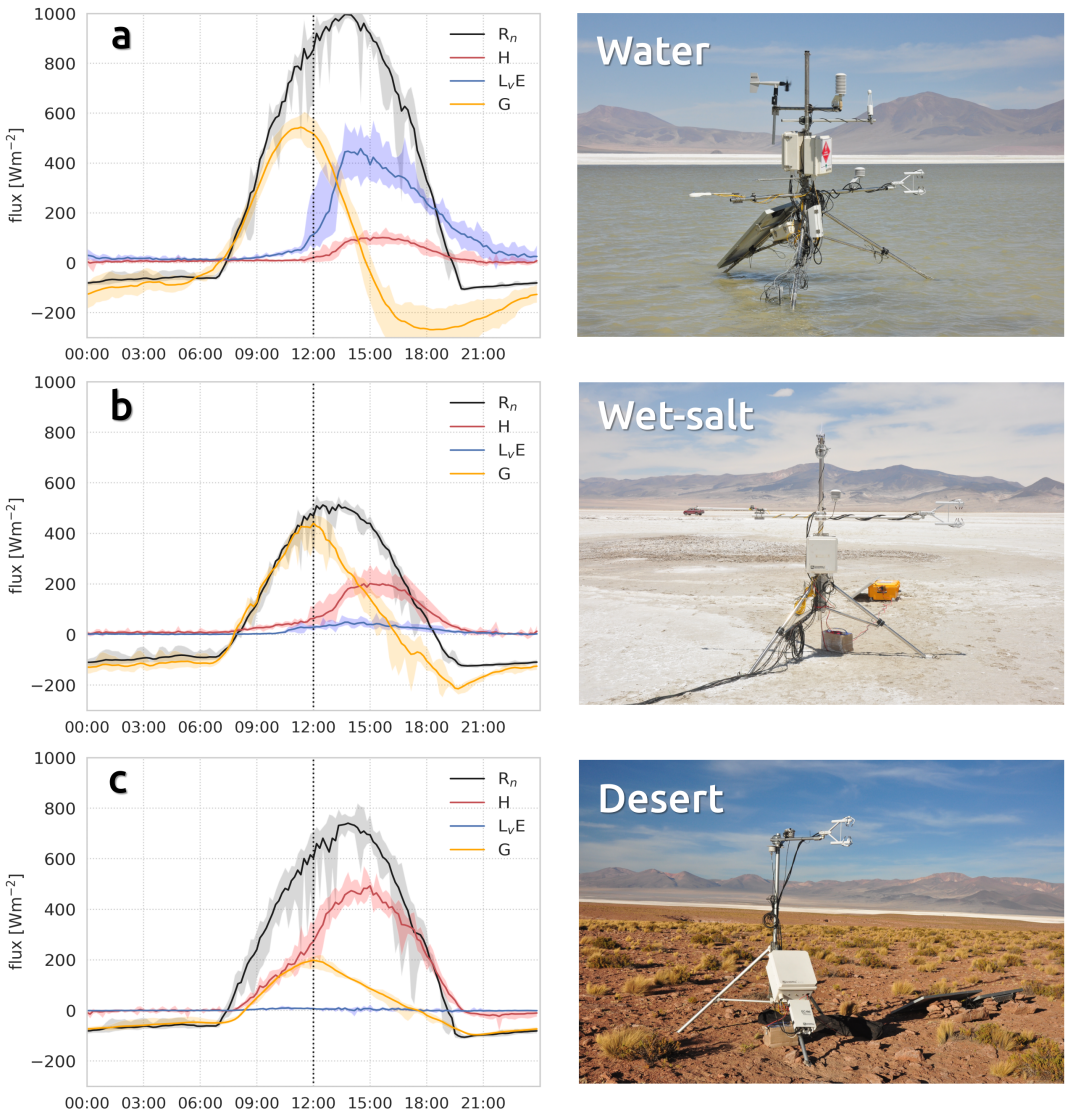

Figure 4.3: Diurnal cycle of the surface energy balance (SEB) observed during the E-DATA field experiment. Mean separated components are shown in colour lines and maxima and minima by shadings. (a), (b) and (c) show the SEB over the water, wet-salt and desert surfaces, respectively. Vertical dotted lines indicate the time of regime change. A photograph of each SEB-station installed is shown at the right side of each graph.

Table 4.2: Radiation and surface energy balance variables measured and inferred from complementary measurements above water, wet-salt and desert surfaces during the E-DATA experiment. Maximum mean values of incoming short- (Sw_{in}) and long-(Lw_{in})wave radiation, albedo, surface temperature (T_s), R_n, G, L_vE, H and daily mean of Bowen ratio.

	Sw_{in} $[Wm^{-2}]$	Lw_{in} $[Wm^{-2}]$	*Albedo* [-]	T_s [°C]	R_n $[Wm^{-2}]$	G $[Wm^{-2}]$	L_vE $[Wm^{-2}]$	H $[Wm^{-2}]$	*Bowen ratio* [-]
Water	1,250	250	0.12	22	950	500	500	100	0.2
Wet-salt	1,250	250	0.58	20	500	400	50	200	4
Desert	1,250	250	0.21	27	750	200	5	500	100

a larger short-wave outgoing radiation loss and thus much lower R_n.

While R_n shows a clear sinusoidal diurnal cycle, the SEB heat fluxes show two distinct regimes. The first occurs in the morning (07:00 - 12:00 LT) and is characterized by very low values of L_vE ($<$ 30 W m^{-2}), almost zero H, over the water surface for instance. As a result, most of the radiative available energy is used to heat up the lake water and underlying soil sediment ($G \approx R_n$, with values up to 600 W m^{-2}). The second regime occurs in the afternoon to early evening (12:00 - 20:00 LT). It begins with a rapid (2-hour) rise in L_vE and to lesser extent also in H at the expense of G, which diminishes in the afternoon to the point at which it becomes negative and provides additional energy, in addition to the decreasing R_n, to the turbulent fluxes H and L_vE. Focusing on E, its behaviour is atypical for surfaces where water is plentiful and E is mainly driven by the available energy (energy-limited system). Here, our analysis shows that in the morning E is very small even though the levels of R_n are very high, which indicates that it is limited either by turbulence or VPD (see Section 4.2). In turn, in the afternoon, the E-regime changes to the typical R_n-limited type to the point at which it requires additional energy from the soil (G becomes negative even before 15:00 LT).

On the wet-salt and desert surfaces, two similar surface flux regimes are observed, indicating that this feature dominates the entire study site and is not only specific to the water surface. However, there are interesting differences between the wet-salt and desert surfaces with respect to the water surface. In the wet-salt surface all the heat fluxes are much lower, reflecting the limited amount of R_n available (about half of that of water, as shown in Table 4.2). Furthermore, the roles of H and L_vE are reversed, i.e. it is H that suddenly increases when the afternoon regime commences (water and wet-salt surfaces Bowen ratio water of 0.2 and 4, respectively). The salt-crust reduces the soil evaporation of the wet-salt surfaces, in addition to the salt lowering E in general (Kampf et al., 2005) (Fig. 4.3b). In the desert, L_vE is zero all day and R_n is balanced between G and H (Fig. 4.3c). The two regimes are clearly visible and show similarities to the wet-salt regime, with the difference that in the morning regime G and H are similar while in the afternoon regime H is dominant.

In the next section we further analyse the mechanisms that explain the two-regime behaviour in the local SEB fluxes and link them to a description of the local boundary-layer profiles.

4.4.2 Local perspectives: from surface to atmospheric boundary layer

Figure 4.4a shows the mean daily cycle of wind speed (U) and direction (WD) over the water surface. Over wet-salt and desert surfaces, a similar diurnal variability is observed (Appendix B). The morning regime with low turbulent fluxes is related to conditions of very low wind speed ($U < 1$ m s^{-1}) and variable wind direction between the S and SW. The afternoon regime with high turbulent fluxes is related to high wind speeds ($U > 10$ m s^{-1}) and a well-defined wind direction from the West. This wind pattern is typical of this season and has been observed regularly in 2015, 2016, and 2017 as well.

Figure 4.4b shows that as a result of the low wind speed in the morning the aerodynamic resistance is very high ($r_a > 400$ s m^{-1}; turbulent kinetic energy, TKE $\sim$0 m^2 s^{-2}) and E in SDH can be regarded as turbulence-VPD-limited (see Equation 4.1). Note that in absence of any wind the water surface is extremely smooth (de la Fuente & Meruane, 2017; Suárez et al., 2020) and subsequently the surface roughness does not assist in generating shear. Additionally, H over the water is nearly zero as well, meaning that the high r_a is the result of the absence of both shear and buoyancy-generated turbulence. In contrast, for the desert surface, this occurs when the winds are equally low but the temperature gradient is steep enough to sustain a mainly buoyancy-driven H of about 200 W m^{-2}. In the afternoon, when the strong wind starts, r_a drops dramatically and TKE increases in the same manner (4 m^2 s^{-2}, see inset Fig. 4.4a), which results in the onset of the fluxes, when the E regime goes from a turbulence-VPD-limited to a radiation-limited E regime.

We now connect the gradients of temperature (linked to buoyancy forced turbulence) and moisture (linked to the VPD) between the surface of the water and the atmosphere at 1 m height, as well as how these affect E. Figure 4.4c shows the daily cycle of near-surface temperature (T_s), $\sim$1 m height air temperature (T) and surface-1 m thermal gradient (dT), over the water surface. The early morning (03:00 - 07:00 LT) displays low values of dT, where both air and water surface set below 0 °C and stay nearly -constants due to the formation of water ice. In the late morning, T_s and T increase rapidly, and mild thermal gradients corroborate the low H (Fig. 4.3a) and no buoyancy-generated turbulence. In the afternoon, dT increases to about 7 °C and then falls in accordance with the available radiation. Note that there is a lag between T_s and T peaks, where T decreases earlier than T_s. This behaviour is explained by the effect of the wind and cold air advection, which is stronger at 1 m than at the surface. The latter is corroborated by the $H > 0$ W m^{-2} shown in Figure 4.3a from 12:00 LT.

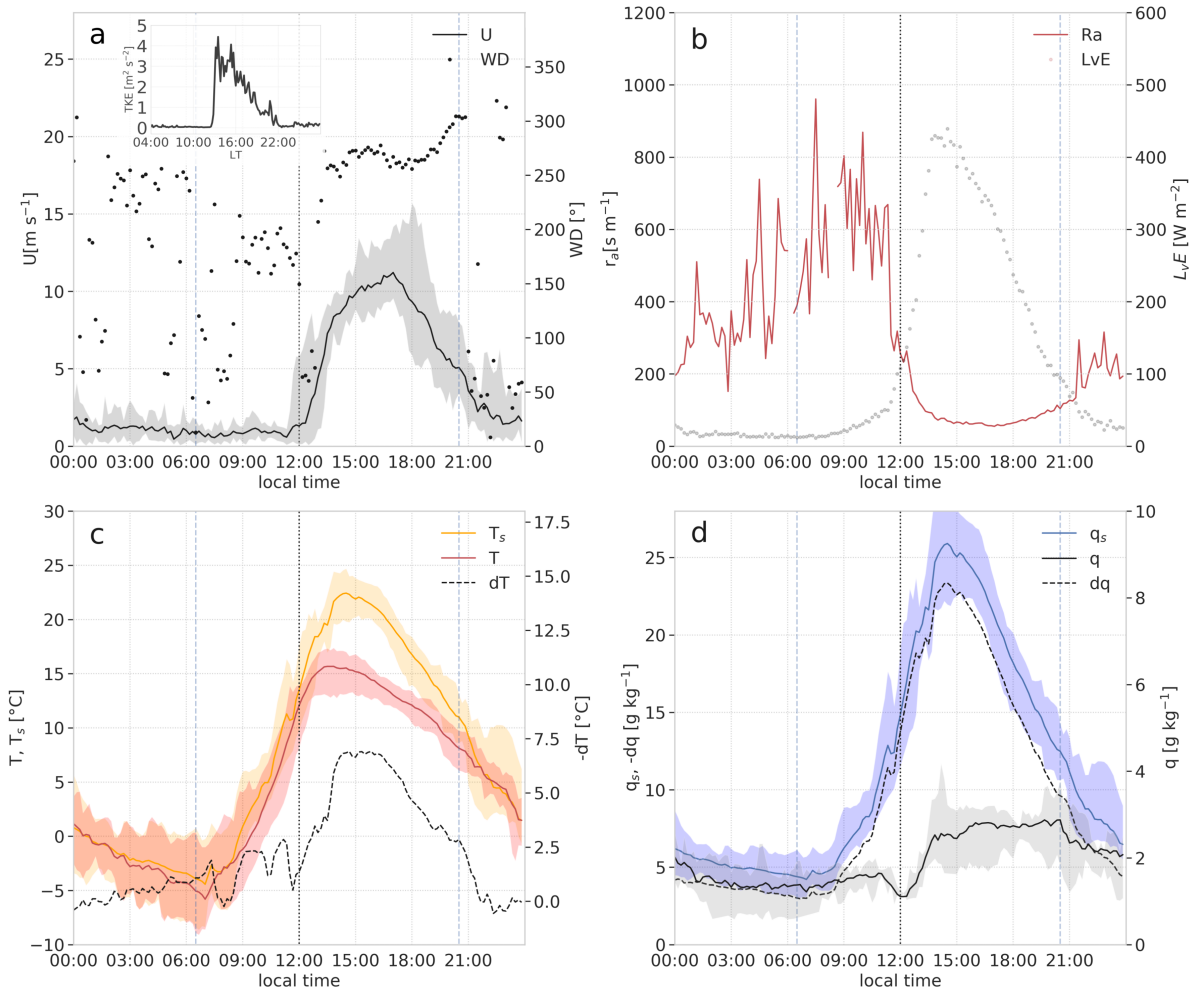

Figure 4.4: (a) Mean diurnal cycle of wind speed (U), turbulent kinetic energy (TKE), and wind direction (WD) of a representative day (November 18^{th}), (b) mean diurnal cycle of aerodynamic resistance (r_a), (c) air temperature (T), surface temperature (T_s) and thermal gradient ($-dT$) and (d) air specific humidity (q), surface saturated specific humidity (q_s) and moisture gradient ($-dq$) observed over the water surface. Vertical dotted lines indicate the time of turbulent regime change, blue dashed lines the sunrise-sunset, and shadings represent maximum and minimum observations. Observations from November 15^{th}-24^{th} 2018.

Figure 4.4d shows the daily cycle of saturated-specific humidity (q_s), 1 m height specific humidity (q) and the surface-1 m humidity gradient (dq), over the water surface. In the morning, dq are small due to q_s being constant according to T_s (ice on water). Note that the gradient is taken between 1 m and z_{0h} (very close to the surface). This does not seem to warrant the system being labeled VPD-limited. However, the absolute q of the IRGA (sensors in Table 4.1) is sensitive to calibration issues, therefore we hypothesize that the gradient very close to the surface could have been smaller, to such a degree that the lack of turbulence results in a thin, water-saturated layer that prevents the creation of a gradient, and as a result leads to very small values E. During the late morning q_s increases according to T_s and q shows a sudden drop of about 1 g kg^{-1}, just before the change in the wind regime. Finally, during the afternoon, q_s reaches its peak and then falls according to T_s. Likewise, q increases by 2 g kg^{-1} revealing, together with T, an advection of cold and slightly moister air into the study site. The advection of heat and moisture is discussed below in the vertical profile measurements and WRF modeling results.

These surface gradients are very dependent on the diurnal evolution of the ABL. Here, we present the vertical profiles at the water and desert surfaces as observed in the morning (Fig. 4.5). During the morning in the desert, the vertical structure of potential temperature, θ and specific humidity, q follows the evolution of a prototypical dry convective ABL (Figures 4.5a and 4.5b). The morning starts (09:00 LT profile) with a shallow unstable layer, corresponding to the unstable surface layer, followed by a stable layer until 1000 m agl. Driven by the surface sensible heat flux (H = 100 W m^{-2}), the ABL rapidly develops into a deep, well-mixed ABL (12:00 LT profile) where the boundary layer is capped by an inversion at h=1,800 m. The entrainment of dry, warm air from above the ABL supports its growth to 12:00 LT. On the basis of the high warming observed from 09:00 to 12:00 LT (Fig. 4.5a), we have estimated a non-local contribution of warm air close to 140 W m^{-2}.

Contrary to this, in the early morning over the water surface, we observe, for both the θ and q profiles (Figures 4.5c and 4.5d, 09:00 LT profiles) a transition from a stable to a close to well-mixed profile. The stable profile at 09:00 LT is quantified in 0.026 K m^{-1}, and starts to decrease its stability to 0.016 K m^{-1} at 10:00 LT, 0.00 1 K m^{-1} at 11:00 LT, and reaching a well-mixed type profile at 12:00 LT ($\partial\theta/\partial t$ with >0.001 K m^{-1}). From 11:00 to 12:00 LT the θ-profile shows an entire well-mixed boundary layer higher than 500 m, which is probably attributable to the desert convective ABL that is dominant on the study site (Fig. 4.5a). In the absence of wind and significant heat fluxes in the morning, the ABL is not driven by surface processes and weak, local (meso-scale) flows are likely to be dominant. Figure 4.6 shows the time-series of a typical day of U, and T of a westward, upslope transect of meteorological stations (see Figure 4.2). Here, in the early morning (03:00 - 06:00 LT) a WNW flow is visible, in which cold air accumulates at the lowest station. Figure 4.6 also shows that in the course of the morning the wind direction veers 180° to ESE. The night downslope and morning upslope circulations are indicative of a

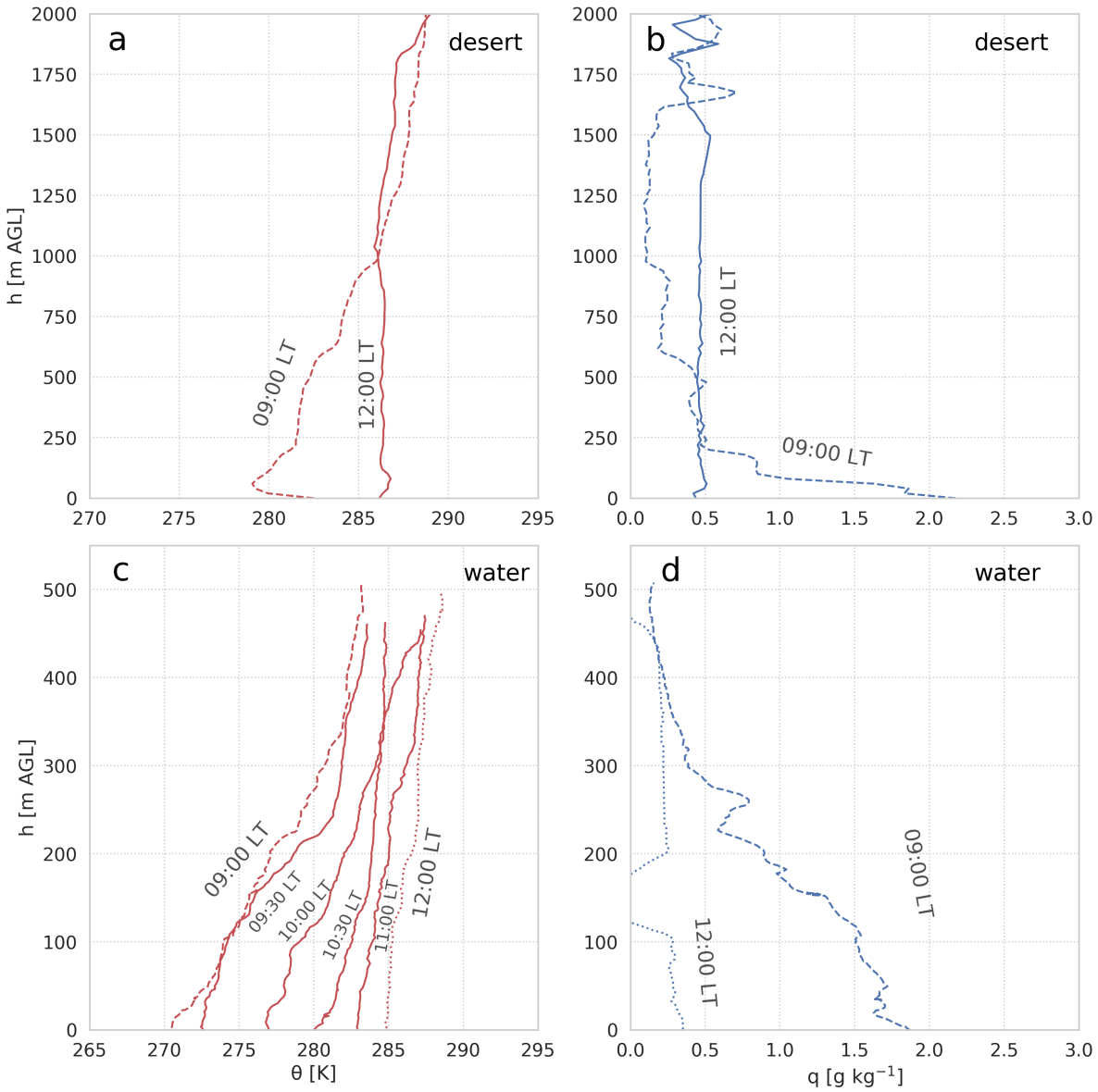

Figure 4.5: Morning vertical profiles of potential temperature (θ), and specific humidity (q) over the desert surface (a and b) 20.35° S - 69.90° W at 3,931 m asl in November 22nd 2018, and over water surface (c and d) 20.27° S - 68.88° W at 3,790 m asl on November 21st 2018.

katabatic (early morning)-anabatic (late morning) circulation between the low-lying saline lake and the surrounding mountain ridges. The anabatic circulation interacting with the top of the boundary layer potentially exhibits return flow that leads to a compensated subsidence over the lake (Whiteman et al., 2004), which would explain the eroding of the stable ABL in the course of the morning (Fig. 4.5c), as well as the warming observed in Figure 4.5a. In section 4.4.3 we return to the observational evidence by combining it with the analysis of the WRF results in order to determine the diurnal variability of these local circulations.

Figures 4.7a and 4.7b depict the wind profiles for the entire day as measured at the desert site. These profiles are very similar to those measured over the water. We therefore assume them as being representative of the entire study site. In the morning the winds are weak (<2 m s^{-1}) coming from different directions through the height, similarly to the ones represented in Figure 4.4a. In the afternoon the westerly wind increases strongly all across the boundary layer but is especially concentrated in a shallow jet near the surface (between 0∼250 m) with maximum wind speeds of ∼15 m s^{-1} at z∼80 m. These observations confirm that the surface winds are coupled to boundary-layer dynamics, which in turn are determined by the regional circulation flows.

Figure 4.7c shows the evolution of the ABL depth as determined from the θ profiles over the desert and water surface. After the strong convective growth in the morning (∼530 m h^{-1}), we observe that the boundary layer height decreases rapidly in the afternoon, from 1600 m agl at 12:00 LT to 750 m agl at 17:00 LT over the water and from 1800 m agl to 650 m agl over the desert. We attribute this decrease to a change in the wind regime, which allows the entrance of air masses with different temperature, moisture, and stability (Figures 4.8a and 4.8b). The mixed ABL values at 15:00 LT are cooler (decrease of ∼55 K) and moister (increase of 3 g kg^{-1}) than those observed at 12:00 LT (Figures 4.5a and 4.5b). Although the advected air is moist, compared to the desert conditions (q ∼0.5 g kg^{-1}), it is still characterized by a very low specific humidity (q ∼3 g kg^{-1}) considering the above-water conditions (q_s >15 g kg^{-1}). Hence, these moisty air mass does not significantly contribute to the E (see VPD subterm in Equation 4.1). Moreover, the ABL during the afternoon at the desert site is characterized by a strong inversion capping at ∼500 m above ground, in which at 18:00 LT θ jumps, Δ4 K (Fig. 4.8a) and q jumps Δq 2 g kg^{-1} (Fig. 4.8b). Likewise, the ABL formed in the afternoon (after regional flow arrival) over the water presents a higher inversion capping that the desert (750 m agl), but lower θ jumps, Δ1 K (Fig. 4.8c), and higher q jumps Δq 3 g kg^{-1} (Fig. 4.8d). Returning to the surface fluxes presented in Figure 4.3a, we can now identify two mechanisms that increase H in the afternoon. The first is wind-enhanced turbulence, which increases the mixing efficiency between the surface and the atmosphere. Second is advection of cool air that increases the θ-gradient and the subsequent near-surface instability of the atmosphere. Based on the turbulent heat fluxes (Fig. 4.3) and the ABL height (Fig. 4.7b), and using the second term of equations (4.3) and (4.4) as a residual, we quantify in Table 4.3) the

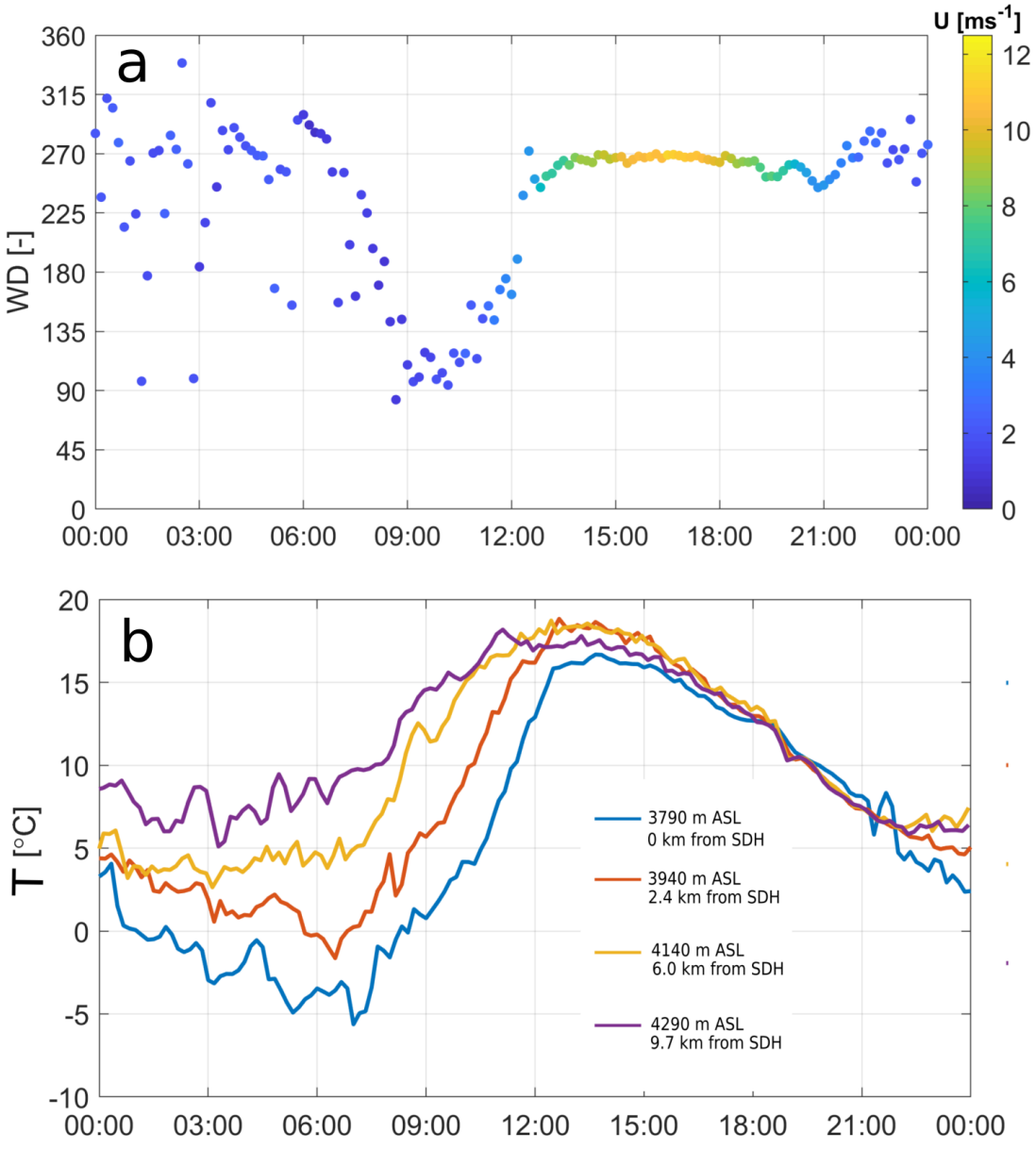

Figure 4.6: (a) Transect-averaged of wind direction (WD) and wind speed (U) the E-DATA on November 21st, 2018. (b) The air temperature of the MET-station transect shown in Fig. 4.2b on November 21st, 2018.

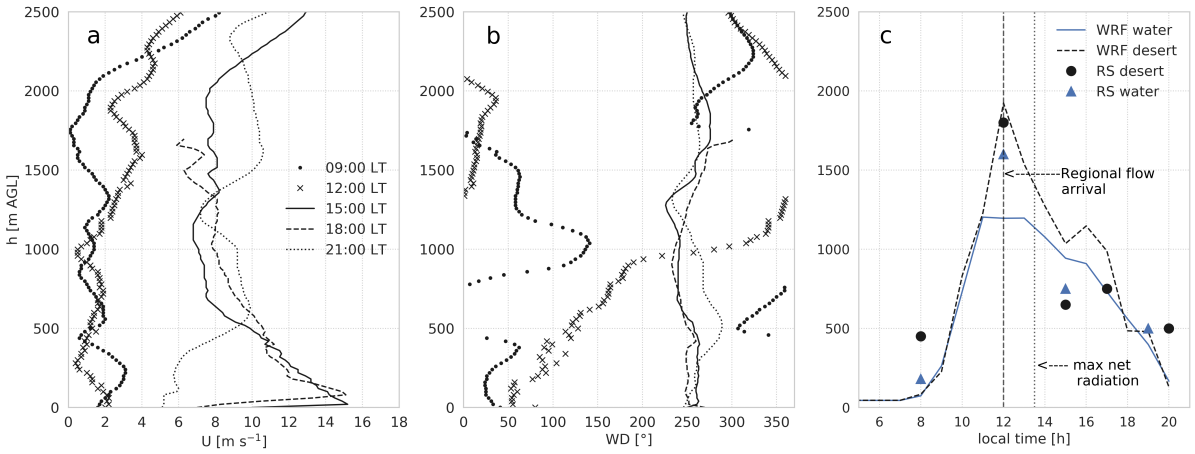

Figure 4.7: (a) Diurnal cycle of wind speed (U) and (b) wind direction (WD) vertical profiles and (c) boundary layer height (h) over the desert (November, 22^{nd}; 20.35° S - 69.90° W; 3931 m asl) and water (November, 21^{st}; 20.27° S - 68.88° W; 3,790 m asl) surfaces determined by radiosounding (RS) and WRF simulation.

local (surfaces fluxes), non-local (entrainment) and regional (advection) contributions to the mixed-layer tendencies of θ and q between 15:00-18:00 LT. It is not surprising that with L_vE=0, the increase in humidity of 0.2 g kg^{-1}h^{-1} is entirely accounted for by regional advection (See computation details in Appendix D). Here the overall trend is relatively small (+0.33 K h^{-1}), given the relatively large H=400 W m^{-2} (17:00 LT), due to the cool-air advection, which largely cancels the local heating.

Table 4.3: The local (surface fluxes), non-local (entrainment flux) and regional (advection) contributions of $\partial q/\partial t$ and $\partial\theta/\partial t$ (equations (4.3) and (4.4)) corresponds to the period between 15:00 and 18:00 LT. These contributions are therefore averaged over this period and were taken above desert and water surfaces. Note that observations above the desert follow satisfactorily the assumptions of the Mixed-layer equations (4.3) and (4.4). Total tendencies, local and non-local contributions are based on SEB stations and radiosounding measurements, whereas advective contributions are estimated as a residual of equations (4.3) and (4.4) (see computation details in Appendix D).

	h	$\partial q/\partial t$	Local	Non-local	Regional	$\partial\theta/\partial t$	Local	Non-local	Regional
	[m]	[g kg^{-1} h $^{-1}$]	[g kg^{-1} h $^{-1}$]	[g kg^{-1} h $^{-1}$]	[g kg^{-1} h $^{-1}$]	[K h^{-1}]	[K h^{-1}]	[K h^{-1}]	[K h^{-1}]
Desert	500	0.20	0.00	0.00	0.20	0.33	2.69	0.00	-2.36
Water	680	0.28	0.86	0.01	-0.59	0.33	0.66	-0.0006	-0.324

The afternoon profiles over water (Figs. 4.8c and 4.8d) show that on the arrival of the afternoon wind regime, the stably stratified boundary layer up to 500 m present at the end of the morning (Figure 4.5c and 4.5d) becomes progressively eroded. In contrast to the eroding shallow mixed layer in the morning, in the afternoon, the destruction of the existing boundary layer structure is driven by the surface processes. This process

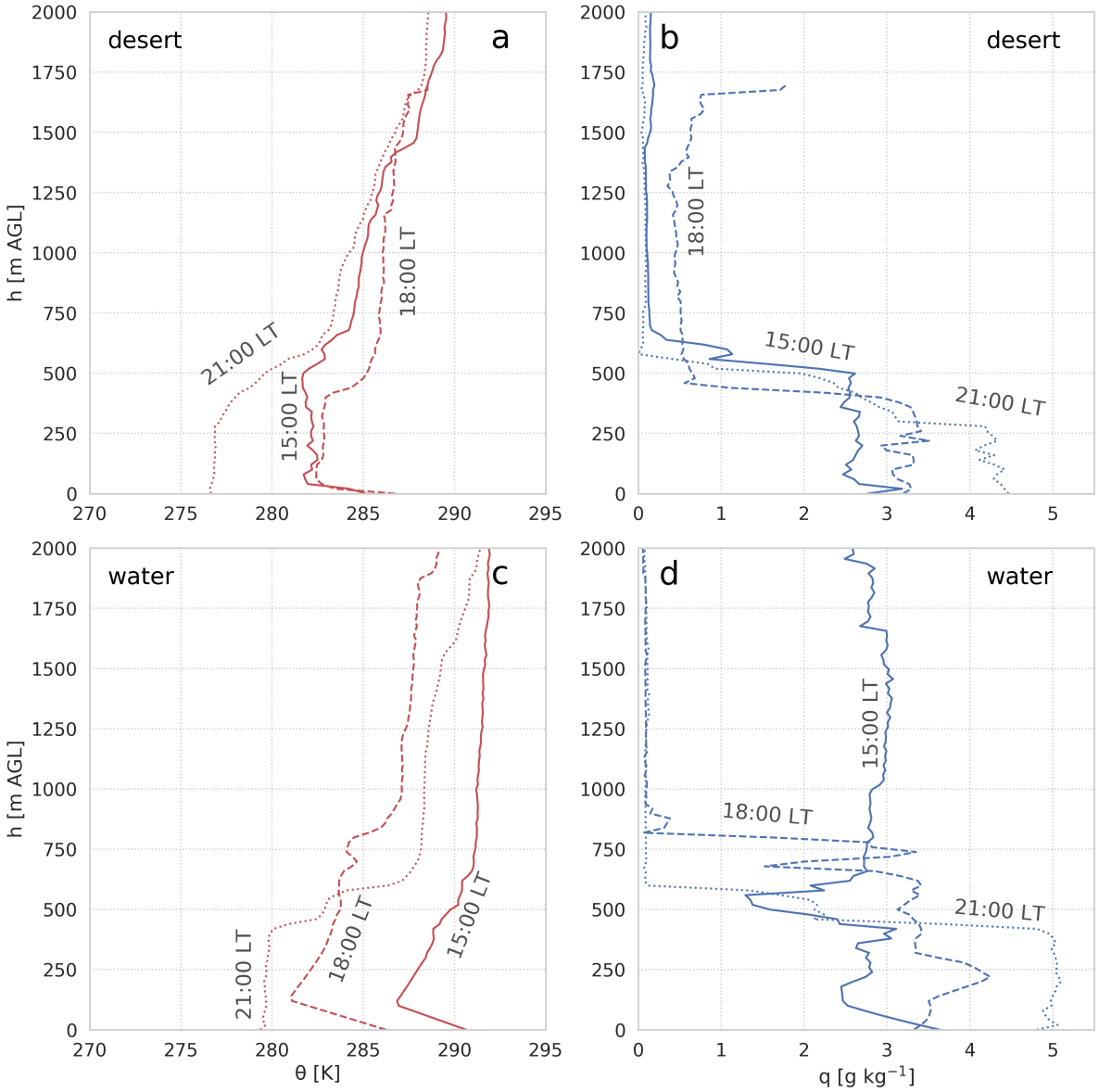

Figure 4.8: Afternoon vertical profiles of potential temperature (θ), and specific humidity (q) over the desert surface (a and b) 20.35° S - 69.90° W at 3,931 m asl on November 22nd 2018, and over the water surface (c and d) 20.27° S - 68.88° W at 3,790 m asl on November 21st 2018.

is explained by: a) enhanced mechanical turbulence from the strong winds of the near-surface jet (Fig. 4.7a); b) higher surface temperature (Fig. 4.4c) by the wind-induced mixing of the shallow water layer, and c) enhanced instability due to the cold air advection. This results in a shallow unstable layer, ranging from 0 m to ∼150 m above the water surface between 15:00 LT and 18:00 LT. These levels are similar to the depth of the jet shown in Figure 4.7a. Regarding the moisture budget, the arrival of the wind flow in the afternoon moistens the unstable layer, while wind shear mixes it, resulting in steadily better-mixed q-profiles. At 21:00 LT an around 400 m-deep well-mixed boundary layer has developed over the water surface. Considering the budgets of local, and non-local versus regional contributions to the q and θ mix layer tendencies over the water surface (Table 4.3), we quantify a major local q contribution of about 0.86 g $kg^{-1}h^{-1}$ between 15:00 and 18:00 LT, and a small non-local contribution of 0.0006 g kg h^{-1}. This moisture contribution exceeds the q-tendency observed, which can be only balanced by the negative regional contribution (-0.59 g $kg^{-1}h^{-1}$). The negative regional contribution of q confirms that even though the advected air is moist compared to the desert conditions, this is still dry for the water surface conditions. The θ-tendency behaves similarly to that of q, whose local contribution of heat is equivalent to double the tendency value, but it is compensated for by cold regional flow (negative θ contribution).

4.4.3 Regional perspectives: modeling multi-scale mechanisms influencing E at SDH

In the previous sections, the measurement results indicate that E in the SDH is largely controlled by small-scale local circulations during the night and morning. This E pattern changes in the afternoon by the formation and arrival of regional meso-scale circulations. In order to better quantify how this circulation influences E at the SHD, we analyse WRF model results of the atmospheric conditions surrounding the SDH, using the regional-scale model WRF. We focus on two issues. The first concerns evaluating whether our measurements are influenced by small flows from katabatic-anabatic effects that dominate nighttime and morning boundary layer in the absence of strong local or regional forcing. The second and more important one is the quantification of insights into the mechanism that generates the strong winds in the afternoon and produce the enhancement of E.

The local conditions that dominate the E in the SDH are analysed in Figure 4.9, which depicts the wind flow and temperature in the study site at 07:00 LT calculated with a grid resolution of 1 km, i.e. an effective resolution of approximately 3 km. The circulation is characterized by a downward flow from the surrounding mountains (z >4,500 m asl) around the lowlands (z ≈3,800) where the saline lake is located, which tends to accelerate over pronounced slopes and closely follows the shape of the terrain. However, the lowest temperatures shown at the bottom of the valley in our observations (Fig. 4.6) are less clearly recognizable in the model (Fig 4.9a), where low temperatures occur in

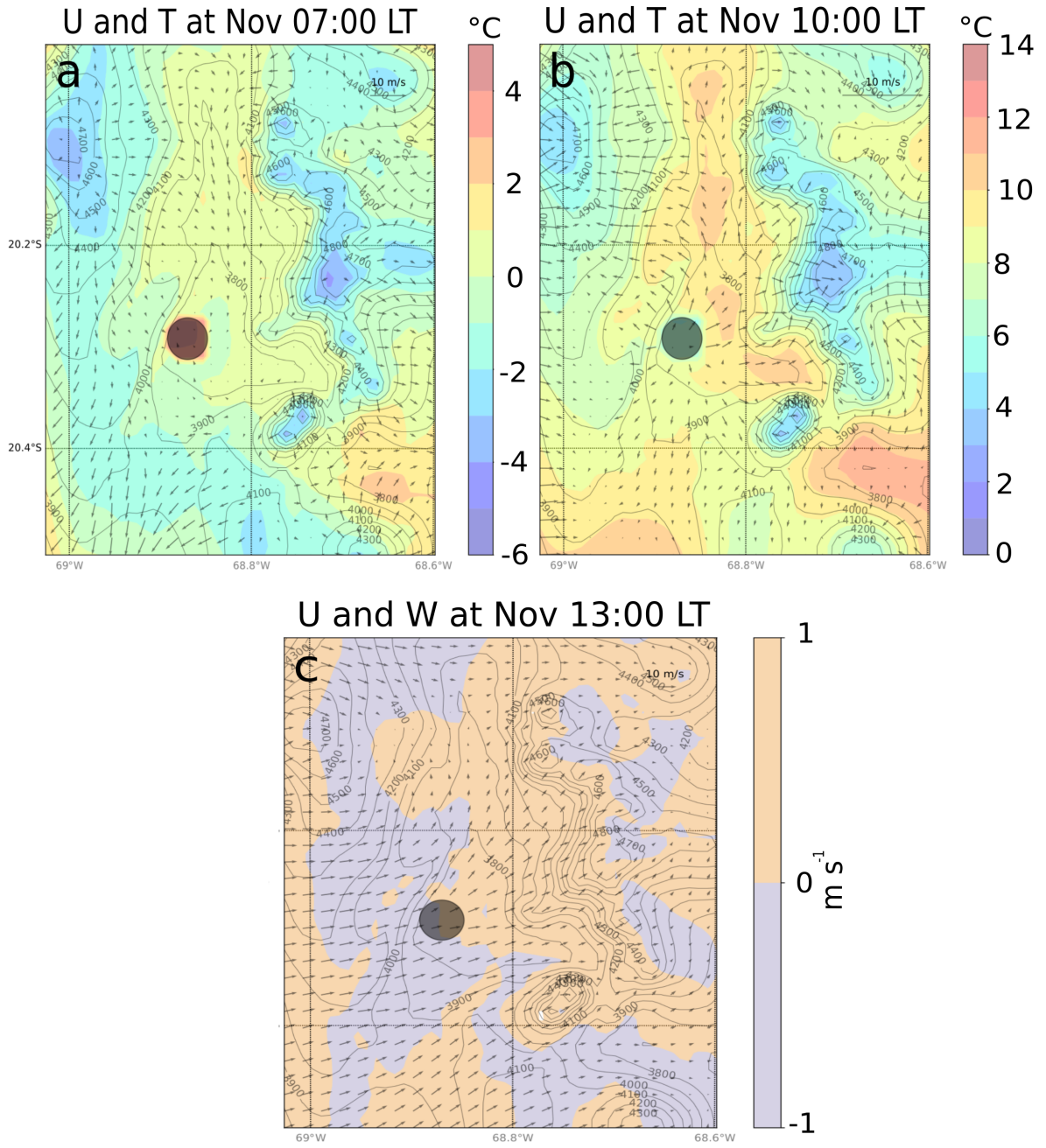

Figure 4.9: E-DATA period-averaged wind flow WRF simulation of domain D04 at 1km-resolution. (a) Surface U and T at 07:00 LT. (b) Surface U and T at 10:00 LT. (c) U and vertical wind (W) at 13:00 LT. The black dot represents the saline lake.

the surroundings of the lake. This down-slope flow is responsible for the stratified layers observed over the water surface at 09:00 LT (Fig. 4.5c). This katabatic flow progressively decreases in the course of the morning whereas a transition from stable to well-mixed layer occurs above the water from 09:00 to 12:00 LT (Fig. 4.5c). Here, we observe two processes that are responsible for the local circulation and the low surface fluxes over the water during the morning (Fig. 4.3a). The first , between 09:00 - 10:00 LT, is an anabatic radial flow from the lake to its surroundings (Fig. 4.9b). The second one, a downward flow produced by the interaction between the anabatic flow with the thermally driven wind during the morning-afternoon transition. This flow shown in Figure 9c produces a compensated subsidence (Whiteman et al., 2004) at the western margin of the SDH valley, which explains the morning stratification over the lake shown in Figure 4.5c.

To characterise the recurrence of the wind pattern and its robustness at larger spatial scales, Figure 4.10 shows averages over 10 days (E-DATA period) of zonal wind speed (U), temperature (T), and specific humidity (q) in the morning (10:00 LT) and afternoon (16:00 LT) in a SW-NE vertical cross-section of the Andes mountains obtained by the WRF model. In the morning we identify two main zones with clear U, T and q conditions. The first corresponds to the coast ($z < 1$ km) over the ocean (70.3° W), where the marine boundary layer (MBL) is characterized by low westerly winds of 2 m s^{-1} (Fig. 4.10a), a thermal inversion capping at ∼1 km height (Fig. 4.10b) and a quite well-mixed MBL with a moisture ranging between 7 and 10 g kg^{-1} (Fig. 4.10c). The second zone corresponds to the western slope of the Andes (70.0° W to 68.5° W) above $z > 1$ km. This zone presents a very low U (∼1 m s^{-1}) that increases to 2 m s^{-1} at the surface up-slope, producing a small local circulation in the SDH basin (see red square in Fig. 4.10a). Likewise, there is a thermal contrast between the land and the top of the MBL (5 K) and incipient heating in the surface (70.0 ° W) together with a vertical thermal stratification of the atmosphere of 0.6 K per 100 m. Finally, low values of moisture are observed at middle altitude lands (∼4 g kg^{-1}), with a variation ∼ -1 g kg^{-1} per km ascended on the slope (Fig. 4.10c).

During the afternoon, the morning conditions rapidly intensify. The U increases at the surface >10 m s^{-1}) along the slope, with a steep variation in its vertical profile, i.e., the weakest zonal winds are between 2 and 4 km asl (∼1 m s^{-1}). Above ∼4 km asl, typical synoptic southwesterly winds are found with speeds around 5 m s^{-1} (Fig. 4.10d). The thermal contrast between the MBL top and the inland desert surface increases up to 10 K in the afternoon, in association with intense land warming. This strong wind circulation is characterized by higher values of the specific humidity (4 - 6 g kg^{-1}) from the top MBL (z: 1-2 km and longitude 70.3° W) along the side of the Andes slope (Fig. 4.10f). This strong advection follows two paths, one reaches the SDH and increase the specific humidity from 1 to 3.5 g kg^{-1}, and the other one returns back westward at ∼2 km asl. Two additional mechanisms on the western slope of the Andes that enhance the surface wind flow are also reproduced by the numerical experiment in WRF. The first mechanism is an anabatic flow formed at the midlands (70.0° W) driven by the high sensible heat

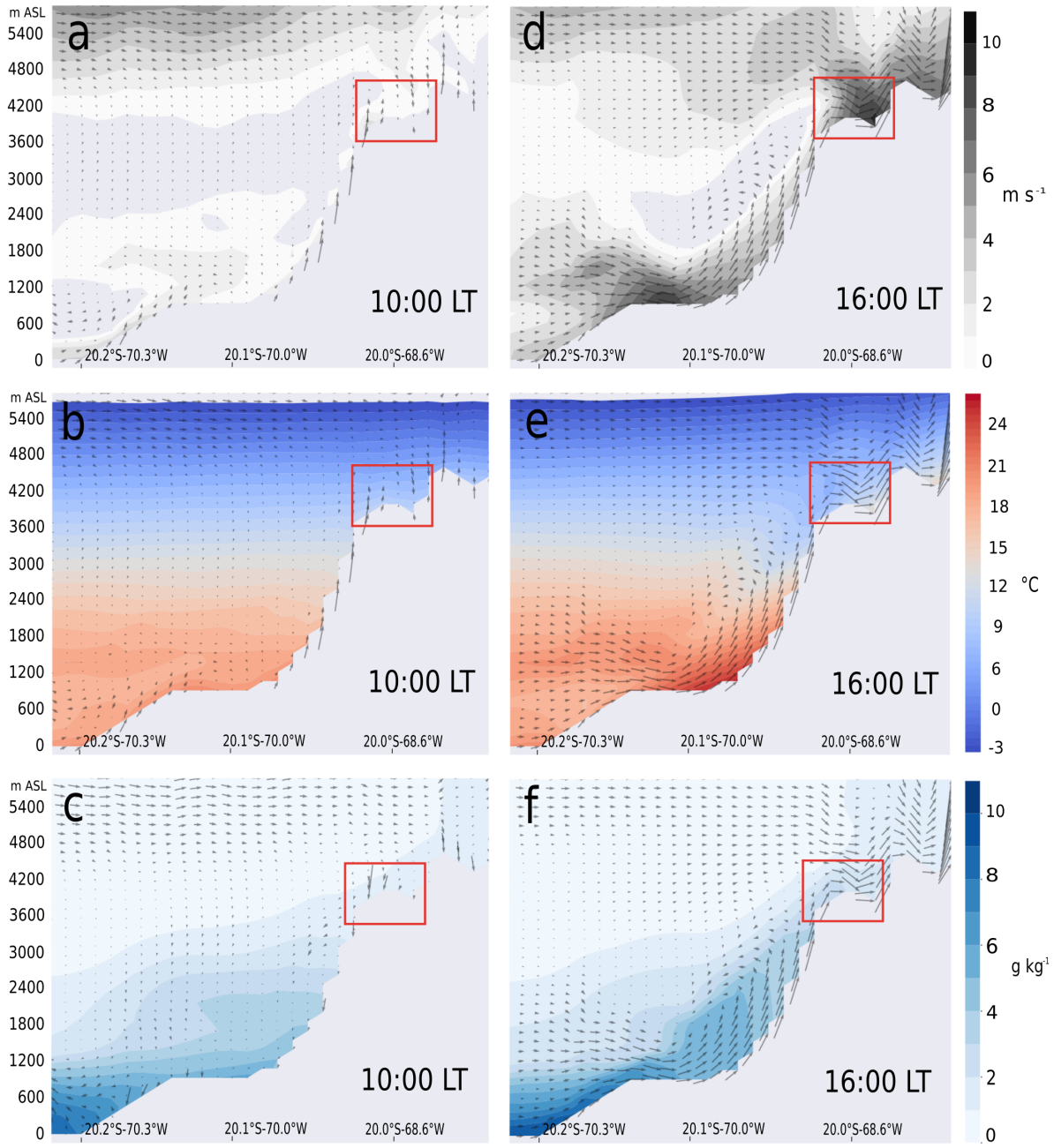

Figure 4.10: Vertical cross-section of diurnal atmospheric circulation on the Pacific Ocean Andes western slope, simulated with WRF for the E-DATA diurnal-averaged along 21.5° S. Black arrows represent U (zonal winds) and WD and the red square the SDH. (a), (b), and (c) represent U, T and q, respectively, during the morning, and (d), (e) and (f) are the same for the afternoon.

fluxes, which corresponds to 73% of R_n. The second mechanism that is superimposed on the anabatic flow is a surface flow acceleration along the slope, which we recognise as flow channeling. This channeling is given by the shape of the topography and the subsidence produced by the SE subtropical anticyclone (Rutllant et al., 2003) over the the SE Pacific Ocean and the western slope of the Andes. The flow is then channeled down into the SDH basin from the SW, producing local subsidence (Fig 4.9c). In summary, the origin of the strong wind that controls the evaporation in the Salar del Huasco originates in the regional daily atmospheric circulation from above the MBL to the Atacama Desert.

4.5 The role of atmospheric circulation on evaporation

Analysis of the observations carried out during the E-DATA field experiment and the WRF simulations enable us to propose a physically based explanation of the main role played by the wind in the control of evaporation in the Salar del Huasco basin.

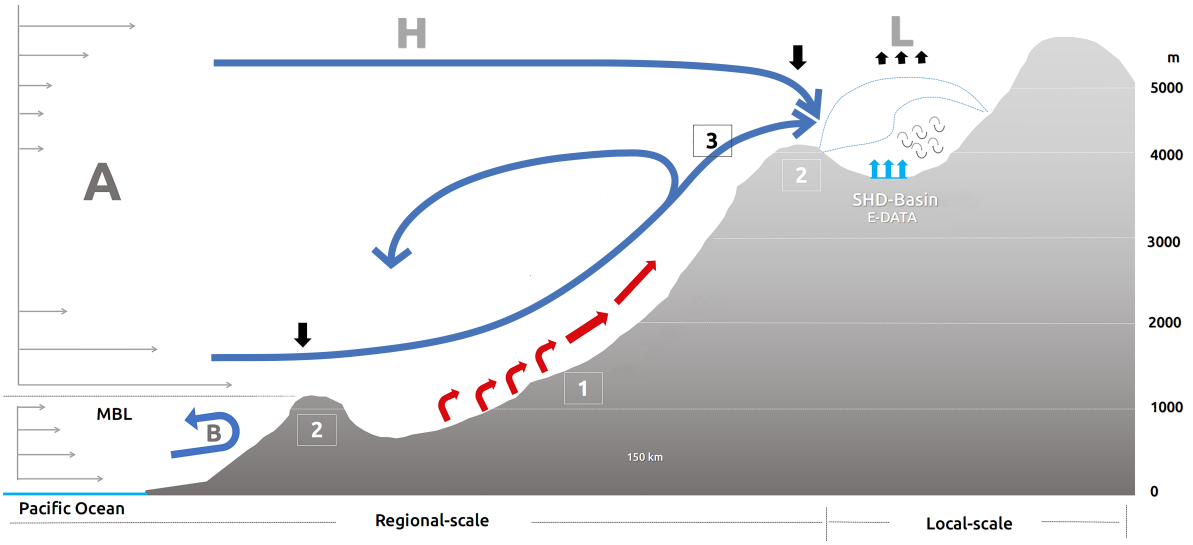

Figure 4.11: The regional and local circulation patterns that act between the Pacific Ocean and the western slope of the Andes. H and L (black arrows) represent the synoptic high and low pressures. A) corresponds to the regional zonal circulation from the top of MBL and (B) corresponds to the zonal circulation within the MBL resulting from the coastal daytime warming. Grey arrows (left) represent the regional zonal wind intensity. 1 (red arrows) indicates the anabatic flow. 2 schematises the topographic channelling process. 3 (blue arrows) shows the advection. Blue dotted line represents the formation of boundary layers, and cyan arrows the E produced by turbulence (circular arrows).

The overall dynamic of the regional atmospheric circulation interacting with local-scale processes described in the results is depicted in Figure 4.11. The regional circulation

is a result of a multitude of processes and mechanisms interacting at scales from about 100 km to 100 m close to SDH. The main dominant atmospheric circulation driver is the thermal contrast between the above the MBL of the Pacific Ocean and the western slope of the Andes. Two principal and independent atmospheric circulations are dominant at daytime on the regional scale: (A) an thermally driven flow from the above the MBL (Rutllant et al., 2003) and (B) a local sea breeze formed within the MBL that interacts with the coastal mountains (Rutllant et al., 2003; Lobos-Roco et al., 2018). Two other phenomena that occur on smaller spatial length scales reinforce this regional flow: anabatic flow (1) and topographic channeling (2), which enhance the inland flow from above the-MBL (A) when this reaches land. The interaction of these meso-scale (A and B) phenomena results in (3) the horizontal advection of air masses driven by the surface winds. Part of this advection transports cold and dry air into the Andes highlands basins, whereas the other part returns back into the midlands forming a small cell (Rutllant et al., 2003). This thermally driven flow interacts with the synoptic flow (4-5 km asl) when both arrive to SDH. This multi-scale regional circulation influences the evaporation at SDH in two ways: by producing mechanical turbulence and by transporting the cold and dry air above the water surface. Both processes lead to an abrupt transition in the diurnal variability of the evaporative pattern over open water: from being almost zero during the morning to large evaporation from the noon.

This regional circulation has already been well studied. Rutllant & Ulriksen (1979) and Rutllant et al. (2003) describe observations of the southwesterly atmospheric circulation for summer and winter at 250 km S of the SDH, as a consequence of the diurnal ocean-land thermal differences. This result corresponds to the circulation system (A) depicted in Figure 4.11. This same pattern as we found has been also reported in numerical experiments performed in November 2008 by Rutllant et al. (2013) as well. Rutllant et al. (2003) also suggested that the atmospheric circulation (B) in Figure 4.11 can be coupled to the system A. This occurs when the marine subsidence inversion is weak, allowing for the entrance of marine air masses to the desert. Our numerical experiment also shows this interaction, from where the air that is advected towards the SDH starts ((3) in Fig. 4.11).

The values of q and T at the level of 1 km asl in our results agree with the vertical profiles observed by Muñoz et al. (2011) for the Atacama coast, which are the same as we observe arriving during the afternoon at SDH. However, further research must investigate the origin of the moist and cold air mass that arrives at SDH, in order to accept or discard the origin suggested by our results. Likewise, Falvey & Garreaud (2005) describe the predominance of westerly winds from the free atmosphere towards the Andes western slope ((A) in Fig. 4.11) during the summer at 500 km N of the SDH. The regional atmospheric circulation for dry periods described by Falvey & Garreaud (2005) agrees with our results for the dry season. Finally, the surface regional atmospheric circulation was also found by Muñoz et al. (2018) in their analysis of surface wind measurements

all around the Atacama Desert. Muñoz et al. (2018) reported predominant SW surface wind speeds below 5 m s^{-1} during the morning, which intensify to 15 m s^{-1} during the afternoon. These results agree with our observations (Fig. 4.4a) and our numerical experiments (Figs. 4.10a and 4.10d).

With respect to the wind-related mechanisms that control evaporation, our research extends to previous observational studies performed under similar environmental conditions. The modeling results of de la Fuente & Niño (2010) show that R_n is mainly balanced by L_vE, which is driven by the afternoon wind during summer in Salar Punta Negra (500 km S of the SDH). They also reported a similar L_vE diurnal cycle, which is close to 0 W m^{-2} in the morning and has a sudden enhancement in the afternoon caused by changes in the pattern of winds (de la Fuente, 2014; de la Fuente & Meruane, 2017). This result agrees with our description of morning-afternoon turbulent regimes shown in Figure 4.3a, but also regarding the diurnal cycle of r_a (Fig. 4.4b). In a different region, the relationship between wind and L_vE has been also observed by de de Bruin et al. (2005) over a crop field surrounded by a desert area in Idaho, USA. de de Bruin et al. (2005) observed that the advection of dry and warm air from the surrounding desert, shows a negative H in the SEB, resulting in ratios of $L_vE/R_n > 1$. However, our results show a different pattern, since over the three different surfaces L_vE/R_n is always lower than 1 and H is positive (Fig. 4.3). On the other hand, Tanny et al. (2008) describe the L_vE diurnal cycle in a water reservoir in northern Israel. They estimated the evaporation rates using several models, and validated their estimates by means of direct evaporation measurements performed with an eddy covariance system. They concluded that a better agreement between measured and estimated E occurs for models that represent better the wind diurnal cycle compared to those that consider the wind contribution to be constant. This agrees with our observations as shown in Figures 4.4a and 4.4b.

Our findings related to ABL dynamic show different results above the SDH compared to classical interpretation of atmospheric boundary layers (Stull, 1988). However, they compare well with previous studies performed in different environments. First, the morning dynamic of the ABL described in section 4.3 has been also reported by Whiteman et al. (2004) and Whiteman (1989) in closed mountain basins in the Alps, the Rocky Mountains and Bush Creek Valley in the US. The authors show similar vertical profiles in the saline lake during the morning at the bottom of the valley. Moreover, the same dynamic of morning anabatic wind and the consequent compensated subsidence has been observed via a conceptual model by Whiteman et al. (2004). Our results share some similarities with those obtained by Batchvarova & Gryning (1998), describing changes in the boundary layer due to the sea-land breeze advection conditions in Athens. Even when geographical differences between these two locations exist, the profiles show the same diurnal evolution of the thermal structure observed over the water surface at SDH (Fig. 4.8c and 4.8d). Likewise, the wind vertical profile reported by Batchvarova & Gryning (1998) agrees with our observations (Fig. 4.7a). This wind profile characterized by a

surface jet has also been observed by Raynor et al. (1979) in the Atlantic's US coastal ridge under summer sea-land breeze conditions.

This research might be extended to contribute to the understanding of the climatology of the evaporation process. For instance, more work needs to be done to obtain evaporation estimates over different seasons, such as the summer rainy season over the desert, where synoptic and radiative conditions change completely. Similarly, more work is needed to reduce the uncertainties in observations, for example by using a range of different methods to integrate the surface heterogeneity. Additionally, WRF simulations might enable us to design numerical experiments to improve our understanding of changes in the regional circulation that can affect wind patterns and therefore evaporation in the highlands. Our results demonstrate that there is significant variability in evaporation at scales below 1 km, and the relevance of coupling regional circulations to micrometeorological experimental studies, thus helping to improve the representation of E in models, and consequently, improving water management in arid regions.

4.6 Conclusions

We investigate the diurnal variability of evaporation in a saline lake at high altitude. By combining surface and atmospheric high-resolution observations taken during the E-DATA field experiment and high-resolution WRF modeling results, we have found that the wind, governed by thermal and orographic differences on different spatial scales, is the main driver of evaporation in the Salar del Huasco. The absence of turbulence (wind) in the morning produces a high aerodynamic resistance that inhibits the transport of moisture from a saturated surface layer over the water into the atmosphere. This occurs when R_n is not a limiting process. During the afternoon the arrival of the regional flow triggers turbulent kinetic energy (4 m^2 s^{-2} after midday) driven by the shear. This enhancement in the turbulent mixing is accompanied by the advection of cold and dry air that enhance the evaporation.

More specifically, our results distinguished two regimes: (1) the morning local regime dominated by high net radiation and ground heat flux, low wind speed ($<$2 m s^{-1}), a low surface-atmosphere moisture gradient ($\sim$3 g kg^{-1}) and an extremely low evaporation rate ($\sim$0 W m^{-2}). During this regime, the principal limiting driver of evaporation is the mechanical turbulence, in the absence of which the air at a saturated specific humidity over the water is unable to mix with the dry atmosphere. Similarly, the available net radiation is almost totally transferred to the soil, acting as a secondary factor in controlling evaporation. (2) The afternoon regional regime dominated by surface fluxes of latent and sensible heat flux, high wind speed ($>$10 m s^{-1}), a very high surface-atmosphere moisture gradient ($\sim$10 g kg^{-1}) and a sudden increase in evaporation over the water (500 W m^{-2}). This regime is no longer limited by wind (turbulence), instead, the decrease in net radiation, in the transition to the evening, characterizes the limiting factor. Similar regime

patterns are observed over wet-salt and desert surfaces. However, the most representative and sensitive variable is the sensible heat flux. For this reason, we conclude that these regimes are representative of the SDH basin and indicate the complexity of the land-atmosphere interaction due to large variations on sub-daily scales and the sub-kilometer surface heterogeneity.

The afternoon regional regime also has an impact on the development of the atmospheric boundary layer, particularly under the afternoon regime. The vertical profiles observations show the interruption of the convective boundary layer growth over the desert. Over the water, an initial mixed layer about 180 m deep is formed in the early morning by katabatic winds. This mixed layer dynamically evolves into a stable layer in the late morning due to a local circulation that entrains warm air aloft, creating a stable stratified layer with thermal gradients of 0.02 K m^{-1}. The afternoon regional wind stops this stabilisation and leads to the formation of an unstable layer driven by high levels of mechanical turbulence production ($u* \sim$0.65 m s^{-1}).

Our explanation relates the local evaporation with regional atmospheric circulations. We found that the regional circulation is due to three interconnected atmospheric phenomena occurring at different spatial scales: (i) at 4,000 m the above of the MBL of the Pacific Ocean characterized by a strong flow towards the land (15 m s^{-1}), (ii) an anabatic circulation driven by the contrast land-ocean (10 K) and (iii) a channeling of the flow occurring at 3,000 m. The concatenation of these three phenomena leads to the daily appearance of strong winds, which then enhances the mechanical turbulence and, therefore, evaporation. Our findings indicate the need to combine complete local measurements with regional modeling to understand the interactions of arid land conditions conditioned by a cold ocean and complex land topography.

Chapter 5

Characterizing the influence of marine stratocumulus cloud-deck on the land fog at the Atacama Desert

This chapter is based on:

Lobos-Roco, F., Vilà-Guerau de Arellano, J., & Pedruzo-Bagazgoitia, X. (2018). Characterizing the influence of the marine stratocumulus cloud on the land fog at the Atacama Desert. *Atmospheric Research*, 214, p. 109–120.

Abstract

Fog in the Atacama Desert is a virtually untapped source of fresh water in the driest place on Earth. Focusing on understanding the role played by marine stratocumulus (Sc) in the development of land-fog, we analyse surface observations made along a steep transect at different heights. These observations are combined with numerical experiments performed using the Weather Research and Forecasting Model (WRF). We find two main diurnal regimes based on atmospheric thermal stability, both of which determine the formation and dissipation of fog. These are (a) a well-mixed regime characterized by low gradients of potential temperature and specific humidity, low diurnal variability, and presence of Sc cloud-fog. (b) A stratified regime characterized by high gradients of potential temperature and specific humidity, high diurnal variability, but no Sc clouds nor presence of fog. By using the parcel method, initialised with surface observations, we characterize the Sc cloud of nine typical fog events, estimating a mean cloud depth of 566 m between 740 m (±150 m) and 1,307 m (±30 m). Fog observations at ground level agree with these cloud-base and cloud-top estimates, showing a liquid water mixing ratio of Sc cloud-fog in the range 0.3 - 0.7 g kg^{-1}. The study reveals that the advection of marine Sc cloud and the stability of the boundary layer are key processes in the formation and dissipation of fog. Sc cloud advection over land is modulated by upwind and driven by topography and local circulation. We conclude that a realistic characterization of Sc cloud-fog is possible by combining limited surface observations and numerical experiments.

5.1 Introduction

Fog in arid regions is regarded as one of the few viable freshwater resources, playing a key role in ameliorating water scarcity (Klemm et al., 2012). In the Atacama Desert, water scarcity produces tensions between industry, civil society, and the environment, all of which are dependent on the limited water resources available to develop (Oyarzún & Oyarzún, 2011). Water is needed for human consumption, but also for energy and food production, the fundamental basis of development (Schewe et al., 2014). The high hydrological potential of the fog harvesting in the Atacama Desert is due both to the interaction between the marine Sc cloud with the abrupt orography, and to its proximity to major population centres such as Antofagasta, Arica and Iquique (Schemenauer & Cereceda, 1994b). Due to these two characteristics, the fog is one of the most viable freshwater resources to be tapped.

The Atacama Desert is believed to be the driest place on Earth, characterized by rainfall of 0.1 mm per decade and large daily temperature variations between 5° C and 30° C (Weischet, 1975). However, the high humidity at the coast provided by the proximity of the Pacific Ocean contrasts with the extreme aridity of the desert itself (Cereceda et al., 1991, 2000). Like other deserts, the Atacama Desert lies on the west face of the continent and owes its extreme aridity to three main processes (Weischet, 1975): (1) downward vertical air masses leading to subsidence motions caused by the Hadley cell, (2) cold-water upwelling led by the Humboldt current, and (3) the steep topography of both the Andes and the coastal mountain ranges, which prevent the humidity from being transported from the Amazon and the Pacific Ocean. Above the ocean, the first two processes also enhance the formation of a Sc cloud deck that covers a large portion of the Subtropical Southeast Pacific (SSEP) around 14° - 30° S (Cereceda et al., 1999). These clouds are transported by the wind until they collide with the steep topography of the mountain ranges (Fig. 5.1). The coast of the Atacama Desert is characterized by high humidity and low thermal oscillations (Cereceda et al., 2008a). Due to the humidity input from the Pacific Ocean, fog persists between 650 m and 1200 m above sea level (asl) (Cereceda et al., 2002).

The coastal region of the desert lies between 18.5° and 23.5° S, around 70° W and within 20 km of the shore (Fig. 5.2). The fog has been largely studied in terms of climate, ecosystems, and water production. del Río et al. (2018), describe the interannual fog variability and its relationship with macroclimatic phenomena. The spatial and temporal distribution of Sc clouds (Osses et al., 2005; Farías et al., 2005; Cereceda et al., 2008a) and the relict vegetation in the so-called fog oases (Cereceda et al., 1991, 2000; Muñoz-Schick et al., 2001) has also been widely described. Regarding the potential freshwater uses, by using standard fog collectors (Schemenauer & Cereceda, 1994a) researchers have measured annual means of fog collected between 1.1 and 7 L m^{-2} collector per day in the range of 850 m and 1,100 m asl (Cereceda et al., 2008a). However, the quantity

and quality of their observations were limited (Cereceda et al., 2008b), mainly due to the lack of meteorological stations and the low frequency of the measurements. For this reason, we still lack an in-depth understanding of the processes that control fog formation, maintenance and dissipation (Cereceda et al., 2008b), particularly with respect to the physical characterization and quantification of the fog and its relation with the marine Sc cloud. Here, we take a fresh look at the fog phenomenon, from a physical and meteorological perspective. By combining surface observations collected at three different meteorological stations in a transect and regional modeling results, we aim to answer the question: what is the physical influence of the marine Sc cloud in the formation, maintenance and dissipation of the land-fog in the Atacama Desert?

The combination of different sources of surface observations with regional modeling results aims for first time to compensate for the lack of high-quality measurements. The surface observations, which included meteorological stations, satellite images and fog collection measurements, were analysed together with the WRF model. This combination of sources enabled us to characterize the vertical and horizontal scales of the marine Sc cloud and its influence on the land-fog system (MS-LF) in their seasonal and diurnal variability.

5.2 Key physical processes under study

The fog in the Atacama Desert is a complex system of interactions between atmosphere and land that range from local to synoptic length scales. The marine Sc cloud deck formed at SSEP covers length scales of 1,000 km from 14° to 30°S. However, the fog produced by the Sc cloud at land just occurs on a length scale of 10 km or less. Our view of the processes of the MS-LF in the Atacama Desert is sketched in Figure 5.1.

The marine Sc cloud deck is a synoptic phenomenon formed as a result of the interaction of two main fluxes over the ocean; surface heat fluxes and subsidence. The left side of Figure 1 depicts the synoptic scale processes. The upward heat and moisture fluxes move from the ocean surface to the top of the atmospheric boundary layer (ABL), where they mix well, condense and form clouds (Bretherton & Park, 2009). This wet and well-mixed air parcel is blocked by the inversion capping caused by the downward flux of dry air (Weischet, 1975), which in turn is due to the subsidence that the Hadley cell produces in subtropical latitudes (Chang, 1995). Here, as a result of the instability created by the longwave radiative cooling at the cloud top, dry air entrains into the cloud layer, producing an exchange between the ABL and the free troposphere (Duynkerke et al., 1995). The Sc cloud deck is transported by the horizontal wind from the south-southwest (S-SW) towards the coastal mountain range of the Atacama Desert. This phenomenon takes place mainly between 18° and 26° S (Cereceda et al., 2000, 2008a).

The horizontal wind transports the Sc cloud deck towards the land where, we hy-

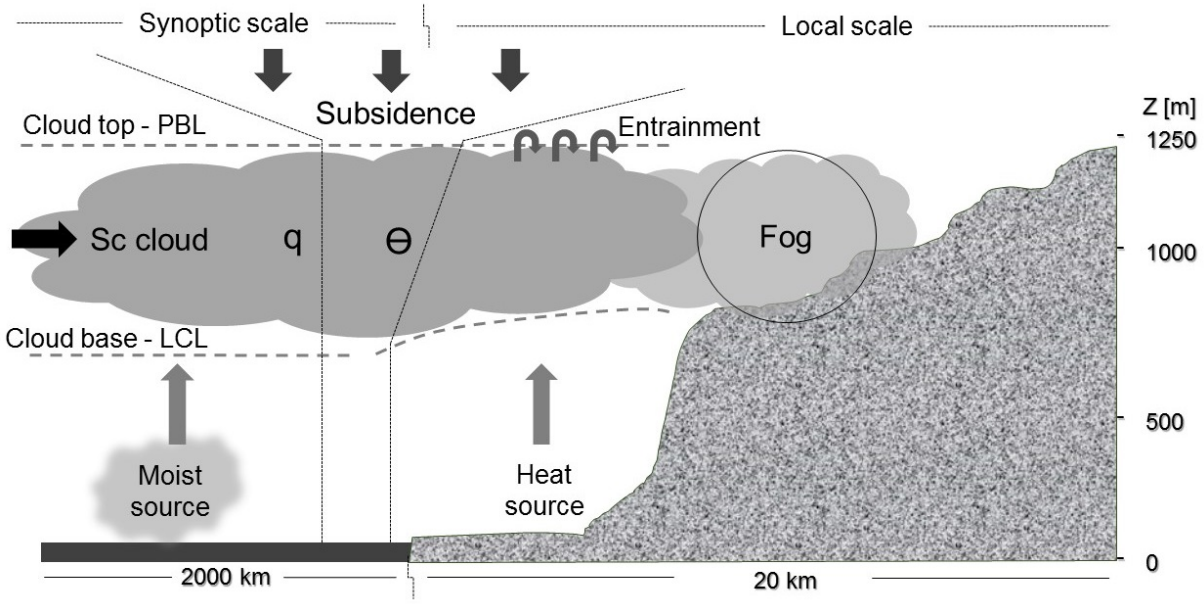

Figure 5.1: Physical processes associated with marine Sc clouds and the land-fog system (MS-LF).

pothesize, it is affected by the buoyancy produced by the land surface heat fluxes that forces the cloud base to rise, leading to the thinning of the cloud deck. We also suggest that the high and steep topography of the coastal Atacama Desert produces an uplifting of the cloud layer, which covers the land until it gradually dissipates inland. These processes occur on a reduced length scale of between 10 km and 50 km. The contact between the Sc cloud deck and the topography is known as fog in the Atacama Desert (Cereceda et al., 2000) (Fig. 5.1). Cereceda et al. (2002), described a general classification for this fog in the Atacama Desert, based on its origin; orographic, advective and radiation fog. This classification is based on its spatial distribution, its effect on the ecosystems and the amount of fog collected. The two first characteristics are formed in the coastal region of the Atacama Desert. The orographic fog is produced by the humid air parcel transported by the wind, which rises due to the presence of the high topography, condensing adiabatically and thus leading to fog formation (Cereceda et al., 2000). The advective fog is produced by the Sc cloud deck above the ocean once it arrives on land (Cereceda et al., 2008a). When it encounters the orography, clouds at ground level are formed, thus the fog (Klemm et al., 2012).

We focus our research on the advective fog, which has been reported by Cereceda et al. (2002) and Cereceda et al. (2008a) as the most frequently observed fog in the research area. We then propose a new classification, based on the stability of the ABL, which takes potential temperature and specific humidity as classification criteria.

5.3 Methods

5.3.1 Surface observations

Surface observations of air temperature, pressure, relative humidity, wind speed and wind direction and fog collection were analyzed to characterize the evolution of the ABL. The observations made at a resolution of one hour were collected from three meteorological stations located at 40 m asl, 1,090 m asl and 1,219 m asl, and fog observations from stations at 1,090 m asl and 1,219 m asl within 20 km of the coast. The fog measurements are taken by a standard fog collector (SFC), which consists of a frame of 1.0 m^{-2} of double polypropylene raschel mesh with a 35% shading coefficient (Schemenauer & Cereceda, 1994a). The units are liters of water per square metre (L m^{-2}), which is equivalent to a depth of water of 1 mm over 1 m^2 of the collector surface. The time unit depends on the data resolution; in our research we use an hourly resolution.

Figure 5.2a shows the contrast between the sea, characterized by a Sc cloud deck, and the land, characterized by a steep topography where fog develops intermittently near the coastline. Figure 5.2b shows the spatial distribution of the meteorological stations and Figure 5.2c a schematic cross-section of their vertical distribution.

The meteorological station located at 40 m asl belongs to the Chilean Civil Aviation Authority (DGAC), at Diego Aracena airport. The stations at 1,090 m asl and 1,219 m asl belong to the Pontifical Catholic University of Chile and Heidelberg University respectively. We focus on the data analysis in 2015, since most of the stations were continuously collecting data starting that year.

Nine representative days of fog events were selected for autumn, winter and spring on the basis of fog collection, seasonality and the quantity and quality of the observations. We calculated the potential temperature (θ) and specific humidity (q), using pressure observed at 40 m asl as a reference. This means that we calculate the changes of a parcel at 1,090 and 1,219 m a.s.l which is forced to descend to 40 m asl (p_0). This enabled us to determine whether the air masses at 40 m have similar characteristics to those of the air masses at 1,090 m and 1,219 m. On the basis of these selection criteria, we determined the difference in the conserved variables between the highest level (1,219 m) and the reference level (40 m). Then, we define the following regimes for the nine cases (days) under study:

$$\frac{\partial \overline{\theta}}{\partial z} \approx \frac{\Delta \overline{\theta}}{\Delta z} \begin{cases} < 3.10 \cdot 10^{-3}\ K\ m^{-1} & Well-mixed \\ > 3.10 \cdot 10^{-3}\ K\ m^{-1} & Stratified \end{cases} \tag{5.1}$$

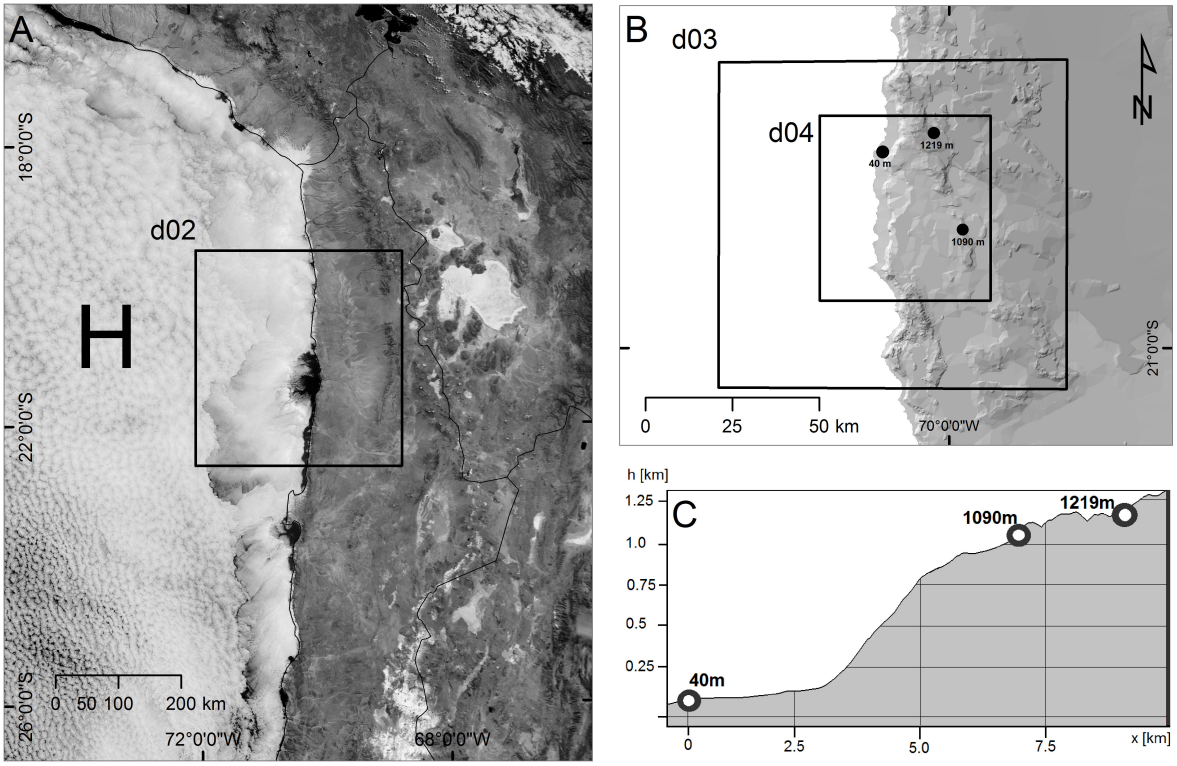

Figure 5.2: Research area; (a) Atacama Desert location MODIS image on July 21^{st}, 2015 and outer WRF model domain. (b) Spatial distribution of surface observations and inner WRF model domains. (c) Schematic cross-section of the vertical distribution of surface observations.

$$\frac{\partial \overline{q}}{\partial z} \approx \frac{\Delta \overline{q}}{\Delta z} \begin{cases} < 1.60 \cdot 10^{-3}\ g\ kg^{-1}\ m^{-1} & Well-mixed \\ > 1.60 \cdot 10^{-3}\ g\ kg^{-1}\ m^{-1} & Stratified \end{cases} \tag{5.2}$$

5.3.2 Cloud characteristics

The cloud characteristics are determined by estimating the cloud base (CB) and the liquid water mixing ratio (q_l) of the cloud by the parcel method, and the cloud top (CT) through a combination of remote-sensing procedures. The cloud characteristics were inferred only for the well-mixed regime days because the θ is conserved until the lifting condensation level (LCL) and q is conserved along the ABL.

To determine the CB, we utilised the parcel method (Wetzel, 1990), which assumes that an air parcel is lifted from the surface without mixing during the ascension following the dry adiabatic until the LCL. The parcel method enables us to infer the vertical profile of ABL in terms of potential temperature (θ), specific humidity (q) and adiabatic water liquid mixing ratio (q_{la}) via surface observations. These thermodynamic variables enable us to calculate the height at which the air condenses (LCL), where specific humidity

equals the saturated specific humidity ($q = q_{sat}$). As Sc clouds form within the ABL, we assume the LCL to be the same as the CB. In our observations surface pressure at 40 m asl is used instead of 1,000 hPa as a pressure reference level for all calculations, employing the parcel method with this reference level for 1,090 m, and 1,219 m. Thus, we did the following: (a) we calculated the changes in an air parcel ascending from 40 m by using θ, p and q of the station at 40 m asl and (b) we calculated the changes in an air parcel ascending from 40 m by using θ and q of the stations at 1,090 and 1,219 m asl

The q_l was estimated by using simple criteria as $q_l = q_s$ - q, if $q_s \geq q$, obtaining a first rough estimate. In order to obtain more realistic values of q_l we developed a simple parameter m to take into account the mixing of air into the parcel method. This parameter is inspired by the method used by Wetzel & Boone (1995). The mixing rate parameter m, which ranges from 0 to 1, represents the amount of air in the environment that is entrained into the parcel along with the rise of the parcel from the surface to the top of the mixed layer. For $m = 0$, there is no air entrained and the parcel conserves its original θ from the surface. For $m = 1$, the air in the parcel is identical to that of the mixed layer when it reaches the top of the mixed layer. We assume that m does not change throughout the mixed layer, so that the contribution of entrained air to the parcel properties for $m \neq 0$ is linear with height. We also assume that the mixing rate is independent of time, height and properties of parcel and environment and is identical for temperature and moisture.

Using these assumptions and the variables presented, the potential temperature and specific humidity of the parcel at a height z read:

$$\theta^p(z) = (1 - m\frac{z}{z_{LCL}})\theta^s + m\frac{z}{z_{LCL}}\theta^{ML} \tag{5.3}$$

$$q^p(z) = (1 - m\frac{z}{z_{LCL}})q^s + m\frac{z}{z_{LCL}}q^{ML} \tag{5.4}$$

The variables representing the state of the parcel are potential temperature θ^p and specific humidity q^p. Additional variables used by the parameterization are the height of the parcel z, the height of the lifting condensation level z_{LCL}, the liquid potential temperature and total specific humidity of the mixed layer θ^{ML}, q^{ML} and at the surface θ^S, q^s, and the (constant) mixing rate parameter m.

Finally, the cloud top (CT) is determined by combining the MODIS cloud cover fraction (CC) and Aster-GDEM digital elevation model. We calculated the mean elevation where the Sc cloud deck collides with the coastal cliffs. We base our calculations on two criteria. The first is that 100% CC needs to overlap a steep slope (>25°), because over flat slopes the cloud can be several metres over the land surface and does not necessarily touch it. The second criterion is that mean elevation must be above 1,219 m because at this altitude we have the highest fog observations. The values of CT obtained correspond

to one measure per day and this study assumes them to be constant throughout the day.

5.3.3 Model setup

The observational analysis is complemented by a numerical experiment performed by the Weather Research and Forecasting Model (WRF) to present the Sc cloud influencing the land. The days selected for the modeling were July 21^{st} and 28^{th}, 2015, which were characterized by well-mixed and stratified conditions, respectively. We used initial boundary-layer conditions of ECMWF for -21/-70 (lat/long) with a time resolution of six hours. Figures 5.2a and 5.2b show the horizontal resolution and domains. Sixty levels are set, including 42 in the first 2000 m. We corrected the sea surface temperature (SST) by +1.5 K in accordance with NOAA observations. The main parameterizations utilized were; for boundary layer physics, the UW boundary layer scheme from CAM5 proposed by Bretherton & Park (2009) and for convection physics the modified Tiedtke scheme proposed by Zhang et al. (2011).

5.4 Atmospheric boundary layer regimes

We identify two regimes, based on the analysis of nine fog events observed in 2015 at MS-FL zone. The first regime characterizes six days under a well-mixed thermal and moist layer. The second regime, describes three days under a stratified thermal and moist layer condition. These regimes are strongly associated with the formation, maintenance and dissipation of Sc cloud-fog.

Table 5.1 summarises the classification and quantification of surface observations for both ABL regimes. It first classifies the regimes according to date and seasonality and then quantifies the stability parameters between the lowest and highest observational stations (40 m - 1,219 m) as the gradient of potential temperature ($\partial\overline{\theta}/\partial z$), the same gradient, but filtering the diurnal variability ($\partial\overline{\theta}/\partial z$ no diurnal) and the gradient of specific humidity ($\partial\overline{q}/\partial z$). Table 5.1 also includes measurements of wind speed and direction measured at 10 m at 40 m asl (ws-40, wd-40), total fog collected (fog_t) and hours of thermal diurnal variability (diurnal-var). Finally, calculations of the cloud base (CB) and cloud top (CT) heights, obtained via the parcel method, are shown.

The well-mixed regime differs from the stratified regime by having low differences in the diurnal $\partial\overline{\theta}/\partial z$ and the non-diurnal $\partial\overline{\theta}/\partial z$ (Table 5.1). For the well-mixed regime, the diurnal variability time of the θ is shorter than 12 hrs (Diurnal-var). Likewise, the ($\partial\overline{q}/\partial z$) in well-mixed regimes is lower than in the stratified regimes, exhibiting peaks below $1 \cdot 10^{-4}$ g kg^{-1} m^{-1}. The mean daily wind comes from S-SW for the nine days analysed, which shows that the marine Sc cloud moves inland under both regimes. They do not display differences in wind speed between regimes, but the wind-speed is higher in

Table 5.1: Surface observations and inferred Sc cloud characterization for the well-mixed (WM) and stratified (ST) regimes. The regimes are described by the dates of the observations (Day); season autumn (A), winter (W) and spring (S); the potential temperature gradient between the highest and lowest stations ($\partial\overline{\theta}/\partial z$); the potential temperature gradient after filtering out the diurnal variation ($\partial\overline{\theta}/\partial z$ no diurnal); the specific humidity gradients between the highest and the lowest stations ($\partial\overline{q}/\partial z$); wind speed and direction measured at 10 m at 40 m asl; total fog collection per day (fog_t); hours of diurnal variability; cloud base (CB) and cloud top (CT).

Day	*Regime*	*Season*	$\partial\overline{\theta}/\partial z$	$\partial\overline{\theta}/\partial z$ $non-diur.$	$\partial\overline{q}/\partial z$	ws 40m	wd 40m	fog_t	*Diur. var*	*CB*	*CT*
			$[K\ m^{-1}]$	$[K\ m^{-1}]$	$[g\ kg^{-1}m^{-1}]$	[m s^{-1}]	[°N]	$[L\ m^{-2}]$	[hrs]	[m]	[m]
18-04-15	WM	A	$3.45 \cdot 10^{-3}$	$2.02 \cdot 10^{-3}$	$1.78 \cdot 10^{-4}$	5.63	211	7.3	9.5	886.3	1,285
29-04-15	WM	A	$5.27 \cdot 10^{-3}$	$3.10 \cdot 10^{-3}$	$4.58 \cdot 10^{-4}$	6.17	166	1.1	12	860.5	1,273
21-07-15	WM	W	$2.36 \cdot 10^{-3}$	$1.84 \cdot 10^{-3}$	$4.41 \cdot 10^{-4}$	6.29	249	13.5	6	784.1	1,366
08-08-15	WM	W	$2.41 \cdot 10^{-3}$	$1.87 \cdot 10^{-3}$	$9.75 \cdot 10^{-4}$	6.83	199	4.1	7	651.5	1,308
17-09-15	WM	W	$3.21 \cdot 10^{-3}$	$1.68 \cdot 10^{-3}$	$7.72 \cdot 10^{-4}$	9.23	202	7.1	10	667.9	1,320
08-10-15	WM	S	$3.22 \cdot 10^{-3}$	$2.18 \cdot 10^{-3}$	$7.89 \cdot 10^{-4}$	9.46	202	6.6	10	593.7	1,292
27-07-15	ST	W	$1.21 \cdot 10^{-2}$	$1.09 \cdot 10^{-2}$	$3.45 \cdot 10^{-3}$	6.79	180	5.6	20	–	–
28-07-15	ST	W	$9.74 \cdot 10^{-3}$	$6.19 \cdot 10^{-3}$	$2.82 \cdot 10^{-3}$	5.29	212	7.4	14	–	–
20-10-15	ST	S	$1.08 \cdot 10^{-2}$	$9.41 \cdot 10^{-3}$	$1.65 \cdot 10^{-3}$	9.25	188	–	20	–	–

spring than in autumn-winter (Table 5.1). The days analysed do not display important differences in the amount of fog collected. Both wind direction and fog collected values are similar to data reported by Cereceda et al. (2008a), for the same seasons (SW winds and 7 L m^{-2} per day). Finally, the CB and CT are shown only for days dominated by a well-mixed regime, presenting a cloud depth average of 566 m.

In order to characterise both regimes in greater depth, we now focus on two representative fog events. Figures 5.3a and 5.3b show the diurnal observations of θ and q at heights 40 m, 1,090 m and 1,219 m, on July 21st, 2015 as a representative example of the well-mixed regime. Likewise, Figures 5.4a and 5.4b show the same diurnal observations, but for a typical stratified regime on July 28th, 2015.

5.4.1 Well-mixed regime

The well-mixed regime is characterized mainly by low gradients of potential temperature and moisture within the ABL (Fig. 5.3a and 5.3b). The daily evolution of θ shows a collapse of the three curves of the observational stations during the night-morning and evening, 0:00 to 12:00 and 18:00 to 00:00 local time (LT). The θ between the lowest and highest station differs by less than 2 K (daily gradient between $1.84 \cdot 10^{-3}$ and $2.36 \cdot 10^{-3}$ K m^{-1}; Table 5.1). Under these conditions, we assume that conserved variables are independent of height, following the well-mixed conditions of the marine Sc cloud. The well-mixed properties are only interrupted by the diurnal variability of inland measurements (1,090 m and 1,219 m) between 12:00 and 18:00 LT.

The q evidences almost no diurnal variation for the three stations (Fig. 5.3b). It also shows a small daily mean difference in moisture of 0.52 g kg^{-1} in the whole ABL height (moisture gradient of $4.41 \cdot 10^{-4}$ g kg^{-1} m^{-1}, table 5.1). The specific humidity is not affected by diurnal variability according to our criteria, which shows that a mixing of the entire ABL takes place throughout the day. The fog was observed in the afternoon, evening and night on July 21st, 2015, including peaks above 2 L m^{-2} and a total amount of 13.4 L m^{-2}. Collected fog-water on the six days classified as well-mixed regimes were similar to those reported by Cereceda et al. (2008a) (annual means of 7 L m^{-2} per day). Fog collection was always observed when the ABL is well-mixed in θ and q, for example, before 12:00 and after 18:00 LT in Figure 5.3a. Related to the regimes described, daily mean wind direction is S-SW of 249 °N, which shows the horizontal transport of oceanic air masses inland (Fig. 5.2a and Fig. 5.10). Wind-speeds ranged around 6 m s^{-1} and were mostly stable under this regime.

Marine air masses thus influence the land fog system under well-mixed conditions. This influence is clear in the observations made close to the ocean at 40 m asl, which has a lower diurnal variation than observations made inland, for example at 1,090 m and 1,219 m (Fig. 5.3a and 5.3b). This has two main reasons. First, observations were made in a transition zone (MS-LF), which lies between the marine boundary layer (MBL), which is characterized by the Sc cloud presence, and the continental boundary layer (CBL), characterized by arid conditions. Secondly, as Sc cloud drives under well-mixed conditions above the ocean (Duynkerke et al., 1995), we relate well-mixed regimes to the advective fog phenomenon reported by Cereceda et al. (2002). However, our findings also demonstrate that well-mixed regimes are related to orographic fog (Cereceda et al., 2002). The latter is due to the collapse of the curves shown in Figures 5.3a and 5.3b, which suggests lifting of the same air parcel as it faced a steep slope. In this case, the air parcel contains the same θ and q at three levels. These findings are further corroborated by the Sc cloud characterization and the WRF numerical experiment.

5.4.2 Stratified regime

Unlike well-mixed regimes, the stratified regime is characterized by large gradients in potential temperature and moisture. As Figure 5.4a shows, $\partial\overline{\theta}/\partial z$ reaches $9.74 \cdot 10^{-3}$ K m^{-1} (Table 5.1) around midday. This means a difference in 11.5 K between the lowest and highest observational station. In common with most marine places, the station at 40 m asl does not show a diurnal variation, but the stations at 1,090 m and 1,219 m display a large diurnal variability reaching the highest θ of 310 K around midday.

This regime also exhibits large differences in moisture within the ABL (Fig. 5.4b). The station at 40 m shows the highest q of around 9 g kg^{-1} from 00:00 to 11:00 LT, while the stations at 1,090 m and 1,219 m q decrease at a rate of $4.2 \cdot 10^{-3}$ g kg^{-1} m^{-1}. However, from midday (12:00 LT) onwards, q is similar at all three observational stations.

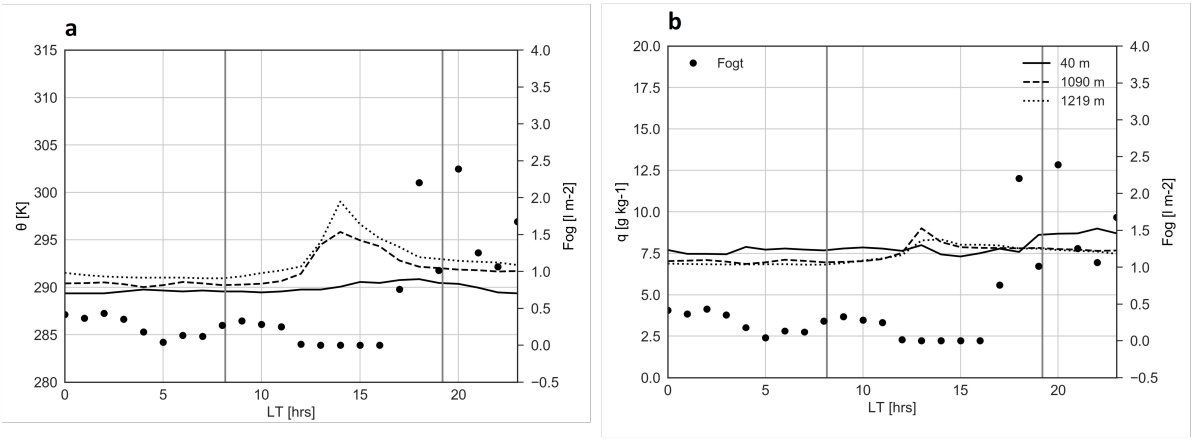

Figure 5.3: Hourly average for (a) θ and (b) q for the well-mixed day of July 21^{st}, 2015. Values represented for stations located at 40 m (solid line), 1,090 m (dashed line), and 1,219 m (dotted line). The sum of fog collected at these three levels (fog_t) is represented by black dots. Sunrise and sunset are shown by grey vertical lines.

Fog collection is observed mainly during the night and evening (00:00 to 09:00 LT and from 20:00 LT). These diurnal measurements are similar to the fog collected under days dominated by well-mixed regime, but with lower peaks. The wind direction blows from SW (212 °N), which shows irrespective of the regime involved, oceanic air masses are transported inland (Fig. 5.10). Wind-speed increases under stratified regimes from 6 to 10 m s^{-1}.

The stratified conditions are explained by the CBL's stronger control of the MS-LF. On the one hand, the measurements at 40 m reveal typical marine conditions that vary only slightly, while those made at 1,090 m and 1,219 m, which additionally lie 20 km inland, display greater variations in θ and q at night and morning. This large variation is evidence of a typical nocturnal stable layer (Stull, 1988), which is stratified in both temperature and moisture. The latter process is enhanced by the radiative cooling that takes place at night, due to the increases in subsidence and katabatic winds (Fig. 5.10a). Thus, typical desert conditions (CBL) influence the MS-LF more than the MBL does during the night, which explains the stratification and dissipation of clouds and fog.

Even during a day dominated by stratified conditions, which dissipates clouds, fog could still be observed at night between 00:00 and 06:00 LT (Fig. 5.4). We have two hypotheses to explain this: the first is that when fog forms at high levels (1,090 m and 1,219 m), there are small differences in θ and q around 06:00 LT. However, they still present large differences with respect to the lowest level (40 m) (Fig. 5.4a and 5.4b). This means that only the highest layer of the ABL is well-mixed. We hypothesise that under these conditions, a thin cloud is advected by the wind inland (Cereceda et al., 2002), but it is decoupled from the bottom of the ABL. Our second hypothesis is that the residual turbulence of the previous day enhances mixing during the night at the top of the ABL.

Thus, after the convection mixes the ABL, a residual layer might have continued to be turbulent at night (Stull, 1988). This could keep the ABL well-mixed and enhance Sc cloud formation at MS-LF, leading to fog on land.

To summarise: on the one hand, the well-mixed conditions are closely related to the advection of marine Sc clouds over the land, which leads to the formation and maintenance of fog over the land. On the other hand, under stratified conditions, Sc clouds and fog dissipate. Even though the regimes suggested characterize an entire day, both regimes might occur in the course of a day. For example, we observe a stratified regime around 15:00 LT on July 21^{st}, 2015 day that is dominated by a well-mixed regime. Likewise, we observe a well-mixed regime after 20:00 LT on July 28^{th}, 2015 day that is dominated by a stratified. The regimes are further studied in the following sections by means of the parcel method of analysis and the WRF numerical experiments.

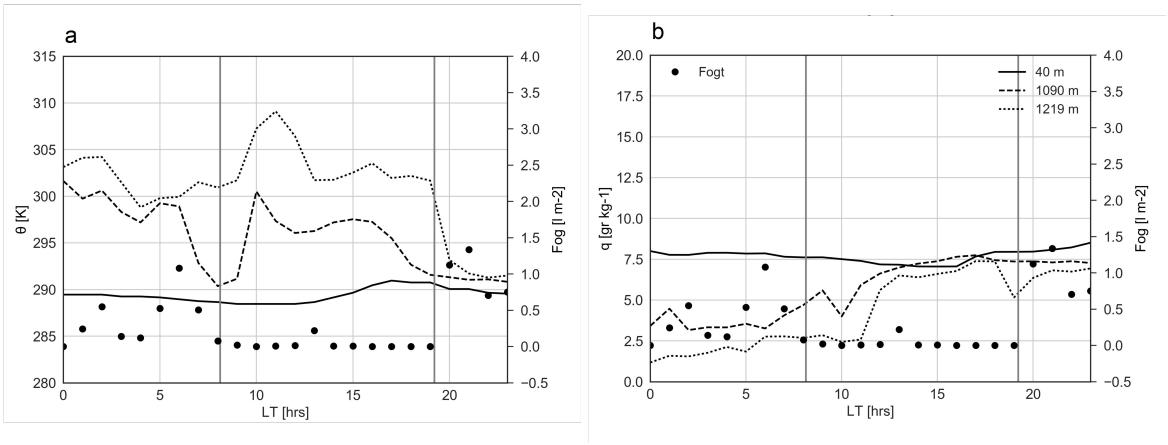

Figure 5.4: Hourly average for (a) θ and (b) q for the stratified day July 28^{st}, 2015. Values for stations placed at 40 m (solid line), 1,090 m (dashed line), and 1,219 m (dotted line). Sunrise and sunset are shown by grey vertical lines. The sum of fog collected at these three levels (fog_t) is represented by black dots. Sunrise and sunset are shown by grey vertical lines.

5.5 MS-LF physical characterization

This section describes the cloud characteristics of well-mixed regimes in terms of cloud base (CB), cloud top (CT) and liquid water mixing ratio (q_l). We used surface observations made at the steep slope to validate the parcel method. These found no significant differences between the two approaches ($p \leq 0.05$). The following sections describe our findings regarding MS-LF characteristics, by means of an analysis of our surface observations.

5.5.1 Sc cloud-fog depth characteristics

Six days with a well-mixed regime in autumn, winter and spring were analysed (Table 5.1). Figure 5.5a shows a six-day-averaged CB of 740 m with a variability of 150 m, a CT of 1307 with a variability of 30 m and a mean cloud depth of around 566 m, above the observation station at 40 m asl Figure 5.5a reveals a diurnal variability during the day, which affects the cloud depth. The Sc cloud is stable at night until 10:00 LT, when surface heat flux increase. This produces a reduction in cloud depth until 20:00 LT, when the CB lowers again, increasing the cloud depth.

The variability in cloud depth is partly explained by the interplay between the following processes. First, during the day, surface sensible and latent heat fluxes become dominant. Large values of the sensible heat flux combined with orographic effects lead to uplifting of the CB. This explains the diurnal variability in the CB, where heat surface fluxes are higher over the inland stations than stations close to the ocean. Furthermore, above the CT, the long wave radiative cooling lead to cloud top turbulence that entrains warm and dry air. This yields to thin the Sc cloud layer (Duynkerke et al., 1995). Unfortunately, these patterns are not identifiable from our observational data, but they are analysed via a modeling approach at the end of this section and in section six of this chapter. Secondly, the subsidence is the process related to the limited variability in the CT ($\pm$ 30 m). Although the Pacific Anticyclone located over the research area during the summer moves NW during the winter, it is always mainly located over the SSEP, which means that small changes in seasonal subsidence produce small changes in CT.

To complete the analysis and describe the relationship between Sc and our cloud-fog observations in greater depth, we describe the diurnal variability of a marine Sc cloud under well-mixed conditions. Three CB values have been estimated from the observation stations located at 40 m asl (solid line), 1,090 m asl (dashed line), and 1,219 m asl (dotted line) (Figure 5.5b). We set the reference pressure at 40 m asl Figure 5.5b shows the diurnal variability in the cloud characteristics on July 21^{st}, 2015. Our findings provide evidence that Sc cloud is always deeper close to the ocean than further inland. We observe this throughout the day, where the cloud layer estimated over station at 40 m asl is at least hundred metres thicker than the cloud estimated at 1,090 m and 1,219 m. Two processes explain this spatial distribution. First, the surface heat fluxes, which produce a thinning of the marine Sc cloud when it arrives into the land. The second process is the uplifting motion of the Sc cloud when it reaches the mountains, as topography forces the cloud to rise. Our CT estimations based on the surface observations are restricted to determine which process governs this pattern. However, the modeling results shown in Figure 5.6 enable us to observe reductions in the cloud depth from the ocean (solid line) to the land (solid colour), which we interpret as a thinning.

Figure 5.5b shows that the altitude at which fog is observed coincides with the cloud layer inferred by observations. For example, fog observed at 1,219 m asl (dots) lies within

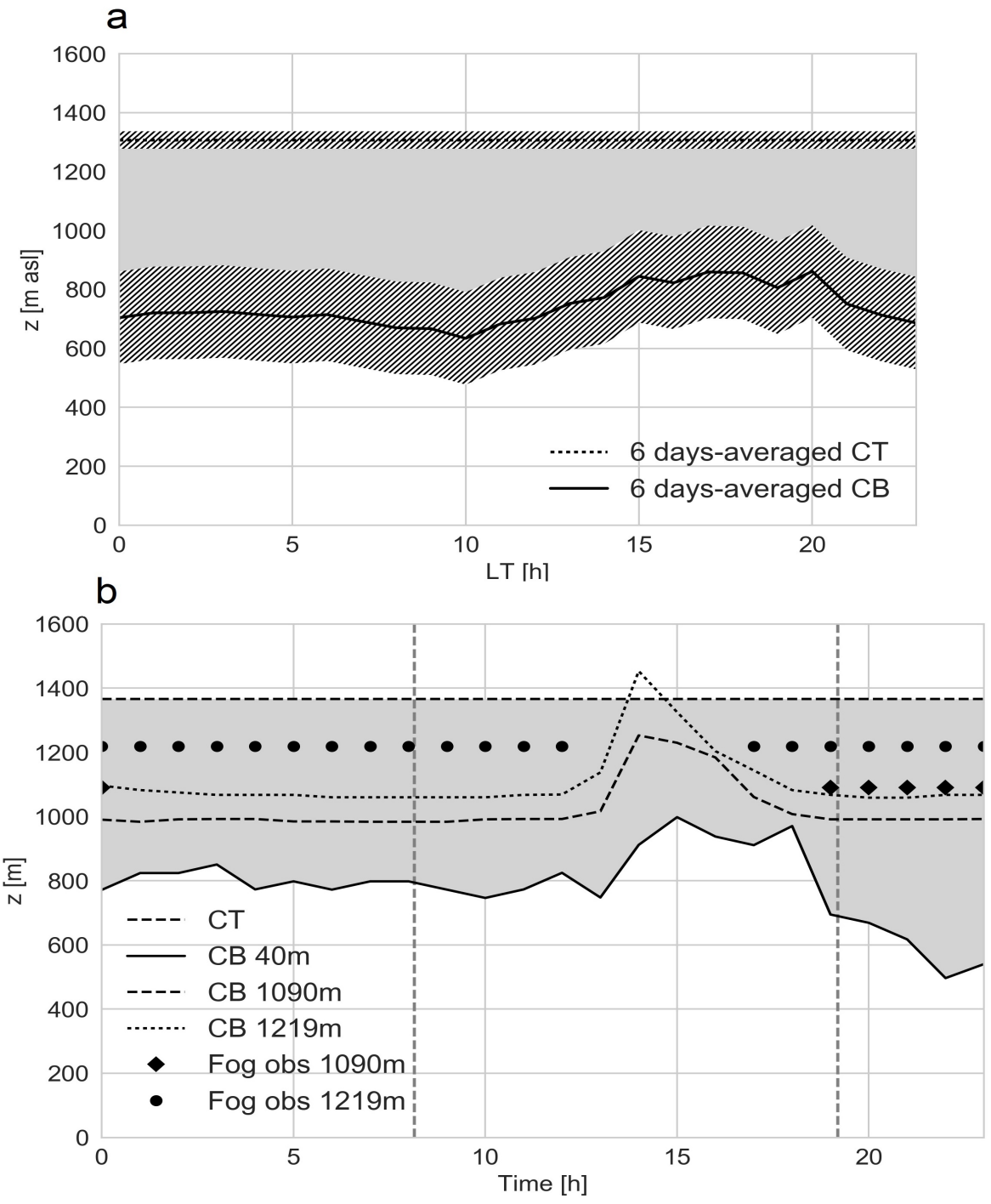

Figure 5.5: Six-day averaged cloud depth, calculated from the reference station (40 m) for 2015. (b) Diurnal variability of cloud depth over surface observations at 40 m, 1,090 m and 1,219 m, calculated from the reference station (40 m) for July 21^{st}, 2015. Fog observation altitude is represented by dots and diamonds.

the estimated cloud layer from 1,219 m asl (between the dotted line and the dashed line of CT). The latter can be interpreted as a validation of our calculations of cloud depth because the fog observations are located inside the cloud layer estimated by surface observations. During the night and early morning (00:00 - 10:00 LT), the Sc cloud depth remains constant and fog is only observed at the highest level (1,219 m). This is closely coupled with well-mixed regimes and marine advection. On the other hand, at midday (12:00 to 18:00 LT) the cloud depth diminishes above the 40 m and 1,090 m stations, and at the 1,219 m station. The CB reaches the CT, resulting in dissipation of clouds. This coincides with no fog observed at 15:00 LT either, where we find a stratification of θ, and therefore a stratified regime (Fig. 5.3, 15:00 LT). Finally, at night (from 22:00 LT), the cloud layer grows because the heating from surface stops and fog is observed at the 1,090 m and 1,219 m stations, both of which were inside their estimated cloud layers (Fig. 5.5b).

To test the reability of our estimates of the Sc cloud characteristics retrieved from surface observation, we led the same situation using WRF. Figure 5.6 shows the cloud layer modeled above two points on the study area. The first is over the sea approximately 50 km from the shore (Marine Sc layer). The second one is at the site of the 40 m station (Land Sc layer). The Sc cloud layer inferred from surface observations is shown as well (dotted line).

The estimated CB agrees well with the one modeled by WRF. The modeled cloud over the land shows differences in CB of around 78 m in the night-morning (00:00 to 10:00 LT) period, with daily means of 140 m. Likewise, modeled cloud over the sea shows differences around 46 m and 70 m in the night-morning phase and daily means, respectively. The CB lies at 800 m in the morning and rises during the afternoon to around 900 m, but it diminishes differently from evening to night. The diurnal CT variability reaches its lowest level during the night and rises again during the morning, stabilising during the day and increasing again in the evening. It ranges from 900 to 1,200 m, being several metres lower than the CT estimated from remote-sensing observations.

The model shows broken clouds over the land at midday and afternoon (10:00 -16:00 LT), which coincide with the intermittent fog collection observed (Fig. 5.5b). Furthermore, over the sea the Sc cloud continues to thin from its CB and CT at midday and during the afternoon. The model confirms the diurnal thinning and break of the cloud layer over both land and sea (Figures 5.3, 5.4 and 5.5b). On the one hand, we observe the presence of the well-mixed regime during the night-morning phase and the change to a stratified regime from 11:00 LT to 16:00 LT. On the other hand, we confirm the thinning process of the Sc clouds as they move from sea to land (Fig. 5.5b). Figure 5.6 always shows a thinner cloud over the land (solid colour) than over the sea (solid line). Cereceda et al. (2008a) also observed a CB and CT between 700 m and 1,200 m, but also broken clouds in the MS-LF zone in July 2002.

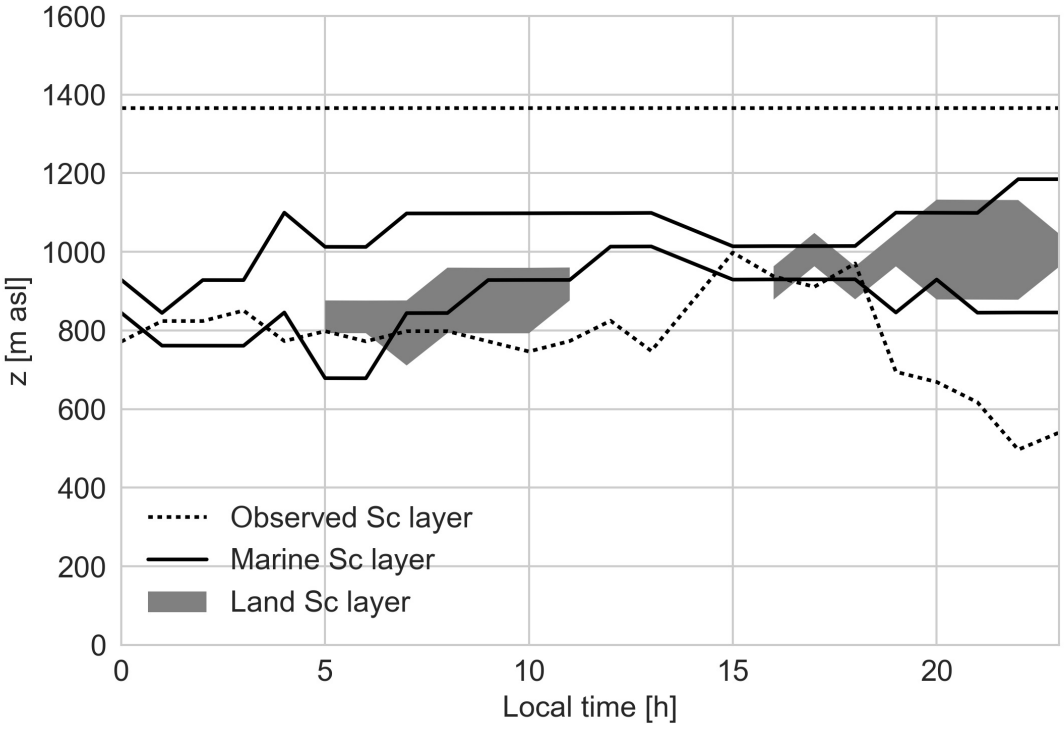

Figure 5.6: Sc cloud layer modeled above a marine (solid line) and land (solid colour) WRF grid point, on July 21^{st}, 2015. The inferred Sc cloud layer is also shown (dotted line).

In summary, the diurnal variability of the marine Sc cloud is produced by a complex set of interactions between the MBL and CBL, understood as the interaction of marine Sc clouds with topography (MS-LF). The upward and downward heat fluxes lead these variabilities, resulting in changes in the cloud depth, liquid water mixing ratio (q_l) and consequently in fog observed.

5.5.2 Cloud liquid water mixing ratio q_l

In order to complete the characterization of the Sc cloud layer, we quantified the liquid water mixing ratio of cloud and fog. Figure 5.7 shows the vertical profile of adiabatic liquid water mixing ratio (q_{la}), liquid water mixing ratio mixed with the environment (q_{lm}) and the liquid water mixing ratio obtained by WRF (q_{lw}), for different times on July 21^{st}, 2015. The q_{la}, is inferred by the parcel method without taking into account mixing with the environment during the uplifting. Thus, the q_l follows the wet adiabatic inside the cloud. The q_{lm} is converted from q_{la} by using a correction factor $m = 1$, which considers a maximum mixing with the environment during the uplifting process. Fog observations are also depicted as heights.

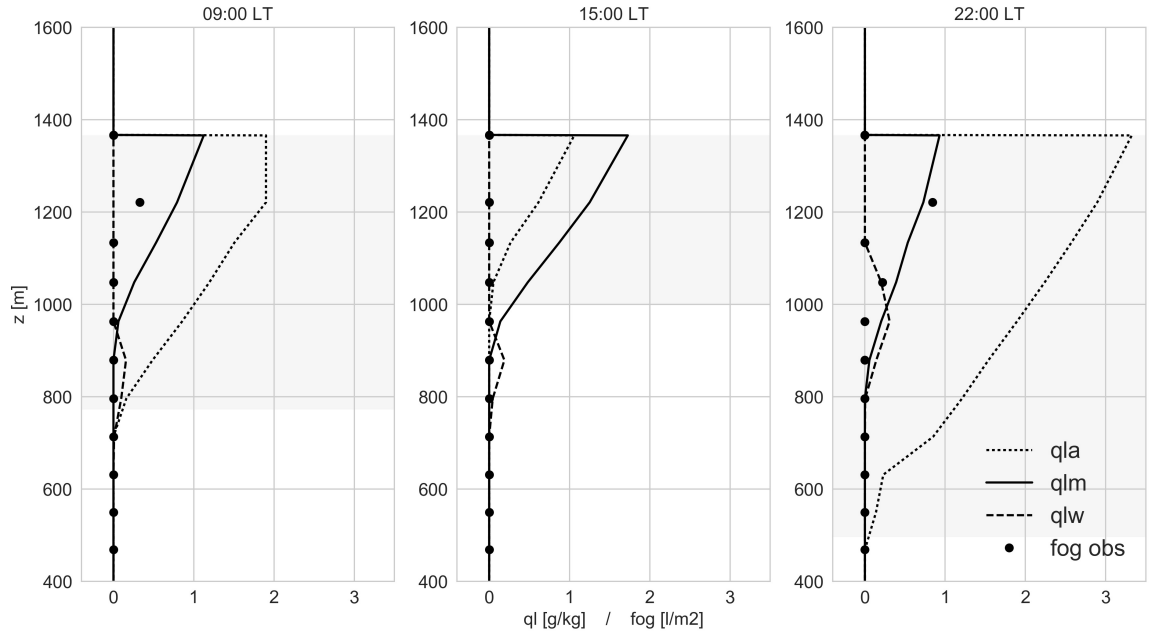

Figure 5.7: Vertical profile of adiabatic liquid water mixing ratio (q_{la}), liquid water mixing ratio considering mixing with environment (q_{lm}) and liquid water mixing ratio given by WRF (q_{lw}). For morning, afternoon and night at July 21^{st}, 2015. Fog is shown by dots and cloud layer is shown as solid color.

In the morning at around 09:00 LT, q_{lw} and q_{la} coincide in the CB, presenting LCLs at 792 m and 772 m, respectively. However, q_{lm} sets the LCL at 935 m, due to the dry air that the mixed layer incorporates into the air parcel during the rise. The morning values of q_{lw} are around 0.3 g kg^{-1}. For q_{lm} the amount of water reaches 1 g kg^{-1} at the estimated CT. The q_{la} is clearly overestimated because it does not consider the mixing during the lifting. The values reported by (Duynkerke et al., 1995) are around 0.3 - 0.5 g kg^{-1}. Therefore, q_{lw} agrees better than q_{lm} and q_{la}. Finally, the amount of fog collected in L m^{-2} has the same distribution at different altitudes as q_{lm}. For example, inside the cloud layer, we observe an increase of q_l with height, and more fog is observed at the highest station (1,219 m).

At 15:00 LT, on the one hand, the model estimates very low values of q_l (< 0.3 g kg^{-1}), which agrees with our observations of the amount of fog (0 L m^{-2}). This drop in liquid water mixing ratio coincides with the observed breaks in the Sc cloud and the dissipation of the fog, related to the stratified regimes which are shown in Figures 5.3, 5.5b and 5.6. On the other hand, both q_{lm} and q_{la} show values over 1 g kg^{-1} or even almost 2 g kg^{-1}. Here, q_{lm} is much higher than q_{la}, which can be explained in terms of two processes. First, the mixed layer is more humid than the surface layer (Figure 5.3b). Then, during the rising of the air parcel, q increases with height. The second process is an uplifting of well-mixed parcel air, driven by the topography, where the same parcel

is forced to rise by the topography while maintaining the same cloud water conditions. However, under stratified conditions, such as those shown at 15:00 LT (Fig. 5.7), the parcel method gives unrealistic estimates. Therefore, we maintain our analysis of the simulated values of q_{lw}.

Finally, at 22:00 LT, q_{lw} and q_{lm} increase similarly, setting the LCLs at 878 m and 849 m, respectively. Both q_{lw} and q_{lm} coincide in the core of the cloud at around 950 m. At the same time, fog also increases with height from 0.3 L m^{-2} to 1 L m^{-2}. The amounts of water mixing ratio are around 0.4 g kg^{-1} in the model and 0.7 g kg^{-1} in q_{lm}. We observed a reduction in q_{lw} from 1130 m, but not in q_{lm}. This is explained by the fact that the WRF model includes dry entrainment from the free troposphere, while q_{lm} does not. These increases in water mixing ratio and fog coincide with the presence of a well-mixed regime (Fig. 5.3).

In conclusion, the mean values of q_{lw} and q_{lm} agree with the amounts of liquid water mixing ratio reported by Duynkerke et al. (1995), Stevens et al. (2003), Garreaud & Muñoz (2004) and Hogan et al. (2005), in their works on marine Sc clouds. From Figure 5.7 we conclude fog collection is closely related to threshold values of q_l that Sc cloud and therefore fog contain. This is because their values increase in similar patterns than q_{lw} does. However, the values of q_l must be higher than 0.3 g kg^{-1} to be observed by the collectors. Finally, the use of the mixing factor $m = 1$ suggests a more realistic liquid water mixing ratio of Sc cloud and fog. However, other processes such as air entrainment from the free troposphere and microphysics of cloud also need to be considered.

5.6 Vertical and horizontal Sc cloud-fog variability

To support our analysis, we simulated the vertical MS-LF variability and its spatial distribution by means of a numerical experiment in WRF. The experiment reveals a complex interplay between the marine Sc cloud and local factors such as topography, local circulation, and synoptic conditions. These interactions enhance the mixing of the ABL by local land-sea circulation and marine Sc cloud advection, which explains the formation and maintenance of fog. The same set of interactions also produces the thermal stratification that dissipates the fog.

5.6.1 Vertical Sc cloud-fog variability

Figure 5.8 shows a West-East cross-section of the Atacama Desert coastal zone, depicting the liquid water mixing ratio q_{lw}, potential temperature and specific humidity at 09:00, 15:00 and 22:00 LT on July 21st, 2015 (well-mixed case). The surface observations are placed above the topography and the figure also includes a diurnal distribution of fog observations (Fig. 5.8d). The experiment models a MBL developed from the ocean surface

to 900-1250 m asl This has a well-defined structure of well-mixed θ and q conditions that reveal the presence of the turbulence that drives Sc cloud formation. The MBL is blocked by topography, which acts as a barrier that prevents marine conditions from having a significant influence farther inland. This influence reaches only as far as 20 km inland and 1250 m height (Fig. 5.1).

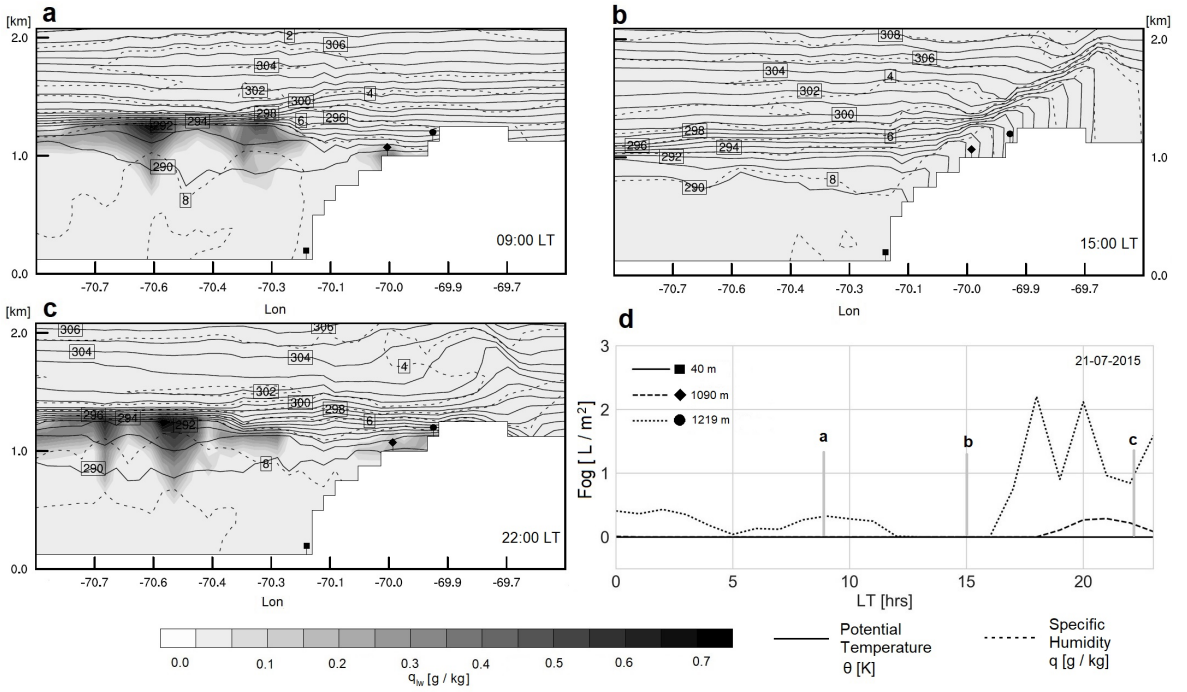

Figure 5.8: (a), (b) and (c), Cross-section of liquid water mixing ratio, q_{lw} (grey scale), potential temperature θ (solid line) and specific humidity q (dashed line) by WRF on July 21^{st}, 2015. The observation stations are shown over the digital elevation model. (d), fog observations on July 21^{st}, 2015 at different altitudes.

At 09:00 LT (Fig. 5.8a), the experiment shows the formation of a thin layer of q_{lw}, which represents the marine Sc cloud. This spans a range of altitudes from 850-900 m to around 1200 m. The values of q_{lw} are within the range of 0.2 to 0.5 g kg^{-1}, with maximum collections of about 0.7 g kg^{-1}. As figure 5.7 shows, q_{lw}, possesses a vertical structure that increases with altitude and has its highest values of q_{lw}, close to the top of the boundary layer. The experiment shows vertical moisture fluxes ($2 \cdot 10^{-3}$ g kg^{-1} m^{-1}), lifting from the ocean to the cloud at longitude -70.6 as Figure 5.8a shows. The marine Sc cloud tends to break down before colliding with the topography, sinking slightly just before arriving on land due to katabatic winds. This breakdown is accompanied by a drop in specific humidity and an increase in θ stratification, due by dry air entraining from the free troposphere at approximately -70.1 longitude and an altitude of 800 m. Here, at the top of the Sc, shortwave radiation partially offsets the longwave radiative cooling. This process, as well as the entrainment of dry air, contributes to thinning and dissipating the Sc cloud. However, the surface fluxes compensate for and maintain the cloud as shown by

the well-mixed condition of θ and q shown in observations Figs. 5.3a and 5.8b (09:00 LT), but also in the simulation illustrated in Fig. 5.8a. Fog observations on land show amounts of only around 0.3 L m^{-2} collected at 1,219 m (black circle). However, the simulation does not show clouds forming at that height in the morning, instead placing them several metres below. During the morning we find a clearly well-mixed ABL (θ and q), which coincides with the regime illustrated in Figure 5.3. The value of θ measured at 09:00 by the stations located at 1,090 m and 1,219 m is 292 K, which satisfactorily matches with the values derived by the experiment. The q measured by the land meteorological stations also fits well with the model, with values within the range of 7 - 7.5 g kg^{-1}.

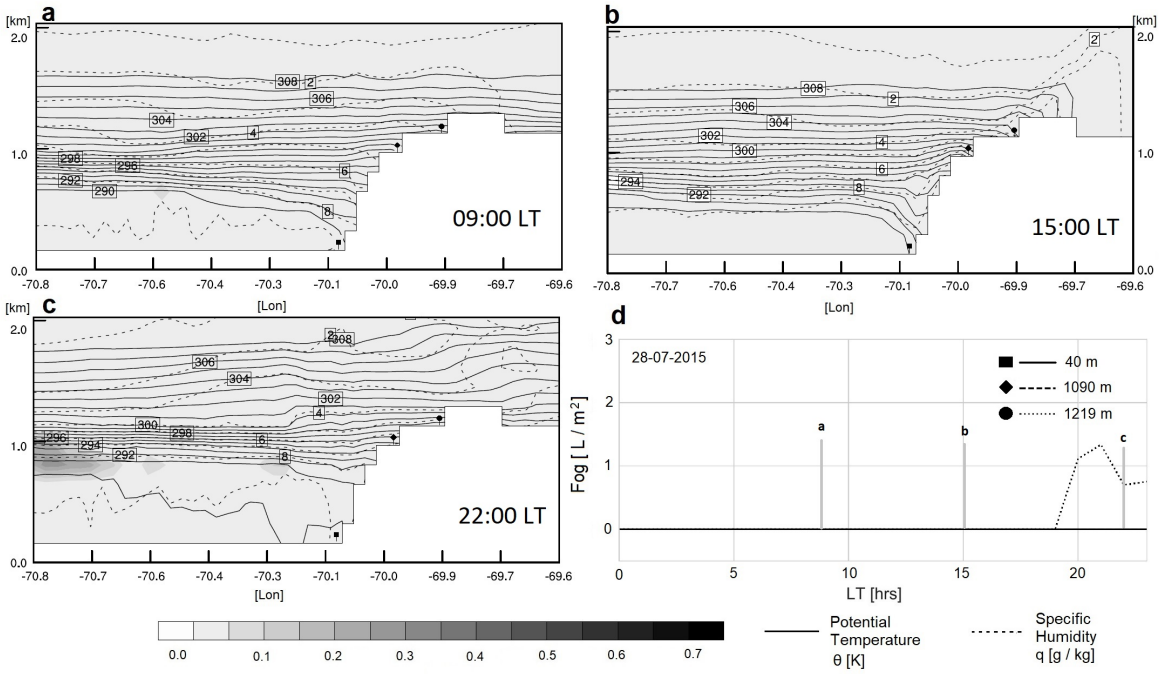

Figure 5.9: (a), (b) and (c), Cross-section of liquid water mixing ratio, q_{lw} (grey scale), potential temperature θ (solid line) and specific humidity q (dashed line) by WRF on July 28^{th}, 2015. The observation stations are shown over the digital elevation model. (d), fog observations on July 28^{th}, 2015 at different altitudes.

During the afternoon, at 15:00 LT (Fig. 5.8b) experiment shows a stratification of θ and q between the altitudes of 800-1200 m, which promotes Sc cloud-fog dissipation. Regarding the latter value, the observations (Fig. 5.3) show a $\partial\overline{\theta}/\partial z$ of about 6 $\cdot 10^{-3}$ K m^{-1} (Table 5.1), which fits well with the experimental observations. The q evidences a strong uplift of humid air at the slope facing the ocean (anabatic winds) that emerges from the better-mixed lower layers of the ABL and the ocean. However, the thermal stratification itself remains at the slope, dissipating the Sc cloud and the fog. During the afternoon, we observe changes in cloud deck, which dissipates because of the rise of dry air entrainment and shortwave radiation at the top of the cloud. These processes enhance the thinning and dissipation of clouds mixing with the dryer air, showing a

vertical stratification of θ. This stratification is present both in the observations shown in Figs. 3a at 15:00 LT, but also in the simulation (Fig. 5.8b). Figure 5.8d does not show any observations of fog at 15:00 LT, which agrees with the experiment.

Finally, at 22:00 LT (Figure 5.8c), the simulation once again reveals the development of a well-mixed ABL, which reaches a height of 1,200 m. We observe the formation of a more robust cloud layer (q_{lw}) at the top of the boundary layer, which is thicker than the cloud layer that formed during the morning, but also with higher values of liquid water (0.5 to 0.7 g kg^{-1}). These values of q_{lw} satisfactorily agree well with the large amounts of fog observed at the top of the boundary layer, which reach values as high as 0.5 to 2.1 L m^{-2}. The cloud formation above the stations contains from 0.2 to 0.4 g kg^{-1} and matches the fog observations (Figure 5.8). Both θ and q show a predominant well-mixed regime that extends to a height of 1,250 m. Likewise, vertical upward fluxes of humid air from the ocean penetrate the cloud layer, providing evidence of the well-mixed process. At night, the breakdown of the cloud also takes place before it arrives at the mountains, but with a weaker downward flux of dry air than in the morning. Finally, the thick marine ABL influence the land above 1,250 m and Eastward of longitude 70 °W.

Figure 5.9 shows the same West-East cross-section of figure 5.8, but for the stratified regime case on July 28th, 2015 (Fig. 5.4). The figure includes the surface observations above the topography and a diurnal distribution of fog observations (Fig. 5.9d). The experiment models a shallow MBL developed from the ocean surface to 700-900 m asl at the night-morning and to 500 m asl during the afternoon. This has a well-defined stratified structure of θ and q, conditions that reveal the presence of a stable layer that drives Sc cloud dissipation. The shallow MBL produces a null influence inland due to the topography and its shallow formation (Fig. 5.9).

In summary, the numerical experiment agrees with our surface observations in terms of θ, q, and the relation q_{lw}-fog, for both well-mixed and stratified cases. Also, the experiment confirms the relationship between the well-mixed regime and Sc cloud-fog formation and maintenance, as well as the stratified regime with Sc cloud-fog dissipation. Our findings also corroborate our initial hypothesis regarding the influence exerted by the MBL over land during fog events (well-mixed dominant regime) and the influence of the CBL over land during fogless events (stratified conditions).

5.6.2 Synoptic conditions of Sc cloud-fog spatial distribution

Figure 5.10 shows the spatial distribution of wind-speed and direction and cloud water mixing ratio of the MS-LF in the WRF experiment on July 21st, 2015 at 09:00, 15:00 and 22:00 LT. The figure shows a horizontal plane of the Atacama coastal desert, with the Pacific Ocean on the West and the continent on the East. The liquid water path, LWP [kg m^{-2}] of the first 150 m from the surface, is represented as fog, but also as a Sc cloud in the range 0-1,500 m (greyscale). We decided to quantify Sc cloud-fog by using

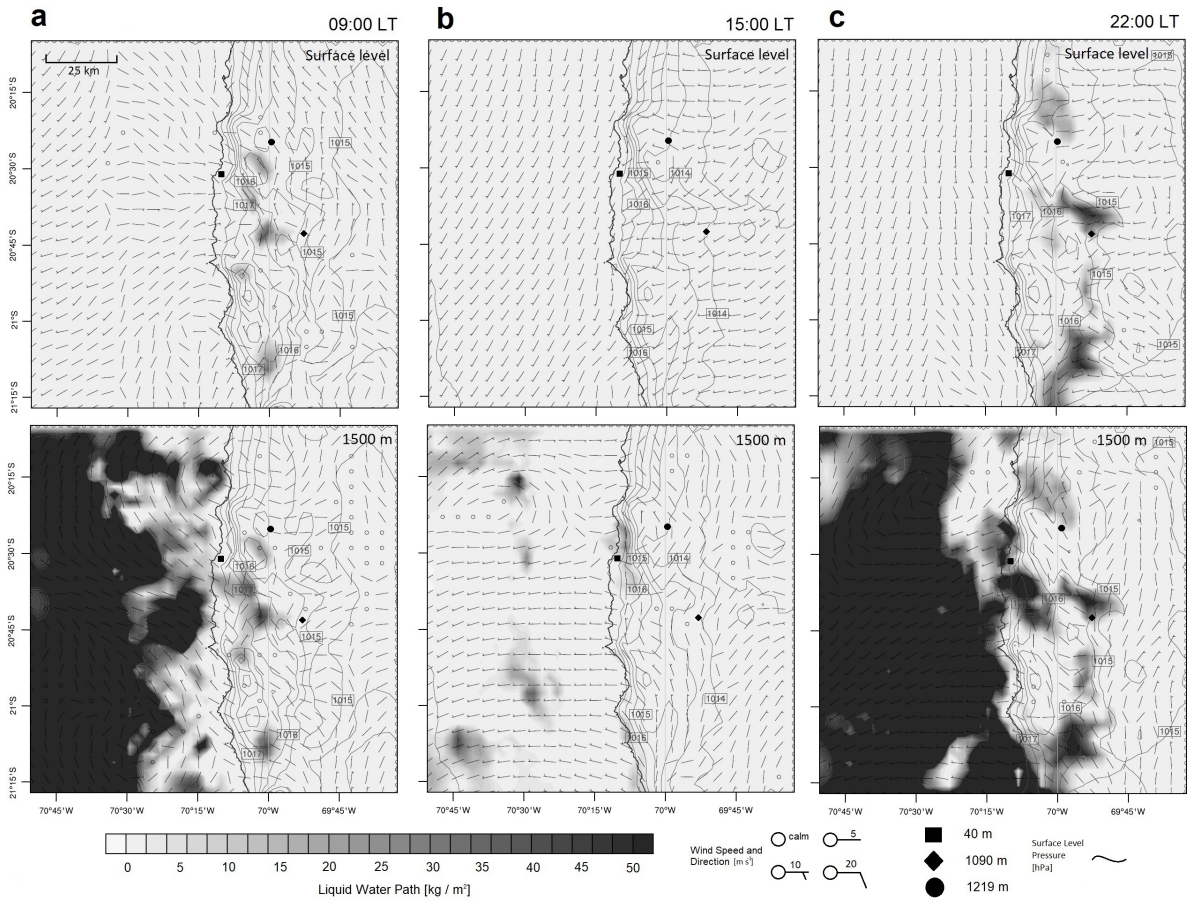

Figure 5.10: Sc cloud-fog, wind speed-direction and surface-level pressure spatial distribution according to the WRF model on July 21st, 2015. Sc cloud-fog water mixing ratio is represented as liquid water path, LWP (grey scale), for the first 150 m and the first 1,500 m. Both variables are plotted at 09:00 LT (a), 15:00 LT (b) and 22:00 LT (c). Meteorological stations are also shown.

the LWP because it includes a sum of a q_l vertical column, expressed as a surface value m^{-2}. The wind speed and direction also represent the regional circulation. Finally, the pressure [hPa] at surface level is shown, for both land and sea.

The topography influences the atmospheric local circulation by acting as a physical barrier to the synoptic winds that blow from S-SW. This is shown in Figure 5.10 as a ridge of surface-level pressure close to the coast. Moreover, due to the diurnal land convection, pressure decrease of about 1 hPa enhances the marine advection into the land.

At about 09:00 LT, katabatic winds from the land to the ocean predominate as they descend the steep slope. At the same time, at 1,500 m synoptic winds blow from the ocean to the land, which advects clouds with LWP above 50 kg m^{-2}. The returned circulation enhances the mixing process, as Figure 5.10a illustrates, and raising the ABL height (Figure 5.8a). As the figure shows, patches of fog form over the land, with values around

10 - 15 kg m^{-2}. However, these values do not match our surface observations (Figure 5.8d), where fog is scarcely observed at 1,219 m (0.3 L m^{-2}). Nevertheless, patches of Sc clouds form at altitudes of 150-1,500 m above the 40 m station, as the estimations retrieved by our observations suggest (Figure 5.5b). We conclude that well-mixed regime in the morning is produced and reinforced by the land-sea local circulation.

During the afternoon, at around 15:00 LT, surface-level pressure drops over land (1,015 to 1,014 hPa), increasing the advection of marine air masses from the S-SW and at speeds of around 10 m s^{-1}. These anabatic winds face the slope and lead to an uplift of moisture, which is transported inland as Figure 5.8b shows, while θ remains stratified. At 1,500 m, winds with similar speeds, but from the west are blocked by the mountain barrier. Thermal stratification and moisture advection can also be seen in our observations (Figure 5.3), where at around 15:00 LT, θ displays larger differences than q. We conclude that this process explains Sc cloud-fog dissipation. In validation of our findings, no patches of fog are shown either by the model at the stations nor in our observations, although some Sc cloud patches were observed over the sea and below 1,500 m.

At night, around 22:00 LT, the surface level pressure rises by around 2 hPa, due to the cooling effect over land and to subsidence (Figure 5.10c), partially inhibiting the inland advection of the marine air masses. Therefore, winds at surface level are deflected from SW to the NW due to topography barrier. The circulation at 1,500 m (843 hPa), is still characterized by SW winds, which pass over the mountain, although their speed drops from 10 to 5 m s^{-1}. The θ and q profiles are well-mixed, due to a combination of effects: (a) local returned circulation, (b) marine Sc cloud advection over land and (c) pressure rise. The mixing produces fog at several places around the mountains, which agree with fog observations (Fig. 5.8d). The model is capable of predicting the presence of fog at stations 1,219 m (black circle) and 1,090 m (black diamond) with values in the range 15 - 40 kg m^{-2}. At 1,500 m, we find a strong advection of marine Sc cloud from SW, with values above 50 kg m^{-2}, which also agrees with observations in which Sc clouds form above all the stations (Fig. 5.5b). The Sc cloud area covered by the numerical experiment agrees with reported Sc cloud satellite observations made by Cereceda et al. (2008a) for July 2002.

In summary, we confirm that fog is produced and maintained under a well-mixed regime, in which local circulation, topography, and subsidence all play key roles. This phenomenon occurs in the morning and evening-night (09:00 and 22:00 LT), when advection of marine Sc air masses facilitates fog formation. During the afternoon (15:00 LT), changes in synoptic conditions and therefore local circulation produce a thermal stratification that dissipates clouds.

5.7 Conclusions

We studied the interaction between marine Sc clouds and land fog by combining surface observations and high-resolution numerical experiments in the Weather Research and Forecasting Model (WRF). Our findings show that this interaction involves either a well-mixed condition or a thermal stratification on the ABL, which forms or dissipates Sc cloud-fog.

The well-mixed regime is characterized by low gradients of potential temperature ($< 3.10 \cdot 10^{-3}$ K m^{-1}) and specific humidity ($< 1.60 \cdot 10^{-3}$ g kg^{-1} m^{-1}). These well-mixed conditions, which are driven mainly by the marine Sc cloud deck, have a small diurnal variability. During the morning hours, the influence of marine Sc cloud advection and the katabatic winds that fall from the slopes enhance the well-mixed condition near the coast. Around midday, increases in surface heat fluxes lead to larger gradients in potential temperature, but enhance the moisture being uplifted through the slope. At night, synoptic winds and Sc cloud advection are blocked by the topography and inversion capping, resulting in a returned local circulation, which reinforces the well-mixed condition. The predominance of the well-mixed regime correlates with fog observations, which are measured in the morning and evening-night.

In contrast, the stratified regime is characterized by high gradients of potential temperature ($> 3.10 \cdot 10^{-3}$ K m^{-1}) and specific humidity ($> 1.60 \cdot 10^{-3}$ g kg^{-1} m^{-1}). This regime is affected by the diurnal variability, which displays the largest changes on diurnal gradients around midday. In the morning of days dominated by stratified regimes, the gradients in the upper levels of the ABL are low often, which produces fog. However, around midday, the surface heat fluxes increase inland, resulting in an uplifting of small amounts of moisture (lower than 0.3 g kg^{-1}), but also a strong stratification of potential temperature (differences until 19 K). The thermal stratification corresponds with fogless observations, produced mainly between 12:00 and 20:00 LT. We can therefore conclude that the stratified regime leads to optimal conditions for the dissipation of Sc cloud-fog.

Our results confirm the usefulness of surface observations analysed by means of a simple parcel method to obtain a first estimate of cloud characteristics such as cloud depth, liquid water mixing ratio and their association with fog over land. Together with the analysis of WRF results, this has enabled us to provide an explanation of the role played by marine Sc cloud in fog formation, and of the land processes involved.

Chapter 6

Optical-Microwave Scintillometer evaporation measurements over a saline lake in a heterogeneous setting in the Atacama Desert

This chapter is based on:

Lobos-Roco, F., Hartogensis, O., Vilà-Guerau de Arellano, J., Aguirre, F., de la Fuente, A., & Suárez, F. (2021b). Optical-microwave scintillometer evaporation measurements over a saline lake in a heterogeneous setting in the Atacama Desert. (Manuscript under revision). *Journal of Hydrometeorology*.

Abstract

Estimating lake evaporation is a challenge due to both practical considerations and theoretical assumptions embedded in indirect methods. For the first time, we evaluated measurements from an optical microwave scintillometer (OMS) system over an open water body under arid conditions. The OMS is a line-of-sight remote sensing technique that can be used to measure the sensible- and latent heat fluxes over horizontal areas with path lengths ranging from 0.5-10 km. We installed an OMS at a saline lake surrounded by a wet-salt crust in the Salar del Huasco, a heterogeneous desert landscape in the Atacama Desert. As a reference, we used Eddy Covariance systems installed over the two main surfaces in the OMS footprint. We performed a footprint analysis to reconstruct the surface contribution to the OMS measured fluxes (80% water and 20% wet-salt). Furthermore, we investigated the applicability of the Monin-Obukhov Similarity Theory (MOST) which was needed to infer fluxes from the OMS-derived structure parameters to the fluxes. The OMS structure parameters and MOST are compromised due to the effects of the surface heterogeneity and the non-local processes induced by regional circulation. We mitigated these effects locally by fitting MOST coefficients to the site conditions. The adjusted MOST coefficients lowered by a factor of 1.64 compared to using standard MOST coefficients. For H and L_vE, we obtained zero-intercept linear regressions with correlations, R^2, of 0.92 and 0.96, respectively. We conclude that advances in MOST are needed to successfully apply the OMS method in landscapes characterized by complex heterogeneity such as the Salar del Huasco.

6.1 Introduction

In deserts, water is confined to specific areas such as saline lakes, rivers, wetlands, and salt flats, all of which act as highly localized evaporative pathways (Rosen, 1994). For example, the mountain regions of the Atacama Desert (Altiplano) are formed by consecutive endorheic basins. These basins catch precipitation which then enters the hydrological system. From this system, the water wells up at specific sites and produces relatively small shallow lakes surrounded by extended salt-flats (Uribe et al., 2015). In this water-limited environment, evaporation is highly relevant since it represents the principal cause of water loss in the basins.

In arid regions, measuring evaporation over small saline lakes is particularly complicated for three main reasons. First is the surface heterogeneity, with strong contrasting surface fluxes (Suárez et al., 2020), requiring the necessity of a footprint analysis to interpret the measured evaporation. Second, the atmospheric boundary layer dynamics and their influence on the surface fluxes are affected by non-local effects such as entrainment and advection of heat, moisture, and momentum (Lobos-Roco et al., 2021b). Last, measuring evaporation over open waters always represents a challenge since installing instruments in water is technically difficult (Tanny et al., 2008; Nordbo et al., 2011).

To estimate evaporation, various direct and indirect methods with different theoretical assumptions and footprints were used and depend on the spatial scale of the subject under investigation (Abtew & Melesse, 2012; Shuttleworth, 2008). Within this context, we evaluated the applicability of an Optical Microwave Scintillometer (OMS) to estimate open water evaporation in arid regions. A scintillometer consists of a transmitter and a receiver. The transmitter emits a light beam towards the receiver, which measures the intensity of the fluctuations (the scintillation effect) caused by the turbulent transport of sensible heat and moisture crossing the instrument's path. The OMS combines two scintillometers with different wavelengths: the Large Aperture Scintillometer (LAS) operates an optical light-beam, while the MicroWave Scintillometer (MWS) operates a microwave beam (Green et al., 2001; Kohsiek & Herben, 1983). The optical beam is primarily sensitive to temperature fluctuations induced by the sensible heat flux, whereas the microwave beam is sensitive to both heat and water vapor (Hill et al., 1980).

The OMS presents several advantages related to its large footprint (10 to 100 km2) and its capacity to integrate heterogeneous landscapes (Lagouarde et al., 2002). The OMS is specifically convenient for measuring evaporation over open water since the transmitter and receiver can be installed on opposite shores, concentrating the central part of the instrument's footprint over the water body. However, the OMS method also presents disadvantages in the flux calculation due to its dependency on the Monin-Obukhov Similarity Theory (MOST, Monin & Obukhov (1954)) and its underlying assumptions, such as horizontal homogeneity and the non-influence of outer scale processes. This theory

connects turbulence-related quantities to turbulent fluxes through standard formulations determined empirically in field experiments and assumed to be universally applicable. This assumption is questionable when non-local contributions to the exchange process intervene (Kooijmans & Hartogensis, 2016; Li et al., 2012).

The Altiplano of the Atacama Desert region presents interesting conditions to evaluate the strengths and weaknesses of the OMS method. We performed a 10-day field experiment called E-DATA (Chapter 2), which was aimed at understanding the processes that control the evaporation of the saline lake in the Salar del Huasco (SDH) in the Altiplano of the Atacama Desert (Suárez et al., 2020; Lobos-Roco et al., 2021b). Part of the E-DATA experiment included the critical evaluation of the OMS method to determine open water evaporation in a heterogeneous setting. To this end, we installed an OMS over the saline lake along with a small network of three Eddy Covariance systems, including one in the water body, covering the heterogeneous surfaces in the SDH to serve as a reference.

Within this framework, we addressed the following research question: how accurate are the evaporation measurements performed by an OMS over an open water body under arid and windy atmospheric conditions? To answer this question, we integrated into our analysis: (1) the dynamic surface and atmospheric boundary-layer conditions, and (2) the evaluation of the MOST functions used to derive the surface fluxes and the impacts of both footprints and MOST function on the measurement of surface fluxes.

6.2 Methodology

This section begins with an overview of the measurement principles of the OMS and the EC systems, followed by descriptions of the calculation steps required to obtain surface fluxes from the OMS and EC measurements. Lastly, we describe the model used for calculating the OMS and EC footprints.

6.2.1 OMS versus EC method

Figure 6.1 provides an overview of some key aspects of the OMS and EC methods. Figure 6.1a summarizes the processing chain of the OMS to obtain surface fluxes from the OMS light intensity fluctuations, expressed as the variance of logarithm of the intensity fluctuations, $\sigma^2_{ln(I)}$. The OMS beams experience fluctuations in the intensity of the light due to the eddies that cross them. The statistic that captures the intensity of these fluctuations, $\sigma^2_{ln(I)}$, is related to the structure parameter of the refractive index, C_n^2 (step I in Fig. 6.1a), which is a spatial statistic that quantifies the turbulence intensity. The turbulent eddies that mainly contribute to the scintillation effect are of one typical size, i.e., the aperture diameter, D (= 0.15 m) for the LAS and the Fresnel length-scale, $F = \sqrt{\lambda L}$, for the MWS, where λ (= 1.8mm) is the wavelength and L is the scintillometer

path length ($0.5 < \mathrm{L} < 10$ km). Typical values for F are 1–3 m. These eddy sizes typically correspond to the spectral inertial sub-range (Kolmogorov, 1941). The LAS is mainly sensitive to temperature fluctuations, whereas the MWS is sensitive to both temperature and humidity fluctuations brought about by the transport of turbulent eddies. Combining the measurements from both scintillometers allows to solve the temperature and humidity fluctuations in terms of the structure parameters of temperature and humidity, C_T^2 and C_q^2 (step II in Fig. 6.1a). These structure parameters, along with additional measurements of wind speed, U, and an estimate of the roughness length, z_0, are related to the fluxes of H and L_vE following Monin-Obukhov similarity formulations (step III in Fig. 6.1a). In Section 6.2.2 and 6.2.3, we make the processing steps more explicit.

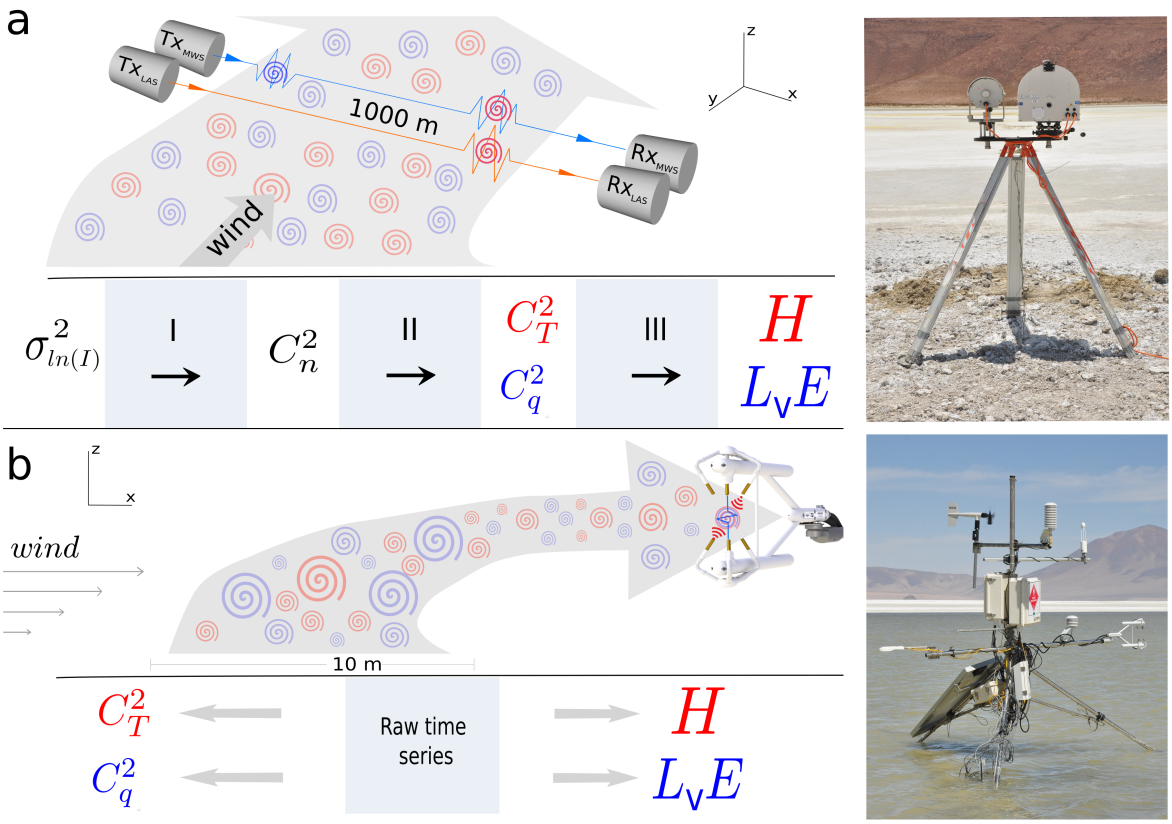

Figure 6.1: Flowchart of the steps used to calculate the sensible (H) and latent heat (L_vE) fluxes using the Optical-Microwave Scintillation method (a) and Eddy Covariance method (b). The large arrows depict how the turbulent eddies are advected from their source area (footprint) to the scintillometer and EC sensor paths. A picture of every instrument is depicted next to the schemes.

Figure 6.1b highlights the main differences of the Eddy-Covariance (EC) method in determining surface fluxes with respect to the OMS method: 1) Fluxes are calculated directly (i.e., do not rely on MOST) from the time-series of high-frequency measurements of the 3D wind vector (u, v, w), air temperature (T) and water vapor (q) as the covariance

of the vertical wind speed, w, and T for the sensible heat flux ($H \sim \overline{w'T'}$), with for the latent flux ($L_vE \sim \overline{w'q'}$) and with for the momentum flux ($\tau \sim \overline{w'u'}$). In contrast to the scintillometer that only considers a limited range of inertial-range eddy-sizes around one dominant eddy-scale in the flux estimate, the EC method integrates all eddy-sizes that contribute to the flux transport. The EC footprint, i.e., the source area of the turbulent eddies measured, is typically smaller than the scintillometer as it samples turbulent eddies at one point rather than over a path.

6.2.2 OMS fluxes

In the following section, we will explain the three processing steps of the OMS outlined in Figure 1a. The first processing step relates the raw scintillation statistic, $\sigma^2_{ln(I)}$ [-], to C_n^2 [m$^{-2/3}$] for the optical and microwave scintillometer (step I in Fig. 6.1a). This relationship, which assumes that the OMS is only sensitive to eddies in the inertial sub-range, is expressed through wave propagation theory in a turbulent medium (Tatarski, 1961) from which it follows that:

$$C^2_{n,opt} = C_{opt} D^{7/3}_{opt} L^{-3} \sigma^2_{ln(I)}, \tag{6.1}$$

$$C^2_{n,mw} = C_{mw} F^{7/3}_{mw} L^{-3} \sigma^2_{ln(I)}. \tag{6.2}$$

Where F_{mw} corresponds to the Fresnel length-scale ($F = \sqrt{\lambda L}$), D_{opt} is the optical scintillometer aperture diameter (0.15 m), and C_{opt} (0.907) and C_{mw} (3.425) are coefficients determined for each experimental setup and rely on the ratio between F and D (e.g (Ward et al., 2015)).

The second processing step determines the structure parameters of temperature, C_T^2 [K^2 m$^{-2/3}$], and water vapor, C_q^2 [(kg kg^{-1})^2 m$^{-2/3}$] (step II in Fig. 6.1a), where the wavelength-dependent structure parameter of the refractive index ($C^2_{n,\lambda}$), can be expressed as follows (Hill, 1997):

$$C^2_{n,\lambda} = A^2_{T,\lambda} \frac{C_T^2}{T^2} + A^2_{q,\lambda} \frac{C_q^2}{q^2} + 2A_{T,\lambda} A_{q,\lambda} \frac{C_T q}{Tq} \tag{6.3}$$

where $A_{T,\lambda}$ and $A_{q,\lambda}$ are dimensionless coefficients that depend on wavelength, pressure, temperature, and specific humidity (Ward et al., 2013). Two versions of Equation 6.3 can be defined, i.e., one for the LAS (λ=880 nm) and one for the MWS (λ=1.8 mm). Equation 6.3, however, contains three unknown variables (C_T^2, C_q^2 and C_T^q), so a third expression is needed to solve the equations. Here, two approaches can be followed. The first one is a method introduced by Lüdi et al. (2005), which uses the covariance between

the LAS and MWS intensity fluctuations. This defines a cross structure parameter of the refractive index between the two wavelengths used, $C_{n,opt,mw}$. Thus, a third expression of Equation 6.3 is provided, which allows us to solve the three unknowns. The method provided by Lüdi et al. (2005) is quite sensitive to errors in the correlation measurement. Therefore, we used the second method, elaborated by Hill (1997). This method prescribes a value for r_{Tq}, the correlation coefficient between temperature and humidity, which is related to C_T^2 and C_q^2. The advantage of the Hill method is that the calculations are more robust, i.e., less sensitive to measurement errors, but good representative values for r_{Tq} must be known a priori (Stoffer, 2018). Following the Hill-method, the solution for C_T^2 and C_q^2 from Equation 6.3 is given by:

$$C_T^2 = \left[A_{q,mw}^2 C_{n,opt}^2 + A_{q,opt}^2 C_{n,mw}^2 + 2A_{q,opt}A_{T,mw}r_{Tq}\sqrt{C_{n,opt}^2 C_{n,mw}^2}\right]\frac{T^2}{\gamma^2} \tag{6.4}$$

$$C_q^2 = \left[A_{T,mw}^2 C_{n,opt}^2 + A_{T,opt}^2 C_{n,mw}^2 + 2A_{T,opt}A_{T,mw}r_{Tq}\sqrt{C_{n,opt}^2 C_{n,mw}^2}\right]\frac{q^2}{\gamma^2} \tag{6.5}$$

where, $\gamma = A_{T,mw}^2 A_{q,opt}^2 - A_{T,opt}^2 A_{q,mw}^2$.

The third and last processing step is to connect C_T^2 and C_q^2 to the surface fluxes in the framework of MOST (step III in Fig. 6.1a), which states that turbulence variables can be made dimensionless using MOST scaling variables as a function of the stability parameter z/L_{ob}:

$$f_{C_T^2}(z/L_{ob}) = \frac{z^{2/3}C_T^2}{\theta_*^2}, \tag{6.6}$$

$$f_{C_q^2}(z/L_{ob}) = \frac{z^{2/3}C_q^2}{q_*^2}, \tag{6.7}$$

where θ_* and q_* are turbulent scaling variables for temperature and specific humidity and z/L_{ob} is a dimensionless stability parameter where is the measurement height and L_{ob} the Obukhov length. $f_{C_T^2}$ and $f_{C_q^2}$ are empirical functions that have the following base shape for unstable conditions (Wyngaard et al., 1971):

$$f_{C_X^2} = c_1(1 - c_2\frac{z}{L_{ob}})^{-2/3}, \tag{6.8}$$

where X stands for T or q. c_1 and c_2 are coefficients that depend on stability and are considered universal when the standard assumptions for MOST of homogeneous and

isotropic turbulence are met. However, no unanimity exists on the universality of $f_{C_T^2}$ and $f_{C_q^2}$ coefficients (Beyrich et al., 2012), which indicates that MOST assumptions are often violated. Kooijmans & Hartogensis (2016) provided an overview of the and coefficients and reported in the literature and they proposed their own values based on eleven data field experiments performed with the same instrumentation and with uniform data processing (see Table 6.2).

To determine the sensible heat flux, defined in the MOST framework as $H = -\rho c_p u_* \theta_*$, where ρ is the air density, c_p the specific heat capacity at constant pressure, u_* the friction velocity. Here, θ_* is solved iteratively from Equation 6.7 in conjunction with expressions for the friction velocity u_* taken from standard flux profile relationships and the definition of the Obukhov length, L_{ob} given by respectively

$$u_* = \frac{kU}{ln(\frac{z_U}{z_0}) - \Psi_m(\frac{z}{L_{ob}}) + \Psi_m(\frac{z_0}{L_{ob}})}, \tag{6.9}$$

and

$$L_{ob} = \frac{Tu_*^2}{kg\theta_*}, \tag{6.10}$$

where k is the von Karman constant (taken as 0.4), U the wind speed measured at z, z_0 the surface roughness length, Ψ_m are stability correction functions (Businger et al., 1971; Dyer, 1967), T is the air temperature, and g the gravity acceleration. Once u_* and L_{ob} are solved as part of the sensible heat flux calculation, we can solve q_* directly from Equation 6.7 and from there on, the latent heat flux follows from its definition in the MOST framework ($L_v E = \rho L_v u_* q_*$).

The OMS data were processed from raw data to fluxes, according to the steps outlined in Figure 6.1a. The raw 1 kHz intensity signals were filtered using a high pass filter (31 s for the LAS and 71 s for the MWS for low crosswind conditions and 10 s and 20 s for high crosswind conditions, respectively) to avoid the contribution of absorption fluctuations to the scintillation statistic, $\sigma^2_{ln(I)}$. Structure parameters of T and q were calculated according to the methodology proposed by Hill (1997) where we assumed, based on the EC measurements, the values of r_{Tq} were +0.7 for the day and +0.3 for the night. r_{Tq}=+0.7 is a typical daytime value reflecting the strong correlation between T and q fluctuations as they are mostly being transported by the same turbulent eddies. The positive r_{Tq} values for the night-time are a-typical, which is caused by small, but positive H and $L_v E$ during the nighttime. Additionally, we used A_T and A_q coefficients (Ward et al., 2015) evaluated with data from a Vaisala WXT520 all-weather sensor which was supplied with the Radiometer Physics (RPG) MWS. We use the internal data acquisition system of the RPG-MWS to record the raw OMS (LAS and MWS) data. The data processing

was made using our own code in Matlab and Python scripts, following the steps depicted in this section. Fluxes were computed using the MOST functions for unstable conditions defined by Kooijmans & Hartogensis (2016), but also using site-fitted MOST functions presented in the results section. z_0 was solved from the wind flux-profile relations (Eq. 6.9) with prescribed u_* from the EC systems. The OMS fluxes were calculated at a temporal resolution of 10-min.

6.2.3 EC fluxes

EC data were processed using the flux-software package EddyPro v 6.2.2 (Fratini & Mauder, 2014) from LI-COR Biosciences Inc. (Lincoln, Nebraska, USA) to obtain the turbulent fluxes of latent and sensible heat, and the momentum at a temporal resolution of 10-min. All necessary standard data treatment and flux correction procedures were included, such as axis rotation with the planar-fit procedure (Wilczak et al., 2001), raw data screening including spike removal (Vickers & Mahrt, 1997), interval linear detrending, and low-pass filtering correction (Massman, 2000). Structure parameters from EC data were estimated using the structure-function equation (Hartogensis, 2006): $C_X^2 = \overline{(x(r_1) - x(r_2))}/r_{1,2}^{2/3}$ with $x = q$ or T. The spatial separation $r_{1,2}$ was approximated through the wind speed and time step ($U\Delta t$) using nominal values of 0.5 m and 1 m. An average C_X^2 for the two separation distances was used in this analysis. For a more detailed explanation of the Eddy Covariance instrumentation and data processing, see Suárez et al. (2020) and Lobos-Roco et al. (2021b).

6.2.4 OMS and EC footprints

To quantify the source area that determines the measurements over heterogeneous surfaces, a footprint model is a useful tool (Meijninger et al., 2002a). In simple words, it represents the 'field view' of an instrument defined by an upwind area as a function of measurement height (Schuepp et al., 1990), the current wind regime, surface fluxes and characteristics (Leclerc & Foken, 2014). Footprints are especially relevant when measurements are performed below the so-called blending height (Wieringa, 1976). The footprints are calculated using the advection-diffusion model proposed by (Horst & Weil, 1992) which was derived for a point measurement such as the EC method. To extend this to a scintillometer path footprint, the path between transmitter and receiver is discretized in N steps, where the point footprint at each location, x_i, is convoluted with the path weighting function (Hartogensis et al., 2003) of the LAS and MWS (Meijninger et al., 2002a) resulting in a representative source or footprint area (S_{path}):

$$S_{path} = \sum_{i=1}^{N} W_{path}(x_i) S_{point}(x_i, y, z, z_0, \frac{z}{L_{ob}}, U, \sigma_v) \tag{6.11}$$

where S_{point} represents the point-source function (Neftel et al., 2008) as a function of:

the horizontal positions x_i and y, the measurement height, z, the Monin-Obukhov dimensionless stability parameter, z/L_{ob}, the wind speed, U, and σ_v as the standard deviation of the lateral wind speed component that is used to model the Gaussian lateral spread. Finally, the footprints have been truncated to a 95 % cumulative contribution.

6.3 Site and data description

This section describes the E-DATA experiment where our OMS and EC data were gathered. Moreover, we provide a detailed description of the atmospheric and surface conditions observed during the E-DATA experiment expressed by the boundary layer development, wind regime, surface heterogeneity, footprints, and roughness length.

6.3.1 E-DATA experiment

The data used in this study was gathered during the E-DATA experiment (Suárez et al., 2020; Lobos-Roco et al., 2021b) performed at the saline lake of SDH (20.2 °S, 68.8 °W, 3,790 m ALS) in the Altiplano of the Atacama Desert from 13 to 24 November 2018. The Salar del Huasco is representative of a typical natural hydrological system of the Altiplano region of Chile, characterized by a closed basin surrounded by complex topography of volcanic origin (Fig. 6.2a). Its hydrological functioning is given by the balance between occasional convective showers in the summer and a long dry season during the rest of the year (de la Fuente et al., 2021). Even so, these basins sustain permanent wetlands and feed the saline lake continuously with water through seepage from a complex hydrogeological system, making SDH one of the few pathways of evaporation in the region.

E-DATA was designed to study the evaporation in arid environments at local and regional scales over heterogeneous surfaces (Suárez et al., 2020). Part of the experiment was to collect data with an OMS installed over a ∼15-cm deep saline lake in the middle of the salt-flat (see Fig. 6.2b). The OMS was in operation from 13 to 24 November 2018. Measurements from most of these days were non-reliable for two main reasons. Firstly, we experienced problems with the beam alignment between the transmitter and receiver due to the strong wind speed combined with the soft, unstable wet-salt and mud surface. Secondly, there were technical problems with the storage of the raw data. The internal computer of the RPG-MWS was not powerful enough to store the raw data at 1kHz, which resulted in missed samples. Therefore, we used the data of one representative day (15 November 2018) to analyze the OMS method, as it was one of the few days with good quality measurements. This is a restriction but, as reported by Suárez et al. (2020) and Lobos-Roco et al. (2021b), all days in the campaign showed very similar behavior in surface fluxes (See Fig. 6.5). Therefore, we are confident that what we learned from our one golden day is representative of a typical day in late spring in our study area.

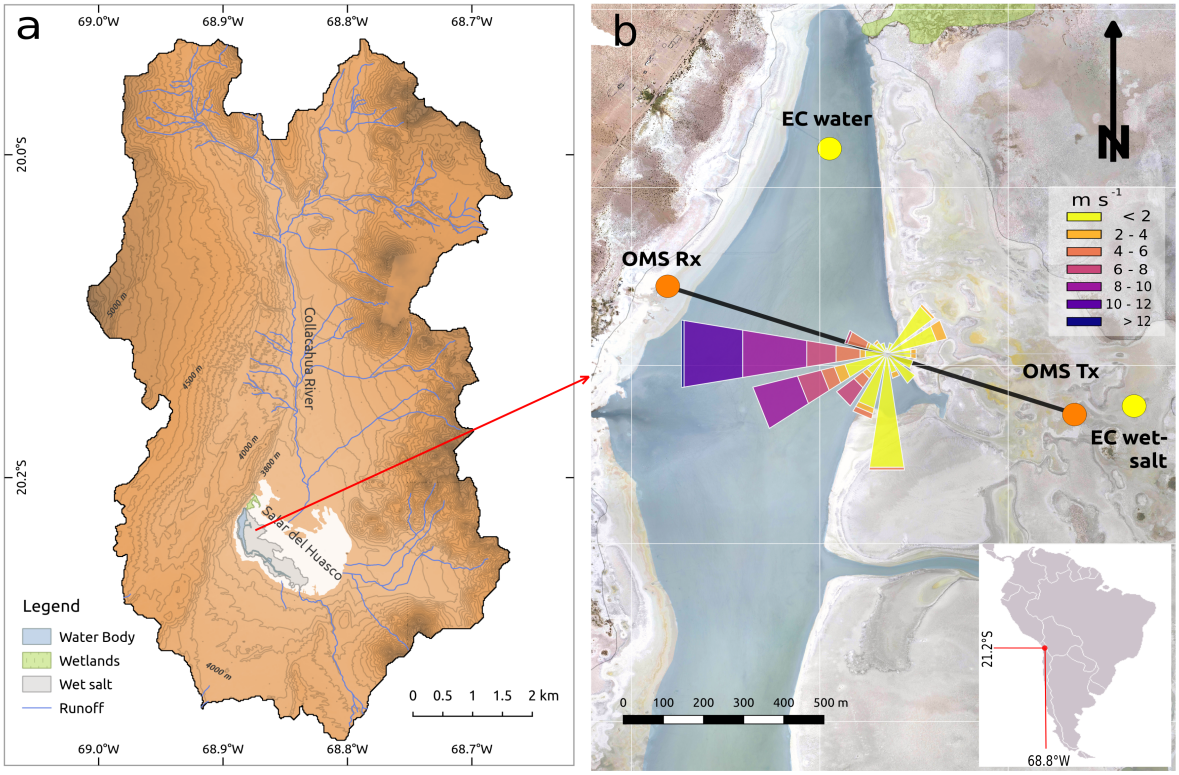

Figure 6.2: tudy area. (a) Salar del Huasco basin and saline lake. (b) Installation of the OMS and EC systems. Orange circles represent the OMS receiver (R_X) and transmitter (T_X), solid black line the OMS path and yellow circles the EC systems. Windrose indicates wind speed and direction of 15 November 2018.

Table 1 and Figure 6.2b show the specific details of the OMS and EC systems installed. The OMS path length between the transmitter (T_x: 20.283°S, 68.870°W) and receiver (R_x: 20.280°S, 68.880 °W) was 1,070 m. We intended to place the OMS transmitter and receiver close to the shoreline ensuring an all-water footprint. In the end, we chose to install the OMS some distance from the shorelines where there was a somewhat higher and firmer waterlogged wet-salt. In all, the OMS path covered 300 m of wet-salt and 770 m of water. The path crossed the saline lake from the NW to SE, offset Northward by 45 degrees with respect to the main wind speed (Fig. 6.2b). The transmitter and receiver were placed at 1.8 m above the wet-salt, which was 0.5 m higher than the water surface, resulting in an OMS beam height of 2.3 m above the water. It is noteworthy to mention that the MWS beam size in the middle of the path, marked by the Fresnel length, reached 1.4 m. We believe that the days with bad MWS data are possibly explained by misalignment of the instrument resulting in nonphysical, high $\sigma^2_{ln(I)}$ values due to ground reflections of the MWS beam. In addition, Eddy-Covariance (EC) systems were installed over the lake (20.277°S, 68.882°W) and over a wet-salt surface (20.283°S, 68.875°W). Finally, to connect the analysis of the surface fluxes with the ABL dynamics,

Table 6.1: Sensors and variables measured by the OMS and EC in the E-DATA experiment: large aperture scintillometer (LAS), microwave scintillometer (MWS), structure parameter of temperature (C_T^2) and humidity (C_q^2), sensible heat flux (H), latent heat flux (L_vE), friction velocity (u_*), air temperature (T), ∼5 cm temperature (T_s), relative humidity (RH), air pressure (p), parallel wind component (u), lateral wind component (v), vertical wind component (w), specific humidity (q), potential temperature (θ), incoming shortwave ($S_w\downarrow$), outgoing shortwave ($S_w\uparrow$), incoming longwave ($L_w\downarrow$), outgoing longwave ($L_w\uparrow$) radiation and net radiation (R_n).

Instrument	Sensor	Variable measured	Variable estimated	height (m)	Measurement freq.	Manufacturer
OMS	LAS	C_T^2	H	2.1	1-min	Kipp & Zonen
	MWS	C_q^2	L_vE	2.1		RPG
	WXT520	T, RH, p, u, v	u_*	2.7		Vaisala
EC_{water}	IRGASON	u, v, w, T, T_s, q	H, L_vE,	1	10-min	Campbell Scientific
	CNR4	$S_w\downarrow$,$S_w\uparrow$, $L_w\downarrow$,$L_w\uparrow$	R_n	1	10-min	Kipp & Zonen
$EC_{wet-salt}$	IRGASON	u, v, w, T, T_s, q	H, L_vE,	1.5	10-min	Campbell Scientific
	NR-Lite2	R_n	-	1.5	10-min	Kipp & Zonen
Radiosonde	iMet-4	T, RH, p, u, v	θ, q	0-2000	3-hours	InterMet System Inc.

radiosondes were launched on 19 November 2018, at 09:00, 12:00, 15:00 and 18:00 LT from the lake surroundings (20.35°S - 68.90°W; 3,953 m above sea level). The radiosondes were launched for measuring vertical profiles of potential temperature (θ) and specific humidity (q) within the first 2 km from the surface.

6.3.2 E-DATA atmospheric and surface conditions

This subsection describes the atmospheric and surface conditions observed during the E-DATA experiment to provide a context for interpreting the scintillometer flux measurements. We will focus on two aspects. First, we will focus on the non-local processes associated with the regional atmospheric circulation that affect the atmospheric boundary layer development through advection and entrainment. Second, we will focus on the surface heterogeneity between water and wet-salt in terms of near-surface temperature, net radiation, surface fluxes, roughness length, and how these areas are represented in the OMS footprint.

Atmospheric boundary layer

The non-local processes that define the land-atmosphere exchange in the Salar del Huasco are governed by a regional circulation pattern between the wet, cool and low-

elevation Pacific Ocean and the dry, hot and high elevation of the Atacama Altiplano where the Salar del Huasco is located. This circulation is responsible for the two well-marked wind regimes observed over the entire Salar basin during the experiment (Fig. 6.3). The first wind regime corresponds to the relatively calm conditions that occur in the morning (06:00 to 12:00 LT) and is characterized by low wind speeds (<2 m s^{-1}). During this regime, there is not a prevalent wind direction. The second wind regime corresponds to strong turbulent conditions that occur from noon onward (12:00 to 21:00 LT), which are characterized by high wind speeds (>10 m s^{-1}). During this regime, there is a predominant Westerly wind direction (250°-290°). The nature of this well-defined circulation has been analyzed in detail using observations and regional scale modelling studies (Lobos-Roco et al., 2021b; Suárez et al., 2020; Muñoz et al., 2018; Rutllant et al., 2003).

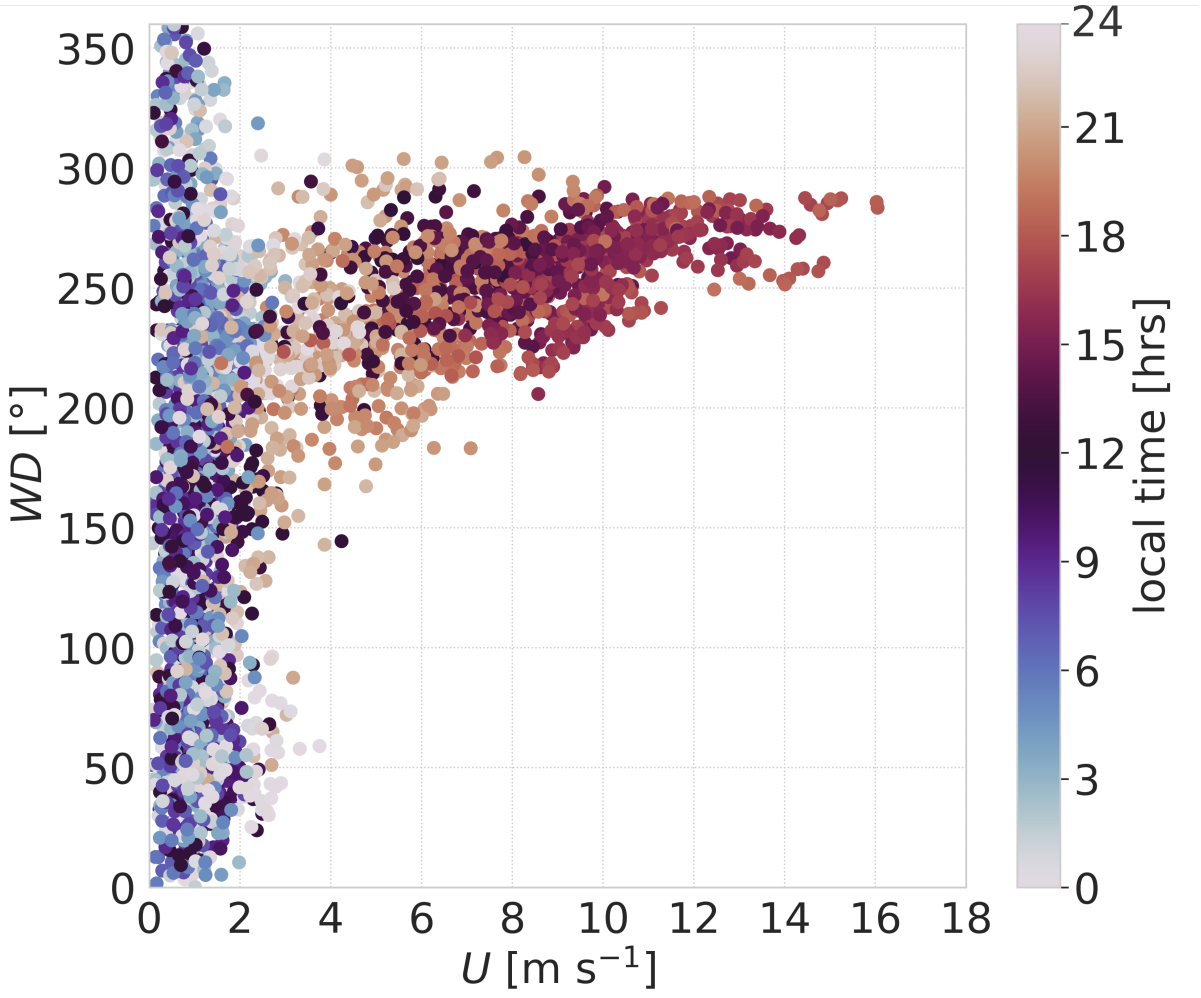

Figure 6.3: Diurnal relationship between wind speed (U) and wind direction (WD) obtained by EC over water and wet-salt surfaces.

Figure 6.4 shows the diurnal evolution of the potential temperature, θ (upper panels)

and the specific humidity, q (lower panels) vertical profiles within the ABL. These profiles show a thermally stable ABL at 09:00 LT, which rapidly develops to 1,800 m at 12:00 LT, becoming ∼15 K warmer with respect to the morning. The morning boundary layer development is dominated by the surface- and entrainment fluxes leading to a reduction of the inversion layer jump to ∼1 K. The rapid boundary layer growth is interrupted after midday, where the ABL decays abruptly to 500 m. The decrease in the ABL height is associated with the advection of relatively cold air from the Pacific Ocean to the study area by a regionally driven wind-regime introduced in Figure 6.3 (see also Lobos-Roco et al. (2021b) and Suárez et al. (2020)).

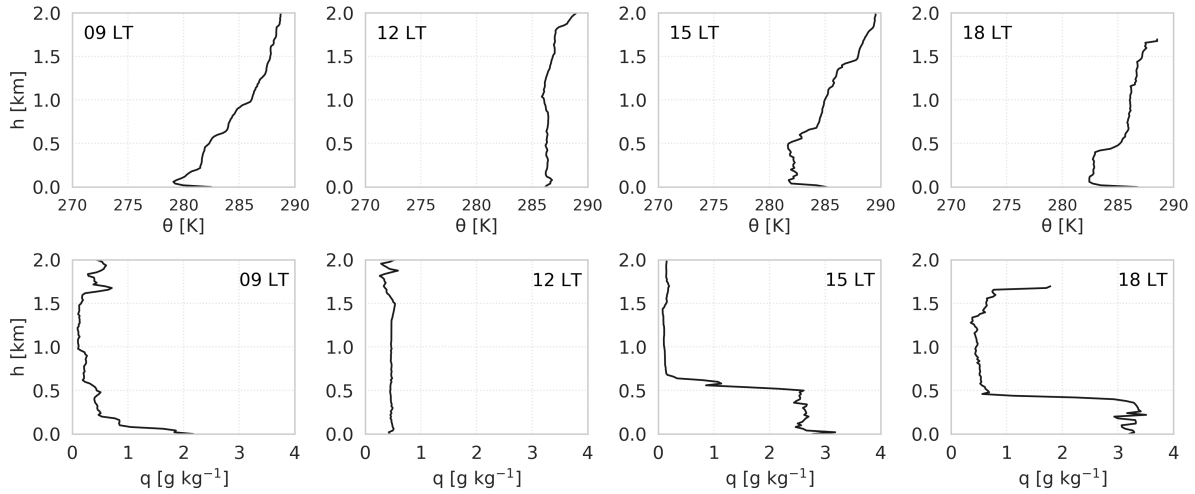

Figure 6.4: Atmospheric boundary layer conditions measured during E-DATA on 19 November 2018. Upper panels: Diurnal cycle of the potential temperature radiosounding profiles. Bottom panels: Diurnal cycle of specific humidity radiosounding profiles.

A similar pattern is observed for moisture in the bottom panels of Figure 6.4. Here, a layer with a negative humidity gradient grows fast in the morning until it is interrupted in the early afternoon by the regional flow. The moisture profile shows that the air in the shallow boundary layer caused by the regional flow is relatively moister, i.e., we observe an increase of the specific humidity from <1 g kg^{-1} to 3.5 g kg^{-1}.

Surface heterogeneity

To demonstrate the level of surface heterogeneity of the area covered by the OMS and EC measurements, we show time series of near-surface temperature, net radiation (R_n), and turbulent surface fluxes measured at the EC stations over the water and wet-salt surfaces (Fig. 6.5). In general terms, during the day, the near-surface (∼5 cm height) temperature is lower for the water surface (see Fig. 6.5b), so less longwave outgoing radiation will be lost to the atmosphere. In addition, a considerably higher albedo is observed over the wet-salt (0.58) compared to the water surface (0.12) (Lobos-Roco et al., 2021b).

As a result of the differences in surface temperature and albedo during the afternoon, much more radiation energy is available at the water's surface, which shows maximum values of ∼900 W m^{-}2 compared to the maximum values of ∼500 W m^{-}2 over the wet-salt surface. These remarkable differences in R_n have repercussions in the partitioning of the sensible and latent heat fluxes. Figure 6.5a and b also show the surface fluxes of latent heat (L_vE) and sensible heat (H) over wet-salt and water averaged along the E-DATA period. The first characteristic observed is the day-to-day low variability (shades) in the surface fluxes, evidence that the same diurnal cycle occurs every day. Even though both surfaces are water-saturated, their flux characteristics are completely different. To begin with, the fluxes over the wet-salt are smaller by a factor of ∼3 compared to the water surface given the much-reduced amount of net radiation available. In addition, $H > L_vE$ for the wet-salt, whereas $L_vE > H$ for the water surface. This is remarkable since the wet salt crust is waterlogged. The hyper salt concentrations, however, impede the water escaping from the surface (e.g., Salhotra et al. (1985); Oroud (1999)). As a result, most of the energy is dedicated to heating the air. We recognized that two aspects are equal for both surfaces. The first aspect is the sudden increase of fluxes at 12:00 LT aligned with the arrival of the strong winds that break the virtually absent turbulent mixing seen in the morning (Lobos-Roco et al., 2021b). The second is the fact that is positive during both the day and night, meaning that the atmosphere is unstable even during nighttime conditions. Lobos-Roco et al. (2021b) argues that the unstable nighttime condition is related to a katabatic flow that drains cold air from the surrounding mounting ridges into the Salar. However, it also might be related to the high heat capacity of the surface, causing heating of near-surface air further into the night.

6.3.3 Footprint analysis

The source area or footprint is highly dependent on the wind regime (Figure 6.3). Figure 6.6a-d shows the footprints for both scintillometers (LAS and MWS) and the EC systems (water and wet-salt) at two representative times of each wind regime (09:00 LT and 16:00 LT, respectively). The footprints have been truncated to a 95% cumulative contribution. Both scintillometer and EC footprints are considerably smaller in the morning compared to the afternoon due the different wind and related flux regimes. Their orientation changes according to the wind direction. Under all conditions, the EC footprints cover only a small portion of the surface above which they are installed (Table 6.1). The scintillometer footprints, on the other hand, always cover a mix of both water and wet-salt. On average, about 2/3 of the LAS and MWS footprints are covered by water and 1/3 wet-salt. The difference in the path weighting function means that the LAS footprints are more weighted towards the center of the path (Evans et al., 2012) and therefore, cover a slightly larger area of water compared to the MWS footprints.

This systematic difference can also be seen in Figure 6.6e which expresses the time dependent footprint proportions covering water and wet-salt for the two scintillometers

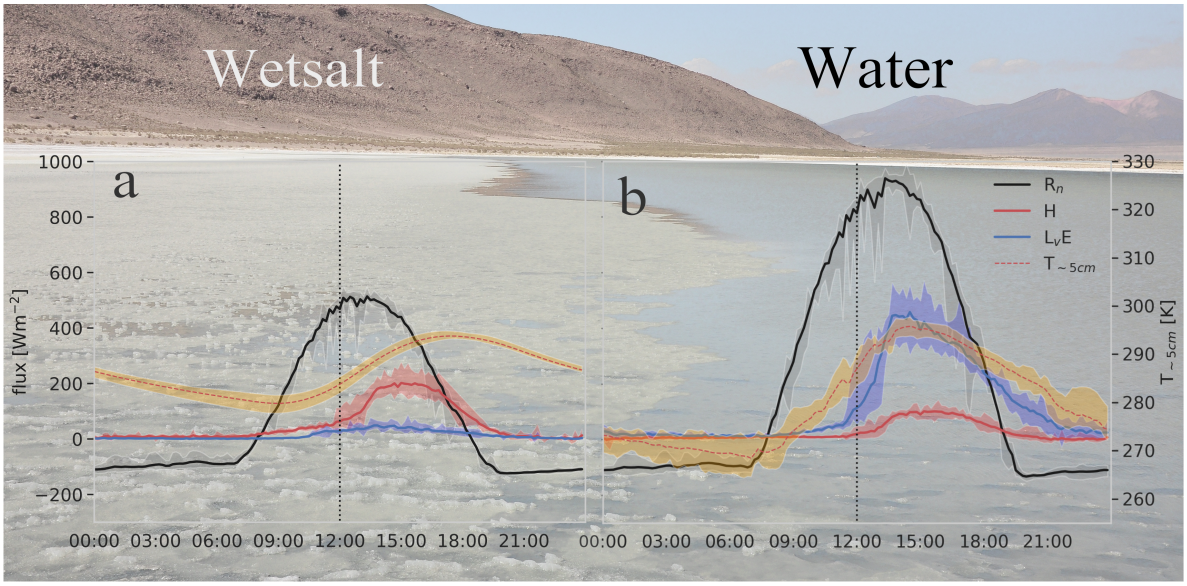

Figure 6.5: Diurnal-averaged time series of near-surface (∼5cm) temperature, net radiation and turbulent fluxes over the wet-salt (a) and water (b) surfaces during the E-DATA period. The picture behind exemplifies the wet-salt and water surface during the experiment.

on 15 November 2018. Driven by the wind regimes, we observe two distributions of footprints. During daytime when the winds are generally from the West and they become strong during the afternoon, the distribution is roughly 80% water and 20% wet-salt. In the evening and night, the contributions of both surfaces to the scintillometer footprints are much more variable depending on the wind direction with contributions from water varying between 50%- 80% and wet-salt between 20% - 50%. The diurnal cycle of the OMS water/wet-salt footprint proportion is only relevant when surface fluxes observed over both water and wet-salt surfaces are significantly different (Fig. 6.6e). The strong difference in flux regimes between the two surfaces demonstrates the importance of constructing a footprint-weighted composite of the EC fluxes when comparing them with those of the scintillometers.

Roughness length

For the OMS flux calculations, an accurate estimate of z_0, is crucial given the fact the measurements were conducted close to the surface (∼2 m height) and the afternoon winds were strong. Under these conditions, mechanically generated turbulence is a key process in determining the fluxes (see Eqs. 6.7, 6.10). The wet-salt and water surfaces are very smooth, and an appropriate z_0-estimate is, therefore, not trivial. We solved z_0 from the wind flux profile relation (Eq. 6.9) using the estimates of U, u_* and from the EC stations of water and wet-salt. The results, presented in Figure 6.7, show that for low wind speeds, z_0 is ill-defined and for high wind speeds, its value converges to a

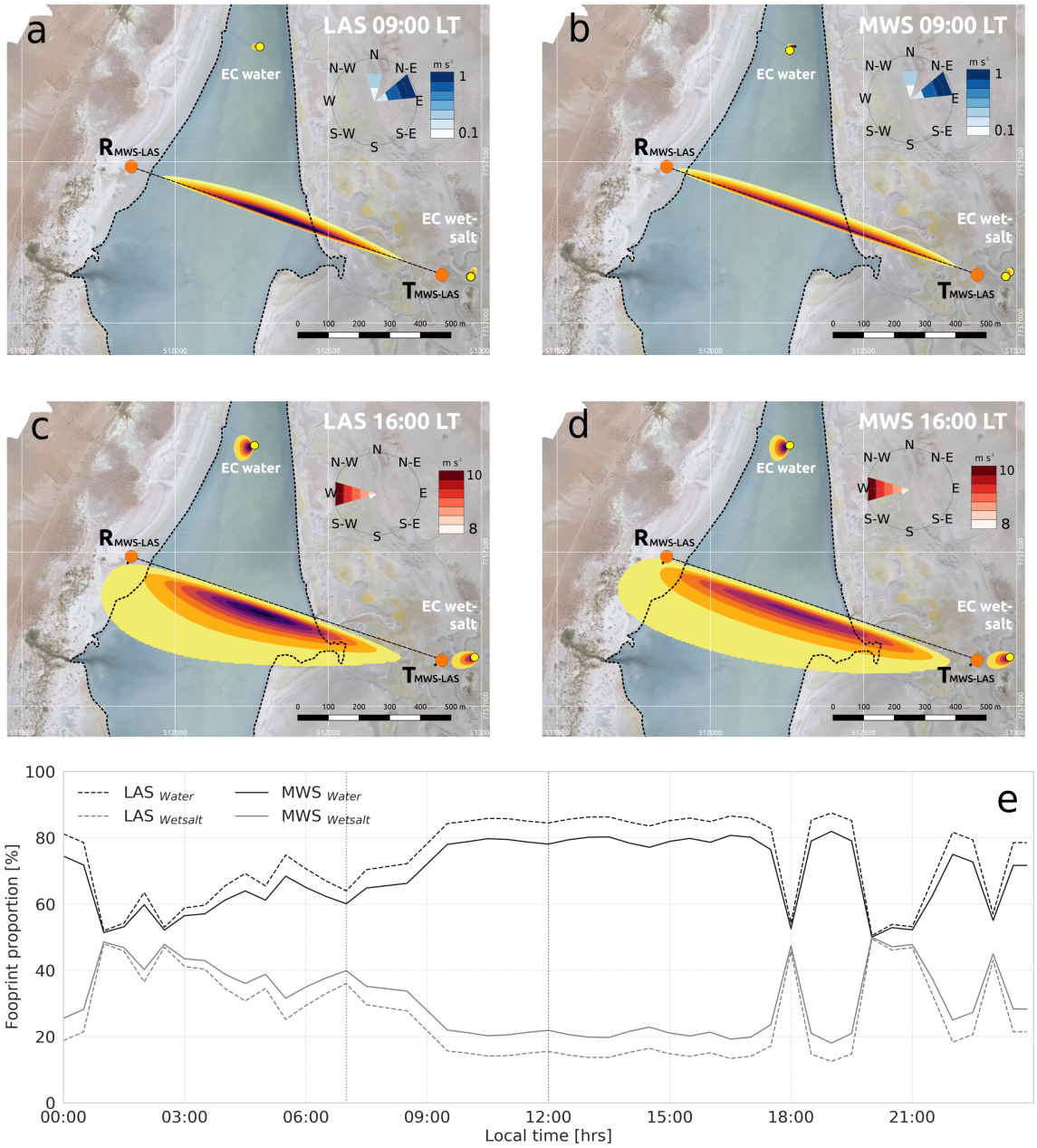

Figure 6.6: Footprints of the LAS and EC (a, c) and of the MWS and EC (b, d) over the water and wet-salt surfaces for representative hours of wind regimes on 15 November 2018. Colors (given without scale) represent the percentage contribution of that area to the total footprint. The wind roses characterize the wind regimes for the same day between 7:00-12:00 LT (a, b) and 12:00-20:00 LT (c, d). The background image is a georeferenced mosaic based on a drone flight on 18 November 2018. e) Diurnal cycle of LAS and MWS percentage footprint contributions from the water (solid lines) and wet-salt surface (dotted lines).

value indicated by the solid lines (Mahrt et al., 2001). On average, the water surface is smoother with $z_0 = 4 \cdot 10^{-5}$ m against $z_0 = 2 \cdot 10^{-4}$ m for the wet-salt surface. The shallow water becomes choppy in the afternoon, but this is not intense enough to cause z_0 to be a function of wind speed (Charnock, 1955). A weighted value considering the typical afternoon footprints over these two surfaces yields a value of z_0 $1.5 \cdot 10^{-4}$ m that we used in the flux calculations.

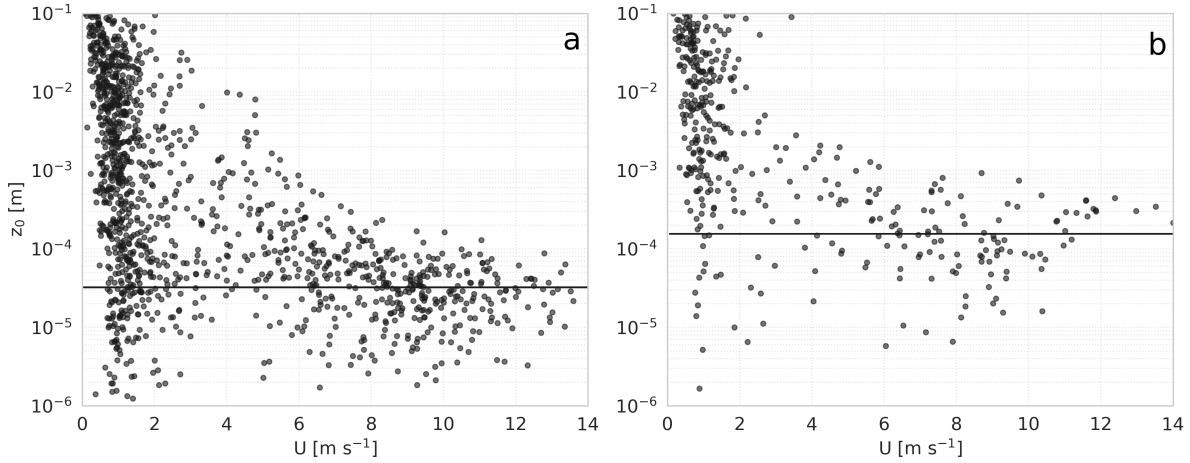

Figure 6.7: Relationship between roughness length (z_0) and wind speed over (a) water surface and (b) wet-salt surface. Wind speed data are taken from the Eddy Covariance systems. The solid lines express the values to which z_0 converges for high wind speeds.

6.4 Results and discussion

6.4.1 MOST functions

To assess the representativity of MOST for the special conditions in the Salar del Huasco, Figure 6.8 shows the C_T^2 and C_q^2 dimensionless groups (Eqs. 6.6 and 6.7) as a function of z/L_{ob} for EC-based structure parameters (Fig. 6.8a, b) and OMS structure parameters (Fig. 6.8c, d) together with standard Kooijmans & Hartogensis (2016) and site-fitted MOST functions. The EC-based structure parameters are composed values from the wet-salt and water EC systems and reflect data from the entire ten days E-DATA experiment, whereas the OMS structure parameters only include data from 15 November 2018. The data points in Figure 6.8 were filtered by excluding values for which $|H| < 5$ W m^{-2}. In addition, in Figure 6.8a-b the C_T^2 and C_q^2 dimensionless groups were filtered based on a 25% confidence interval. The structure parameters from the EC systems along with the EC-flux derived variables, θ_*, q_* and L_{ob} are weighted by the OMS water/wet-salt footprint proportions (wfp subscript). The data points are marked by the wind regime, where not surprisingly, the points associated with the strong wind conditions are on the neutral side of the $-z/L_{ob}$ range.

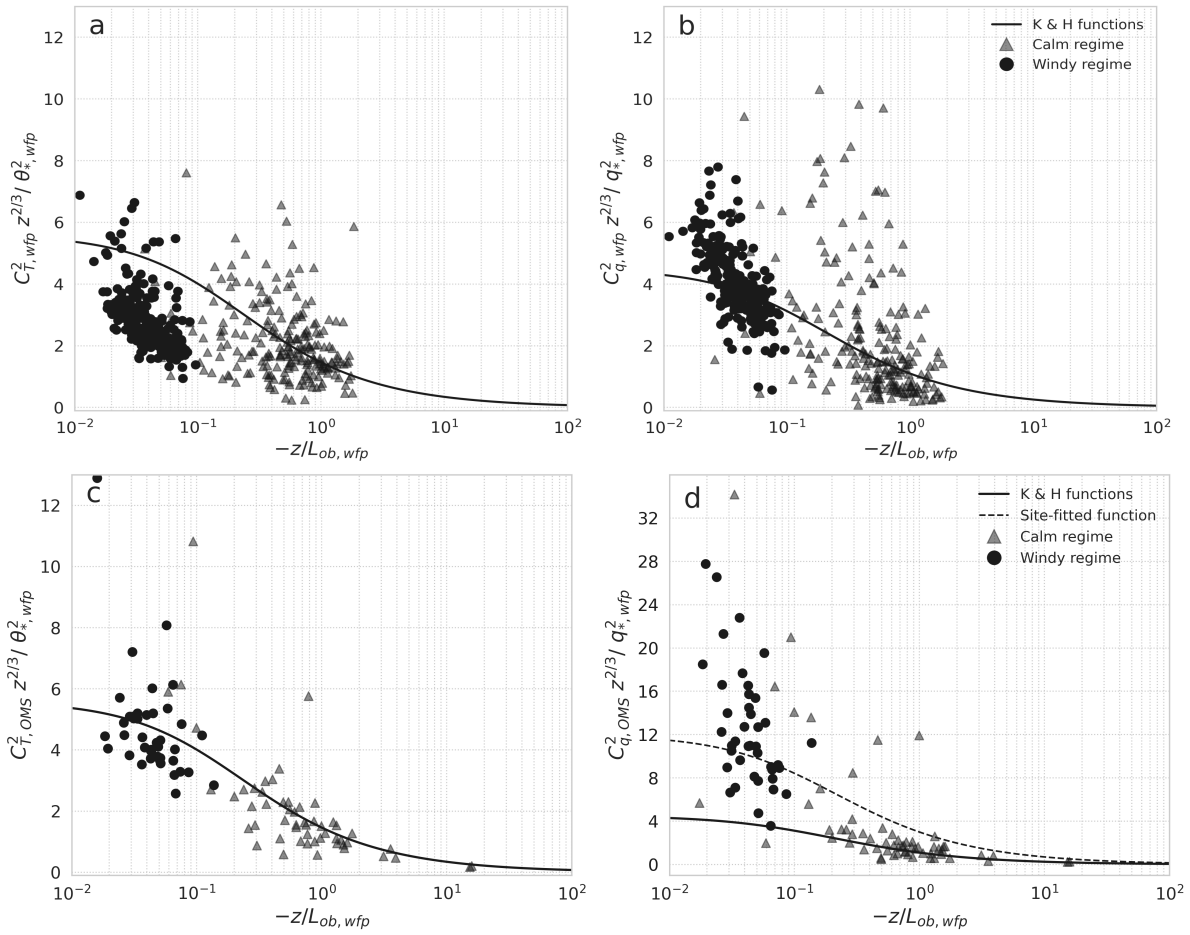

Figure 6.8: Dimensionless C_T^2 and C_q^2 groups versus stability parameter (z/L_{ob}). (a, b) C_T^2 and C_q^2 dimensionless group using parameters from EC water and wet-salt weighted by the OMS footprint (wfp) during the E-DATA period. (c, d) C_T^2 and C_q^2 dimensionless group using structure parameters measured by the OMS and the remaining parameters from EC water and wet-salt weighted by the OMS footprint (wfp) during 15 November 2018. MOST functions proposed by Kooijmans & Hartogensis (2016) and the proposed ones in this study are shown in solid and dashed lines, respectively. The experimental data points are marked by their wind regime (windy >4 m s^{-1} between 13:00-20:40 LT and calm <4 m s^{-1} between 23:40-13:00 LT).

Figure 6.8a shows that standard MOST functions slightly overestimate the C_T^2 data points during the windy regime, but data is well represented during the calm wind conditions. Likewise, Figure 6.8b shows that standard MOST functions represent both windy and calm regimes well for the C_T^2 dimensionless group data points. Figures 6.8c and d show that for C_T^2, the standard MOST functions of Kooijmans & Hartogensis (2016) cover the experimental data points reasonably well. However, for C_q^2, the experimental data points are far above both, the standard MOST function, and the EC data points (Fig 6.8b). Assuming that there are no instrumental issues related to these EC-OMS C_q^2 differences, we identified a key aspect that plays a role here. The OMS and EC measure below the blending height. As the EC footprints are entirely above water and wet-salt surfaces (Fig. 6.6), no interaction between their respective internal boundary layers affects the measurements. However, in the case of OMS, 2/3 of the footprint is covered by water and 1/3 by wet-salt, with an order of magnitude difference of L_vE flux regime (Fig. 6.5). This high contrast contributes to having strong humidity fluctuations within the internal boundary layers at the transition between the two surfaces, elevating the measured C_q^2 by the OMS. For C_T^2 (Fig. 6.8c), higher values are observed for the OMS as compared to the EC. However, the difference is less pronounced since the contrast between H flux surfaces is less as well. Note that both EC and OMS are under a setting governed by a regional advection and entrainment of air not originating from the Salar (Lobos-Roco et al., 2021b). Such regional circulation contributes to 40% of the total diurnal moisture budget above the water surface and this phenomenon might cause additional humidity fluctuations. However, our data do not show evidence of this since we observe high differences between the C_q^2 of EC and OMS, where the same conditions are supposed to affect both instruments. It is also under these conditions of no horizontal homogeneity and regional advection that MOST fails.

To mitigate these effects, we adopted a practical approach to eye-fit alternative MOST relations that inherently consider the enhanced structure parameters. Our motivation to use an eye-fit rather than a statistical approach, like the one performed by Kooijmans & Hartogensis (2016), is that we only have a single day of measurements available, whereas other methods require significant amounts of data. We did this for C_q^2, whereas for C_T^2, we use the coefficients determined by Kooijmans & Hartogensis (2016). The proposed line is depicted in Figure 8d and the coefficients that define it are given in Table 6.2.

6.4.2 Impact of footprint and MOST on surface fluxes

In this section, we demonstrate that it is essential to consider the impacts of the footprint and MOST functions when comparing the performance of the OMS in a complex environment like the Salar del Huasco.

Figure 6.9 shows the diurnal cycle of surface fluxes measured by EC over water and

Table 6.2: Kooijmans & Hartogensis (2016) MOST function coefficients for unstable conditions (base function in Eq. 6.8). Between brackets the site-adapted coefficients for Salar del Huasco study case, 15 November 2018 (Fig. 6.8d).

MOST functions	c_1	c_2
$f_{C_T^2}$	5.6	6.5
$f_{C_q^2}$	4.5 (12)	7.3 (7)

wet-salt surfaces as well as the diurnal cycle combining both EC system fluxes, but weighting them using the OMS-footprint (EC_{wfp}) presented in Figure 6.6e. EC_{wfp} resembles most of the EC fluxes over water (80%) than wet-salt (20% wet-salt) during daytime. Given the high flux contrast between wet-salt and water, the 20% wet-salt seen in the OMS footprint significantly influences the composed fluxes. This is the case for L_vE, where during daytime, it is ∼75 W m^{-2} over wet-salt versus ∼550 W m^{-2} over water, the EC_{wfp} L_vE is ∼100 W m^{-2} lower than that of the water surface. For the sensible heat flux (Fig. 6.9c), the absolute values of the fluxes are lower and the contrast between the two surfaces is less extreme resulting in an EC_{wfp} H that is only ∼10 W m^{-2} higher than that of the water surface. The orthogonal regression (Figs. 6.9b, d) between EC water, wet-salt, and wfp show a similar message: the quantification of the differences in L_vE and H of water and wet-salt with respect to EC_{wfp}.

When performing scintillometer measurements over heterogenous terrain under the blending height (Wieringa, 1976), the structure parameters of the individual surfaces within the footprint will be sensed by the instrument (Meijninger et al., 2002a). In our study, the OMS was installed close to the surface (2.3 m), and it is safe to assume we were below the blending height (Meijninger et al., 2002a). Due to the non-linear relationship between structure parameters and surface fluxes, there will be a difference between the EC flux weighted by the OMS footprint (EC_{wfp}), and the EC flux calculated using structure parameters weighted by the OMS footprint ($EC_{C_X^2,wfp}$) (Lagouarde et al., 2002; Meijninger et al., 2006). The latter more accurately simulates the way of measuring the OMS. To quantify the difference between the two approaches, we constructed the OMS footprint-weighted indirect EC flux estimate through C_X^2 ($EC_{C_X^2,wfp}$) following these steps: (1) applied an inverse MOST procedure using standard MOST function coefficients (Kooijmans & Hartogensis, 2016), where we obtained C_T^2 and C_q^2 for the EC fluxes over water and wet-salt; (2) applied the OMS-weighted footprint factors to construct simulated OMS-path-weighted structure parameters; and finally (3) calculated the fluxes based on the path averaged structure parameter values.

Figure 6.10 shows the difference between the two approaches described above. The big contrast in C_q^2 between water and wet-salt, connected to their contrast in L_vE (see Fig. 6.5a, b) and the non-linear relationship between C_q^2 and L_vE, cause a difference

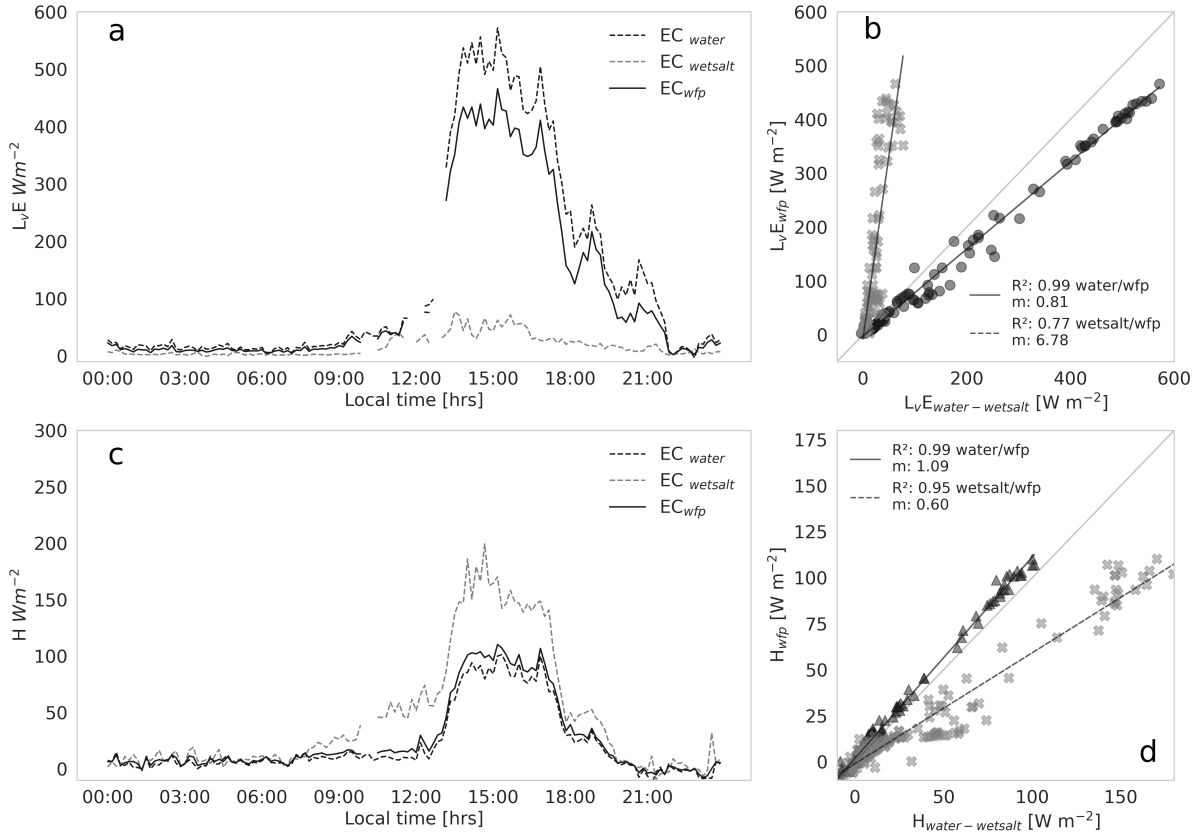

Figure 6.9: Diurnal cycle of surface fluxes (a, c) and orthogonal regression (b, d) between EC over water and wet-salt and an OMS-footprint composed EC flux (EC_{wfp}) for November 15, 2018. m indicates the regression slope, grey color refers to wet-salt and black to water. Triangles, circles and crosses are set to differentiate the data source.

of ∼15% between EC_{wfp} and $EC_{C_X^2,wfp}$. So, this is a significant factor to consider when validating OMS derived fluxes with a footprint composite of EC fluxes. For the sensible heat fluxes, the difference is negligible which is related to the much smaller fluxes with less contrast between the two surfaces (see Fig. 6.5).

Next, we will look at the difference in OMS derived fluxes with standard MOST functions (Eq. 6.8) taken from Kooijmans & Hartogensis (2016) and site-fitted MOST functions as determined in Figure 6.8 and Table 6.2. Figure 6.11 shows an overestimation of L_vE (factor of 1.64) if standard MOST functions are used. This is a clear indication that MOST assumptions are violated in the Salar del Huasco basin. In part, this has to do with the surface heterogeneity, noting that we measured below the blending height and measurements were thus sensitive to the non-MOST turbulence behavior at the transition between the two contrasting surfaces in the OMS footprint. In addition, regional advection of dry air has a strong influence on the local humidity (Lobos-Roco et al., 2021b). Consequently, the relationship between the measured humidity fluctuations and local fluxes do not follow the standard relationships.

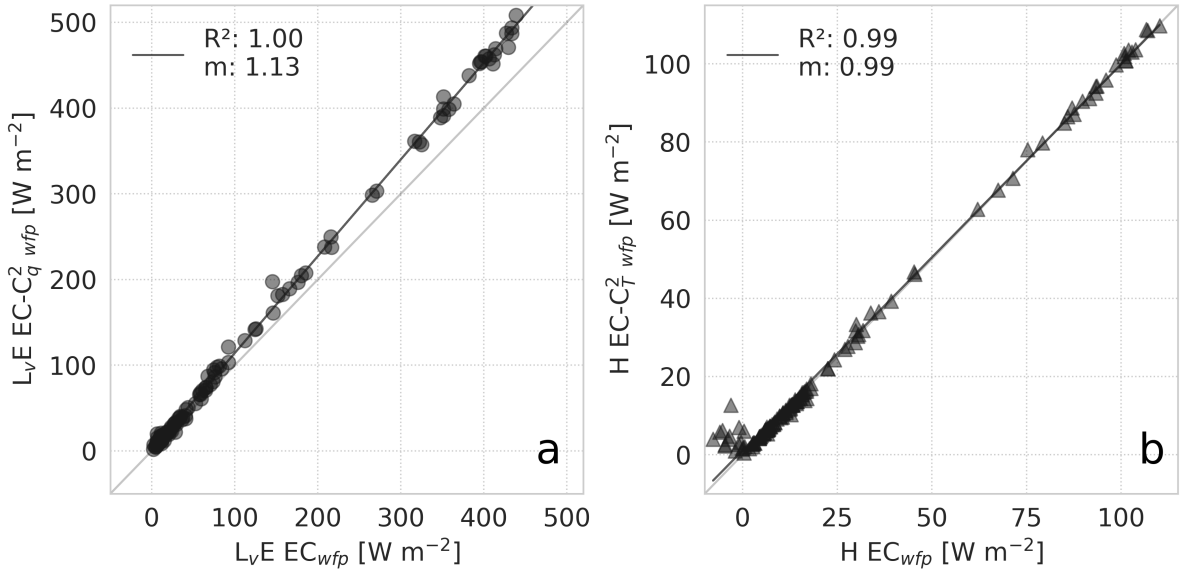

Figure 6.10: Relationships of latent- (a) and sensible (b) heat fluxes between OMS-footprint weighted, direct EC flux estimates (EC_{wfp}) and indirect EC flux estimates through C_X^2 ($\mathrm{EC}_{C_X^2,wfp}$).

Figure 6.12 brings together the results presented so far, i.e., OMS fluxes based on site-fitted MOST functions ($\mathrm{OMS}_{site-fitted-MOST}$), and EC_{wfp} and $\mathrm{EC}_{C_X^2,wfp}$ fluxes that serve as references. In general, we observe a reasonable agreement. The orthogonal regressions in Figures 6.12b and 6.12d are based on $\mathrm{EC}_{C_X^2,wfp}$ as this more closely resembles the OMS flux estimate given the fact that we measured below the blending height. After all the careful and guided treatment of the data, we arrive at zero-intercept linear regression with slope coefficients of 0.95 and 1.07 and correlation coefficients, R^2, of 0.92 and 0.96 for L_vE and H, respectively.

In the consecutive presentation of the results from Figures 6.9 to 6.12, we have paid more attention to the impacts of the footprint and MOST functions during the daytime on the absolute values of the fluxes. Here, the differences seen in the L_vE fluxes were most noteworthy for both the footprint and MOST functions. By comparing the daily averaged fluxes, the picture is slightly different. Here, the daily averaged impact of EC_{wfp} and the fluxes over water are, on average, about $\sim$6 W m^{-2} for both H and L_vE, resulting in a difference of 22% for H and 4.5% for L_vE. The impact that MOST function coefficients have on surface fluxes is significantly higher as compared to the footprint impact. Daily averaged fluxes calculated using standard MOST functions are 34% higher for L_vE as compared to the latent heat flux based on the site-fitted MOST relations.

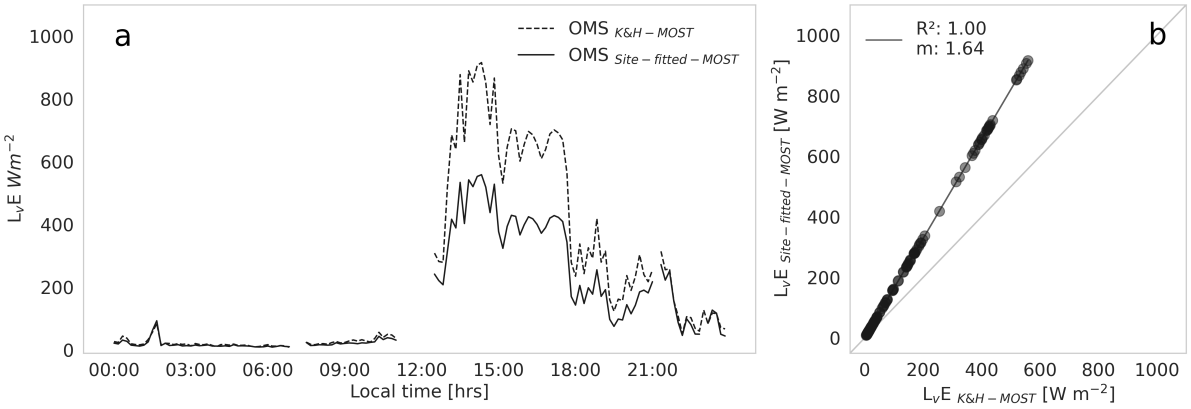

Figure 6.11: Diurnal cycle (a) and orthogonal regression (b, d) of latent heat flux from OMS data calculated with standard- and site-fitted MOST functions. m indicates the regression slope.

6.5 Conclusions

This paper studies the capability of an Optical-Microwave Scintillometer (OMS) to measure evaporation over a saline lake in a heterogeneous setting in the Atacama Desert. Our research question, "how accurate can the measurements of an OMS over an open water body be under arid conditions?", was inspired by the possibility of the OMS to be installed at the borders of an open water body. We conclude that the OMS is capable to measure open water evaporation without the need to install instrumentation in the water. However, care must be taken to not include (unwillingly) surrounding areas with contrasting flux regimes in the OMS footprint. We argue that with measurements below the blending height an enhanced level of temperature- and humidity fluctuations is observed. This is due to the passage of the scintillometer beam though the internal boundary layer that defines the transition between the different surfaces. As a result, Monin-Obukhov Similarity Theory (MOST) relations, needed to infer the sensible- and latent heat fluxes from the measured structure parameters of temperature and humidity, can potentially fail. The OMS dependence on the Monin-Obukhov Similarity Theory, which relies on the assumption of locally driven, undisturbed turbulence is a weakness that requires further study.

For our study focusing on a saline lake in the Salar del Huasco, the OMS deployment proved to be challenging due to the unstable ground near the water edge. We therefore extended the path such that the instrument transmitter and receiver were installed on stable ground with a waterlogged salt surface. The resulting scintillometer setup was defined by an installation height of 2.3 m (i.e. can be considered below the blending height) and a path-length of 1,070 m covering a mixed footprint of open water and a waterlogged salt surface with a daytime footprint coverage of ∼80% and ∼20% respectively. Relevant

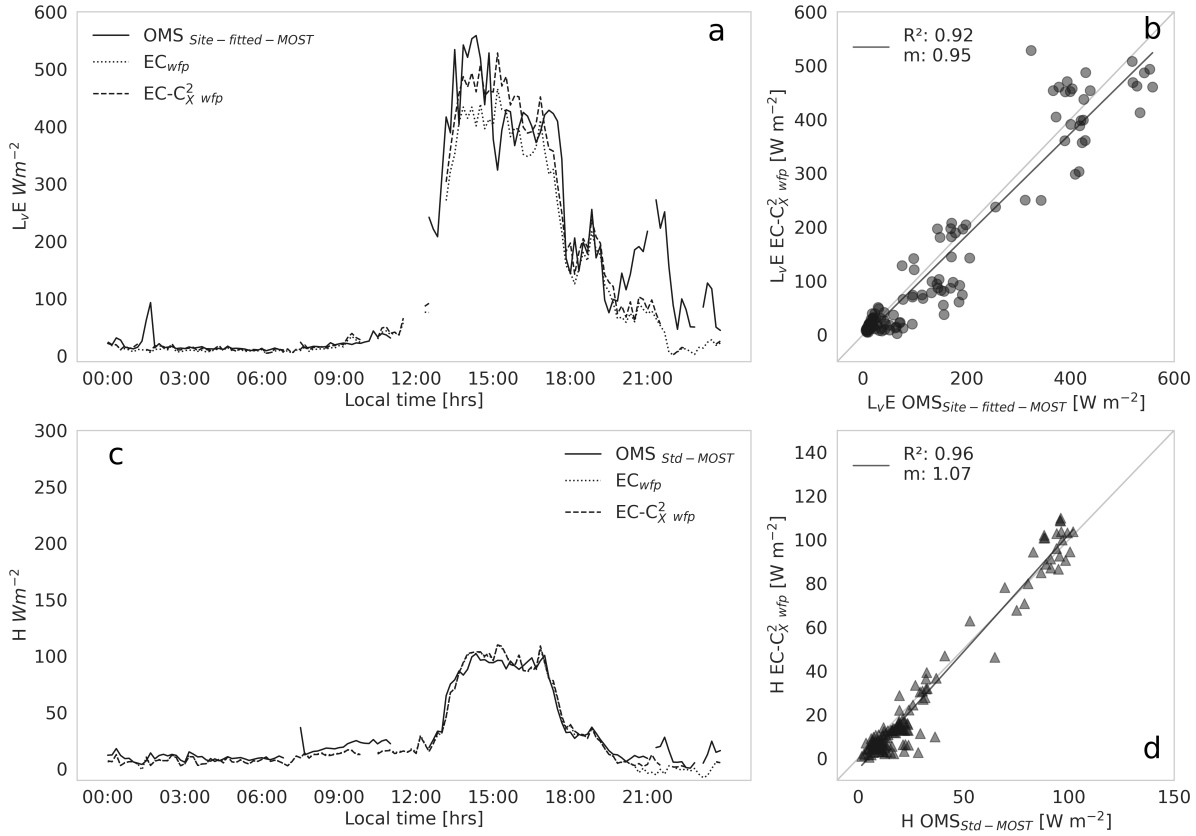

Figure 6.12: Diurnal cycle of surface fluxes (a, c) and orthogonal regression (b, d) between the OMS with site-fitted MOST functions and OMS-footprint weighted, direct EC flux estimates (EC_{wfp}) and indirect EC flux estimates through C_X^2 ($EC_{C_X^2,wfp}$). m indicates the regression slope, grey color refers to wet-salt and black to water. Triangles, circles and crosses are set to differentiate the data source.

in our evaluation and as a, we installed an Eddy Covariance (EC) system over the open-water and one over the wet-salt surface. Even though both surfaces in the footprint were water saturated, they were strongly heterogeneous in their flux regimes due to their different evaporation properties. In short, the amount of available energy was much less over the wet-salt surface compared to the water surface (maximum R_n values of 900 W m^{-2} over water versus 500 W m^{-2} over the wet salt) due to the larger albedo and lower surface temperature. The salt also impeded evaporation leading to $H > L_vE$ in contrast to the water surface where $L_vE > H$. The large contrast in fluxes was especially visible in L_vE values (maximum values of 75 W m^{-2} over wet-salt versus 550 W m^{-2} over water). For H values, the contrast was also notable but much less pronounced (maximum values of 200 W $^{-2}$ over wet-salt versus 100 W m^{-2} over water). In addition to the local heterogeneity, the fluxes were governed by a regional wind-driven turbulence regime with a low-wind, low flux regime during the night and morning and strong-wind, high flux regime during the afternoon.

The mixed footprint setup including a transition between the heterogeneous surfaces marked by disturbed turbulence made that our evaluation of the OMS fluxes against those measured by EC focused on the following three points. In our evaluation of the OMS fluxes against those measured by EC we addressed the heterogenous setting of the OMS measurements by critically evaluating the MOST functions, estimating an OMS footprint composing EC flux and discussing the regional scale driven turbulence regime. Concerning these three issues our main findings are:

First, we evaluated the Monin-Obukhov Similarity Theory (MOST) functions used to infer the OMS measured structure parameters to fluxes. We did this for both the scintillometer as well as the EC data derived structure parameters for temperature, C_T^2, and humidity, C_q^2. Here, we found that for C_T^2, our data correspond well to the standard MOST functions as determined by Kooijmans & Hartogensis (2016) which was based on many experiments. For C_q^2 however, we observe much higher OMS values than those based on the EC data. We attribute this to the aforementioned internal boundary layer disturbances at the transition between the surfaces. The OMS C_T^2 values are also somewhat higher than those from the EC data, but the difference is limited as the sensible heat flux contrast between the two surfaces is much less than that for C_q^2. To compensate for the elevated OMS C_q^2 values, we adopted a practical approach by using site-adapted MOST coefficients. We should note that our approach to adjust C_q^2 MOST functions to account for disturbances at the transition of the two heterogeneous surfaces assumes that the instrument was otherwise performing well. This was ensured by strict filtering the available data. In the end, we only used one day of data as the other days showed unphysically high scintillation intensities, likely due to a minor misalignment that might have caused surface reflections of the beam. Also, we strictly high pass filtered the raw 1 kHz data to exclude potential absorption fluctuations. Here, we adopted filter constants depending on the wind regimes.

Second, following the approach by (Meijninger et al., 2002a) for scintillometer measurements performed below the blending height, we validated the OMS against a composed flux consisting of OMS-footprint weighted EC fluxes over the two surfaces. In addition, we considered the non-linear relationship between structure parameters and surface fluxes in the footprint analysis that lead to an increase in EC composed L_vE of 15%. All things combined, we reach a zero-intercept linear regression with an R^2 of 0.92 and a slope of 0.95 when comparing the evaporation of the OMS against the OMS footprint composed EC estimates. We should note that the impact of the OMS site-adapted MOST coefficients on L_vE yielded a 34% reduction of the fluxes.

Third, we also discussed the influence of the regionally driven wind-regime that controls the boundary layer development and turbulent mixing and is responsible for the advection and entrainment of dry air to the study area. These aspects influence both the EC and OMS measurements. Judging by the differences in structure parameters derived

from the OMS and EC and how these influence the dimensionless MOST relations, it seems that the local MOST functions, in either the water or the wet-salt, are not really affected by these non-local disturbances.

Finally, the weakness of the OMS method is its dependence on the Monin-Obukhov Similarity Theory, which relies on the assumption of locally driven fluxes. This assumption is often violated in (semi-)arid regions where strong spatial contrasts in the temperature and humidity lead to temperature and humidity fluctuations that are driven by non-local processes such as regional circulations and internal boundary layers. Our approach was to introduce site-fitted MOST functions. We do not see this as a general solution but merely as a way to quantify the impact of the MOST violation. This is a challenge that we must overcome for the OMS to be used as a standard method for evaporation over open water bodies.

Chapter 7

Conclusions and Outlook

7.1 Conclusions

This thesis aimed to answer the overarching question: What are the physical mechanisms that drive evaporation in the Atacama Desert at multiple spatio-temporal scales? To address this, we broke the question down into four specific research questions. We have answered these questions in the following sections.

Chapter 3

What processes are involved in sub-diurnal, seasonal, and interannual open water evaporation variability?

We investigated the multi-temporal variability of actual evaporation from sub-diurnal to climatological scales in a high-altitude saline lake ecosystem in the Atacama Desert. Our findings revealed that evaporation from the saline lake of Salar del Huasco is controlled by different processes depending on the time scale. Firstly, at the sub-diurnal scale, the wind regime (aerodynamic contribution driven by wind shear) is the main driver of evaporation. The wind speed acts as a physical mechanism that is able to mix the saturated air above the water surface with the dry air of the surface layer. The absence of wind yields very low values of turbulence that act as a limiting factor of the surface turbulent fluxes. Secondly, at the seasonal scale, the principal driver is radiation (net available energy), which is characterized by significant seasonal variations. For example, maximum radiation rates are reached during spring (October, November and December), minimum ones during winter (July, August and September), and a high variability is observed during summer (January, February and March). Consequently, these radiative variations result in seasonal variation of evaporation. In analyzing the main contribution to the evaporation by using the Penman equation, we found the following: the radiative contribution is 73% of the seasonal changes in evaporation, during the periods in which radiation plays a principal role. Likewise, our analysis suggests that seasonal evaporation (related to seasonal radiation variability) is the principal driver of the decreases of lake water surface ($R^2 = 0.92$). In addition, our results show that seasonality of moisture transport at a synoptic scale correlates with seasonal variation of local evaporation. Thirdly, at an interannual scale, the ENSO phenomenon modulates evaporation mainly during summers, a phenomenon that also affects precipitation rates. We found that warm and cool ENSO phases are associated with higher evaporation and precipitation rates, respectively. Our results show that warm ENSO phases (El Niño) increase evaporation rates by 15%, whereas cool phases (La Niña) decrease it by 4%.

Chapter 4

In the interplay between regional and local scales, what is the role of the wind-induced turbulence in controlling the diurnal cycle of evaporation as compared to radiation and vapor pressure deficit?

We answered this question by investigating the diurnal variability of the physical processes that drive evaporation at the saline lake from regional to local spatial scales. Special attention was paid to the processes at a regional-scale and to the physical conditions that trigger them. Firstly, our findings show that the wind, governed by thermal and orographic differences on different spatial scales, is the main driver of evaporation in the Salar del Huasco. Here, and elaborating more in depth with respect to the results found at Chapter 3, we identify two main regimes. (1) The local morning regime is dominated by high net radiation and ground heat flux, low wind speed (< 2 m s^{-1}), a surface-atmosphere moisture gradient ($\sim$3 g kg^{-1}), and an extremely low latent heat flux ($\sim$0 W m^{-2}). During this regime, the principal limiting driver of evaporation is mechanical turbulence. Here, the absence of wind and low sensible heat flux, trigger to a stratification of the boundary layer. (2) The regional afternoon regime is dominated by high surface fluxes compared to the morning, where high wind speed (> 10 m s^{-1}), triggered by regional circulations, a very high surface-atmosphere moisture gradient ($\sim$10 g kg^{-1}), and a sudden increase in latent heat flux over the water ($\sim$500 W m^{-2}) was found. The same surface fluxes diurnal variability was found over all surfaces. Here, the decrease in net radiation in the transition to the evening becomes the limiting factor. Secondly, the regional afternoon regime also impacts the development of the atmospheric boundary layer (ABL), where vertical thermal profiles capped the convective boundary layer growth (up to 1,800 m) over the desert and water. This interruption is characterized by the entrance of air masses with different properties, resulting in a shallow (400 m), cooler, and relatively moist well-mixed boundary layer towards the evening. Finally, we provided an explanation of the origin of the wind in the afternoon regime. By systematically performing numerical experiments, we found that the regional circulation results from three interconnected atmospheric phenomena occurring at different spatial scales: (i) at approximately 1,200 m asl the top of the marine boundary layer (MBL) is characterized by a strong flow towards the land (15 m s^{-1}), (ii) an anabatic circulation driven by the contrast land-ocean (10 K) and (iii) channelling of the flow occurring at 3,000 m due to the topography, more specifically the wind movement through an Andes mountain pass. The concatenation of these three phenomena leads to the daily appearance of strong winds, which then enhances the mechanical turbulence and, thus, evaporation in the afternoon.

Chapter 5

What is the influence of the marine stratocumulus cloud in the formation, maintenance, and dissipation of the land-fog system in the Atacama Desert?

We approached this question by studying the interaction between marine stratocumulus (Sc) clouds and the coastal mountains of the Atacama Desert. More specifically, special attention was paid to the influence of the MBL on the land-fog system and the inland moisture transport. Our findings, based on discontinues profile observation of station located at the coastal cliffs, show that this interaction involves either a well-mixed regime or a thermal stratification of the MBL, which forms or dissipates Sc cloud-fog. The well-mixed regime is characterized by low gradients of potential temperature ($< 3.10 \cdot 10^{-3}$ K m^{-1}) and specific humidity ($< 1.60 \cdot 10^{-3}$ g kg^{-1} m^{-1}). These well-mixed conditions, driven mainly by the marine Sc cloud deck, have a small diurnal variability. The predominance of the well-mixed regime correlates with the presence of fog quantified by observations ($\sim$1.5 L hour^{-1}), which were measured in the morning and evening-night. The stratified regime is characterized by high gradients of potential temperature ($> 3.10 \cdot 10^{-3}$ K m^{-1}) and specific humidity ($> 1.60 \cdot 10^{-3}$ g kg^{-1} m^{-1}). In contrast to the other regime, this stable regime is affected by diurnal variability, which displays significant changes on diurnal gradients around midday. The thermal stratification corresponds with fogless observations. These clear conditions were mainly observed between 12:00 and 20:00 LT. Therefore, we can conclude that the stratified regime leads to optimal conditions for the dissipation of Sc cloud-fog. The thermodynamic classification of the MBL, and its interaction with the coastal mountains of the Atacama Desert, enable to explain the role of marine Sc clouds in fog formation and inland moisture transport. Both phenomena contribute to decreases the MBL temperature, increasing the ocean-land thermal contrast that drives the regional flow affecting the Altiplano region's evaporation, as discussed in Chapter 4.

Chapter 6

How accurate are the evaporation measurements performed by an OMS over an open water body under arid and windy atmospheric conditions?

We addressed this question by studying the capability of an Optical-Microwave Scintillometer (OMS) to measure evaporation over a saline lake in a heterogeneous setting in the Atacama Desert. We paid special attention to the very localized conditions like surface heterogeneity (surface energy balance, albedo, roughness length, and footprint)

and ABL dynamics. In evaluating the OMS fluxes against those measured by the eddy-covariance (EC), we critically evaluated the Monin-Obukhov Similarity Theory (MOST) functions to determine its validity under heterogeneous surface conditions. To this end, we estimated an OMS footprint composing EC flux and discussing the regional scale driven turbulence regime. Considering these three issues, we reached several conclusions. Firstly, we found that for the structure parameter of temperature (C_T^2), our data corresponded well to the standard MOST functions as determined by Kooijmans and Hartogensis (2016). For the structure parameter of humidity (C_q^2), however, we observed much higher OMS values compared to the EC data. We attributed this to the formation of an internal boundary layer disturbance at the transition between the surfaces. To account for the effects of this internal boundary layer in our observations, we adopted a practical approach by using site-adapted MOST coefficients. Secondly, we validated the OMS against a composed flux consisting of OMS footprint-weighted EC fluxes over the water and wet salt surfaces, considering the non-linear relationship between structure parameters and surface fluxes in the footprint analysis. All things combined, we reached a zero-intercept linear regression (R^2 of 0.92) between evaporation measured by the OMS and composed EC fluxes, where the impact of the site-adapted MOST coefficients yielded a 34% reduction in evaporation fluxes. Thirdly, we discussed the influence of the regionally driven wind regime that controls the boundary layer development and turbulent mixing (Chapter 4). These aspects influenced both the EC and OMS measurements. However, it seems that the local MOST functions, in either the water or the wet salt, were not affected by these non-local disturbances. Finally, we concluded that the OMS instrument is able to measure open water evaporation without the need of installing instrumentation in the water. In doing these observations, it is important to take care in not including (unwillingly) surrounding areas with contrasting flux regimes in the OMS footprint. Despite this, the OMS dependence on the MOST, which relies on the assumption of locally driven, undisturbed turbulence, is a weakness that requires further study.

Concluding words

As an overarching conclusion, this thesis improves our understanding of the physical processes that govern evaporation in the Atacama Desert, both from multi-temporal and -spatial perspectives.

From larger to smaller temporal scales, evaporation is controlled by different processes that modulate, regulate or control it. On an interannual scale, local evaporation of the Salar del Huasco is modulated by the ENSO global-scale phenomenon, which sets the climatic conditions that enhance or decrease evaporation. One condition occurs during the warm ENSO phases (El Niño), where evaporation anomalies increase by 15%, and during cool ENSO phases (La Niña), evaporation anomalies decrease by 4%. The mod-

ulation that ENSO produces on evaporation is only present during the summer, when ENSO effects on climate conditions are significant. On a seasonal scale, radiation contributes to 73% of the total evaporation, whereas the aerodynamic component constitutes 27%. This regulation that radiation exerts on evaporation is based on its seasonal variability. For example, evaporation rates and radiation are at its minimum during winter and maximum during late spring. Likewise, both variables show high scattering during summer as a result of the cloudy and rainy seasons. On a sub-diurnal temporal scale, local evaporation is mainly controlled by wind-driven mechanical turbulence. The absence of wind speed during the morning represents the principal limiting factor because, without wind (shear) and in the presence of low sensible heat flux (buoyancy), no physical mechanisms exist to transport the saturated air from the wet surfaces into the dry atmosphere. During the afternoon, the arrival of a strong flow triggers evaporation, which decreases accordingly with decreases in net radiation that represent the limiting factor at the end of the day.

Evaporation on a sub-diurnal scale is also governed by different physical processes that interact at different spatial scales. At local scales, the surface heterogeneity controls the amount of energy available to produce surface fluxes and the soil moisture available to evaporate. For example, high net radiation is found at the water surface because of its lower albedo compared to the wet-salt surface, resulting in higher evaporation fluxes. Likewise, higher evaporation fluxes are observed over wet-salt surfaces than over the desert surfaces, due to higher soil moisture availability. These surface conditions interact with the main driver of evaporation, the wind speed. At a very localized scale, this interaction triggers the formation of internal boundary layers over the heterogeneous surfaces, which contribute to the development of the ABL above the so-called blending height. However, this interaction remains unclear and needs further research. Surface conditions control the ABL development during the morning and non-local processes during the afternoon. During the morning, the ABL shows a convective growth over the desert and the lake, reaching approximately 1,800 m above the ground. This growth is interrupted at noon by the arrival of a regional-scale flow, which brings in cooler and relatively moister air masses compared to those present at the Salar del Huasco. This advection results in a shallow and well-mixed ABL towards the evening. Finally, on a larger-scale perspective, the regional flow that interrupts the ABL convective growth and impulses the local evaporation over wet surfaces during the afternoon results from the thermal contrast between the Pacific Ocean and the Atacama Desert. This thermal contrast, which increases up to 10 K during the afternoon, produces a strong land-sea breeze from above the MBL towards the Andes. An anabatic flow enhances the land-sea breeze at the piedmont of the Andes, where simultaneously, the shape of the topography channels the breeze. This breeze, driven by the ocean, brings to the Salar del Huasco air masses with different temperatures, humidity, and momentum that enhance evaporation in the Altiplano region.

7.2 Outlook

With our results, based on systematic surface and airborne observations and complemented by numerical simulations with a high resolution around the observational site, we were able to identify, characterize and quantify the complex physical processes that control evaporation at multi-spatiotemporal scales. However, the scientific challenge of quantifying the water resources in arid regions relies on accurately representing these physical processes in hydrometeorological models. For this purpose, further research must address the temporal variability of evaporation from different surfaces located in different areas of the Altiplano, the seasonality of the regional-scale flow, the interaction between wet surfaces and the surface layer, the representativity of our findings in the Salar del Huasco in similar environments, and the role of evaporation on the water balance.

The findings on the temporal variability of open water evaporation from sub-diurnal to climatic scales at the saline lake of the Salar del advances our understanding of how long-term processes affect our water resources. However, open waters are not the most extended evaporation pathways in the Atacama Desert. Therefore, expanding our understanding of long-term evaporation variability over other surfaces like wet-salt, dry-salt, wetlands, and sparse vegetation over shallow groundwater is crucial for quantifying water loss at the basin-scale. In this regard, we still need to learn about the role of salt chemistry as a limiting factor on the evaporation of such surfaces, as well as the stomata resistance of such water-stressed plants that compose the so-called bofedales (wetlands of the Altiplano region).

Regarding larger spatial scales (>100 km), the description, quantification, and simulation of the ocean-land regional flow that controls the sub-diurnal evaporation in the Altiplano region analysed in this thesis contribute to connecting the non-local processes with the local evaporation. However, further research must be carried out in order to understand the regional flow's seasonal variability. It is essential to bridge this knowledge gap by more effectively quantifying the relationship between this variability and the MBL, which controls the thermal contrast that produces such flow. Special attention must be paid to how synoptic-scale systems, more specifically high-pressure systems, like the formation of the stratocumulus cloud deck over the ocean affect this regional flow. Likewise, it is crucial to comprehend the synoptic-scale summer flow, which controls the rainy season and affects evaporation. Moving to more local scales, during this thesis, we used observations to describe the ABL dynamic and its interaction with heterogeneous surfaces. Nonetheless, there is still a lot to learn here, for example, the ABL interaction with non-local phenomena such as entrainment, gravity waves, and rainstorms and the formation of dust devils and their impact on evaporation. In so doing, we will be able to find better parameterizations of these phenomena to be implemented on larger-scale weather and climate models. Likewise, we need to improve our understanding of the interaction of heterogeneous surfaces with the regional advection and the consequent for-

mation of internal boundary layers at a very localized scale. Finally, it is worth exploring the exchange between the atmosphere and the groundwater, which is one of the least understood flows of the water balance.

Our findings in the Salar del Huasco allow us to better understand most of the scales and processes involved in the evaporation in such a place. Even though the Salar del Huasco is one of the smallest basins ($\sim$1,400 km^2) in the Altiplano region that presents significant features for studying evaporation, the representativity of our findings must be corroborated in basins with different spatial scales, topography, and location. For example, in catchments like Salar de Uyuni, with an area of $\sim$60,000 km^2 and a salt surface of $\sim$10,000 km^2, the roles of the surface, the ABL, and regional flow might impact the evaporation budget differently not only because of its differing spatial scale but also due to the topography and the fact that it is located farther from the ocean. Likewise, in high-altitude lakes such as the Titikaka lake ($\sim$8,000 km^2) and Poopo lake ($\sim$3,000 km^2), each of which has greater depth and thus a different albedo, the surface energy balance might play a more relevant role than larger-scale atmospheric flows.

Finally, further research should be done on the adaptation of evaporation budget methods, like the Penman equation, to the specific physical conditions of the desert, such as surface heterogeneity conditions, non-local processes, and regional advection influences. These adaptations would allow us to measure using an evaporation-budget method adapted to arid regions that could be implemented through parameterizations in larger-scale hydrometeorological models. In addition, more evaporation observations and experiments in different environments are needed, especially in salt flats with diverse chemical compositions, in wetlands, over snow cover, etc, promoting constant and long-term weather monitoring. All this with the aim of quantifying accurately the water balance, and therefore, contributing to improve water resource management in arid regions.

Chapter 8

Appendix

Appendix A: Site-adapted Penman Equation

Here, we introduce the radiative and aerodynamic contributions to the Penman (1948) equation. We also provide a physical meaning to the two coefficients used in the modified Penman equation: the coefficient to compensate for the absence of surface energy balance closure (c_{EBNC}) and the coefficient to account for the ice conditions (c_{ice}) above the saline lake of Salar del Huasco. The modified Penman equation reads as:

$$L_vE = \overbrace{c_{ice}\frac{s}{s+\gamma}c_{EBNC}(R_n - G)}^{\text{Radiative}} + \overbrace{\frac{\rho_a c_p}{s+\gamma}\frac{1}{r_a}(e_s - e)}^{\text{Aerodynamic}}, \tag{8.1}$$

where s [Pa K^{-1}] is the slope of the saturated vapor pressure curve, γ [Pa K^{-1}] is the psychrometric constant, R_n [W m^{-2}] is the net radiation, G [W m^{-2}] is the ground heat flux, ρ [kg m^{-3}] is the dry air density, c_p [J K^{-1} kg^{-1}] is the air's specific heat at constant pressure, r_a [s m^{-1}] is the aerodynamic resistance, e_s [Pa] is the saturated vapor pressure, T_a [K] is the air temperature, and e [Pa] is the vapor pressure at a measured level. Below, we detail the calculation and justification of each term in equation 8.1.

A1 Radiative contribution

The radiative contribution to the latent heat determined from Equation 8.1 depends on the available energy, i.e., R_n – G. Net radiation, R_n, is estimated as:

$$R_n = Sw_{in} - Sw_{out} + Lw_{in} - Lw_{out} = (1-\alpha)Sw_{in} + Lw_{in} - Lw_{out} \tag{8.2}$$

where Sw_{in} [W m^{-2}] is the incoming shortwave radiation, which is provided by the ERA5 dataset (Hersbach et al., 2020); Sw_{out} [W m^{-2}] is the outgoing shortwave radiation; $\alpha = 0.13$ [-] is the albedo, obtained during the E-DATA field campaign (Suárez et al., 2020; Lobos-Roco et al., 2021b); Lw_{in} [W m^{-2}] is the incoming longwave radiation; and Lw_{out} [W m^{-2}] is the outgoing longwave radiation.

The Lw_{in}, which includes the cloud influence, is calculated using the model suggested by Sugita & Brutsaert (1993). This model corrects the clear-sky incoming longwave radiation ($Lw_{in,cs}$) calculated with the Stefan Bolztmann law, in the following way:

$$Lw_{in} = Lw_{in,cs}(1 + c_1 c_f^{c2}) = \sigma\epsilon T_a^4(1 + c_1 c_f^{c2}) \tag{8.3}$$

where σ is the Stefan Boltzmann constant ($5.67 \cdot 10^{-8}$ W m^{-2} K^{-4}); ϵ=0.68 is the air emissivity, which is derived from E-DATA measurements, and T_a is the air temperature at 2-m height, obtained from ERA5 downscaled data; and are empirical constants (Sugita & Brutsaert, 1993); and c_f is the cloud factor proposed by Crawford & Duchon (1999):

$$c_f = 1 - \frac{Sw_{in}}{0.9c_s} \tag{8.4}$$

Here, c_s corresponds to the extraterrestrial incoming shortwave radiation multiplied by 0.9 to get the percentage of radiation that reaches the surface at ∼4,000 m asl empirically determined during the E-DATA experiment.

The Lw_{out} is calculated using the methodology suggested by Holtslag & Van Ulden (1983):

$$Lw_{out} \equiv \sigma T_a^4 c_3 R_{n,ini} \tag{8.5}$$

where $c_3 = 0.02$ is an empirical coefficient, and $R_{n,ini}$ corresponds to an initial value of net radiation, estimated as $0.76Sw_{in}$, according to E-DATA observations (Suárez et al., 2020). Then, $R_{n,ini}$ is solved iteratively using the following expression:

$$R_{n,ini} = (1 - \alpha)Sw_{in} + Lw_{in} - Lw_{out} \tag{8.6}$$

One iteration consists of solving Equation 8.5 using $R_{n,it}$. The value of Lw_{out} is then used in Equation 8.6 for solving $R_{n,it}$. Finally, this new value of $R_{n,it}$ is used again in Equation 8.6. After ten iterations, Lw_{out} values do not change significantly.

The ground heat flux, G, which is required to estimate the available energy, is determined as a function of net radiation as:

$$G = c_4 R_n \tag{8.7}$$

where $c_4 = 0.25$ corresponds to an empirical coefficient based on the R_n/G ratio observed during the E-DATA experiment for $Sw_{in} > 50$ W m^{-2}.

Figure 8.1 shows an orthogonal regression estimated through this model and Rn-obs observed over the saline lake, which validates the net radiation estimated by the model (see equation 8.2).

A2 Aerodynamic contribution

To calculate the aerodynamic term (equation 8.1), we use T_a, specific humidity, q, and wind speed at 2 m, U, from the ERA5 downscaled dataset (Chapter 3). We parametrize the aerodynamic resistance term, r_a, by prescribing values for the two wind regimes observed by Lobos-Roco et al. (2021b). Figure 8.2 shows the prescribed values for r_a , being r_a= 60 s m^{-1} for $U > 3$ m s^{-1} (windy regime during the afternoon) and r_a= 250 s m^{-1} for $U < 3$ m s^{-1} (calm regime during the morning). This prescription is given by the

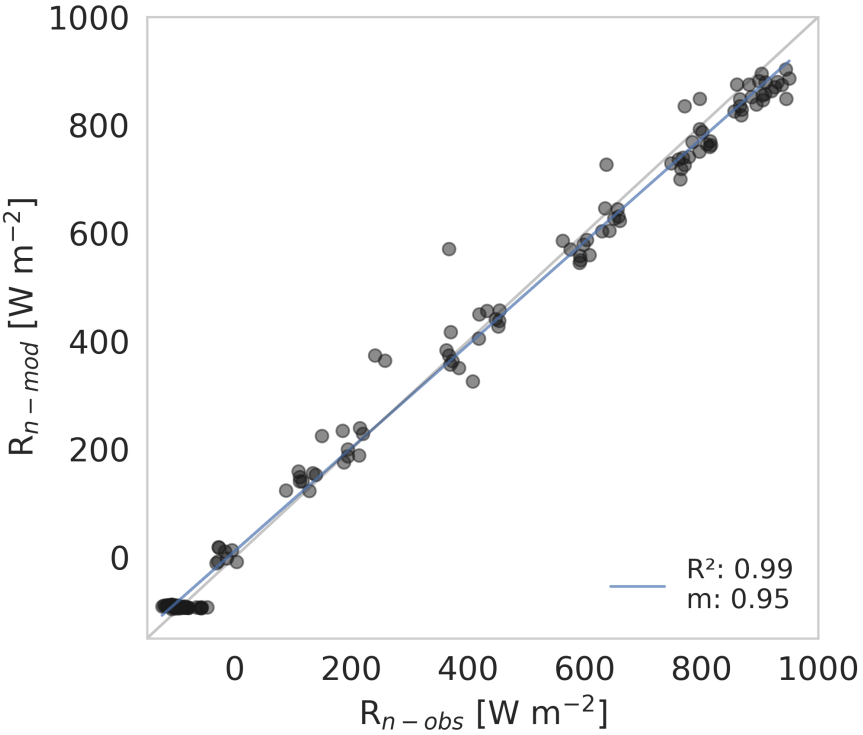

Figure 8.1: Orthogonal regression between Rn observed in the E-DATA field campaign and that modeled using equation 8.1.

rapid change of r_a in the transition of the two diurnal wind regimes, where these values are representative. It is important to stress two aspects that justify this prescription. Firstly, there are no significant changes in the aerodynamic contribution term of Equation 8.1 when $r_a > 200$ s m^{-1}. For this reason, we decide to use a wind regime averaged value. Secondly, the main idea behind estimating evaporation through Equation 8.1 is to use standard meteorological data readily available in a simple way.

The saturated vapor pressure, e_s, which is also required in the aerodynamic contribution term, is approximated using the August–Roche–Magnus equation (Moene & Van Dam, 2014):

$$e_{sat}(T_{ak}) = 611 exp[\frac{a(T_{ak} - 273.15)}{-b + T_{ak}}] \tag{8.8}$$

where T_{ak} [K] is the absolute air temperature obtained from the ERA5 downscaled data, and a and b are 17.625 and -30.03, respectively.

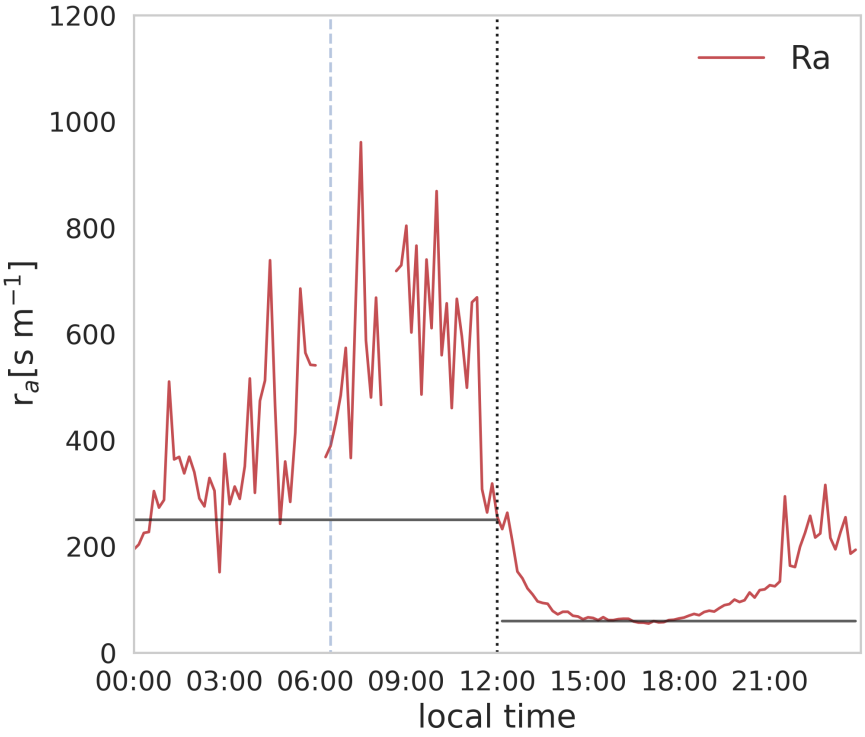

Figure 8.2: Diurnal averaged aerodynamic resistance observed above the water surface during the E-DATA, and the black lines are the prescribed values under calm and windy regimes.

A3 Energy balance non-closure coefficient

Since the Penman equation assumes a perfect energy balance closure, and the E-DATA field data show a significant energy imbalance (Suárez et al., 2020), we introduce the energy balance non-closure coefficient, c_{EBNC}. Hence, this coefficient corrects the available energy to improve the energy balance closure. We observe two different non-closure balances that depend on the wind regime (Fig. 8.3). Therefore, we set $c_{EBNC} = 0.3$ for $U < 0.3$ m s^{-1} (calm regime during the morning) and $c_{EBNC} = 0.7$ for $U > 3$ m s^{-1} (windy regime during the afternoon).

A4 Ice coefficient

Ice formation significantly restricts evaporation because it isolates the water from the atmosphere below a thin ice cover. Then, in the absence of wind, the available energy is used first to melt the ice before water evaporation occurs. Vergara-Alvarado (2017) demonstrated that a ∼3-5 cm thick ice cover in the Salar del Huasco saline lake reduced the turbulent fluxes to zero by creating an isolating layer between the water surface and the atmosphere. Thus, neglecting ice formation leads to an overestimation of the latent heat flux. A complete ice model requires the derivation of heat transfer fluxes or an elaborated parameterization using variables and parameters that usually are not available

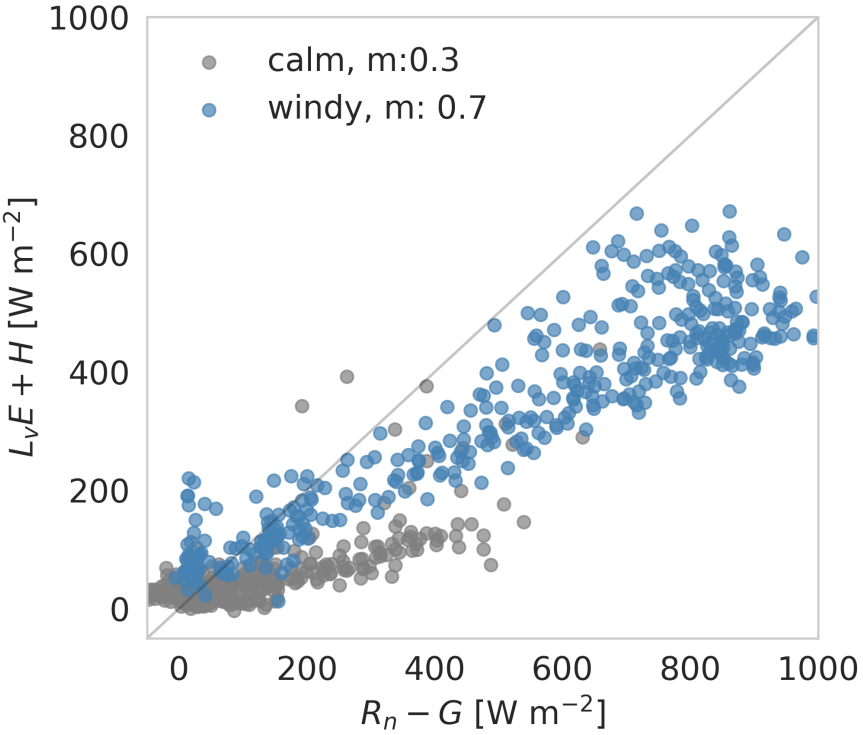

Figure 8.3: Surface energy balance observed at the water surface during the E-DATA under calm and windy regimes.

in standard meteorological datasets (Echeverría et al., 2020). For this reason, we use an ice coefficient, c_{ice}, which ranges between 0 and 1, that is related to the number of hours under freezing conditions. We assumed that ice melting occurs when air temperatures are below 270 K. Table 8.1 shows the categorization of the freezing hours (FH) and the corresponding c_{ice}. Figure 8.4 shows the effect that the ice coefficient has in estimating latent heat flux during freezing days together with a time series of the freezing hours during the E-DATA.

Table 8.1: Categorization of freezing hours and the ice coefficient.

Freezing hours (FH)	Ice coefficient c_{ice}
$8 >$ FH	0.30
$4 <$ FH < 8 for day	0.40
$4 <$ FH < 8 for night	0.78
FH < 4	1.0

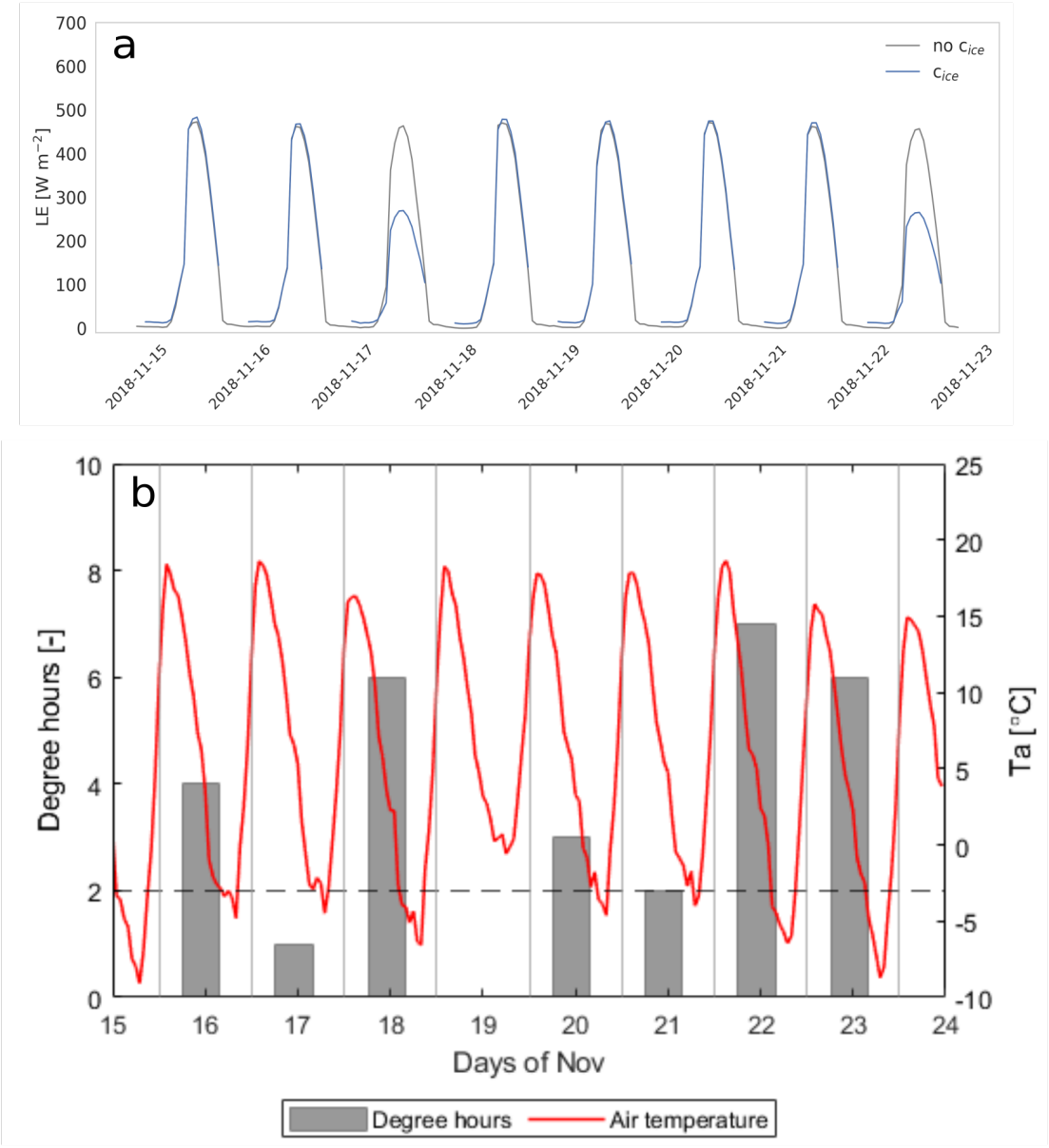

Figure 8.4: (a) The effect of the ice coefficient into the site-adapted Penman evaporation estimates. (b) Degree hours and air temperature time series.

Appendix B: Uncertainty of E-DATA observations

In this section we briefly address the uncertainties related to surface and airborne measurements performed during the E-DATA field experiment and the WRF modeling results. Complementary information can be found in Suárez et al. (2020).

B1 Surface observations

The Eddy Covariance (EC) method is regarded as the most reliable method to measure L_vE and H fluxes. However, energy balance non-closure (Eder et al., 2014; Mauder et al., 2007) is found everywhere. Our results show imbalances of the SEB that range between 15 and 30% (Suárez et al., 2020), which agrees with several field experiments performed in the last decades (Eder et al., 2014). In addition, some instrumental issues might contribute to measurement uncertainties related to the following three reasons: (1) to obtain R_n over the desert and wet-salt surfaces we used a less accurate sensor that did not measure all four radiation components, as opposed to that used at the water surface. For that reason, R_n over the desert was corrected (see section 4.3.1) due to the unrealistic values we obtained. However, R_n measurements might still mean an overestimation of the wet-salt surfaces, which would contribute to energy balance closure problems; (2), G was measured using soil flux plates buried 5 cm from the air-surface interface (desert, water, and wet-salt surfaces). Consequently, G must be corrected to account for heat storage in the soil or in the water body. The different surfaces complicated the installation of the soil sensors, which might underestimate G, which is an important component of the SEB at the SDH (de la Fuente & Meruane, 2017); (3) The exchange processes on larger scales might have a significant influence on the energy balance, due to the landscape heterogeneity (Foken, 2008). Advection and entrainment phenomena might add uncertainty to the SEB balance. However, our measurements limit us to evaluated them properly, and they are beyond the scope of this study.

B2 Airborne observations

The uncertainty of the airborne measurements is related to the sensors carried by the radiosonde and UAV, the measurement footprints and to the disturbance the UAV's propellers might have caused to the sensor. Firstly, the sensors carried by the radiosonde and UAV were different models from the same manufacturer (Table 2.1), which might have led to differences in the observations. Secondly, the flight path (measurement footprint) followed by the two instruments was not exactly the same, in that the radiosonde flew at a height of around 10 km and up to 50 km NE of the launch site, while the UAV flew at an altitude of only 500 m from the launch site, with no horizontal travel. This means that different measurements of the vertical air column were made, which contributed to the uncertainty. Finally, to avoid the UAV's propellers disturbing the sensor during the take-off, we only use the profiles obtained during UAV landing, i.e. from 500 m to ground

level. Nevertheless, during the landing, the propellers also might affect, although to a lesser extent, the sensor readings.

Appendix C: Desert and wet-salt wind, temperature, and moisture conditions

Similar to Figure 4.4 in Chapter 4, Figures 8.5 and 8.6 of this appendix show the mean diurnal cycle of wind speed and direction, aerodynamic resistance, thermal and moisture gradients between the surface and the measurement level for desert and wet-salt surfaces. These figures support the homogeneous wind conditions (a, b) in the SDH-basin and contextualize the heterogeneous thermal (c) and moisture (d) gradients between the surface and the measurement height.

Appendix D: Calculations of contributions to tendency term $\partial q/\partial t$ and $\partial\theta/\partial t$ in Table 4.3

According to Equations 4.3 and 4.4, the tendency terms $\partial q/\partial t$ or $\partial\theta/\partial t$ shown in Table 4.3 represent the change of potential temperature and specific humidity within the boundary layer during a specified time period. These tendencies are calculated as the average of well-mixed values of θ and q taken by the radiosoundings launched at 15:00 and 18:00 LT. For instance, over the desert site, Figure 4.8a indicates a θ difference of $\sim$1 K between 15:00 and 18:00 LT, i.e. a tendency term is 0.33 K per hour. The local contribution corresponds to the turbulent fluxes, $\overline{w'q'_s}$ (L_vE) and $\overline{w'\theta'_s}$ (H) in the right-hand side of equations 4.3 and 4.4. This contribution is calculated using the averages surface fluxes (Fig. 4.3) and the averaged boundary layer height (Fig. 4.8) over the same time period. For example, for the desert site we measured $\sim$0 W m^{-2} of latent heat flux between 15:00 and 18:00 LT at a height of 500 m. The non-local contribution corresponds to the entrainment flux, $\overline{w'q'_e}$ and $\overline{w'\theta'_e}$ in the right-hand side of equations 4.3 and 4.4. This is calculated by using the vertical velocity obtained from the boundary layer growth and time (Δh/Δt), and the change in the maximum vertical gradient, Δq or $\Delta\theta$ between the same time period. Following the example of the desert, between 15:00 and 18:00 LT (Δh/Δt) presents a small change and Δq has almost no change, then no entrainment contribution was considered. Finally, the regional contribution corresponding to the larger-scale circulation quantifies the mean horizontal wind and the horizontal gradient of θ and q. This is the second term of the right-hand side of equations 4.3 and 4.4. In the absence of observations of the horizontal gradients and aiming to characterize the contribution using exclusively the observations gathered in E-DATA, the regional advection is estimated as a residual of each equation. Following the example above, at the desert surface between 15:00 and 18:00 LT there is no turbulent fluxes neither entrainment

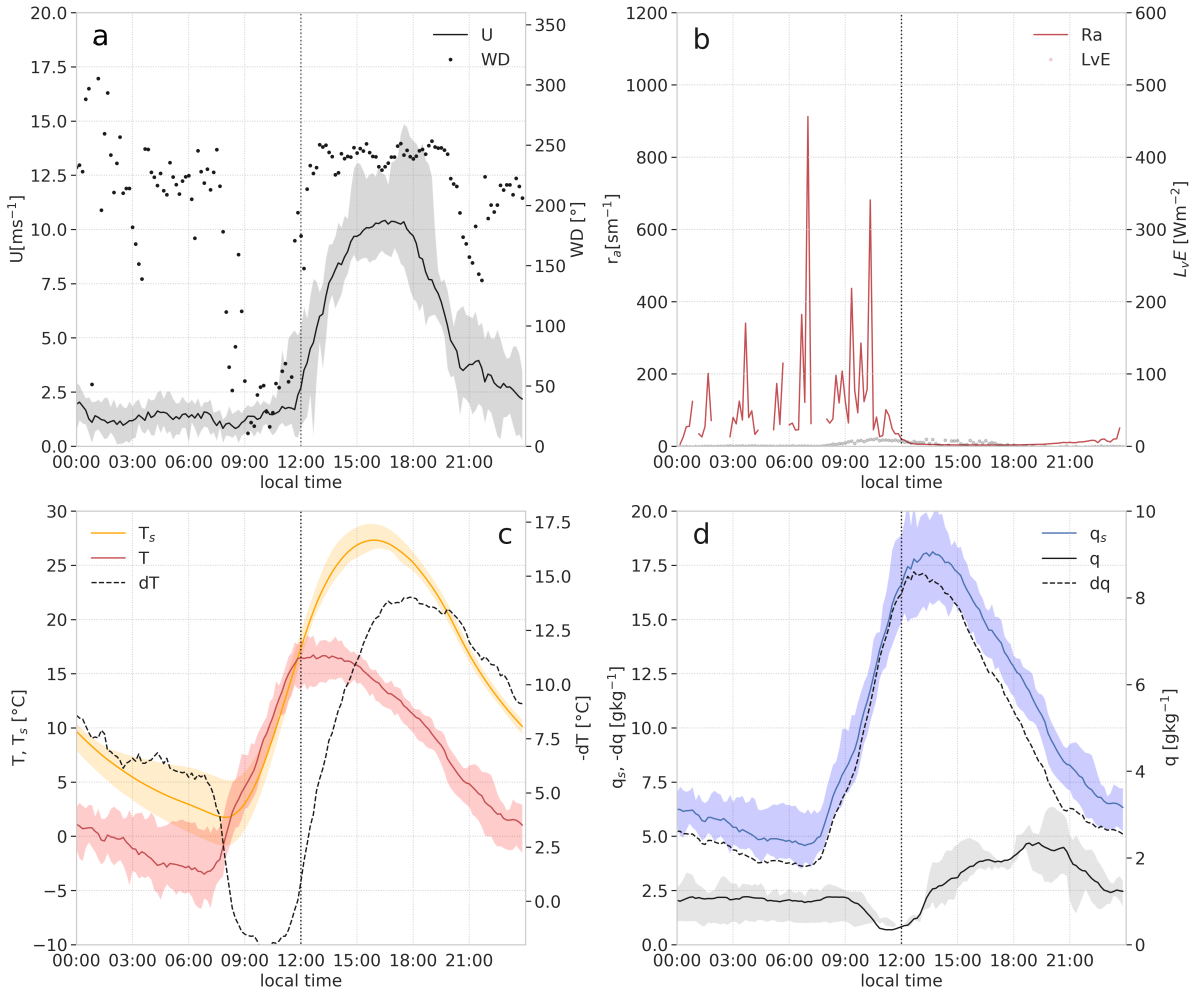

Figure 8.5: (a) Mean diurnal cycle of wind speed (U) and wind direction (WD) of a representative day (November 18^{th}), (b) mean diurnal cycle of aerodynamic resistance (r_a), (c) air temperature (T), surface temperature (T_s) and thermal gradient ($-dT$) and (d) air specific humidity (q), surface saturated specific humidity (q_s) and moisture gradient ($-dq$) observed over the **desert** surface. Vertical dotted lines indicate time of turbulent regime change and shadings represent maximum and minimum observations. Observations from November 15^{th}-24^{th} 2018.

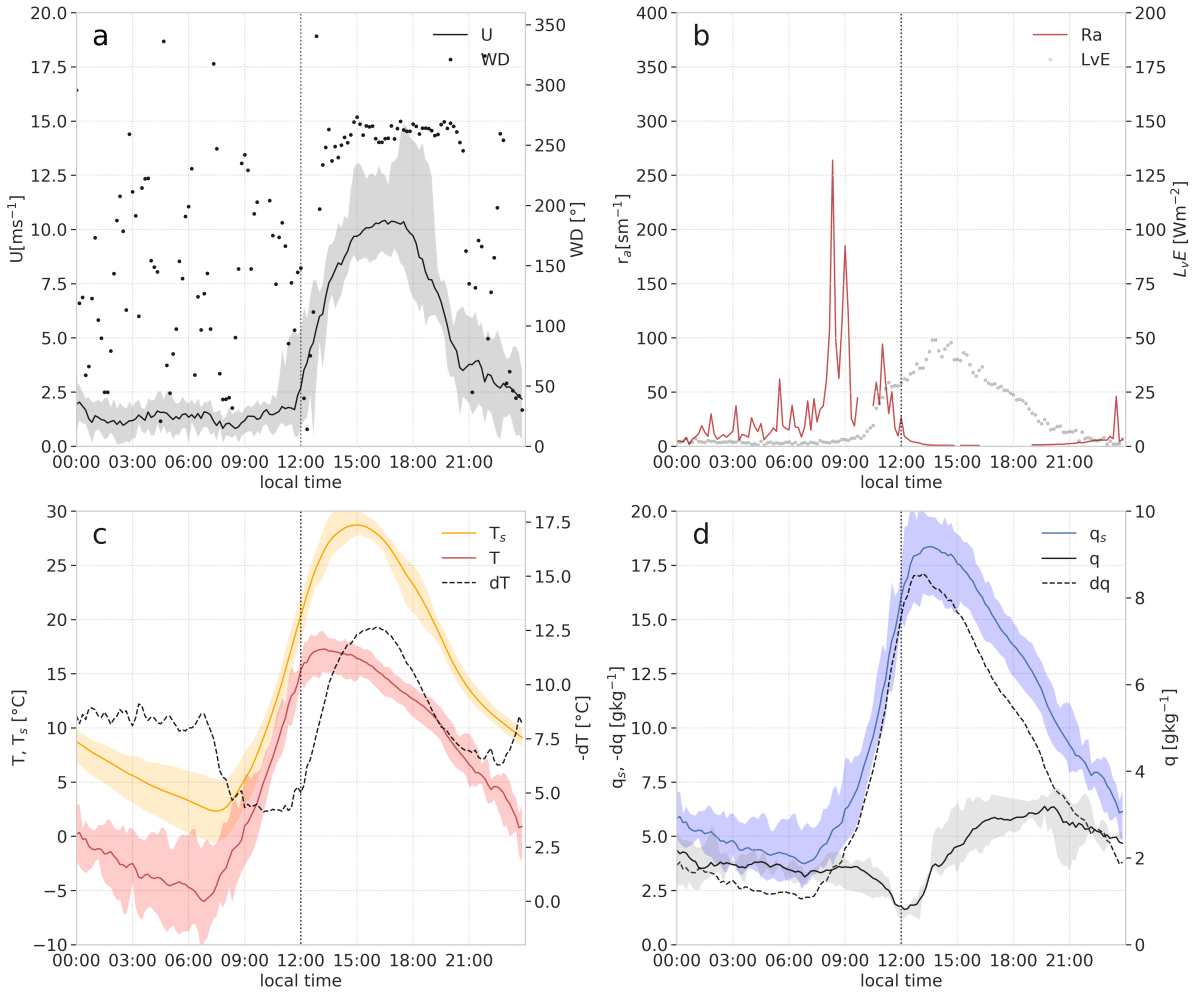

Figure 8.6: (a) Mean diurnal cycle of wind speed (U) and wind direction (WD) of a representative day (November 18^{th}), (b) mean diurnal cycle of aerodynamic resistance (r_a), (c) air temperature (T), surface temperature (T_s) and thermal gradient ($-dT$) and (d) air specific humidity (q), surface saturated specific humidity (q_s) and moisture gradient ($-dq$) observed over the **wet-salt** surface. Vertical dotted lines indicate time of turbulent regime change and shadings represent maximum and minimum observations. Observations from November 15^{th}-24^{th} 2018.

fluxes to $\partial q/\partial t$ because the latent heat flux is $\sim$0 W m^{-2} and Δq is constant. However, the tendency term is 0.2 g kg^{-1} per hour. This means that according to the budget equation (4.4), the only way to have a positive tendency of moisture is through the larger-scale advection.

References

Abtew, W., & Melesse, A. (2012). *Evaporation and evapotranspiration: measurements and estimations*. Springer Science & Business Media.

Aceituno, P. (1988). On the functioning of the southern oscillation in the south american sector. part i: Surface climate. *Monthly Weather Review*, *116*, 505–524.

Aceituno, P. (1992). El Niño, the Southern Oscillation, and ENSO: Confusing names for a complex ocean–atmosphere interaction. *Bulletin of the American Meteorological Society*, *73*, 483–485.

Ameriflux (2021). https://ameriflux.lbl.gov/.

Batchvarova, E., & Gryning, S. E. (1998). Wind climatology, atmospheric turbulence and internal boundary-layer development in Athens during the MEDCAPHOT-TRACE experiment. *Atmospheric Environment*, *32*, 2055–2069.

Beyrich, F., Bange, J., Hartogensis, O. K., Raasch, S., Braam, M., van Dinther, D., Graf, D., van Kesteren, B., van den Kroonenberg, A. C., Maronga, B. et al. (2012). Towards a validation of scintillometer measurements: the litfass-2009 experiment. *Boundary-layer meteorology*, *144*, 83–112.

Blin, N., Hausner, M., Leray, S., Lowry, C., & Suárez, F. (2021). Potential Impacts of climate change on an aquifer in the arid Altiplano, northern Chile: the case of the protected wetlands of the Salar del Huasco basin. Manuscript Accepted. *Journal of Hydrology: Regional Studies*, *0*.

Böhm, C., Reyers, M., Schween, J. H., & Crewell, S. (2020). Water vapor variability in the atacama desert during the 20th century. *Global and Planetary Change*, *190*, 103192.

Bretherton, C. S., & Park, S. (2009). A new moist turbulence parameterization in the community atmosphere model. *Journal of Climate*, *22*, 3422–3448.

de Bruin, H., Hartogensis, O., Allen, R., & Kramer, J. (2005). Regional advection perturbations in an irrigated desert (rapid) experiment. *Theoretical and applied climatology*, *80*, 143–152.

de Bruin, H., Van den Hurk, B., & Kohsiek, W. (1995). The scintillation method tested over a dry vineyard area. *Boundary-Layer Meteorology*, *76*, 25–40.

Budds, J. (2004). Power, nature and neoliberalism: the political ecology of water in chile. *Singapore Journal of Tropical Geography*, *25*, 322–342.

Businger, J. A., Wyngaard, J., Izumi, Y., & Bradley, E. F. (1971). Flux-profile relationships in the atmospheric surface layer. *Journal of Atmospheric Sciences*, *28*, 181–189.

Cereceda, P., Larraín, H., Lázaro, P., Osses, P., Schemenauer, R., & Fuentes, L. (1999). Campos de tillandsias y niebla en el desierto de Tarapacá. *Revista de Geografía Norte Grande*, *13*, 3–13.

Cereceda, P., Larrain, H., Osses, P., Farías, M., & Egaña, I. (2008a). The climate of the coast and fog zone in the Tarapacá Region, Atacama Desert, Chile. *Atmospheric Research*, *87*, 301–311.

Cereceda, P., Larrain, H., Osses, P., Farías, M., & Egaña, I. (2008b). The spatial and temporal variability of fog and its relation to fog oases in the Atacama Desert, Chile. *Atmospheric Research*, *87*, 312–323.

Cereceda, P., Larrain, H., Osses, P., Lazaro, P., Garcia, J., & V. Hernandez (2000). El factor clima en la floración del desierto en los años "El Niño" 1991 y 1997. *Revista de geografía Norte Grande*, *27*, 37–52.

Cereceda, P., Osses, P., Larrain, H., Farías, M., Lagos, M., Pinto, R., & Schemenauer, R. (2002). Advective , orographic and radiation fog in the ´ region , Chile Tarapaca. *Atmospheric Research*, *64*, 261–271.

Cereceda, P., Schemenauer, R. S., & Cereceda P, S. R. (1991). The occurrence of fog in Chile. *Journal of Applied Meteorology*, *30*, 1097–1105.

Chang, E. K. (1995). The influence of hadley circulation intensity changes on extratropical climate in an idealized model. *Journal of Atmospheric Sciences*, *52*, 2006–2024.

Charnock, H. (1955). Wind stress on a water surface. *Quarterly Journal of the Royal Meteorological Society*, *81*, 639–640.

Crawford, T. M., & Duchon, C. E. (1999). An improved parameterization for estimating effective atmospheric emissivity for use in calculating daytime downwelling longwave radiation. *Journal of Applied Meteorology*, *38*, 474–480.

Dee, D. P., Uppala, S. M., Simmons, A., Berrisford, P., Poli, P., Kobayashi, S., Andrae, U., Balmaseda, M., Balsamo, G., Bauer, d. P. et al. (2011). The era-interim reanalysis: Configuration and performance of the data assimilation system. *Quarterly Journal of the royal meteorological society*, *137*, 553–597.

Demergasso, C., Chong, G., Galleguillos, P., Escudero, L., Martínez-Alonso, M., & Esteve, I. (2003). Tapetes microbianos del salar de llamará, norte de chile. *Revista chilena de historia natural*, *76*, 485–499.

Dibike, Y. B., & Coulibaly, P. (2006). Temporal neural networks for downscaling climate variability and extremes. *Neural networks*, *19*, 135–144.

DIHA-PUC (2009). Hydrogeological characterization for the development of new water supply sources in priority areas in northern Chile, regions XV, I., II and III. *In Final Report VIII, Pilot System, 1st Region: Salar Del Huasco., Department Ingeniería Hidráulica y Ambiental, Pontificia Universidad Católica de Chile and Dirección General de Aguas: Santiago, Chile, 2009*.

Dorador, C., Vila, I., Imhoff, J. F., & Witzel, K. P. (2008). Cyanobacterial diversity in salar de huasco, a high altitude saline wetland in northern chile: an example of geographical dispersion? *FEMS microbiology ecology*, *64*, 419–432.

Dorador, C., Vila, I., Remonsellez, F., Imhoff, J. F., & Witzel, K.-P. (2010). Unique clusters of archaea in salar de huasco, an athalassohaline evaporitic basin of the chilean altiplano. *FEMS Microbiology Ecology*, *73*, 291–302.

Dorador, C., Vila, I., Witzel, K.-P., Imhoff, J. F. et al. (2013). Bacterial and archaeal diversity in high altitude wetlands of the chilean altiplano. *Fundam. Appl. Limnol*, *182*, 135–159.

Duynkerke, P. G., Zhang, H. Q., & Jonker, P. J. (1995). Microphysical and Turbulent Structure of Nocturnal Stratocumulus as Observed during ASTEX. *Journal of the Atmospheric Sciences*, *52*, 2763–2777.

Dyer, A. (1967). The turbulent transport of heat and water vapour in an unstable atmosphere. *Quarterly Journal of the Royal Meteorological Society*, *93*, 501–508.

Echeverría, S., Hausner, M. B., Bambach, N., Vicuña, S., & Suárez, F. (2020). Modeling present and future ice covers in two antarctic lakes. *Journal of Glaciology*, *66*, 11–24.

Eder, F., De Roo, F., Kohnert, K., Desjardins, R. L., Schmid, H. P., & Mauder, M. (2014). Evaluation of two energy balance closure parametrizations. *Boundary-layer meteorology*, *151*, 195–219.

Ek, M. B., Mitchell, K. E., Lin, Y., Rogers, E., Grunmann, P., Koren, V., Gayno, G., & Tarpley, J. D. (2003). Implementation of Noah land surface model advances in the National Centers for Environmental Prediction operational mesoscale Eta model. *Journal of Geophysical Research D: Atmospheres*, *108*, 1–16.

van der Ent, R. J. (2014). A new view on the hydrological cycle over continents. *PhD Thesis, TU Delft*, .

van der Ent, R. J., Savenije, H. H., Schaefli, B., & Steele-Dunne, S. C. (2010). Origin and fate of atmospheric moisture over continents. *Water Resources Research*, *46*.

Evans, J., McNeil, D., Finch, J., Murray, T., Harding, R., Ward, H., & Verhoef, A. (2012). Determination of turbulent heat fluxes using a large aperture scintillometer over undulating mixed agricultural terrain. *Agricultural and Forest Meteorology*, *166*, 221–233.

Falvey, M., & Garreaud, R. D. (2005). Moisture variability over the South American

Altiplano during the South American low level jet experiment (SALLJEX) observing season. *Journal of Geophysical Research Atmospheres*, *110*, 1–12.

Falvey, M., & Garreaud, R. D. (2009). Regional cooling in a warming world: Recent temperature trends in the southeast pacific and along the west coast of subtropical south america (1979–2006). *Journal of Geophysical Research: Atmospheres*, *114*.

Farías, M., Cereceda, P., Osses, P., & Cárdenas, R. N. (2005). Comportamiento espacio-temporal de la nube estratocúmulo, productora de niebla en la costa del desierto de Atacama (21° lat. S., 70° long. W.), durante un mes de invierno y otro de verano. *Investigaciones Geograficas*, *56*, 43–61.

Foken, T. (2008). The energy balance closure problem: an overview. *Ecological Applications*, *18*, 1351–1367.

Fratini, G., & Mauder, M. (2014). Towards a consistent eddy-covariance processing: an intercomparison of eddypro and tk3. *Atmospheric Measurement Techniques*, *7*, 2273–2281.

de la Fuente, A. (2014). Heat and dissolved oxygen exchanges between the sediment and water column in a shallow salty lagoon. *Journal of Geophysical Research: Biogeosciences*, *119*, 1129–1146.

de la Fuente, A., & Meruane, C. (2017). Spectral model for long-term computation of thermodynamics and potential evaporation in shallow wetlands. *Water Resources Research*, *53*, 7696–7715.

de la Fuente, A., Meruane, C., & Suarez, F. (2021). Long-term spatiotemporal variability in high andean wetlands in northern chile. *Science of the Total Environment*, *756*, 143830.

de la Fuente, A., & Niño, Y. (2010). Temporal and spatial features of the thermohydrodynamics of shallow salty lagoons in northern Chile. *Limnology and Oceanography*, *55*, 279–288.

Garratt, J. R. (1992). *The Atmospheric Boundary Layer*. Cambridge University Press.

Garreaud, R., & Aceituno, P. (2001). Interannual rainfall variability over the south american altiplano. *Journal of climate*, *14*, 2779–2789.

Garreaud, R., Vuille, M., & Clement, A. C. (2003). The climate of the altiplano: observed current conditions and mechanisms of past changes. *Palaeogeography, palaeoclimatology, palaeoecology*, *194*, 5–22.

Garreaud, R. D., & Muñoz, R. (2004). The diurnal cycle in circulation and cloudiness over the subtropical southeast Pacific: A modeling study. *Journal of Climate*, *17*, 1699–1710.

Green, A., Astill, M., McAneney, K., & Nieveen, J. (2001). Path-averaged surface fluxes determined from infrared and microwave scintillometers. *Agricultural and forest mete-*

orology, *109*, 233–247.

Gunson, A., Klein, B., Veiga, M., & Dunbar, S. (2012). Reducing mine water requirements. *Journal of Cleaner Production*, *21*, 71–82.

Haghighi, E., Short Gianotti, D. J., Akbar, R., Salvucci, G. D., & Entekhabi, D. (2018). Soil and atmospheric controls on the land surface energy balance: A generalized framework for distinguishing moisture-limited and energy-limited evaporation regimes. *Water Resources Research*, *54*, 1831–1851.

Hartogensis, O., Watts, C., Rodriguez, J., & de Bruin, H. (2003). Derivation of an effective height for scintillometers: La poza experiment in northwest mexico. *Journal of Hydrometeorology*, *4*, 915–928.

Hartogensis, O. K. (2006). Exploring Scintillometry in the Stable Atmospheric Surface Layer. *Ph. D. Thesis, Wageningen University & Research, Wageningen, The Netherlands*, .

Hausner, M. B., Suárez, F., Glander, K. E., Giesen, N. v. d., Selker, J. S., & Tyler, S. W. (2011). Calibrating single-ended fiber-optic raman spectra distributed temperature sensing data. *Sensors*, *11*, 10859–10879.

van Heerwaarden, C. C., Vila-Guerau de Arellano, J., Gounou, A., Guichard, F., & Couvreux, F. (2010). Understanding the daily cycle of evapotranspiration: A method to quantify the influence of forcings and feedbacks. *Journal of Hydrometeorology*, *11*, 1405–1422.

van Heerwaarden, C. C., Vilà-Guerau de Arellano, J., Moene, A., & Holtslag, A. (2009). Interactions between dry-air entrainment, surface evaporation and convective boundary-layer development. *Quarterly Journal of the Royal Meteorological Society*, *1291*, 496.

Hernández-López, M. F., Braud, I., Gironás, J., Suárez, F., & Muñoz, J. F. (2016). Modelling evaporation processes in soils from the huasco salt flat basin, chile. *Hydrological Processes*, *30*, 4704–4719.

Hersbach, H., Bell, B., Berrisford, P., Hirahara, S., Horányi, A., Muñoz-Sabater, J., Nicolas, J., Peubey, C., Radu, R., Schepers, D. et al. (2020). The era5 global reanalysis. *Quarterly Journal of the Royal Meteorological Society*, *146*, 1999–2049.

Heusinkveld, B. G., Jacobs, A. F., Holtslag, A. A., & Berkowicz, S. M. (2004). Surface energy balance closure in an arid region: Role of soil heat flux. *Agricultural and Forest Meteorology*, *122*, 21–37.

Higgins, C. W., Pardyjak, E., Froidevaux, M., Simeonov, V., Parlange, M. B., Higgins, C. W., Pardyjak, E., Froidevaux, M., Simeonov, V., & Parlange, M. B. (2013). Measured and Estimated Water Vapor Advection in the Atmospheric Surface Layer. *Journal of Hydrometeorology*, *14*, 1966–1972.

Hill, R. (1997). Algorithms for obtaining atmospheric surface-layer fluxes from scintillation measurements. *Journal of Atmospheric and Oceanic Technology*, *14*, 456–467.

Hill, R., Clifford, S., & Lawrence, R. S. (1980). Refractive-index and absorption fluctuations in the infrared caused by temperature, humidity, and pressure fluctuations. *JOSA*, *70*, 1192–1205.

Hogan, R. J., Gaussiat, N., & Illingworth, A. J. (2005). Stratocumulus liquid water content from dual-wavelength radar. *Journal of Atmospheric and Oceanic Technology*, *22*, 1207–1218.

Holtslag, A., & Van Ulden, A. (1983). A simple scheme for daytime estimates of the surface fluxes from routine weather data. *Journal of Applied Meteorology and Climatology*, *22*, 517–529.

Hong, S. Y., Noh, Y., & Dudhia, J. (2006). A new vertical diffusion package with an explicit treatment of entrainment processes. *Monthly Weather Review*, *134*, 2318–2341.

Horst, T., & Weil, J. (1992). Footprint estimation for scalar flux measurements in the atmospheric surface layer. *Boundary-Layer Meteorology*, *59*, 279–296.

Houston, J. (2006a). Evaporation in the atacama desert: An empirical study of spatio-temporal variations and their causes. *Journal of Hydrology*, *330*, 402–412.

Houston, J. (2006b). Variability of precipitation in the atacama desert: its causes and hydrological impact. *International Journal of Climatology: A Journal of the Royal Meteorological Society*, *26*, 2181–2198.

Huerta-Viso, A. (2021). Estimating evaporation of a salt lake in the Atacama Desert with standard meteorological station data. *M. Sc. Thesis, Wageningen University & Research, Wageningen, The Netherlands*, .

Iacono, M. J., Delamere, J. S., Mlawer, E. J., Shephard, M. W., Clough, S. A., & Collins, W. D. (2008). Radiative forcing by long-lived greenhouse gases: Calculations with the AER radiative transfer models. *Journal of Geophysical Research Atmospheres*, *113*, 2–9.

Janjić, Z. I. (1996). The surface layer in the NCEP ETA model. In *Eleventh Conference on Numerical Weather Prediction, American Meteorological Society* (pp. 19–23).

Jiménez, P. A., de Arellano, J. V. G., Dudhia, J., & Bosveld, F. C. (2016). Role of synoptic- and meso-scales on the evolution of the boundary-layer wind profile over a coastal region: the near-coast diurnal acceleration. *Meteorology and Atmospheric Physics*, *128*, 39–56.

Johnson, E., Yáñez, J., Ortiz, C., & Muñoz, J. (2010). Evaporation d'eaux souterraines peu profoundes dans des bassins endoreiques de I'Altiplano Chilien. *Hydrological Sciences Journal*, *55*, 624–635.

Kain, J. S., & Fritsch, J. M. (1993). Convective Parameterization for Mesoscale Models:

The Kain-Fritsch Scheme. *The Representation of Cumulus Convection in Numerical Models*, (pp. 165–170).

Kampf, S. K., Tyler, S. W., Ortiz, C. A., Muñoz, J. F., & Adkins, P. L. (2005). Evaporation and land surface energy budget at the Salar de Atacama, Northern Chile. *Journal of Hydrology*, *310*, 236–252.

Kimball, B., & Jackson, R. (1975). Soil heat flux determination: a null-alignment method. *Agricultural Meteorology*, *15*, 1–9.

Klemm, O. et al. (2012). Fog as a fresh-water resource: Overview and perspectives. *Ambio*, *41*, 221–234.

Klemp, J. B., Dudhia, J., & Hassiotis, A. D. (2008). An upper gravity-wave absorbing layer for NWP applications. *Monthly Weather Review*, *136*, 3987–4004.

Kohsiek, W., & Herben, M. (1983). Evaporation derived from optical and radio-wave scintillation. *Applied optics*, *22*, 2566–2570.

Kolmogorov, A. N. (1941). The local structure of turbulence in incompressible viscous fluid for very large reynolds numbers. *Cr Acad. Sci. URSS*, *30*, 301–305.

Kooijmans, L. M., & Hartogensis, O. K. (2016). Surface-layer similarity functions for dissipation rate and structure parameters of temperature and humidity based on eleven field experiments. *Boundary-Layer Meteorology*, *160*, 501–527.

Kumar, A., & Wen, C. (2016). An oceanic heat content–based definition for the pacific decadal oscillation. *Monthly Weather Review*, *144*, 3977–3984.

Kumar, J., Brooks, B.-G. J., Thornton, P. E., & Dietze, M. C. (2012). Sub-daily statistical downscaling of meteorological variables using neural networks. *Procedia Computer Science*, *9*, 887–896.

Lagouarde, J.-P., Bonnefond, J.-M., Kerr, Y., McAneney, K., & Irvine, M. (2002). Integrated sensible heat flux measurements of a two-surface composite landscape using scintillometry. *Boundary-layer meteorology*, *105*, 5–35.

Leclerc, M. Y., & Foken, T. (2014). *Footprints in micrometeorology and ecology* volume 239. Springer.

LePage, B. A. (2011). *Wetlands: integrating multidisciplinary concepts*. Springer Science & Business Media.

Li, D., Bou-Zeid, E., & de Bruin, H. A. (2012). Monin–obukhov similarity functions for the structure parameters of temperature and humidity. *Boundary-layer meteorology*, *145*, 45–67.

Lictevout, E., Maass, C., Córdoba, D., Herrera, V., & Payano, R. (2013). *Recursos Hídricos de la Región de Tarapacá - diagnóstico y sistematización de la información*.

Lobos-Roco, F., Hartogensis, O., Vilà-Guerau de Arellano, J., Aguirre, F., de la Fuente,

A., & Suárez, F. (2021a). Optical-Microwave Scintillometer Evaporation measurements over a Saline Lake in a Heterogeneous Setting in the Atacama Desert. (Manuscript Under Review). *Journal of Hydrometeorology*, (pp. –).

Lobos-Roco, F., Hartogensis, O., Vilà-Guerau de Arellano, J., de la Fuente, A., Muñoz, R., Rutllant, J., & Suárez, F. (2021b). Local Evaporation Controlled by Regional Atmospheric Circulation in the Altiplano of the Atacama Desert. *Atmospheric Chemistry and Physics*, *21-11*, 1–38.

Lobos-Roco, F., Hartogensis, O., Vilà, J., Fuente, A. d. l., & Suarez, F. (2020). Dataset of local evaporation controlled by regional atmospheric circulation in the altiplano of the atacama desert, .

Lobos-Roco, F., Vilà-Guerau de Arellano, J., & Pedruzo-Bagazgoitia, X. (2018). Characterizing the influence of the marine stratocumulus cloud on the land fog at the Atacama Desert. *Atmospheric Research*, *214*, 109–120.

Lüdi, A., Beyrich, F., & Matzler, C. (2005). Determination of the turbulent temperature–humidity correlation from scintillometric measurements. *Boundary-layer meteorology*, *117*, 525–550.

Ma, H. Y. et al. (2018). CAUSES: On the Role of Surface Energy Budget Errors to the Warm Surface Air Temperature Error Over the Central United States. *Journal of Geophysical Research: Atmospheres*, *123*, 2888–2909.

Mahrt, L., Vickers, D., Sun, J., Jensen, N. O., Jørgensen, H., Pardyjak, E., & Fernando, H. (2001). Determination of the surface drag coefficient. *Boundary-Layer Meteorology*, *99*, 249–276.

Massman, W. (2000). A simple method for estimating frequency response corrections for eddy covariance systems. *Agricultural and Forest Meteorology*, *104*, 185–198.

Mauder, M., & Foken, T. (2004). Documentation and instruction manual of the eddy covariance software package TK2 Arbeitsergebn. *University of Bayreuth, Abt Mikrometeorolgy*, *26*, 42.

Mauder, M., Oncley, S. P., Vogt, R., Weidinger, T., Ribeiro, L., Bernhofer, C., Foken, T., Kohsiek, W., de Bruin, H. A., & Liu, H. (2007). The energy balance experiment ebex-2000. part ii: Intercomparison of eddy-covariance sensors and post-field data processing methods. *Boundary-Layer Meteorology*, *123*, 29–54.

McColl, K. A., Salvucci, G. D., & Gentine, P. (2019). Surface flux equilibrium theory explains an empirical estimate of water-limited daily evapotranspiration. *Journal of Advances in Modeling Earth Systems*, *11*, 2036–2049.

McNaughton, K. G. (1976). Evaporation and advection II: evaporation downwind of a boundary separating regions having different surface resistances and available energies. *Quarterly Journal of the Royal Meteorological Society*, *102*, 193–202.

Meijninger, W., Beyrich, F., Ludi, A., Kohsiek, W., & Bruin, H. D. (2006). Scintillometer-based turbulent fluxes of sensible and latent heat over a heterogeneous land surface–a contribution to litfass-2003. *Boundary-Layer Meteorology*, *121*, 89–110.

Meijninger, W., Hartogensis, O., Kohsiek, W., Hoedjes, J., Zuurbier, R., & de Bruin, H. (2002a). Determination of area-averaged sensible heat fluxes with a large aperture scintillometer over a heterogeneous surface–flevoland field experiment. *Boundary-Layer Meteorology*, *105*, 37–62.

Minvielle, M., & Garreaud, R. D. (2011). Projecting rainfall changes over the South American Altiplano. *Journal of Climate*, *24*, 4577–4583.

Moene, A. F., & Van Dam, J. C. (2014). *Transport in the atmosphere-vegetation-soil continuum*. Cambridge University Press.

Monin, A. S., & Obukhov, A. M. (1954). Basic laws of turbulent mixing in the surface layer of the atmosphere. *Contrib. Geophys. Inst. Acad. Sci. USSR*, *151*, e187.

Monteith, J. L. (1965). Evaporation and environment. In *Symposia of the Society for Experimental Biology* (pp. 205–234). volume 19.

Muñoz, R. C., Falvey, M. J., Arancibia, M., Astudillo, V. I., Elgueta, J., Ibarra, M., Santana, C., & Vásquez, C. (2018). Wind energy exploration over the Atacama Desert : A numerical model-guided observational program. *Bulletin of the American Meteorological Society*, *99*, 2079–2092.

Muñoz, R. C., Zamora, R. A., & Rutllant, J. A. (2011). The coastal boundary layer at the eastern margin of the southeast Pacific (23.4°S, 70.4°W): cloudiness-conditioned climatology. *Journal of Climate*, *24*, 1013–1033.

Muñoz-Schick, M., Pinto, R., Mesa, A., & Moreira-muñoz, A. (2001). El Niño 1997-1998 Fog oases during the El Niño Southern Oscillation 1997-1998 , in the hills south of Iquique , Tarapacá region , Chile. *Revista Chilena de Historia Natural*, *74*, 1–14.

Neftel, A., Spirig, C., & Ammann, C. (2008). Application and test of a simple tool for operational footprint evaluations. *Environmental Pollution*, *152*, 644–652.

Nordbo, A., Launiainen, S., Mammarella, I., Lepparanta, M., Huotari, J., Ojala, A., & Vesala, T. (2011). Long-term energy flux measurements and energy balance over a small boreal lake using eddy covariance technique. *Journal of Geophysical Research: Atmospheres*, *116*.

Oroud, I. (1999). Temperature and evaporation dynamics of saline solutions. *Journal of Hydrology*, *226*, 1–10.

Osses, P., Barría, C., Farías, M., & Cereceda, P. (2005). La nube estratocúmulo en Tarapacá, Chile. Validación de imágenes GOES mediante observación en tiempo real (17 al 26 de julio del año 2002).

Oyarzún, J., & Oyarzún, R. (2011). Sustainable development threats, inter-sector con-

flicts and environmental policy requirements in the arid, mining rich, Northern Chile territory. *Sustainable Development*, *19*, 263–274.

Pastorello, G., Trotta, C., Canfora, E., Chu, H., Christianson, D., Cheah, Y.-W., Poindexter, C., Chen, J., Elbashandy, A., Humphrey, M. et al. (2020). The fluxnet2015 dataset and the oneflux processing pipeline for eddy covariance data. *Scientific data*, *7*, 1–27.

Paulson, C. A. (1970). The mathematical representation of wind speed and temperature profiles in the unstable atmospheric surface layer. *Journal of Applied Meteorology and Climatology*, *9*, 857–861.

Penman, H. (1948). Natural evaporation from open water, bare soil and grass. *Proceedings of the Royal Society of London. Series A. Mathematical and Physical Sciences*, *193*, 120–145.

Philander, S. (1985). El niño and la niña. *Journal of Atmospheric Sciences*, *42*, 2652–2662.

Philander, S. G. H. (1983). El niño southern oscillation phenomena. *Nature*, *302*, 295–301.

Philip, J. (1987). Advection, evaporation, and surface resistance. *Irrigation science*, *8*, 101–114.

Raynor, G. S., Sethuraman, S., & Brown, R. M. (1979). Formation and Characteristics of Coastal Internal Boundary Layers During Onshore Flows. *Boundary-Layer Meteorology*, *16*, 487–514.

Revsbech, N. P., Madsen, B., & Jørgensen, B. (1986). Oxygen production and consumption in sediments determined at high spatial resolution by computer simulation of oxygen microelectrode data. *Limnol. Oceanogr*, *31*, 293–304.

del Río, C., Lobos-Roco, F., Latorre, C., Koch, M. A., García, J.-L., Osses, P., Lambert, F., Alfaro, F., & Siegmund, A. (2021). Spatial distribution and interannual variability of coastal fog and low clouds cover in the hyperarid atacama desert and implications for past and present tillandsia landbeckii ecosystems. *Plant Systematics and Evolution*, *307*, 1–23.

del Río, C., Rivera, D., Siegmund, A., Wolf, N., Cereceda, P., Larraín, H., Lobos-Roco, F., Garcia, J.-L., Osses, P., Zanetta, N., & Lambert, F. (2018). ENSO Influence on Coastal Fog-Water Yield in the Atacama Desert, Chile. *Aerosol and Air Quality Research*, *18*, 127–144.

Rosen, M. R. (1994). *The importance of groundwater in playas: A review of playa classifications*.

Rutllant, J., Fuenzalida, H., & Aceituno, P. (2003). Climate dynamics along the arid northern coast of Chile: The 1997-1998 Dinámica del Clima de la Región de Antofagasta (DICLIMA) experiment. *Journal of Geophysical Research D: Atmospheres*, *108*, 1–13.

Rutllant, J., Muñoz, R. C., & Garreaud, R. D. (2013). Meteorological observations on the

northern Chilean coast during VOCALS-REx. *Atmospheric Chemistry and Physics*, *13*, 3409–3422.

Rutllant, J., & Ulriksen, P. (1979). Boundary-layer dynamics of the extremely arid northern part of Chile - The Antofagasta Field Experiment. *Boundary-Layer Meteorology*, *17*, 41–55.

Salhotra, A. M., Adams, E. E., & Harleman, D. R. (1985). Effect of salinity and ionic composition on evaporation: Analysis of dead sea evaporation pans. *Water Resources Research*, *21*, 1336–1344.

Schemenauer, R. S., & Cereceda, P. (1994a). A Proposed Standard Fog Collector for Use in High-Elevation Regions. *Journal of Applied Meteorology*, *33*, 1313–1322.

Schemenauer, R. S., & Cereceda, P. (1994b). Fog collection's role in water planning for developing countries. *Natural Resources Forum*, *18*, 91–100.

Schewe, J. et al. (2014). Multimodel assessment of water scarcity under climate change. *PNAS*, *111*, 3245–3250.

Schuepp, P., Leclerc, M., MacPherson, J., & Desjardins, R. (1990). Footprint prediction of scalar fluxes from analytical solutions of the diffusion equation. *Boundary-Layer Meteorology*, *50*, 355–373.

Shuttleworth, W. J. (2008). Evapotranspiration measurement methods. *Southwest Hydrology*, *7*, 22–23.

Skamarock, W. C., Klemp, J. B., Dudhia, J., Gill, D. O., Barker, D. M., Wang, W., & Powers, J. G. (2008). *A description of the Advanced Research WRF version 3*. Technical Report, .

Stevens, B. et al. (2003). Dynamics and Chemistry of Marine Stratocumulus - DYCOMS-II. *Bulletin of the American Meteorological Society*, *84*, 579–593.

Stoffer, R. (2018). Revisiting Raw Data Processing of Combined Optical-Microwave Scintillometers. *M. Sc. Thesis, Wageningen University & Research, Wageningen, The Netherlands*, .

Stull, R. B. (1988). *An Introduction to Boundary Layer Meteorology*. Springer Sciences and Bussines Media.

Suárez, F., Aravena, J., Hausner, M., Childress, A., & Tyler, S. (2011). Assessment of a vertical high-resolution distributed-temperature-sensing system in a shallow thermohaline environment. *Hydrology and Earth System Sciences*, *15*, 1081–1093.

Suárez, F., Lobos-Roco, F., de la Fuente, A., Vilà-Guerau de Arellano, J., Prieto, A., Meruane, C., & Hartogensis, O. (2020). E-data: A comprehensive field campaign to investigate evaporation enhanced by advection in the hyper-arid altiplano. *Water*, *12*, 745.

Sugita, M., & Brutsaert, W. (1993). Cloud effect in the estimation of instantaneous downward longwave radiation. *Water Resources Research*, *29*, 599–605.

Sullivan, P. P., Moeng, C.-H., Stevens, B., Lenschow, D. H., & Mayor, S. D. (1998). Structure of the entrainment zone capping the convective atmospheric boundary layer. *Journal of the atmospheric sciences*, *55*, 3042–3064.

Tanny, J., Cohen, S., Assouline, S., Lange, F., Grava, A., Berger, D., Teltch, B., & Parlange, M. B. (2008). Evaporation from a small water reservoir: Direct measurements and estimates. *Journal of Hydrology*, *351*, 218–229.

Tatarski, V. (1961). Wave propagation: Wave propagation in a turbulent medium. vi tatarski. translated by ra silverman. mcgraw-hill, new york, 1961. 285 pp. *Science*, *134*, 324–325.

Timmermann, A., An, S.-I., Kug, J.-S., Jin, F.-F., Cai, W., Capotondi, A., Cobb, K. M., Lengaigne, M., McPhaden, M. J., Stuecker, M. F. et al. (2018). El niño–southern oscillation complexity. *Nature*, *559*, 535–545.

Uribe, J., Munoz, J. F., Gironas, J., Oyarzun, R., Aguirre, E., & Aravena, R. (2015). Assessing groundwater recharge in an andean closed basin using isotopic characterization and a rainfall-runoff model: Salar del huasco basin, chile. *Hydrogeology Journal*, *23*, 1535–1551.

USGS (2021). U.S. Geological Survey, 2021. *Mineral commodity summaries 2021*, *https://doi.org/10.3133/mcs2021*, p. 0–200.

Vergara-Alvarado, J. (2017). Estudio de la variabilidad intradiaria de los flujos de calor, masa y moméntum en la interfaz aire-agua de una laguna somera salina del Altiplano chileno. *Universidad de Chile, Disponible en http://repositorio.uchile.cl/handle/2250/146416*, .

Vickers, D., & Mahrt, L. (1997). Quality Control and Flux Sampling Problems for Tower and Aircraft Data. *Journal of Atmospheric and Oceanic Technology*, *14*, 512–526.

Vilà G. A., J., van Heerwaarden, C. C., van Stratum, B. J., & Van Den Dries, K. (2015). *Atmospheric Boundary Layer. Integrating Air Chemistry and Land Interactions*. Cambridge University Press.

Vuille, M., Bradley, R. S., & Keimig, F. (2000). Interannual climate variability in the central andes and its relation to tropical pacific and atlantic forcing. *Journal of Geophysical Research: Atmospheres*, *105*, 12447–12460.

Ward, H., Evans, J., Hartogensis, O., Moene, A., de Bruin, H., & Grimmond, C. (2013). A critical revision of the estimation of the latent heat flux from two-wavelength scintillometry. *Quarterly Journal of the Royal Meteorological Society*, *139*, 1912–1922.

Ward, H., Evans, J. G., Grimmond, C. S. B., & Bradford, J. (2015). Infrared and millimetre-wave scintillometry in the suburban environment–part 1: Structure param-

eters. *Atmospheric Measurement Techniques*, *8*, 1385–1405.

Weischet, W. (1975). Las condiciones climaticas del desierto de Atacama como desierto extremos de la tierra. *Revista de Geografia Norte Grande*, *1*.

Wetzel, P. J. (1990). A Simple Parcel Method for Prediction of Cumulus Onset and Area-Averaged Cloud Amount over Heterogeneous Land Surfaces. *Journal Of Applied Meteorology*, *29*, 516–524.

Wetzel, P. J., & Boone, A. (1995). A parameterization for land-atmosphere-cloud exchange (PLACE): documentation and testing of a detailed process model of the partly cloudy boundary layer over heterogeneous land. *Journal of Climate*, *8*, 1810–1837.

Whiteman, C. D. (1989). Morning Transition Tracer Experiments in a Deep Narrow Valley. *Journal of Applied Meteorology*, *28*, 626–635.

Whiteman, D., Pospichal, B., Eisenbach, S., Weihs, P., Clements, C. B., Steinacker, R., Mursch-Radlgruber, E., & Dorninger, M. (2004). Inversion breakup in small Rocky Mountain and Alpine basins. *Journal of Applied Meteorology*, *43*, 1069–1082.

Wieringa, J. (1976). An objective exposure correction method for average wind speeds measured at a sheltered location. *Quarterly Journal of the Royal Meteorological Society*, *102*, 241–253.

Wilczak, J. M., Oncley, S. P., & Stage, S. A. (2001). Sonic Anemometer Tilt Correction Algorithms. *Boundary-Layer Meteorology*, *99*, 127–150.

Williams, W., Carrick, T., Bayly, I., Green, J., & Herbst, D. (1995). Invertebrates in salt lakes of the bolivian altiplano. *International Journal of Salt Lake Research*, *4*, 65–77.

Wyngaard, J., Izumi, Y., & Collins, S. A. (1971). Behavior of the refractive-index-structure parameter near the ground. *JOSA*, *61*, 1646–1650.

Zhang, C., Wang, Y., & Hamilton, K. (2011). Improved Representation of Boundary Layer Clouds over the Southeast Pacific in ARW-WRF Using a Modified Tiedtke Cumulus Parameterization Scheme *. *Monthly Weather Review*, *139*, 3489–3513.

Zúñiga, L., Campos, V., Pinochet, H., & Prado, B. (1991). A limnological reconnaissance of lake tebenquiche, salar de atacama, chile. *Hydrobiologia*, *210*, 19–24.

Acknowledgements

I've spent the last four years immersed in science, working in different countries, time zones, and climates. This would not have been possible without the help and support of all the people that have surrounded me.

Quiero agradecer primero a mi familia, a mi madre Magaly Roco por impulsarme desde niño a los estudios (y a veces por obligación durante los veranos!) y por recordarme que al publicar honre a mi padre y madre (Lobos-Roco et al.). A mi padre Andres Lobos, por celebrar con entusiasmo cada uno de mis logros y por apoyarme en absolutamente todo, incluso cuando estoy equivocado. Y, a mis hermanes Micaela, Natalia y Alonso, por estar siempre presentes cuando los necesito para sufrir o reír.

Quiero agradecer y recordar especialmente a Felipe Herrera Urrutia (†), quien me inspiró a seguir el camino de las ciencias y me mostró el rigor, pasión y entusiasmo con el que se consiguen las cosas. No puedo dejar de mencionar a Eleonora Fiorin (grazie mille) por todo su apoyo y amor durante estos años de presencias y ausencias, por mostrarme que, trabajando duro, todo se puede y por la increible portada de esta tesis. También, a nuestro perro Amaru Alexis, que gracias a sus miradas y jugarretas, tuve las pausas necesarias para pensar, respirar y avanzar. I want to especially thank my supervisors, Jordi, Oscar, and Francisco, for their work on my formation. To Jordy, for being like a father in science, guiding me in every single step from the moment he saw me, drinking mate, in the MSc thesis market until the PhD defense. To Oscar for teaching me his technical field skills, writing tricks, and sharing his passion for science. Finally, to Francisco for believing in me since the beginning and always trusting my decisions. I really hope to keep doing science with you.

I also thank my friends (and paranymphs) Santiago Botía for his help, support, and friendship in our eternal cycling tours. Also, to Auke Visser for all his help with the defense ceremony and party. I thank the entire MAQ team from Wageningen University for making me part of the team. Especially to Kees, Reinder, Xabi, Imme, Alba, Sandra, Aris, Ruben and Sjoerd. I also would like to thank all people from the Pontificia Universidad Católica de Chile involved in this journey, Camilo del Río, Francisca Aguirre, Matias[2], Raul and Mane. But also, people from Universidad de Chile, Alberto de la Fuente, Ricardo Muñoz and Jose Rutllant. Un especial agradecimiento a Pedro Luca y su familia, por el

apoyo que nos brindaron en su hermoso Salar del Huasco.

A mis amigos latinos, quienes cumplieron el rol de la familia en Holanda, a Alejandro, Cristina, Felipe C., Francisco, Eka y Dani, y a mis amigos chilenos de Saonda Decap, Rodolfo y Bucci, por todos estos años de amistad, consejos y apoyo incondicional. Also, I thank Xavier, Escarcha, Nachito, Loeki, Joeri, Alex, Laci, and lately, Francisca (obrigado) and Aureo, for always being there when I needed them to clear my mind climbing or just sharing. Finalmente a mis amigos de Iquique, Fran, Teo, Julio, Eduardo, Chopo, Denisse y Pablo que estuvieron siempre atentos a mi trabajo y salud mental.

About the author

My life has always been driven by three main things: music, climbing, and science. However, in defining moments, I have always chosen science.

I was born in the green and wet southern Chile, on the entrance of Patagonia. In my younger years, I moved to Iquique, my parent's hometown, in the driest place on Earth: the Atacama Desert. There, I completed my schooling while developing my musical skills. When I finished school, I had to decide whether to follow a musical career or keep studying. Inspired by the landscapes of the Atacama Desert, I decided to study Earth Sciences.

To do it, I had to move back to the south, this time to Santiago, where I studied geography at the Pontificia Universidad Católica de Chile. There, I confirmed my interest in the Atacama Desert, doing a BSc thesis about the spatiotemporal changes on one of the unique glaciers of this desert. During my BSc, I also developed my passion for rock climbing and mountaineering. After my Bachelor studies, I started working in a research station specialized in fog collection in the Atacama Desert. There, I silently collected meteorological data for four years. During these working years, I started my climbing entrepreneurship, which allowed me to climb every rock in that desert. After these four years, I was awarded a scholarship to pursue an MSc in Climate Studies at Wageningen University (WUR), the Netherlands. At that moment, I had to decide if I would continue the climbing path or renounce it to keep studying, and once again I chose science.

I started the MSc at WUR in 2015, and I did my thesis about the physical influence of the marine stratocumulus cloud in the land fog formation system. After my MSc thesis, the Meteorology and Air Quality group of WUR offered me a PhD for investigating the evaporation at the saline lakes of the Altiplano Region of the Atacama Desert. I accepted, choosing science once more, this time probably forever.

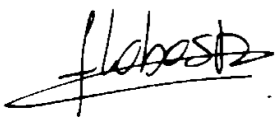

Peer-reviewed journal publications

Lobos-Roco, F., Vilà-Guerau de Arellano, J., & Pedruzo-Bagazgoitia, X. (2018). Characterizing the influence of the marine stratocumulus cloud on the land fog at the Atacama Desert. *Atmospheric Research*, 214, p. 109–120.

Lobos-Roco, F., Hartogensis, O., Vilà-Guerau de Arellano, J., de la Fuente, A., Muñoz, R., Rutllant, J., & Suárez, F. (2021). Local evaporation controlled by regional atmospheric circulation in the Altiplano of the Atacama desert. *Atmospheric Chemistry and Physics*, (pp. 1–38).

Lobos-Roco, F., Hartogensis, O., Vilà-Guerau de Arellano, J., Aguirre, F., de la Fuente, A., & Suárez, F. (2021). Optical-microwave scintillometer evaporation measurements over a saline lake in a heterogeneous setting in the Atacama Desert. (Manuscript under revision). *Journal of Hydrometeorology*.

Lobos-Roco, F., Hartogensis, O., Suárez, F., Huerta-Viso, A., Benedict, I., de la Fuente, A. & Vilà-Guerau de Arellano, J. (2021). Multi Temporal Analysis of Evaporation on a Saline Lake in the Atacama Desert. (Manuscript under discussion). *Journal of Hydrology and Earth System Sciences*.

Suárez, **F., Lobos-Roco, F.**, De La Fuente, A., Vilà-Guerau de Arellano, J., Prieto, A., Meruane, C., & Hartogensis, O. (2020). E-DATA: A comprehensive field campaign to investigate evaporation enhanced by advection in the hyper-arid altiplano. *Water*, 12, 745.

del Río, C., **Lobos-Roco, F.**, Siegmund, A., Tejos, C., Osses, P., Huaman, Z., Meneses, J. & García, J. L. (2021). GOFOS, ground optical fog observation system for monitoring the vertical stratocumulus-fog cloud distribution in the coast of the Atacama Desert, Chile. *Journal of Hydrology*, 597, 126190.

del Río, C., **Lobos-Roco, F.**, Latorre, C., Koch, M. A., García, J. L., Osses, P., Lambert, F., Alfaro, F. & Siegmund, A. (2021). Spatial distribution and interannual variability of coastal fog and low clouds cover in the hyperarid Atacama Desert and implications for past and present Tillandsia landbeckii ecosystems. *Plant Systematics and Evolution*, 307(5), 1-23.

García, J. L., **Lobos-Roco, F.**, Schween, J. H., del Río, C., Osses, P., Vives, R., Pezoa, M., Siegmund, A., Latorre, C., Alfaro, F., & Loehnert, U. (2021). Climate and coastal low-cloud dynamic in the hyperarid Atacama fog Desert and the geographic distribution of Tillandsia landbeckii (Bromeliaceae) dune ecosystems. *Plant Systematics and Evolution*, 307(5), 1-22.

Netherlands Research School for the
Socio-Economic and Natural Sciences of the Environment

D I P L O M A

for specialised PhD training

The Netherlands research school for the
Socio-Economic and Natural Sciences of the Environment
(SENSE) declares that

Felipe Andrés Lobos Roco

born on June 19th 1987 in Puerto Varas, Chile

has successfully fulfilled all requirements of the
educational PhD programme of SENSE.

Wageningen, 29th March 2022

Chair of the SENSE board

Prof. dr. Martin Wassen

The SENSE Director

Prof. Philipp Pattberg

The SENSE Research School has been accredited by the Royal Netherlands Academy of Arts and Sciences (KNAW)

KONINKLIJKE NEDERLANDSE
AKADEMIE VAN WETENSCHAPPEN

The SENSE Research School declares that **Felipe Andrés Lobos Roco** has successfully fulfilled all requirements of the educational PhD programme of SENSE with a work load of 34.0 EC, including the following activities:

SENSE PhD Courses

- Environmental research in context (2018)
- Research in context activity: 'Organising the Atmosphere-Vegetation-Soil Interaction Workshop and scientific meetings with local researchers' (2018-2019)

Other PhD and Advanced MSc Courses

- Essential of scientific writing and presenting, Wageningen Graduate Schools (2018)
- Poster and Pitching, Wageningen Graduate Schools (2018)
- E-DATA scientific tour 2018, Pontificia Universidad Catolica de Chile (2018)
- Workshop on 'Eddy Covariance systems installation and operation', Direccion de Investigacion, Ciencia y Tecnologia de la Universidad Catolica (2019)
- Workshop: 'Fog in arid regions', Heidelberg University (2021)

Management and Didactic and scientific communication Skills Training

- Assisting in the MSC course 'Field training land-atmospheric interactions' (2019)
- Assisting in the Msc course 'Transporte de Calor en el medio ambiente' (2019-2021).
- Teaching the MSc course 'Natural fundamentals of physical geography' (2021)

Oral Presentations

- *Characterizing the influence of the marine stratocumulus cloud on the land fog at the Atacama Desert*. The coastal fog geo-ecosystems in the Chilean-Peruvian Desert: understanding biosphere-atmosphere interactions, 25-28 November 2019, Iquique, Chile
- E*vaporation measurements with an Optical-Microwave Scintillometer over a Saline Lake bordered by a wet-salt-crust under a Regional-Wind driven turbulence regime*. Water congress, 7-9 July 2021, Online, Chile and the Netherlands

SENSE coordinator PhD education

Dr. ir. Peter Vermeulen

This research received funding from:

Wageningen University Sandwich PhD Programme project no.5160957644, Graduate School of the Wageningen Institute for Environment and Climate Research (WIMEK).

Chilean National Agency of Research and Development through ANID-FONDECYT projects 1170850, 1181222, and 1210221.

Cover design by Eleonora Fiorin